Structural Characterization of Composite Thin-film and Dispersed Phase Conjugated Polymer/Fullerene Composites

Jeffrey John Richards

A dissertation

submitted in partial fulfillment of the

requirements of the degree of

Doctor of Philosophy

University of Washington

2014

Reading Committee:

Lilo Pozzo, Chair

Daniel Schwartz

Hugh Hillhouse

David Ginger

Program Authorized to Offer Degree:

Chemical Engineering

University of Washington

Abstract

Structural Characterization of Composite Thin-film and Dispersed Phase Conjugated Polymer/Fullerene Composites

Jeffrey John Richards

Chair of the Supervisory Committee:

Professor Lilo D. Pozzo

Department of Chemical Engineering

Controlling the structural morphology of conjugated polymer/fullerene composites is an important aspect in improving the performance of polymer solar cells. The efficiency of exciton dissociation and carrier transport to the working electrodes are both a function of the size and distribution of polymer and fullerene domains within the active layer. In the current solution processing paradigm, these characteristics are intrinsically linked to the detailed process history of the film. This fact compromises the promise of polymer solar cells as an inexpensive renewable energy technology because performance gains made in the laboratory may not translate well to scaled-up manufacturing processes. Aqueous dispersions of conjugated polymer/fullerene nanoparticles have the potential to address this challenge. Similar to their thin-film counterparts, the performance of photovoltaic devices derived from conjugated polymer/fullerene composite nanoparticles (CNPs) is a function of the structural morphology within each nanoparticle. However, unlike thin-film active layer produced from organic solvents, the structure of CNPs is fixed during their formulation. Because of this fact, the structure can be identified in the dispersed phase and tied, using single particle characterization, to its photovoltaic performance before it is deposited into a device. Therefore, the optimization of

devices derived from CNPs can be broken into two discrete problems: improving the **intrinsic** properties of a nanoparticle as a function of how it is produced and optimizing the **extrinsic** properties of devices through the deposition of optimized CNPs.

Acknowledgements

"If I have seen further it is by standing on the shoulders of giants."

-Sir Isaac Newton

There are countless individuals who have contributed to the work contained within this thesis. In addition to my advisor, Lilo, I would like to thank the contributions from my committee members. I have had many fruitful discussions with you over the years that have significantly influenced the direction and quality of this research. Thank you also to the Pozzo group members, former and present, and all my collaborators. It is a privilege to have worked with such intelligent, thoughtful and caring individuals.

Also, thank you to the graduate students in the Chemical Engineering Department. I am constantly reminded that the culture in this department is unique and I know that I have benefited both personally and professionally from both the friendships that we developed and many late-night discussions we have had.

Thank you also to the IGERT Bioenergy program as well as the COE Dean's Fellowship program for funding my research.

Dedication

To my wife, Jackie, whose love and support I cherish.

Table of Contents:

List of Figures

List of Tables

Chapter 1: Introduction to Organic Photovoltaics

The development of an inexpensive, highly efficient means to convert solar energy into useful work is of fundamental importance in developing renewable alternatives to energy derived from fossil fuels. Other than geothermal, nuclear, and tidal energy, many of the most abundant, renewable power sources under serious development today rely on transduction of solar radiation to mechanical, electrical, or thermal energy. Photovoltaic devices, as their name implies, convert solar radiation directly to electricity with no intermediate steps. To do so, they require no moving parts, generate only heat as waste, and emit nothing except what is required for their production in order to produce energy.[1] While the advantages of photovoltaic energy are manifold, there are some significant drawbacks.[2] Traditional photovoltaics rely heavily on direct sunlight to function efficiently; therefore, the amount of power derived from a solar installation will vary with weather, time of day, and geospatial location.[3] Another challenge is that the cost to manufacture photovoltaic panels is still relatively capital intensive. The total systems cost as well as poor suitability for solar power delivered to electricity grids remain barriers to further adoption of photovoltaic power as a primary renewable energy source around the world.[4]

Currently, these issues are an active area of research within the scientific community. Improved electrical energy storage in the form of hydrogen production and better batteries has lessened the effects of intermittent power supplied from solar panels to the grid. The promises of smart grid technology will also make it possible to cope better with the intermittent power supplied by the many renewable power sources currently under development.[5] The last few decades have seen incremental reductions in the price of solar panels. This reduction has been driven primarily by the active commercialization of mono- and multi- crystalline silicon solar panels, and thin-film technologies like CdTe/CIGS as shown in Figure 1.1. Many manufacturers in the US, Canada,

China and Japan project increased capacity through the year 2014.[6] To date, module cost has decreased linearly each year as the number of modules shipped has grown exponentially. Currently, leading solar manufacturers sell their Si modules for \$0.30-\$0.70/W_p, which on a sunny day is priced competitively with the average price of electricity in the United States (\$0.28-\$0.60/W).[7] First Solar, a recently founded company that produces CdTe thin-film photovoltaic modules is nearing the price point of Si modules at \$0.70/W_p.[8] These factors combined with federal government subsidy have made photovoltaic energy an option to both individual consumers and large scale power utilities, particularly in regions of the United States with the highest solar insolation.[5] World-wide adoption of solar energy is rapidly increasing with both China and India recently renewing their commitments to expand their renewable energy portfolio of solar and wind.

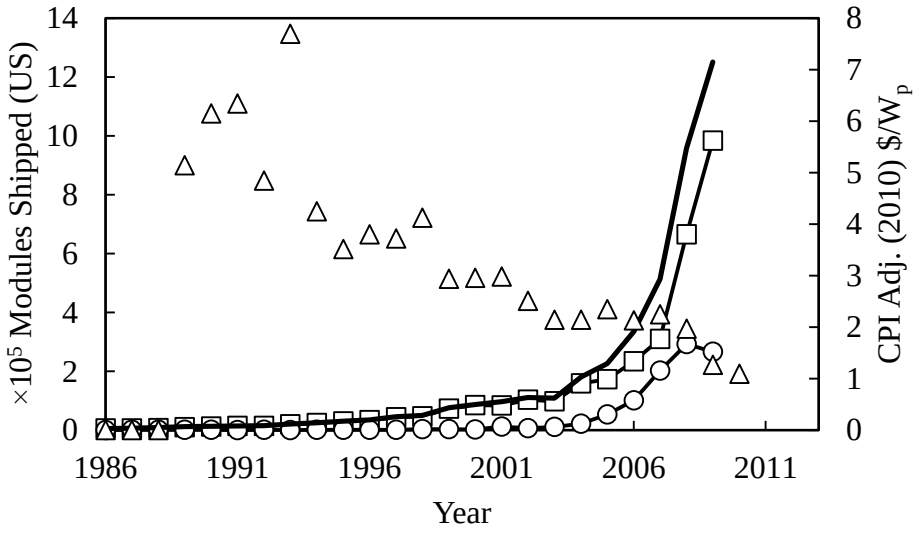

Figure 1.1. Statistics from the Energy Information Administration on solar panel manufacture, and module cost adjusted for inflation using CPI (2010). This figure shows the cost adjusted for consumer price index (CPI) of solar modules per year (triangles), the total number of thin-film (squares) and silicon (circles) modules shipped in the US per year, and the cumulative total of both thin-film and silicon (black line).

In the US, as consumer education has increased as to both the financial and environmental benefits of solar power, demand for photovoltaic modules will increase. In fact, in Hawaii, subsidies encouraging investments in solar power have been so successful (10% of residences have installed PV) that utilities are struggling to now balance supply with peak load demand. The EIA projects that total power consumption in the United States will increase by ~15% over the next 20 years, and the proportion of that power derived from solar energy is projected to nearly double.[7]

The outlook for solar energy production in the United States and around the world is therefore a positive one. As first generation PV technology looks toward the future, there are some challenges on the horizon. In addition to efficiency, materials and manufacturing costs remain the largest contribution to the cost of solar power.[9] Issues including the cost required to produce highly pure c-Si wafers, concerns about sustainability of the supply chain for tellurium, and concerns about disposal of cadmium remain some of the ongoing uncertainties for state of the art PV technology. Also, the increasingly high capital investment required for large scale manufacturing has made further investment in manufacturing facilities relatively uncertain.[10] Ultimately, the most promising photovoltaic technologies for delivering terawatt scale module production are those that are derived from earth abundant materials that can be produced using scalable, low-cost processing techniques without the use of toxic materials.[11]

1.1 Place for OPV: Market potential

Organic photovoltaics (OPV), namely solar cells derived primarily from materials containing C, H, N, S, and O, are widely viewed as a technology with potential to simultaneously meet the need for terawatt scale PV module production at a low cost.[12,13] OPVs are derived from small molecule and polymer semiconductors with conjugated backbones, which afford the material

semiconducting properties. These materials that are now widely exploited in electronics, including organic light emitting diodes (OLEDs) and organic field effect transistors (OFETS). Some of these technologies are now reaching commercial relevance.[14] The low-temperature solution processability of these materials enables thin-film roll-to-roll manufacturing techniques, which substantially reduce the cost of large-scale module production.[15] It also opens the possibility for these materials to be coated directly onto plastic substrates so modules can be produced with flexible form factors relatively inexpensively.[16] Another significant advantage is that due to the organic components used in the production of these semiconductors, no mining is necessary for their production. The combination of low-temperature processing, low-cost, scalable manufacturing with abundant, recyclable materials makes solar cells derived from organic semiconductors an area worthy of further research for the next generation of high efficiency photovoltaic modules. While OPV technology is promising from a manufacturing perspective, the last three decades have seen only incremental improvement in performance.[17–19] In 2013, the record for lab scale polymer solar cells reached ~9% by Solarmer, a leading manufacturer of polymer solar cells (PSCs).[20] Significant improvement in performance is still needed in order for OPV technology to be perceived as a credible competitor with c-Si PV or other inorganic thin-film PV. Greater mechanical compliance, improved thermal stability, and a further reduction in the balance of system costs for the production of modules are also still necessary.[11,21]

While terawatt scale energy production is the highest goal driving OPV development, there are applications where their low-cost and flexible form factors make OPV particularly attractive. These niches require photovoltaic modules that can generate sufficient amounts of electricity (0.05-5 W) to power electronic components or charge a battery without adding to the weight or

complexity of a product. A good example of this application is the incorporation of solar modules directly into fabrics.[22–24] In this implementation, it is envisioned that OPV could be incorporated onto commercial products like clothing or tents and act as both a power source and the coloring agent/dye.[22] Another implementation is integration of solar modules onto structural components of autonomous vehicles. In these applications, solar power coatings can harvest enough solar energy to power sensors and other electronic components without the need for integrated electrical wiring. This reduces the overall weight of the vehicle, increasing its longevity and reducing fuel costs. For both commercial and niche applications to be realized module efficiencies ranging from 5-10% must be achieved.[25] In order to do so, a greater understanding of the photovoltaic process in OPVs and new manufacturing techniques that can control the morphological characteristics of the active layer are needed so that higher efficiencies can be achieved regardless of the coating operation.

1.2 Photophysics of OPV:

The generation of current in an organic photovoltaic device is a result of a cascade of processes that begins with the absorption of a photon and ends with the extraction of charges at external electrodes where the current can be used to do useful work. A step-by-step schematic of this process is shown in Figure 1.2 and the bullets i-iii. summarize the sequence of events that must occur in order to generate current.[26,27]

i. Absorption of a photon generates an exciton.
ii. Diffusion and dissociation of the exciton to an interface.
iii. Transport of free carriers out of the film.

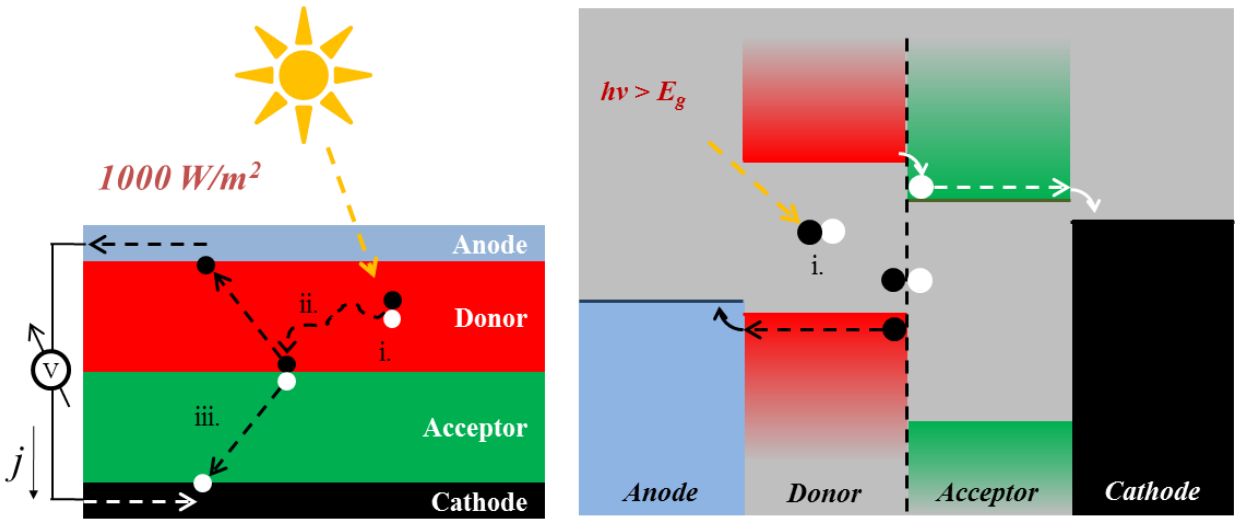

Figure 1.2. Simple bilayer concept demonstrating exciton generation, dissociation and free carrier transport through the bulk donor/acceptor domains within the device. The energy diagram at right shows the energy cascade of electron and hole transport through the bulk domains of an organic semiconductor.

Breaking this process down begins with the electromagnetic radiation (be it from the sun or another external light source) transmits through an electrode, illuminating the active layer (the layer that contains the organic semiconductors). In the manifestation in Figure 1.2, the active layer is comprised of a donor and acceptor species sandwiched between two working electrodes, one cathode and one anode, which are connected to an external circuit. Each photon absorbed within the active layer by either the donor or acceptor generates an exciton, a strongly coupled charge state consisting of an electron and hole. In order to dissociate this electron-hole pair, the binding energy of the exciton must be overcome. For an isolated semiconductor at room temperature, the exciton binding energy is many times kT and therefore, very few excitons intrinsically dissociate into free carriers. Therefore, a second semiconductor with a sufficient offset in its lowest unoccupied molecular orbital (LUMO) is required for spontaneous dissociation of the exciton. If the diffusional time scale of the exciton brings it to a donor/acceptor interface within its lifetime, the exciton dissociates and the donor will become

hole-rich and the acceptor electron-rich. If not, the exciton will recombine. This adds a constraint on the design of OPVs that the farthest distance to an interface in a device must be ~20 nm, as excitons can typically only diffuse ~10 nm.[26] The next fundamental process is the transport of free carriers through the bulk semiconducting domains of the thin-film. The hole mobility of the donor domains and electron mobility of the acceptor domains must be sufficiently high such that transport through them is faster than the rate of geminate recombination (charge carriers that recombine back across the donor/acceptor interface).[28] Therefore the active layer must consist of not only high mobility, but direct charge transport pathways to the electrodes.

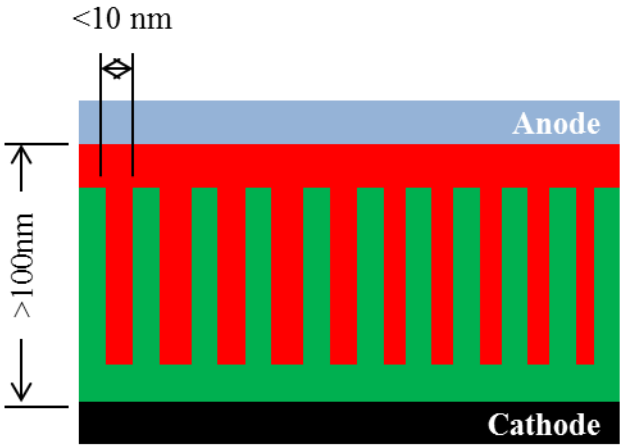

Figure 1.3. Schematic of a hypothetical ordered heterojunction structure. The ordered heterojunction concept requires the film be thick enough that it absorbs all of the incident radiation, but with domains sufficiently small and interconnect that all the excitons generated are able reach an interface, dissociate, and the resulting free carriers transported to the external electrodes.

Finally, at this stage the free carriers can exit the device, transit an external circuit and do useful work. Based on these design criteria, the ordered heterojunction concept shown schematically in Figure 1.3 has been proposed as a potentially ideal morphology for the thin-film active layer of an OPV. This hypothetical structure ensures high internal quantum efficiency by maximizing the

donor/acceptor interface, minimizing the domain size, and maintaining interconnected high mobility pathways for carrier transport.[29]

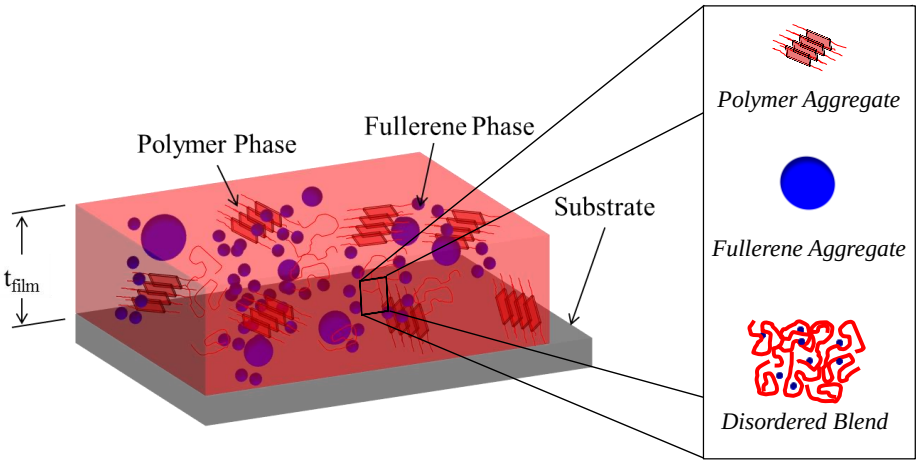

Figure 1.4. Schematic of thin-film composite active layer of OPV solar cell and its fundamental components.

The ordered heterojunction concept, while a useful conceptual model, fails to adequately describe the actual morphology observed in OPV devices.[30] The most efficient OPV technologies are based on polymer solar cells (PSC) where the active layer is a composite of a conjugated polymer and fullerene derivative. Fullerene derivatives are n-type semiconductors synthesized from natural forms of carbon (C_{60}/C_{70}). These are used typically in conjunction with p-type conjugated polymers in PSCs owing to their solution processability, high electron mobility, and fast carrier dynamics. In polymer/fullerene OPVs, the active layer is a composite film that contains a mixture of many distinct phases including regions of disordered polymer containing dilute molecularly dispersed fullerene, a polymer crystalline phase that excludes fullerene, and potentially even a fullerene rich phase that excludes polymer or is comprised of crystalline fullerene. From a morphological standpoint, the efficiency of a PSC is therefore a function of the relative concentration, orientation and distribution of these domains within the film.

1.3 Aqueous Dispersions of Composite Conjugated Polymer/Fullerene Nanoparticles:

Herein is the challenge for polymer/fullerene composites to realizing commercial relevance: morphological control must be a robust, scalable process that can achieve optimum performance for a set of materials. In the current paradigm of PSC processing, there are a large number of factors that can influence the morphological characteristics of the polymer/fullerene composite. Many of these include solvent choice, coating method, drying time, annealing conditions, material solubility, substrate choice, blend ratio, device geometry, and have been enumerated in a great number of individual investigations within the literature. This work has established strong ***process-function*** relationships between the electronic properties of a PSC and how it was processed as shown in Figure 1.5. However, what is missing is a more detailed understanding of the structure-function relationships: the connection between the optimum distribution, concentration and orientation of domains within the composite and the best performance. The fact that these relationships do not exist compromises the promise of PSC as a viable commercial technology as the processes recipe that determines the best performance on a laboratory scales (i.e. using spin-coating) will not necessarily translate to an industrial scale (i.e. using roll-to-roll coating) where factors like drying time and substrate choice may be significantly different. Without the deeper understanding about the structural characteristics that lead to a given performance metric, little scientific insight from the laboratory scale can adapted to guide the design.

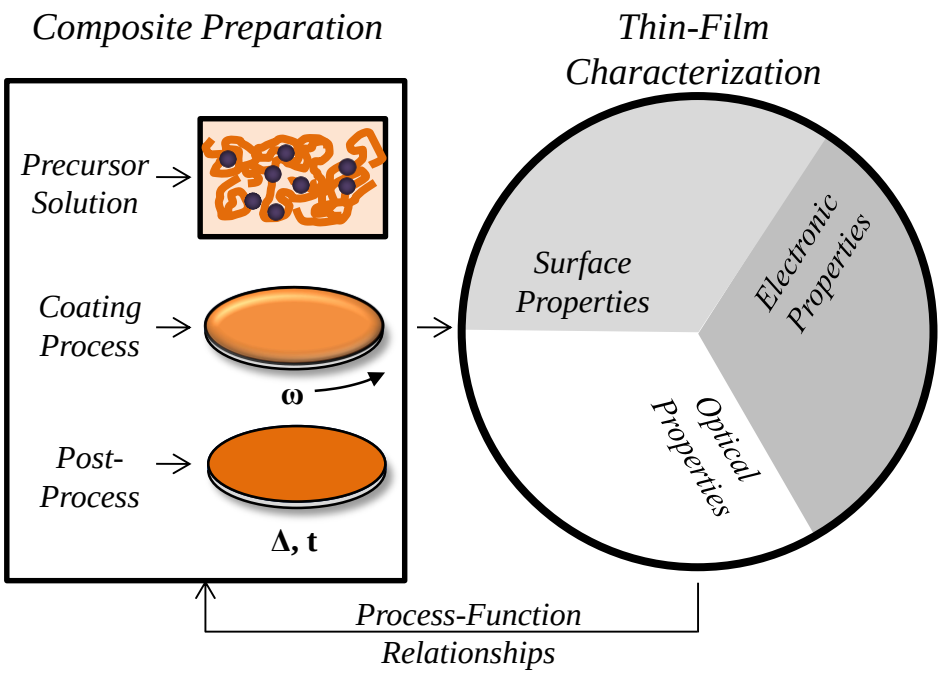

Figure 1.5. Schematic for the current paradigm of solution phase processing.

An alternative approach to address this issue is to fabricate sub-micron-sized composite nanoparticles that have been previously engineered for optimum performance based on their internal structure and composition as depicted in Figure 1.6. This concept stems from the investigation of conjugated polymer nanoparticles dispersions applied to PSC applications.[31–33] Initial studies incorporated physical mixtures of conjugated polymer nanoparticles into thin-films PSCs.[34] This was motivated by the hypothesis that the finite size of these nanoparticles would constrain the degree of phase segregation in all-conjugated polymer solar cells, resulting in smaller more intimately mixed domains than if the materials were processed from a common solvent. However, devices made in this fashion showed only modest performance compared to their solution processed counterparts.[35,36] Additionally, this work showed that thermal annealing eliminates the benefit of using the nanoparticle approach with respect to domain size as the degree of phase-segregation was independent of the whether the films were processed from

solution or from the nanoparticles. Renewed interest in nanoparticles for PSC has arisen recently. Specifically, driven by the realization that a superior strategy to creating PSCs derived from aqueous dispersions of polymer nanoparticles is to create composite nanoparticles (CNPs) that incorporate both the conjugated polymer and a fullerene derivative into a single nanoparticle.[33] This was originally motivated by the hope that this strategy would afford superior domain-size control and the benefits of aqueous processing as compared to the evaporation of organic solvents.

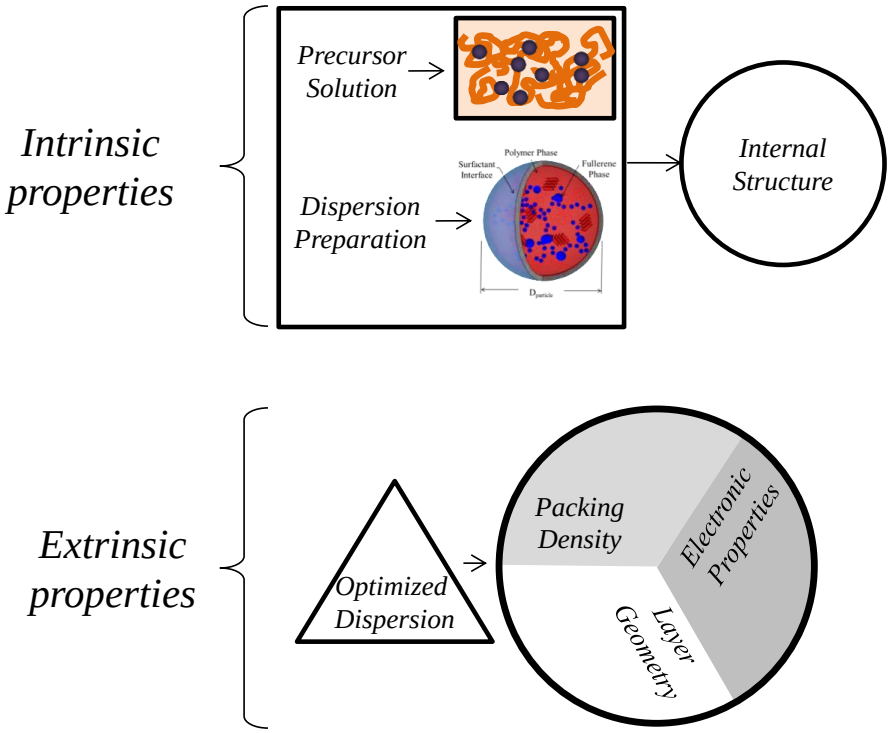

Figure 1.6. Schematic for nanoparticle characterization separating the intrinsic elements of nanoparticle formulation from the extrinsic elements of device fabrication.

When we started investigating this problem, we became interested in a relatively simple idea that these nanoparticles could enable. This idea is outlined schematically in Figure 1.6. By creating a composite nanoparticle dispersion, the structural morphology of the components within each nanoparticle are fixed when the particle solidifies during formulation and therefore are

independent of the process by which the particles are deposited into a thin-film. It is therefore possible to view each nanoparticle as a working micro-solar cell, and the challenge of making PSC from these micro-solar cells can be broken up into a two-step process. First interrogate the intrinsic properties of the nanoparticles with respect to their morphology, composition, and optical properties, and relate these factors to the intrinsic performance of each nanoparticle. The size of the particle, its composition (e.g. ratio of P3HT to PCBM), its specific morphology, and the crystallinity of each component all influence carrier generation and transport of out of the particle. Second optimize the extrinsic properties of the device. Extrinsic effects are those that cannot be directly related to the individual particles, such as the distribution and density of nanoparticles deposited within the active layer, the nature/effectiveness of the contact area between particles and the electrode, or even if the coating process results in monolayers or multilayers of particles. These effects will also have direct relation to the final device efficiency but they are separable from intrinsic effects and presumably they should be optimized separately from the nanoparticle. This thesis outlines nanoparticle formulation strategies in Chapter 2 and discusses the intrinsic nanoparticle properties in Chapter 6 and how they are related to intrinsic nanoparticle performance in Chapter 7. Chapter 8 details our work in developing new coating techniques which will fully exploit the characteristics of our optimized formulations to produce high quality thin-films from these nanoparticles.

References:

1. Hegedus, S.; Luque, A. Achievements and Challenges of Solar Electricity from Photovoltaics. *Handb. Photovolt. Sci. Eng. Second Ed.* **2011**, 1–38.

2. Agüero, J. R.; Member, S.; Steffel, S. J. Integration Challenges of Photovoltaic Distributed Generation on Power Distribution Systems. In *IEEE Power and Energy Society General Meeting*; 2011; pp. 1–6.

3. Begovic, M. M.; Kim, I.; Novosel, D.; Aguero, J. R.; Rohatgi, A. Integration of Photovoltaic Distributed Generation in the Power Distribution Grid. *2012 45th Hawaii Int. Conf. Syst. Sci.* **2012**, 1977–1986.

4. Chaar, L. El; Lamont, L. a.; Zein, N. El Review of Photovoltaic Technologies. *Renew. Sustain. Energy Rev.* **2011**, *15*, 2165–2175.

5. Moslehi, K.; Kumar, R.; Member, S. A Reliability Perspective of the Smart Grid. *IEEE* **2010**, *1*, 57–64.

6. EIA *Overview Energy Perspectives Consumption by Source*; 2007.

7. Administration, E. I. *Annual Energy Outlook 2013*; 2013.

8. Fthenakis, V. Sustainability of Photovoltaics: The Case for Thin-Film Solar Cells. *Renew. Sustain. Energy Rev.* **2009**, *13*, 2746–2750.

9. Wolden, C. a.; Kurtin, J.; Baxter, J. B.; Repins, I.; Shaheen, S. E.; Torvik, J. T.; Rockett, A. a.; Fthenakis, V. M.; Aydil, E. S. Photovoltaic Manufacturing: Present Status, Future Prospects, and Research Needs. *J. Vac. Sci. Technol. A Vacuum, Surfaces, Film.* **2011**, *29*, 030801.

10. Conibeer, G. Third-Generation Photovoltaics. *Mater. Today* **2007**, *10*, 42–50.

11. Medford, A. J.; Lilliedal, M. R.; Jørgensen, M.; Aarø, D.; Pakalski, H.; Fyenbo, J.; Krebs, F. C. Grid-Connected Polymer Solar Panels: Initial Considerations of Cost, Lifetime, and Practicality. *Opt. Express* **2010**, *18 Suppl 3*, A272–85.

12. Günes, S.; Neugebauer, H.; Sariciftci, N. S. Conjugated Polymer-Based Organic Solar Cells. *Chem. Rev.* **2007**, *107*, 1324–38.

13. Kietzke, T. Recent Advances in Organic Solar Cells. *Adv. Optoelectron.* **2007**, *2007*, 1–15.

14. Kippelen, B.; Brédas, J.-L. Organic Photovoltaics. *Energy Environ. Sci.* **2009**, *2*, 251.

15. Krebs, F. C.; Gevorgyan, S. a.; Alstrup, J. A Roll-to-Roll Process to Flexible Polymer Solar Cells: Model Studies, Manufacture and Operational Stability Studies. *J. Mater. Chem.* **2009**, *19*, 5442.

16. Krebs, F. C. Fabrication and Processing of Polymer Solar Cells: A Review of Printing and Coating Techniques. *Sol. Energy Mater. Sol. Cells* **2009**, *93*, 394–412.

17. Li, L.; Lu, G.; Yang, X.; Zhou, E. Progress in Polymer Solar Cell. *Chinese Sci. Bull.* **2007**, *52*, 145–158.

18. Hoppe, H.; Sariciftci, N. S. Organic Solar Cells: An Overview. *J. Mater. Res.* **2011**, *19*, 1924–1945.

19. Brabec, C. J. Organic Photovoltaics: Technology and Market. *Sol. Energy Mater. Sol. Cells* **2004**, *83*, 273–292.

20. Green, M. A.; Emery, K.; Hishikawa, Y.; Warta, W. Solar Cell Efficiency Tables. **2009**, *2008*, 85–94.

21. Jorgensen, M.; Norrman, K.; Krebs, F. C. Stability/degradation of Polymer Solar Cells. *Sol. Energy Mater. Sol. Cells* **2008**, *92*, 686–714.

22. Krebs, F. C.; Biancardo, M.; Winther-Jensen, B.; Spanggard, H.; Alstrup, J. Strategies for Incorporation of Polymer Photovoltaics into Garments and Textiles. *Sol. Energy Mater. Sol. Cells* **2006**, *90*, 1058–1067.

23. Schubert, M. B.; Werner, J. H. Flexible Solar Cells for Clothing. *Mater. Today* **2006**, *9*, 42–50.

24. Shrotriya, V. Polymer Power. *Nat. Photonics* **2009**, *3*, 447–449.

25. Krebs, F. C.; Tromholt, T.; Jørgensen, M. Upscaling of Polymer Solar Cell Fabrication Using Full Roll-to-Roll Processing. *Nanoscale* **2010**, *2*, 873–86.

26. Brabec, C. J.; Sariciftci, N. S.; Hummelen, J. C. Plastic Solar Cells. *Adv. Funct. Mater.* **2001**, *11*, 15–26.

27. Tang, W. Two Layer Organic Photovoltaic Cell. *Appl. Phys. Lett.* **1985**, *48*, 183–185.

28. Al-Ibrahim, M.; Ambacher, O.; Sensfuss, S.; Gobsch, G. Effects of Solvent and Annealing on the Improved Performance of Solar Cells Based on Poly(3-Hexylthiophene): Fullerene. *Appl. Phys. Lett.* **2005**, *86*, 1–3.

29. Gregg, B. A.; Ferrere, S.; Pichot, F. Interfacial Processes in Organic-Based Solar Cells. *Org. Photovoltaics II* **2002**, *4465*, 31–42.

30. Hoppe, H.; Sariciftci, N. S. Morphology of Polymer/fullerene Bulk Heterojunction Solar Cells. *J. Mater. Chem.* **2006**, *16*, 45.

31. Richards, J. J.; Weigandt, K. M.; Pozzo, D. C. Aqueous Dispersions of Colloidal Poly(3-Hexylthiophene) Gel Particles with High Internal Porosity. *J. Colloid Interface Sci.* **2011**, *364*, 341–50.

32. Landfester, K. The Generation of Nanoparticles in Miniemulsions. *Adv. Mater.* **2001**, *13*, 765–768.

33. Andersen, T. R.; Larsen-Olsen, T. T.; Andreasen, B.; Böttiger, A. P. L.; Carlé, J. E.; Helgesen, M.; Bundgaard, E.; Norrman, K.; Andreasen, J. W.; Jørgensen, M.; *et al.* Aqueous Processing of Low-Band-Gap Polymer Solar Cells Using Roll-to-Roll Methods. *ACS Nano* **2011**, *5*, 4188–96.

34. Kietzke, T.; Neher, D.; Landfester, K.; Montenegro, R.; Güntner, R.; Scherf, U. Novel Approaches to Polymer Blends Based on Polymer Nanoparticles. *Nat. Mater.* **2003**, *2*, 408–12.

35. Landfester, K.; Montenegro, R.; Scherf, U.; Guntner, R.; Asawapirom, U.; Patil, S.; Neher, D.; Kietzke, T. Semiconducting Polymer Nanospheres in Aqueous Dispersion Prepared by a Miniemulsion Process. *Adv. Mater.* **2002**, *14*, 651–655.

36. Lee, S. H.; Lee, Y. B.; Park, D. H.; Kim, M. S.; Cho, E. H.; Joo, J. Tuning Optical Properties of Poly(3-Hexylthiophene) Nanoparticles through Hydrothermal Processing. *Sci. Technol. Adv. Mater.* **2011**, *12*.

Chapter 2. Formulation of Composite Nanoparticles

Many techniques have been developed to formulate water insoluble materials into nanoparticle dispersions. These include *1.)* the transfer of a solution of hydrophobic materials of interest into a miscible, poor solvent while mixing (i.e. crashing out), *2.)* direct miniemulsion synthesis using surfactant micelles, and *3.)* bulk emulsification of the material solubilized in a suitable, volatile oil and subsequent oil removal.[1] For the formulation of conjugated polymer/fullerene CNPs, bulk emulsification is the preferred route because of its flexibility, simplicity and precise control over the composition internal to the nanoparticle.[2,3] Unfortunately, while considerable control over the particle's composition is possible, unlike other production strategies the size and distribution of components within the nanoparticle is somewhat challenging to tune and control.

2.1 Formulation and Characterization of CNPs Produced using Bulk Emulsification Techniques

The preparation of conjugated polymer nanoparticles dispersed in water is described elsewhere, but in brief, the water-insoluble materials are dissolved in a common, volatile solvent.[4] This solution is then emulsified in water containing surfactant. The resulting emulsion is then placed under vacuum and the volatile oil removed resulting in stable nanoparticles containing the water-insoluble components. The average size of a nanoparticle is a direct function of the size and distribution of emulsion droplets produced. For solar cell applications, it is highly desirable to produce nanoparticles with radii ranging from 20-250 nm *(the blue region in Figure 2.1)*. Depending on the desired diameter of the dispersed phase, the appropriate emulsification technique must be chosen. A simple design rule for the size of a nanoparticle resulting from a given oil droplet uses the volume fraction, ϕ, of the soluble organic component contained within the oil droplet as shown in Equation 2.1.[5]

$$2.1 \quad D_{CNP} \equiv D_{emul}\phi^{1/3}$$

This simple model assumes that there is no exchange of soluble materials between emulsion droplets and there is little coalescence during the removal of the oil phase. In the production of CNPs using bulk emulsification, surfactant is used to maintain oil droplet stability during the emulsification step. Small molecule surfactants are ideal for this process because they have a high diffusivity and large affinity for the oil-water interface. Therefore, very small emulsion droplets can be formed through high-shear mixing without significant coalescence or flocculation. During the emulsification process the surfactant is present in excess, normally > 5 × CMC. This excess surfactant serves two roles: *1)* prevents coalescence of the oil droplets, and *2)* ensures all of the oil phase can be fully stabilized in the emulsion phase. Most conjugated polymers and fullerenes are entirely insoluble in both the aqueous phase and surfactant micelles. Therefore, bulk exchange of material from emulsion droplet to emulsion droplet is unlikely. The implications of equation 2.1 are that nanoparticle size is very sensitive to the emulsion droplet diameter and to the volume fraction of solids in the oil phase. This relationship is depicted in Figure 2.1. The way this diagram should be read is to draw a vertical line up from the volume fraction that the oil phase is at and then over to the left axis to determine the nanoparticle size.

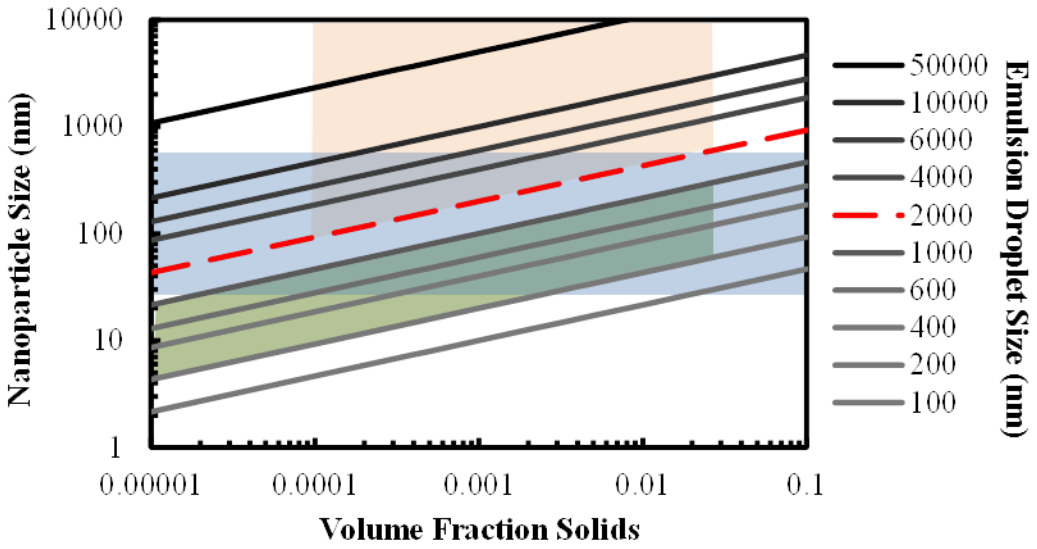

Figure 2.1. Process diagram for CNP formulation. Blue region represents desired diameter range, green region the sizes accessible using high shear emulsification, and the pink region represents the sizes accessible using droplet techniques.

We have explored a number of emulsification techniques which can be generally divided into two categories. The first being bulk emulsions formed using droplet production techniques (i.e. microfluidic flow-focusing and shear-induced droplet formation) *(the pink region in Figure 2.1)* and the second, those formed as a result of high shear mixing *(the green region in Figure 2.1)*. Neither of these two classifications of methods is able to produce nanoparticles over the entire desired size range, and there are a number of challenges associated with each method.

Droplet pinch-off methods to create oil-in-water emulsions are a common means to form polymer latexes.[6] Microfluidic devices (T-junctions, core/sheath flows) can be used to create monodisperse droplets of oil in a bulk water phase with very tight control of size.[7] The same can also be accomplished using droplet break-off in a co-flowing stream.[8] Both methods rely on the formation of a droplet at the outlet of an orifice which then grows and pinches off as a result of the shear induced by the flow of water around the droplet. Because of this process, the ultimate droplet diameter is constrained to about twice the orifice diameter. Therefore, it is difficult to produce substantial quantities of emulsion droplets smaller than ~2 μm. While in principle, 2 μm oil droplets could access the nanoparticle size regime based on Equation 2.1, this requires very low ϕ_{solids} and therefore, the production rate is impractical for real applications.

High shear mixing techniques like ultrasonication, membrane extrusion, and impellor emulsification all rely on the rapid break-up of bulk emulsions into micro- and nano-emulsion droplets. In general, the greater the amount of power applied through the emulsification process, the smaller the resulting oil droplets.[9,10] The added benefit of this emulsification technique is its scalability. The accessible emulsion droplet size range for these techniques is typically less than

~1000 nm. These emulsions, however, do not have a very controlled size distribution. Therefore, the specific choice of emulsification technique is a balance between having control the distribution of size of the nanoparticle formulation and the speed/quantities of materials that can be made.

2.2. Ultrasonication: A Simple Means to Form Composite Nanoparticles

To test the design rule in Equation 2.1, regiorandom P3HT was used as a model polymer for the production of conjugated polymer nanoparticles. Regiorandom P3HT (Rrand-P3HT) does not crystallize and therefore, its spectroscopic signal can be related directly to its local environment. Figure 2.2 shows the size of Rrand-P3HT nanoparticles produced by sonication Rrand-P3HT dissolved in chloroform solutions in 40 mM SDS as a function of the volume fraction of Rrand-P3HT dissolved in the chloroform phase measured using Dynamic Light Scattering (DLS).

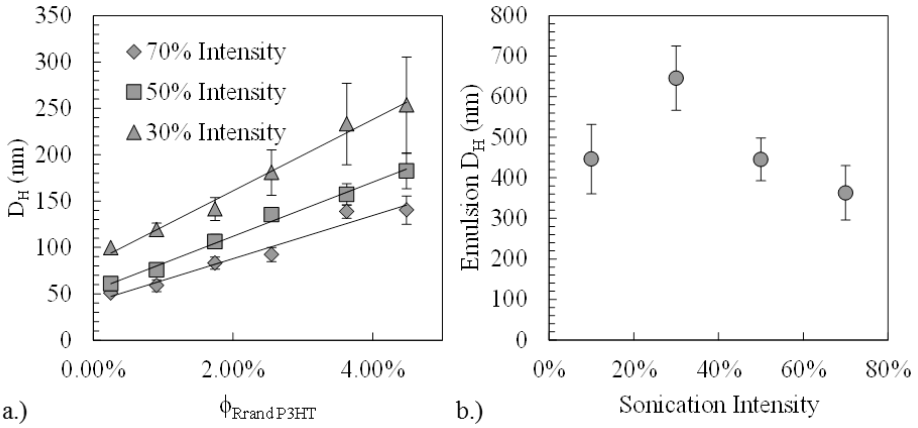

Figure 2.2. a.) Hydrodynamic diameter (D_H) of Rrand P3HT nanoparticles formed from solutions of Rrand P3HT in Chloroform with varying volume fraction, b.) Average emulsion droplet diameter formed as a function of sonication intensity as determined from DLS.

The average emulsion droplet size for the sonication intensities tested is shown in Figure 2.2.b. As expected, for sonication intensity exceeding 30%, the nanoparticle size was reduced as the intensity increased. At low sonication intensities, there was an unexpected decrease in emulsion

droplet diameter. During the ultrasonication process, above 30% intensity, there is foaming observed during the emulsification. Foaming of the emulsion results in a reduction of emulsification efficiency, which explains how low sonication powers that do not cause foaming could result in smaller oil droplets than those produced at high power where there is foaming. Another important observation evident in Figure 2.2.a is the dependence of nanoparticle size on volume fraction of Rrand-P3HT in the chloroform phase. It appears to be linear instead of power-law as expected by Equation 2.1. The solids content of the chloroform phase affects the average diameter of the emulsion droplets formed during sonication. Higher solids content solutions produce larger emulsions droplets on average likely a result of increased viscosity of the oil phase. Another important feature of the DLS results shows that larger particles have proportionally broader distributions of overall size.

2.3 Spectroscopic Characterization of CNP Dispersions in Water

There are many fundamental aspects about the dispersion of semiconducting materials into aqueous solution that are of practical interest to the utilization of these materials in organic electronics. The local environment of the conjugated polymer in the dispersed state determines the spectroscopic characteristics observed for the dispersions. Second, the presence of oxygen/water or ionic surfactant could potentially lead to conjugated polymer degradation. Therefore, study of these degradation mechanisms is important for PSC applications.[11] To address these issues, two model conjugated polymer dispersions have been produced. The dispersions were made by emulsifying a 10 mg/mL solution of Rrand-P3HT in chloroform using membrane extrusion (400 nm pore size) and ultrasonication (70% Intensity). Membrane extrusion produces smaller nanoparticles with a more narrow size distribution as shown in figure 2.3.a.

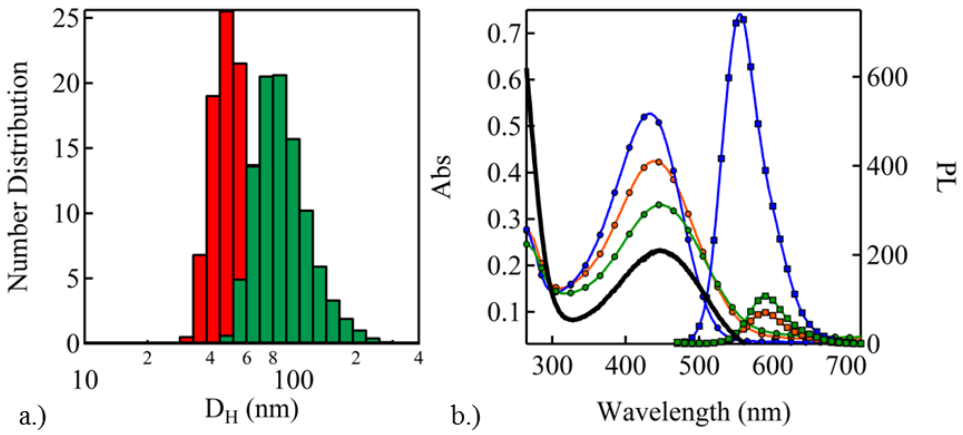

Figure 2.3. a.) DLS results from Rrand-P3HT dispersions produced using sonication (green) and membrane extrusion (red), b.) UV-Vis and PL spectra for dispersions of Rrand-P3HT nanoparticles made using sonication (green) and extrusion (red), 10 mg/mL solution of Rrand-P3HT in chloroform (blue), and the absorption spectra for a Rrand-P3HT film spin-coated on glass (black).

The UV-Visible absorption and photoluminescence spectra for both dispersions are shown in Figure 2.3b along with that for Rrand-P3HT (blue line) in chloroform and spin-coated Rrand-P3HT film (black line). The smaller dispersion shows a λ_{shift}=8 nm and the larger dispersion shows λ_{shift}=16 nm red-shift in the position of the peak max in the absorption spectra relative to Rrand-P3HT dissolved in chloroform. The origin of this shift is likely due to interchain interactions resulting in an increase in conjugation length. Interestingly, as the dispersion diameter increases, it increasingly resembles a bulk Rrand-P3HT film as seen in Figure 2.3 a. The photoluminescence spectra in Figure 2.3.b are measured for an excitation of λ=450 nm. There is indication of photoluminescence quenching in the dispersion phases relative to the soluble Rrand-P3HT. The ratio of PL_{max}/Abs_{max} is 8 times smaller for the smaller diameter dispersion compared with the PL_{max}/Abs_{max} for the larger dispersion, which was only 4 times smaller. Therefore, the larger dispersion particle shows a smaller degree of photoluminescence quenching. This could be a result a smaller fraction of the surface area of the particles being

exposed to the oil/water interface, where the local dipole moment is significantly different from "bulk" P3HT. Interestingly despite the larger red-shift present in the larger dispersion particles, the position of the PL_{max} is the same as the smaller dispersion particles, $\lambda = 587$ nm. The position of the PL_{max} for the Rrand-P3HT/$CHCl_3$ solution is $\lambda = 550$ nm, a total shift of 37 nm or ~0.142 eV.

The dispersion particles are stabilized by a layer of SDS at the nanoparticle/aqueous interface. Previous study of fluorescent materials shows that surfactants are extremely effective at sequestering hydrophobic materials from water.[12,13] This fact may explain the stability of conjugated polymers dispersions in water. Based on the absorption spectra of Rrand-P3HT it is clear that the material is not being specifically doped by the sulfates in the SDS or free hydroxides within the water phase. Doping would appear as decrease in the main peak absorbance for Rrand-P3HT and an increase in the absorbance in the near IR.[14] It is also possible to see a blue-shift in the absorption spectra, which would imply photo-oxidative cleavage had occurred.[15] Both of these scenarios would result in photoluminescence bleaching. Time studies performed on the Rrand-P3HT dispersions monitored as a function of surfactant type and concentration show no degradation over the course of several months. The final degradation mechanism for these dispersions is the presence of molecular oxygen, which readily diffuses into thin-films of conjugated polymers and induces localized trap states. These trap sites reduce the charge carrier mobility of the polymer phase and are difficult to detect with UV-Visible spectroscopy as their presence induces only small changes in the magnitude of the absorption peak.

Figure 2.4. P3HT/PCBM dispersions prepared with varying P3HT/PCBM Ratio.

Using bulk emulsification composite nanoparticles spanning the entire composition range from pure PCBM to pure P3HT can be made with relatively uniform size. The corresponding UV-Visible absorption spectra are shown in Figure 2.5a.

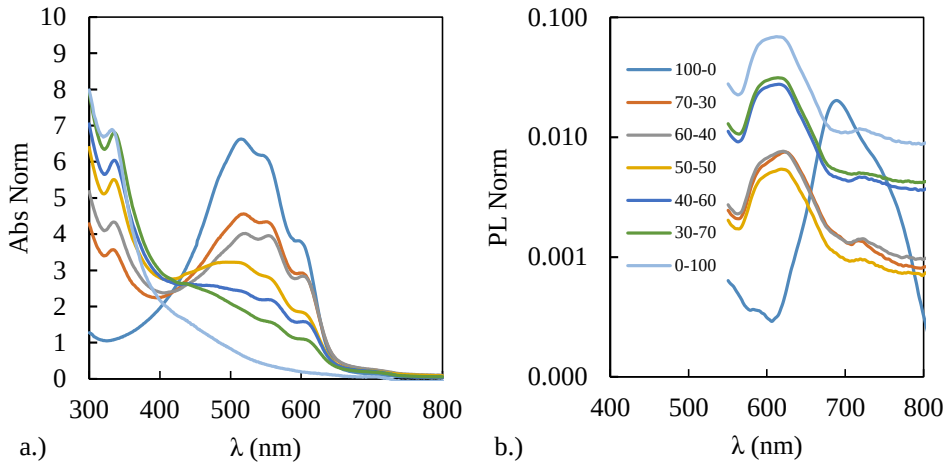

Figure 2.5. a.) UV-Vis Spectra of SNP prepared with different P3HT/PCBM contents, and b.) corresponding photoluminescence data.

A clear color shift is evident as the composition swings from pure P3HT to pure PCBM. The UV-Visible spectra are normalized to concentration and clearly show changes consistent with changing composition internal to the particles. There are also structural changes evident in the degree of crystallinity observed in the P3HT phase of the particles indicated by the change in

ratio between the UV-Visible absorption peak at 610 nm to that at 538 nm. From the photoluminescence measurement, there is a clear shift in the peak position going from pure P3HT to blended particles. The disappearance of the peak at 675 nm implies the PL quenching typical of blends of P3HT/PCBM. An additional PL feature from PCBM is evident in all of the samples below a composition ratio of 60-40 P3HT/PCBM. This indicates that the only photoluminescent feature is originating from PCBM within the particle and intensity of this peak roughly scales with the fullerene content within the particles. Interestingly, the 70-30 blend sample shows a slight shift in the PL spectra. This new feature may derive from charge transfer states generated within the volume of the particle.

Spectroscopy is therefore a useful tool to identify the appropriate blend composition for CNPs. At the point where the PL is fully quenched from the polymer phase, all photons absorbed by the polymer are converted to electron hole pairs. Within the internal domains of the particle deposited into a thin-film for example, the resulting efficiency of charge transport will be a function of the internal structure of these particles. In principle for large particles, the optical cross-sections of the particles can be used to reconstruct the three-dimensional distribution of material within the particle. However, this is requires accurate measurements for the indices of refraction and absorption coefficients of the materials. While many measurements of these values have been reported in the literature for blended P3HT/PCBM films, the translation of thin-film absorption spectra to that of spherical colloid particles is non-trivial and requires application of Mie theory.

Instead, we measured compositional maps using transmission electron microscopy (TEM) with energy dispersive X-ray spectroscopy (EDS). EDS is an analytical technique that excites inner shell electrons from a material leaving a hole that is filled with outer shell electrons. If the

conditions are right, an X-ray will be ejected from the sample whose energy is directly related to the difference in energy between the high-energy and the lower-energy shell electron. Figure 2.6 shows representative compositional maps for typical nanoparticle formulations of P3HT and PCBM.

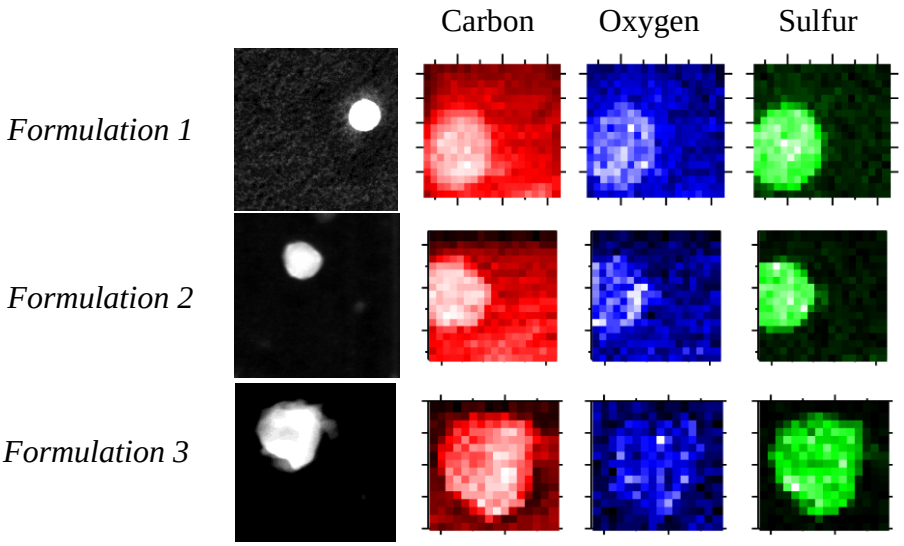

Figure 2.6. EDS TEM images of carbon, oxygen, sulfur maps for particles as a function of composition.

From the micrographs, it is possible to confirm the composition of the particles based on the clear presence of sulfur, oxygen and carbon. Because P3HT contains sulfur and PCBM contains oxygen, it is in principle possible to differentiate P3HT and PCBM rich domains. However, there are several challenges with this approach. First, these composition maps are constructed by taking a spectrum at each pixel position within the particle. At each pixel position a narrow electron beam, diameter of ~1 nm, illuminates the sample for a specified period of time. As electrons propagate into the sample, this beam broadens as a result of collisions within the material. From these collisions, the EDS spectrum is obtained and mapped to the pixel position as shown in Figure 2.7a. The spectrum obtained from given pixel position will be a complex function of the thickness of the sample at that point and its composition. Monte Carlo simulation

techniques are necessary to quantitatively link the maps measured using EDS to the radial distribution of elements within the nanoparticles.[16] Nonetheless, radial averages can be made and these are shown for a representative particle in Figure 2.7b. Based on the radial average there does appear to be systematic changes in the ratio of the sulfur and oxygen contents to the carbon content. This suggests that the particles are not uniform spheres with an even distribution of P3HT and PCBM. Because, these maps are a projection of a three dimensional object onto a two-dimensional plane, the distributions plotted in Figure 2.7b cannot be used to reconstruct the radial compositional profiles without more advanced modeling.

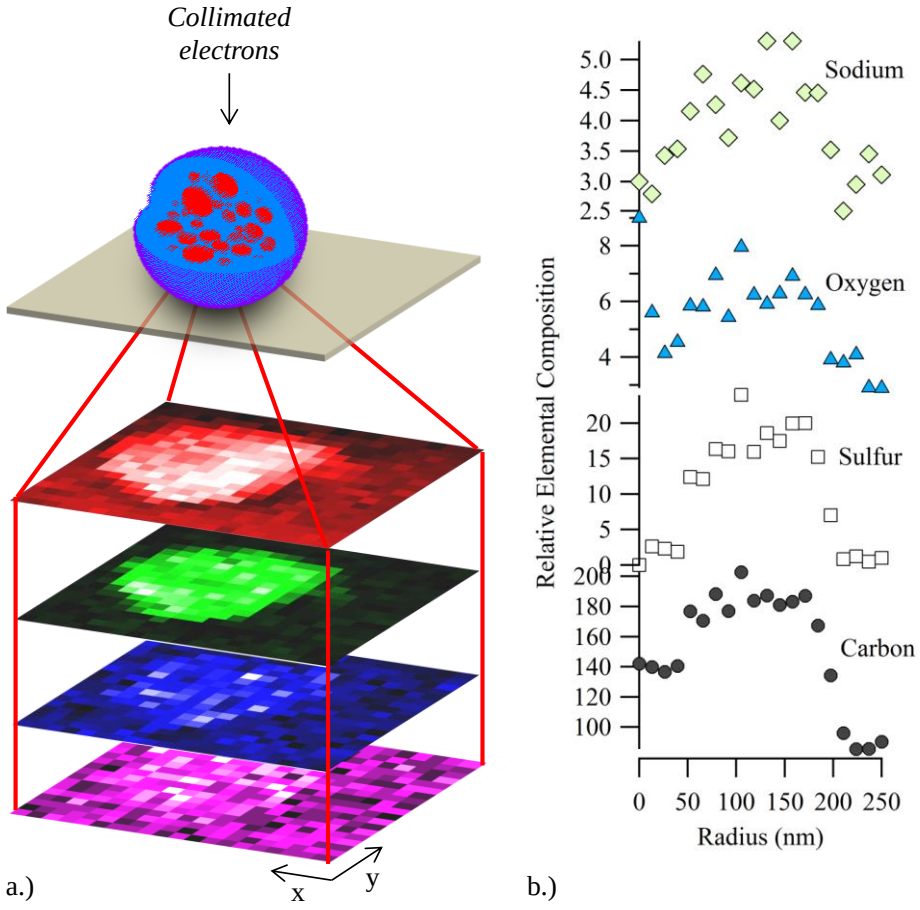

Figure 2.7. a.) EDS Spectra Schematic, and b.) representative EDS spectra radially binned a function of composite for a Pregel Latex particle image.

Other limitations of this technique include that it is destructive and very low throughput. Therefore, it takes a very long time to obtain representative spectra for a given sample. This limits the ability to rationally design the structure of the composite nanoparticles for device applications.

References

1. Landfester, K. Miniemulsion Polymerization and the Structure of Polymer and Hybrid Nanoparticles. *Angew. Chem. Int. Ed. Engl.* **2009**, *48*, 4488–507.

2. Landfester, K.; Montenegro, R.; Scherf, U.; Guntner, R.; Asawapirom, U.; Patil, S.; Neher, D.; Kietzke, T. Semiconducting Polymer Nanospheres in Aqueous Dispersion Prepared by a Miniemulsion Process. *Adv. Mater.* **2002**, *14*, 651–655.

3. Kietzke, T.; Neher, D.; Kumke, M.; Ghazy, O.; Ziener, U.; Landfester, K. Phase Separation of Binary Blends in Polymer Nanoparticles. *Small* **2007**, *3*, 1041–8.

4. Landfester, K. The Generation of Nanoparticles in Miniemulsions. *Adv. Mater.* **2001**, *13*, 765–768.

5. Loxley, A.; Vincent, B. Preparation of Poly(methylemethacrylate) Microcapsules with Liquid Cores. *J. Colloid Interface Sci.* **1998**, *208*, 49–62.

6. Baroud, C. N.; Gallaire, F.; Dangla, R. Dynamics of Microfluidic Droplets. *Lab Chip* **2010**, *10*, 2032–45.

7. Yobas, L.; Martens, S.; Ong, W.-L.; Ranganathan, N. High-Performance Flow-Focusing Geometry for Spontaneous Generation of Monodispersed Droplets. *Lab Chip* **2006**, *6*, 1073–9.

8. Umbanhowar, P. B.; Prasad, V.; Weitz, D. a. Monodisperse Emulsion Generation via Drop Break Off in a Coflowing Stream. *Langmuir* **2000**, *16*, 347–351.

9. Bibette, J.; Morse, D. C.; Witten, T. A.; D.A., W. Stability Criterion for Emulsions. *Phys. Rev. Lett.* **1992**, *69*, 2439–2444.

10. Bibette, J.; Calderon, F. L.; Poulin, P. Emulsions : Basic Principles. *Reports Prog. physics. Phys. Soc.* **1999**, *969*, 969–1033.

11. Taden, A.; Landfester, K.; Antonietti, M. Crystallization of Dyes by Directed Aggregation of Colloidal Intermediates: a Model Case. *Langmuir* **2004**, *20*, 957–61.

12. Piok, T.; Gadermaier, C.; Wenzl, F. P.; Patil, S.; Montenegro, R.; Landfester, K.; Lanzani, G.; Cerullo, G.; Scherf, U.; List, E. J. W. The Photophysics of Organic Semiconducting Nanospheres: a Comprehensive Study. *Chem. Phys. Lett.* **2004**, *389*, 7–13.

13. Lee, S. H.; Lee, Y. B.; Park, D. H.; Kim, M. S.; Cho, E. H.; Joo, J. Tuning Optical Properties of Poly(3-Hexylthiophene) Nanoparticles through Hydrothermal Processing. *Sci. Technol. Adv. Mater.* **2011**, *12*.

14. Kawai, T.; Nazakazono, M.; Sugimoto, R.; Yoshino, K. Crystal Structure of Poly(3-Alkythiophene) and Its Doping Affect. *J. Phys. Soc. Japan* **19992**, *61*, 3400–3406.

15. Manceau, M.; Rivaton, A.; Gardette, J.-L.; Guillerez, S.; Lemaître, N. The Mechanism of Photo- and Thermooxidation of Poly(3-Hexylthiophene) (P3HT) Reconsidered. *Polym. Degrad. Stab.* **2009**, *94*, 898–907.

16. Demers, H.; Ramachandra, R.; Drouin, D.; Jonge, N. de The Probe Profile and Lateral Resolution of Scanning Transmission Electron Microscopy of Thick Specimens. *Microsc. Microanal.* **2012**, *18*, 582–590.

Chapter 3. Scattering processes and their use in determination of nanoscale structure

In order to fully characterize the complex interplay between OPV performance and structural morphology of an active layer, a great variety of experimental techniques are needed. [1–4]

1. Spectroscopic techniques – Lifetime of exciton and charge species
2. Scanning probe measurements – Local current density and topology
3. Electron Microscopy – projections of 3-D structures.
4. Macroscopic Electrical characterization – EQE/mobility

However, few of these techniques address directly what structural features within a composite material are responsible for photocurrent generation. Scattering techniques have the power to answer this question. In this thesis, scattering techniques are employed extensively to probe the structural morphology of both thin-film and dispersed phase composites. Each material has its own challenges from a data acquisition and analysis standpoint, but generally the goal is the same: by characterizing the structural morphology of blended thin-films and composite nanoparticles, we hope to gain insight into structure-function dependencies of the bulk heterojunction devices. In this chapter, a brief review of the elastic scattering process is provided and a number of useful terms and expression defined. These will be employed universally in later chapters, and are introduced now for clarity.

3.1 Fundamentals of the Elastic Scattering Processes

Electromagnetic radiation propagates through space with oscillating, orthogonal magnetic and electric fields. While relativistic particles like neutrons are not electromagnetic radiation, their scattering phenomena can be described using similar physics. The magnitude of the electric field can be expressed as $|\boldsymbol{k}_i| = 2\pi/\lambda$, where λ is the wavelength, where $\boldsymbol{k}$ denotes the wave-vector of

incident radiation. When impinging on a sample of interest, the incident radiation induces in a finite volume element, *dV*, within a material a resonant dipole moment that emits radiation in all directions.[5] For elastic scattering processes, there is little energy transfer from the incident radiation to the sample ($E_i \approx E_s$) and the fraction of scattered radiation is small relative to the portion that transmits. Assuming elastic interactions, the magnitude of radiation wave vector emanating from the sample is $|\boldsymbol{k}_s| = 2\pi/\lambda$. For scattering measurements it is typical to measure the scattering intensity as a function of the scattering angle, θ, which is commonly expressed as scattering vector, Q, as shown in Equation 3.1.

$$3.1 \quad Q \equiv k_s - k_i = \frac{4\pi}{\lambda}\sin\left(\frac{\theta}{2}\right)$$

Elastic scattering provides the basis for a number of experimental techniques including small angle X-ray and neutron scattering (SAXS/SANS), X-ray Diffraction (XRD), and grazing incidence small angle neutron and X-ray scattering (GISANS/GISAXS).[6,7]

In order to understand how a scattering experiment is carried out, consider two differential volume elements within a sample. Under the influence of an oscillating electric field, both elements will emit radiation in all directions. One is centered at the origin, *O*, and another at a distance, $|\boldsymbol{r}|$, as shown in Figure 3.1. The scattered intensity, I_s, is measured as a function of angle on a detector at a distance *R* from the sample, where $I_s(Q,t) = |E(Q,t)|^2$. Therefore $I_s(Q,t)$ is defined as the squared amplitude of scattered radiation. The scattered waves produced from each scattering element propagate with magnitude, $\boldsymbol{k}_s$, and due to the finite distance between elements, are phase shifted by $-Q \cdot \mathbf{r}$ radians. This leads to interference, which result in characteristic fluctuations in scattered intensity measured at the detector as a function of scattering vector, *Q*.

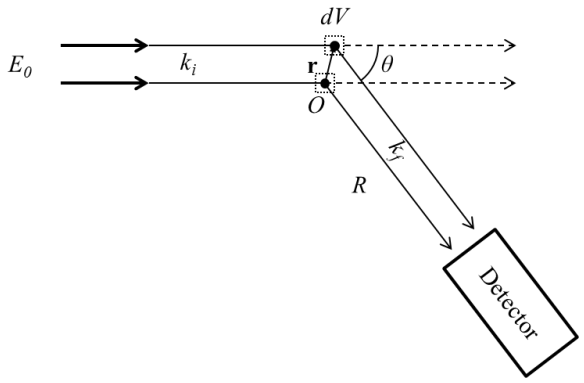

Figure 3.1. Schematic diagram of elastic scattering within a sample showing scattered vectors at the origin, *O*, and a distance |***r***| by a volume element, *dV*. Scattered intensity is measured at a detector distance *R* from the origin.

For structural interrogation, the time-averaged intensity is the Fourier transform of the combined contributions from all of the isolated scattering elements with scattering length, *b*, (Equation 3.2) within the sample.[8]

$$3.2 \quad \left\langle I_s(Q) \right\rangle = \frac{E_0^2}{R^2} \left\langle \sum_{j=1}^{N} \sum_{k=1}^{N} b_j(Q) b_k^*(Q) \exp\left[-iQ \cdot \left(\mathbf{r}_j - \mathbf{r}_k \right) \right] \right\rangle$$

$$\textit{where} \quad b_j(Q) = \int_V \left\langle \frac{k^2}{4\pi} \left[\frac{\varepsilon(\mathbf{r}_j) - \varepsilon_m}{\varepsilon_0} \right] \right\rangle \exp\left(-iQ \cdot \mathbf{r}_j \right) dV$$

There are two important implications of Equation 3.2 that arise as a result of scattering from discrete domains contained within a medium:

(1) The scattering intensity is dependent on the magnitude of scattering lengths of the scattering elements relative to the medium within which they are dispersed,

(2) The scattering intensity is dependent on the instantaneous distribution of these domains within the sample.

These two implications demonstrate the power of a scattering experiment. By measuring the scattering from a material, one obtains the scattered profile, *I(Q)* versus *Q*, which corresponds

directly to the spatial distribution of domains of varying scattering length density, *SLD*, within the sample.[5,9]

3.2 Transmission Scattering Measurements

Dilute liquid dispersions produce isotropic scattering as a result of their random Brownian motion in solution. Therefore transmission SANS/SAXS, are the most common elastic scattering techniques used to characterize their structure. In a transmission SANS or SAXS experiment, a liquid sample is placed in a monochromatic neutron or X-ray beam that passes through the whole liquid volume. Assuming no multiple scattering (i.e. each scattered photon or neutron only interacts once with the sample), the transmission of the incident radiation through the sample is high compared to the scattering intensity. The incident beam is blocked on the detector using a beam stop of fixed diameter. Because the scattered intensity is several orders of magnitude lower than the main beam intensity, a beam stop is necessary to protect the detector from saturation. The accessible resolution of the experiment is determined by the size of the detector, sample-to-detector distance, and beam stop diameter. The scattered radiation is collected for a fixed period of time on a detector placed at a fixed distance and angle from the sample as shown in Figure 3.2.

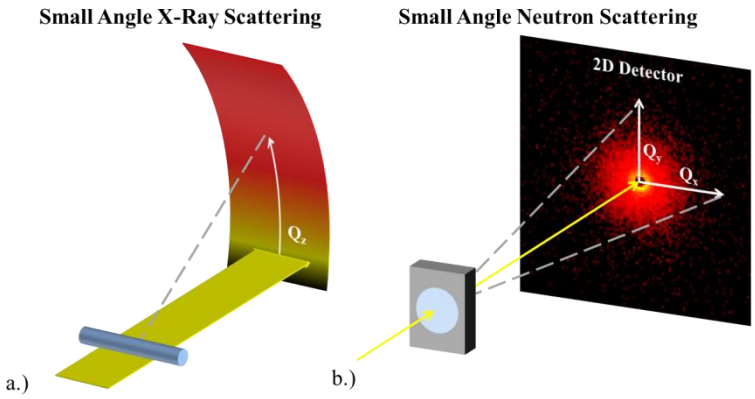

Figure 3.2. a.) Schematic showing SAXS experimental setup, b.) Schematic for SANS experimental setup. The SAXS experiments are performed using slit alignment and the SANS using pinhole alignment.

An Anton Paar SAXSess instrument (Cu-K_α, λ=1.5418 Å) was used for SAXS experiments with slit alignment using a quartz flow-cell for the sample holder. The instrument has a *SDD*=260.1 mm calibrated with silver behenate standard, accessible *Q*-range from 0.06 $Å^{-1}$ to 25 $Å^{-1}$, and the instrumental broadening slit width is 0.35 $Å^{-1}$. Raw 2-D scattering is collected on an image plate which is scanned and read into an image file. The raw detector intensity values at each pixel position are binned and averaged in the Q_z direction resulting in 1-D scattering profiles, $I_{sample}(Q)$ *vs. Q*. The $I_{sample}(Q)$ is then corrected for dark current and the empty cell scattering as shown in Equation 3.3.[9]

$$3.3 \quad I_{corr}(Q) = \left[\frac{\left(I_{sample}(Q) - I_{DC}(Q)\right)}{I_{sample}(Q=0)} + \frac{\left(I_{empty\ cell}(Q) - I_{DC}(Q)\right)}{I_{empty\ cell}(Q=0)} \right]$$

$I_{corr}(Q)$ is then converted to absolute scale ,$I_{abs}(Q)$, by normalizing the sample to the incoherent background of water and scaling it to the known value of 0.01641 cm^{-1}.

SANS measurements were carried out at the National Institute of Standards and Technology National Center for Neutron Research (NCNR) in Gaithersburg Maryland using instruments NG-3 and NG-7 for SANS, and BT-5 for the ultra-high resolution SANS (USANS).[10,11] At the NCNR, thermal neutrons are produced from a fission source. For the USANS experiments, thermal neutrons pass through a graphite filter and a perfect crystal diffractometer before impinging on the sample. The analyzer gives an accessible *Q*-range of 3×10^{-5} – 0.01 $Å^{-1}$ using λ=2.4 Å and $\Delta\lambda/\lambda$=6% in a slit-alignment. For SANS measurements, the thermal neutrons produced in the reactor are passed through cryogenic hydrogen, which moderates the high energy thermal neutrons leaving only cold-neutrons. A mechanical velocity selector then provides a

selectable wavelength range of λ=5 – 20 Å. . The sample is measured at multiple *SDD*'s ranging from 1 – 15m, giving and an accessible *Q*-range 0.0015 – 0.6 $Å^{-1}$. Liquid samples are measured in demountable cells with a fixed path length (1 or 2 mm) and quartz windows. The scattered intensity is collected on a two-dimensional helium detector and raw intensity values binned through radial integration from the beam center producing profiles $I_{sample}(Q)$ vs *Q*. These raw profiles are then corrected using equation 3.5. Absolute scale is determined by measuring the neutron transmission for each sample and normalizing $I_{corr}(Q)$ to the total neutron flux.

For transmission SAXS measurements, useful quantitative information about the sample can be obtained when the scattered intensity is scaled such that the contribution of the scattering intensity from the instrument's configuration (i.e. sample-to-detector distance, incident radiation flux, etc.) is removed.[65] This normalization of scattered intensity puts the data in absolute scale and is a measure of the differential cross-section (Equation 3.4) of the sample. The differential cross-section represents the intensity scattered into a detector solid angle, Ω, per unit sample volume, *V*. By convention this value takes on units of cm^{-1}.[5]

$$3.4 \quad \frac{d\Sigma}{d\Omega}(Q) = \frac{1}{V}\frac{d\sigma}{d\Omega}(Q) = \frac{\langle I_s(Q)\rangle R^2}{V \times E_0^2}$$

With the *I(Q) vs Q* data in absolute scale, predictive structural models of the spatial distribution of scattering domains within a sample can be quantitatively compared to experimental data. If the structural model is appropriate, linear regression analysis can be used to fit the structural parameters of the model to the data. Using a χ^2 test (Equation 3.5), the fit quality can be evaluated for agreement between experimental data, $I_{meas}(Q)$, and the model, $I_{model}(Q)$.[9]

$$3.5 \quad \chi^2 = \frac{\left(I_{model}(Q) - I_{meas}(Q)\right)^2}{I_{model}(Q)}$$

For a sufficiently low χ^2, the model is deemed appropriate thus providing confidence in that the values of the fitted parameters represent the real characteristics of the sample. This is a powerful aspect of scattering measurements because unlike microscopy, scattering is a non-destructive, bulk measurement that can probe a large size and temporal scale simultaneously. In this way, the native conformation of materials under investigation can be interrogated and the fitting results represent the average characteristics of the sample. The full development of scattering theory is discussed elsewhere and beyond the scope of this review.[12]However, in the sections that follow, a brief review of specific theoretical aspects of scattering theory are discussed specifically as they pertain measurements made in sections 4 and 5.

3.3 Grazing Incidence Scattering Measurements

In principle the scattering from thin-films could also be measured using transmission SANS/SAXS.[13,14] However, often these films are mounted on substrates, and there is little sensitivity of the overall scattering pattern to the surface film. In order to render a SAXS/SANS measurement surface sensitive, a film can be oriented at a grazing angle, α_i, relative to the incident main beam and is usually between 0.1 – 0.5° for X-Rays.[15] This technique is called grazing-incidence small angle X-ray scattering (GISAXS) and was developed to elucidate the morphology of nanoscale features in thin-films. A schematic diagram of GISAXS is shown in Figure 3.3.

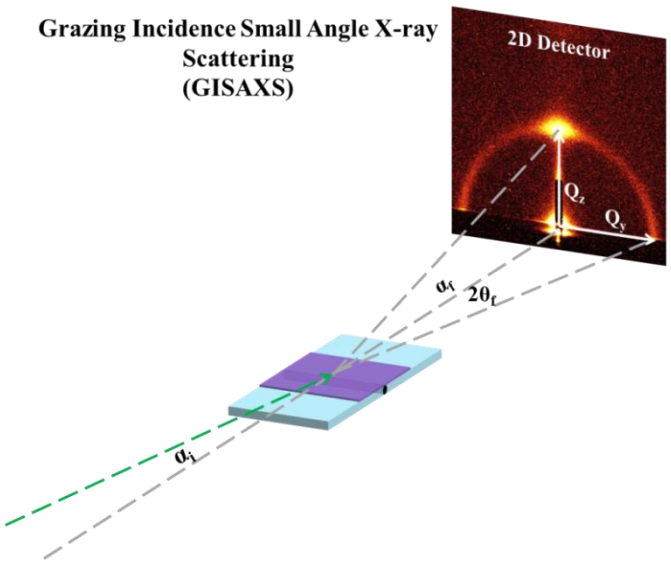

Figure 3.3. Schematic diagram of experimental GISAXS setup. The film is oriented with an angle, α_i, relative to the substrates plane and the scattering angles α_f and $2\theta_f$ relative to the substrate plane. The scattering is detected on a two-dimensional detector and measured as a function of Q_y and Q_z.

At incident angles above the critical angle of the thin-film and below the critical angle of the substrate, the scattering pattern is dominated by the diffuse scattering from features embedded within the film and by the specular reflectivity. Unlike in SANS/SAXS, the scattered intensity from these embedded features is distorted as a result of the complex refraction and reflection of the main beam. Treatment of GISAXS data is much more challenging than for either SANS or SAXS data as the scattering profiles must be treated within the frame-work of the Distorted Wave Born Approximation (DWBA).[16–19] DWBA provides an analytical framework within which the scattering intensity from thin-film features can be treated analytically. Underlying this framework is the following key assumptions:

(1) The scattering intensity from the film is weak compared to the reflection and refraction from the interfaces.[20]

Therefore, the solution for the specular reflection and refraction of the main beam can be decoupled from the contribution of the scattering from the embedded structures.[15] An additional complication arises as a result of the grazing incidence geometry. Because the sample reference plane is not the same as the detector reference plane, the *Q*-vector must be expressed in its matrix form (Equation 3.6), where α_f and $2\theta_f$ are the vertical and horizontal angle in the sample reference plane.

$$3.6 \quad Q \equiv k_s - k_i = \frac{2\pi}{\lambda}\begin{Bmatrix} \cos(\alpha_f)\cos(2\theta_f) - \cos(\alpha_i) \\ \cos(\alpha_f)\sin(2\theta_f) - \cos(\alpha_i) \\ \sin(\alpha_f) + \sin(\alpha_i) \end{Bmatrix}$$

GISAXS measurements were performed with the Anton Paar SAXSess instrument in alignment and a computer controlled goniometer for sample alignment. Calibration of the incident angle is performed using an iterative procedure where the film of interest is raised vertically such that it attenuates half of the main beam intensity while having symmetric intensity decay as a function of the tilting angle. The two-dimensional patterns obtained from a GISAXS measurement are treated with a set of macros implemented in IGORPro to convert pixel positions of the raw scattering images to Q_x, Q_y, and Q_z with respect to the sample reference frame. The scattering patterns were corrected for dark current and normalized to scattering time, but no absolute scale correction was applied.

3.4 The Relationship for I(Q) vs Q – Transmission Geometry

Within the context of a small angle scattering experiment, whether the sample be a dispersion of dilute colloidal particles or a film that has embedded domains within it, the scattered intensity collected on a detector will represent the ensemble average over its entire illuminated volume. In

fact, regardless of shape or distribution of density fluctuations within the sample, *I(Q)* will be proportional to ϕ, the volume fraction of scatters in the sample, V_{part}, the average volume of the scatterer, and $\Delta SLD^2=(SLD_{part}-SLD_{solv})^2$.[21] (Equation 3.7)

$$3.7 \quad I(Q) \sim \phi V_{part} \Delta SLD^2 \text{ where } \phi = N \cdot V_{part} / V$$

The *Q*-dependence comes from the particular details of the scattering entity's shape and the distribution of those domains within the sample. This *Q*-dependent component is commonly expressed as the product of the form factor, *P(Q)*, and the structure factor *S(Q)*, *I(Q)~P(Q)S(Q)*. Therefore, in general form, equation 3.8 shows the relationship between scattering intensity *I* and *Q*.

$$3.8 \quad I(Q) = \phi V_{part} \Delta SLD^2 P(Q) S(Q)$$

The form factor and structure factor are functions that are normalized such that *P(Q*=0*)*=1 and *S(Q*=0*)*=1, and are given by the Patterson function of the particle, Equation 3.9, and the structure factor by Equation 3.10. In Equation 3.9, $\gamma(\mathbf{r})$ is the correlation function of the particle.

$$3.9 \quad P(Q) = \frac{1}{V_{part}} \int_{V_{part}} \gamma(r) e^{-iQ \cdot r} dr$$

$$3.10 \quad S(Q) = 1 + \frac{N}{V} \int \left[g(\mathbf{r}) - 1 \right] \cdot e^{-iQ \cdot \mathbf{r}} d\mathbf{r}$$

Take for example, the form factor for spherical colloidal particles dispersed in water shown in Equation 3.11.[5] In this expression, the parameter *R* defines the sphere's radius and would be a potential fitted parameter to experimental data.

$$3.11 \quad P_{sphere}(Q) = \left[\frac{3\left(\sin\left(QR\right) - QR\cos\left(QR\right)\right)}{\left(QR\right)^3} \right]^2$$

In the dilute case, the interaction between spheres in the dispersion is minimal so the spheres can be treated as a gas ($S(Q)$=1). $P_{sphere}(Q)$ is plotted for monodispere spheres, R=50 Å, in Figure 3.4a. As the spheres become enriched, their volume fraction in solution increases and the positions between spheres will become increasing correlated. For hard spheres of radius, $g(\mathbf{r})=-e^{-U(\mathbf{r})/kT}$, where $U(\mathbf{r})$ is the potential of mean force ($U(\mathbf{r})$ = 0, when $\mathbf{r}>D$ and $U(\mathbf{r})$ = ∞ when r<D). Using the Percus-Yevick closure, $S(Q)$ can be derived analytically and its impact on the scattering profile shown as a function of Q as shown in Figure 3.4b.[22] Below ϕ=0.001, the contribution that interparticle interactions have on the scattering profile is negligible.

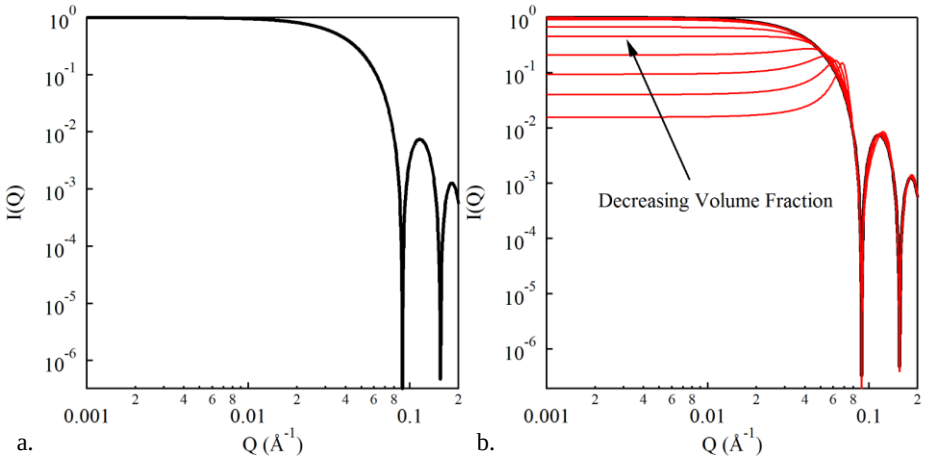

Figure 3.4. a.) Normalized form factor, $P(Q)$, for an isolated sphere, R=50 Å, b.) normalized $P(Q)S(Q)$ plots for hard-sphere interactions demonstrating the effect of interparticle interactions on scattering profiles.

In real systems, the scattering objects are never perfectly monodisperse in either size or shape. Often, there is some average size and distribution that can describe the relative concentration of different scattering objects within a material. In those cases, $I(Q)$ can be calculated from an appropriately weighted average of the particle shapes and sizes which make up the sample. In

principle, for polydispersity in size, if the shape function of a material is known, then the distribution can be determined analytically. Also, if the distribution of size is known *a priori*, then the distribution of shapes can be determined. Commercial scattering packages often include a variety of analytical distributions to account for polydispersity in size including Gaussian, Lognormal, Schultz and Rectangular.[16,23,24] While these distributions are convenient to use because they are typically defined by a small number of parameters, it is of course possible to calculate the scattering from profile resulting from any arbitrary particle size and shape distribution simply by using the appropriate weighting of the monodisperse scattering form factor models from the subpopulations of particles.

$$3.12 \quad I(Q) = \Delta SLD^2 \frac{\sum_i \phi_i V_{part,i} P_i(Q)}{\sum_i \phi_i V_{part,i}}$$

As an example, Figure 3.5a shows the effect of increased polydispersity on the scattering function for spheres with R_{avg} = 50 Å, and increasing polydispersity index (PDI = σ_{stdev}/R_{avg}).

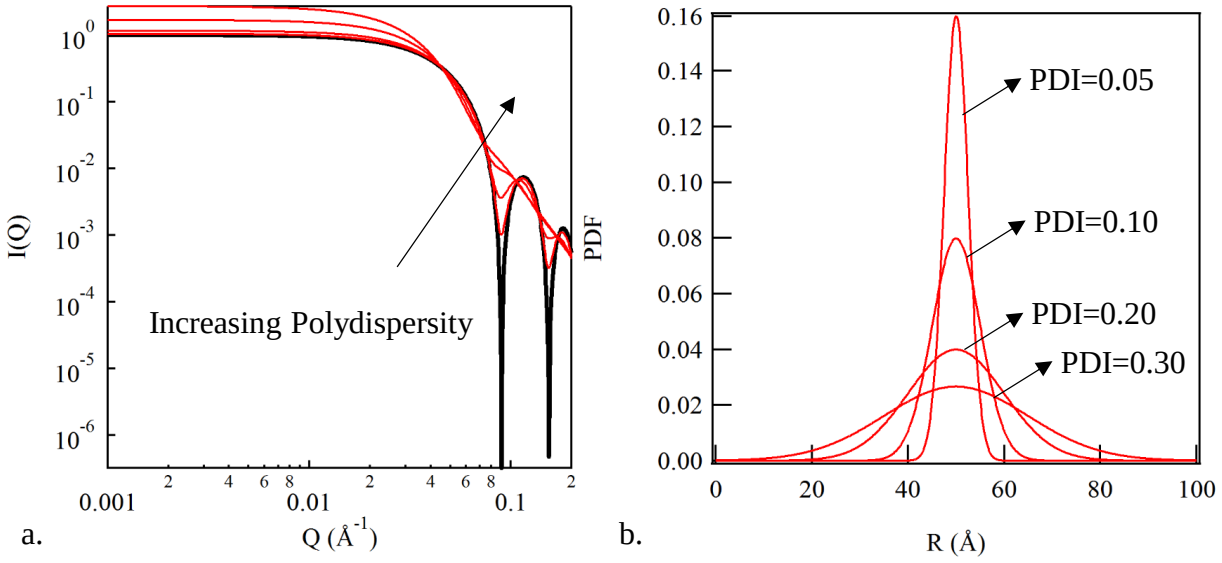

Figure 3.5. a.) $I_{sphere}(Q)$ vs Q for R_{avg} = 50 Å dispersion with increasing polydispersity, b.) Normal distribution of particle sizes for $I_{sphere}(Q)$ profiles in (a.).

From Figure 3.5, the bias of polydispersity for larger particles is evident based on the shift of the scattering curves toward lower Q, and the diminished oscillations at high-Q. This effect is called smearing and in general systems with large degrees of polydispersity can possess large uncertainty in the fitted distribution values.

Another important contribution to smearing can come from instrumental resolution.[25] These include finite divergence of the main beam, wavelength distribution, and finite pixel size. The above analysis neglects any of these contributions to the overall scattering curve. In real measurements, the beam always has some finite dimension and like in the case of SANS, possibly some distribution of wavelengths.[26] It is often that the finite pixel size can be neglected. *I(Q)* models can also be modified to account for instrumental broadening.

$$3.13 \quad I_{corr}(Q) = \int_0^\infty I_{model}(Q) R(\bar{Q}, Q, \Delta Q)\, \mathrm{d}\bar{Q}$$

$$\textit{where} \quad \Delta Q^2 = Q^2 \left(\frac{1}{2\sqrt{2\ln 2}} \frac{\Delta\lambda}{\lambda} \right)^2 + \left(\left(\frac{4\pi}{\lambda} \right)^2 - Q^2 \right) \Delta\theta$$

$$\textit{and} \quad R\left(\bar{Q}, Q, \Delta Q\right) = \frac{1}{\Delta Q\sqrt{2\pi}} \exp\left(-\frac{\left(\bar{Q} - Q\right)^2}{2\left(\Delta Q\right)^2} \right)$$

Mathematically the known smearing contribution can be applied to any analytical model. This procedure is preferably applied to analytical model before fitting to improve the agreement with experimental data. At this point, the discussion has been completely general and only assumes that the measurement is made in transmission geometry. In Chapters 5 and 6, specific implementation of these equations as they pertain to the analysis of small angle scattering data from dispersed CNP colloidal particles will be discussed.

3.5 Deriving the relationship I(Q) vs Q – Grazing Incidence Geometry

The derivation for *I(Q)* vs *Q* in grazing incidence geometry is somewhat more complex than the transmission geometry. It must be applied with much more care depending on the specific details of the experiment. As mentioned in Section 3.4, this treatment falls within the context of the DWBA. For this discussion, we will limit our analysis to particles encapsulated in a thin-film supported on a substrate because it is the geometry that is most closely related to the investigation of structural morphology of polymer/fullerene composite thin-films. Figure 3.6a shows a schematic representation of spheres embedded within a thin-film on a substrate. In this figure, there are four different perturbations that account the interference between the film, substrate and the particles. This image is a depiction of the DWBA framework and the ability to predict the scattering intensity as a function of ***Q***. Accounting for these four different interactions, ***I(Q)*** can be calculated from the expression in Figure 3.6b as the sum of the contribution of each of the four terms weighted by their Fresnel coefficients. This equation is valid for the case of dilute spheres in the thin-film. As the particle concentration increases, the analysis is more sensitive to local *SLD* changes within the film and a graded interface model must be used that can account for composition profile throughout the film as depicted in Figure 3.6c.[17]

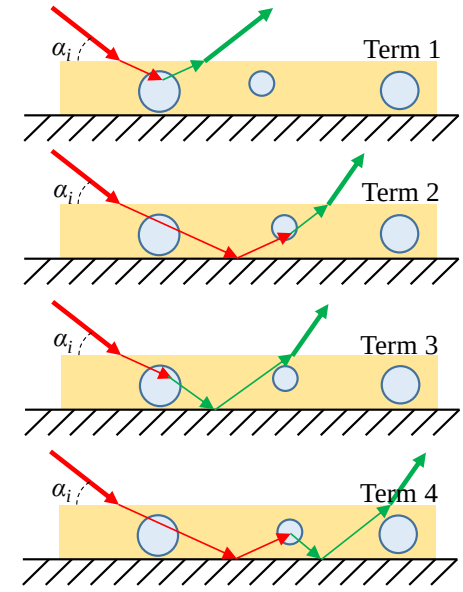

a.

$$I(\mathbf{Q}) = R_0^2 \,|\, T_{2i}T_{2f} \int_{-\infty}^{\infty}\int_{-\infty}^{\infty}\int_{0}^{d} \left(SLD(\mathbf{r}) - SLD_m\right) e^{-i(Q_x r_x + Q_y r_y + Q_{z,term1} r_z)}\, dr_z dr_x dr_y +$$

$$T_{2i}R_{2f} \int_{-\infty}^{\infty}\int_{-\infty}^{\infty}\int_{0}^{d} \left(SLD(\mathbf{r}) - SLD_m\right) e^{-i(Q_x r_x + Q_y r_y + Q_{z,term2} r_z)}\, dr_z dr_x dr_y +$$

$$R_{2i}T_{2f} \int_{-\infty}^{\infty}\int_{-\infty}^{\infty}\int_{0}^{d} \left(SLD(\mathbf{r}) - SLD_m\right) e^{-i(Q_x r_x + Q_y r_y + Q_{z,term3} r_z)}\, dr_z dr_x dr_y +$$

$$R_{2i}R_{2f} \int_{-\infty}^{\infty}\int_{-\infty}^{\infty}\int_{0}^{d} \left(SLD(\mathbf{r}) - SLD_m\right) e^{-i(Q_x r_x + Q_y r_y + Q_{z,term4} r_z)}\, dr_z dr_x dr_y \,|^2$$

b.

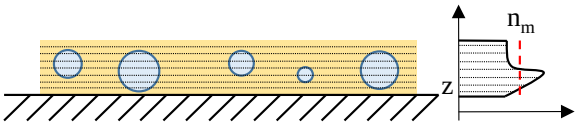

c.

Figure 3.6 a.) Schematic description of all four terms account for in DWBA for GISAXS from particles embedded within a thin-film on a substrate, b.) DWBA formalism for accounting for four terms in DWBA, and c.) schematic depiction of DWBA accounting for the graded interface.

This inevitably leads to a more complex expression for $I(\mathbf{Q})$, which is beyond the scope of this discussion, though likely relevant for thin-film polymer/fullerene composites. Because of the presence of the substrate, the analytical $P(\mathbf{Q})$ form factor models must also be modified to account for the orientation of the particle with respect to the substrate. In addition, planar structural order, polydispersity, and instrumental broadening must be accounted to accurately model scattering from embedded structures within thin-films. In chapter 4, GISAXS patterns collected from thin-film polymer/fullerene composites will be analyzed in both the small angle and wide angle region. This analysis is qualitative and will not generally employ the DWBA, but nonetheless it is important to have an understanding of the processes that underlie a GISAXS experiment so that the structural features interrogated with the technique can be appropriately interpreted.

References:

1. Spano, F. C.; Clark, J.; Silva, C.; Friend, R. H. Determining Exciton Coherence from the Photoluminescence Spectral Line Shape in Poly(3-Hexylthiophene) Thin Films. *J. Chem. Phys.* **2009**, *130*, 074904.

2. Cunningham, P. D.; Hayden, L. M. Carrier Dynamics Resulting from Above and Below Gap Excitation of P3HT and P3HT/PCBM Investigated by Optical-Pump Terahertz-Probe Spectroscopy. *J. Phys. Chem. C* **2008**, *112*, 7928–7935.

3. Li, G.; Shrotriya, V.; Huang, J.; Yao, Y.; Moriarty, T.; Emery, K.; Yang, Y. High-Efficiency Solution Processable Polymer Photovoltaic Cells by Self-Organization of Polymer Blends. *Nat. Mater.* **2005**, *4*, 864–868.

4. Pingree, L. S. C.; Reid, O. G.; Ginger, D. S. Electrical Scanning Probe Microscopy on Active Organic Electronic Devices. *Adv. Mater.* **2009**, *21*, 19–28.

5. Lindner, P, Zemb, T. *Neutrons, X-Rays and Light: Scattering Methods Applied to Soft Condensed Matter*; North-Holland, 2002.

6. Feigin, L. A.; Svergun, D. I. Structure Analysis by Small-Angle X-Ray and Neutron Scattering. *Acta Polym.* **1989**, *40*, 224.

7. Glatter, O.; Kratky, O. *Small Angle X-Ray Scattering*; Academic Press Inc., 1982.

8. Lazzari, R. IsGISAXS Manual http://ln-www.insp.upmc.fr/axe4/Oxydes/IsGISAXS/isgisaxs.htm.

9. Kline, S. R. Reduction and Analysis of SANS and USANS Data Using IGOR Pro. *J. Appl. Crystallogr.* **2006**, *39*, 895–900.

10. Glinka, C. J.; Barker, J. G.; Hammouda, B.; Krueger, S. The 30 m Small-Angle Neutron Scattering Instruments at the National Institute of Standards and Technology. *J. Appl. Crystallogr.* **1998**, *31*, 430–445.

11. Barker, J. G.; Glinka, C. J.; Moyer, J. J.; Kim, M. H.; Drews, a. R.; Agamalian, M. Design and Performance of a Thermal-Neutron Double-Crystal Diffractometer for USANS at NIST. *J. Appl. Crystallogr.* **2005**, *38*, 1004–1011.

12. Feigin, L.A., Svergun, D. I. *Structure Analysis by Small-Angle X-Ray Scattering and Neutron Scattering*.

13. Tate, M. P.; Urade, V. N.; Kowalski, J. D.; Wei, T.; Hamilton, B. D.; Eggiman, B. W.; Hillhouse, H. W. Simulation and Interpretation of 2D Diffraction Patterns from Self-Assembled Nanostructured Films at Arbitrary Angles of Incidence: From Grazing Incidence (above the Critical Angle) to Transmission Perpendicular to the Substrate. *J. Phys. Chem. B* **2006**, *110*, 9882–92.

14. Stribeck, N. *Applications of Synchrotron Light to Scattering and Diffraction in Materials and Life Sciences*; Gomez, M.; Nogales, A.; Garcia-Gutierrez, M. C.; Ezquerra, T. A., Eds.; Springer Berlin Heidelberg: Berlin, Heidelberg, 2009; Vol. 776, pp. 23–60.

15. Vineyard, G. H. Grzing-Incidence Diffraction and the Distorted-Wave Approximation for the Study of Surfaces. *Phys. Rev. B* **1982**, *26*, 1–14.

16. Babonneau, D. FitGISAXS : Software Package for Modelling and Analysis of GISAXS Data Using IGOR Pro. *J. Appl. Crystallogr.* **2010**, *43*, 929–936.

17. Lazzari, R.; Leroy, F.; Renaud, G. Grazing-Incidence Small-Angle x-Ray Scattering from Dense Packing of Islands on Surfaces: Development of Distorted Wave Born Approximation and Correlation Between Particle Sizes and Spacing. *Phys. Rev. B* **2007**, *76*, 125411.

18. Urade, V. N.; Bollmann, L.; Kowalski, J. D.; Tate, M. P.; Hillhouse, H. W. Controlling Interfacial Curvature in Nanoporous Silica Films Formed by Evaporation-Induced Self-Assembly from Nonionic Surfactants. II. Effect of Processing Parameters on Film Structure. *Langmuir* **2007**, *23*, 4268–78.

19. Ehlers, J.; Hepp, K.; Board, E.; Beig, R.; Domcke, W.; Frisch, U.; Hillebrandt, W.; Jaffe, R. L. *Lecture Notes in Physics*.

20. Rauscher, M.; Salditt, T.; Spohn, H. Small-Angle X-Ray Scattering Under Grazing Incidence: The Cross Section in the Distorted-Wave Born Approximation. *Phys. Rev. B* **1995**, *52*, 1–11.

21. Guinier, A.; Fournet, G. *Small Angle Scattering of X-Rays*; Wiley, New York, 1955; p. 7.50.

22. Percus, J. K.; Yevick, G. J. Analysis of Classical Statistical Mechanics by Means of Collective Coordinates. *Phys. Rev.* **1958**, *110*, 1–13.

23. SasView SasView, http://www.sasview.org/.

24. Tjioe, E.; Heller, W. T. ORNL_SAS : Software for Calculation of Small-Angle Scattering Intensities of Proteins and Protein Complexes. *J. Appl. Crystallogr.* **2007**, *40*, 782–785.

25. Lake, J. a. An Iterative Method of Slit-Correcting Small Angle X-Ray Data. *Acta Crystallogr.* **1967**, *23*, 191–194.

26. Pedersen, J. S.; Posselt, D.; Mortensen, K. Analytical Treatment of the Resolution Function for Small-Angle Scattering. *J. Appl. Crystallogr.* **1990**, *23*, 321–333.

Chapter 4. Thin-Film Conjugated Polymer/Fullerene Composites

In the current paradigm of organic photovoltaics production, composite conjugated polymer/fullerene thin-films are produced using solution phase processing. This consists of first dissolving the conjugated polymer and fullerene into a common solvent. The solution is then solution cast onto the desired substrate, and then either solvent or thermal annealed to develop the desired nanophase morphology that gives rise to the best performance. It has been well established that there are a large number of factors that can influence device performance. A non-exhaustive list includes annealing temperature, time, solvent choice, substrates surface energy, material purity, the presence of additives, solubility of the components, molecular weight distribution of the polymer, coating method, film thickness and solution viscosity. The device engineer's job is to identify for a given set of materials (i.e. conjugated polymer and fullerene derivative) the conditions that lead to the best performance. Optimization of performance in this parameter space is an enormous task, yet some heuristics have been developed:

1. For non-crystalline conjugated polymers, fullerene rich films (ϕ_{PCBM}>50 vol%) tend to give rise to better performance.[1,2]
2. The film thickness is usually thinner than what is necessary to absorb all of the light. [3]
3. High boiling point additives in the organic solvent phase lead to a more favorable ‘‘as-cast" state. [4]
4. Long annealing times inevitably lead to morphological degradation due to crystallization of the fullerene.[5–7]
5. Semi-crystallization polymer domains are desirable, but highly ordered polymer crystallites are unfavorable.[8]

These factors are nicely demonstrate in the evolution of morphology in P3HT/PCBM thin-film composites. The development of morphology in these blends is often tied to the crystallization of P3HT in the solid state. This occurs when PCBM becomes supersaturated in the rubbery disordered P3HT domains at temperatures below their common miscibility point (T_{misc} = 205 °C – 290 °C for P3HT and PCBM depending on film composition) and above the glass transition of P3HT (T_{glass}= 12 °C).[9,10] There are no evident thermodynamic phase transitions in P3HT/PCBM blends between these two temperatures.[9] Because of the simultaneous crystallization process, regardless of the specific thermal treatment, the instantaneous morphology that leads to a particular device performance is only a transient one and will likely continue to evolve with time even when the temperature is lowered. While quenching a film from the annealing temperature to ambient conditions slows the evolution of the film morphology, the polymer/fullerene films are still inherently unstable due to the finite solubility and relatively high mobility of PCBM in the amorphous conjugated polymer domains.[11,12] Films will continue to slowly evolve over time as the crystallization of both components proceeds. Under typical annealing conditions (120 °C<T_{anneal}<170 °C), this effect manifests itself as a drop in solar cell performance when longer annealing times are used and PCBM crystal domains overgrow. Performance decreases once the crystal size exceeds the optimal size for ideal bulk heterojunctions because the total interface between p-type and n-type domains decreases with increasing domain size. However, even at modest operating temperatures for polymer solar cells (20°C<T_{op}<80°C), slow structural evolution and performance degradation persists as a result of PCBM crystal growth.[13] This concept is shown schematically in Figure 4.1. This mechanism of degradation is not only a practical challenge for the optimization of active layer morphology in polymer solar cells, but also for making devices that have adequate lifetimes (years) at normal operating conditions.

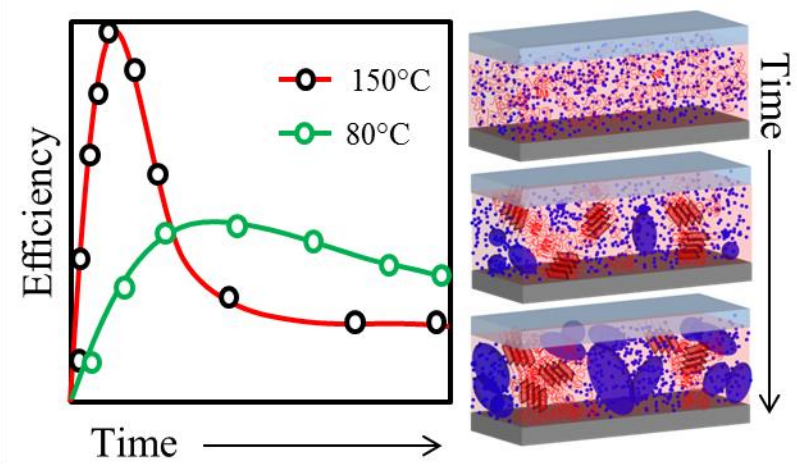

Figure 4.1. Schematic of phase segregation and coarsening occurring inside active layers (right) and for the changes in device performance that are expected to occur as a function of time at different temperatures (left).

There is a therefore a need to improve the thermal stability of polymer/fullerene solar cells by controlling the crystallization of the fullerene phase. Several strategies are currently being pursued. The first approach is the synthesis of compatibilizing agents that function to stabilize the polymer/fullerene interface.[14,15] For example Tsai et al. synthesized a poly(4-vinyltriphenylamine)/P3HT copolymer using quasi-living Grignard metathesis and living anionic polymerization.[16] These molecules have the potential to improve long-term thermal stability as they function like surfactants that prevent further coarsening of the polymer and fullerene phases, but more study is needed to understand the specific effects these materials have on the morphology of the active layers. A second approach that has been employed is the synthesis of fullerenes with different substitution moieties. Using novel chemical routes, it is possible to synthesize fullerenes that are not capable of packing into uniform crystals; therefore phase segregation is only driven by the crystallization of the polymer phase. This approach has been recently demonstrated with a new PCBM derivative consisting of 1,2-dihydromethano-[60] PCBM by Li et al.[17,18] This approach is highly desirable for conjugated polymers that crystallize

into nanofibers because the final domain size is defined by the dimension of the nanofibrils with the fullerene matrix acting like a space-filling glassy matrix. However, in cases where the polymer has a relatively low crystallinity or does not form nanofibers, it is also desirable to have the ability to systematically modify the crystallization of the fullerene phase.[19]

One strategy that is outlined in this chapter is to incorporate C_{60} into the fullerene phase of P3HT/PCBM solar cells in order to systematically modify the crystal habit of PCBM. The solubility of C_{60} in chlorobenzene is only 6-7 mg/mL and this has limited its use in device manufacture. Nevertheless, its use has been demonstrated as a pure n-type material for the fabrication of polymer solar cells via optimization of solvent conditions.[20] Because C_{60} is a precursor to PCBM and many other fullerene derivatives, it also has a lower associated cost and no additional synthesis requirements.

4.1 P3HT/PCBM/C_{60} Thin-Film Characterization

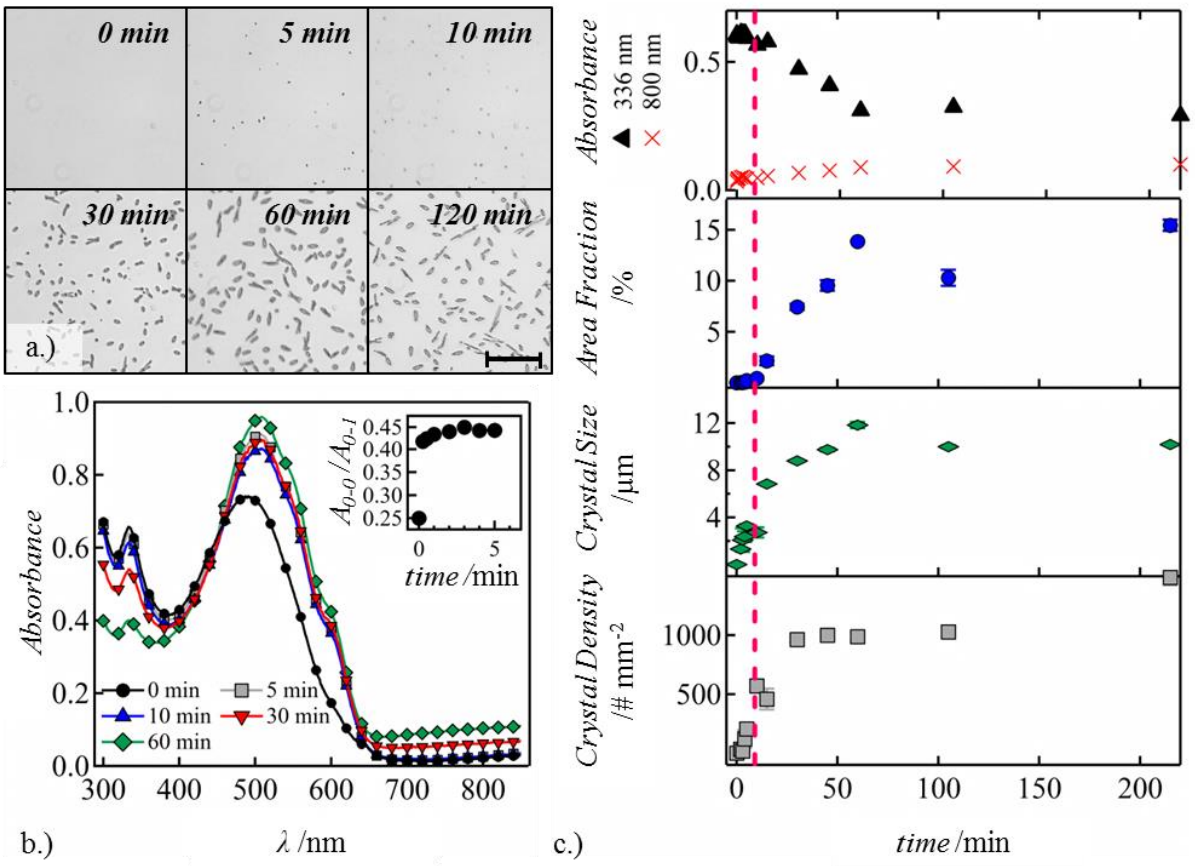

Figure 4.2. a.) Optical micrographs of P3HT/PCBM blends annealed at 150°C at different times *(scale bar is 100 μm),* b.) UV-visible absorption spectroscopy of the films after annealing for different times – inset is the P3HT $A_{0\text{-}0}/A_{0\text{-}1}$ ratio vs. time (min), c.) Summary of UV-visible absorption and optical microscopy data showing crystallite density, crystallite size, fractional area occupied by the crystallites on the film's surface, and the value of absorbance at λ = 336 nm. The dashed red line signifies the formation of visible PCBM aggregates on the film's surface.

Optical micrographs and UV-Visible absorption spectra (Figure 4.2) of P3HT/PCBM blends spin-coated on glass and annealed at 150 °C are shown in Figure 4.2a and Figure 4.2b respectively**.** We used these two techniques to monitor the extent of large-scale crystal overgrowth in the films. Image analysis applied to the micrographs provided a means to quantify the total area occupied by visible crystallites, their number, and their average size, which is equivalent to the side length of a square with the same area as each crystallite. Specific

signatures of PCBM overgrowth can also be observed in the UV-Visible absorption spectra in Figure 4.2b. After the spectra are normalized to account for differences in film thickness, there is a clear decrease in absorbance at a wavelength of 336 nm. This peak is the lowest energy absorption feature for PCBM and its decrease indicates migration of isolated PCBM molecules to join large PCBM crystallites. As seen in Figure 4.2c, the decrease in the peak at 336 nm that begins around 5 minutes (marked by the dotted red line) corresponds almost exactly with a slight increase in the absorbance background at higher wavelengths (< 650 nm). This is expected as large PCBM aggregates will block or scatter a larger fraction of the incident light at all wavelengths.

Figure 4.2 shows that PCBM overgrowth began after only 5 minutes of annealing. After 5 minutes annealing, the P3HT achieved its maximum crystallinity as indicated by the A_{0-0}/A_{0-1} ratio (inset, Figure 4.2b where A_{0-0} = 605 nm and A_{0-0} = 538 nm).[21] At this point, the number density and average size of visible crystallites increased rapidly. This corresponded to a decrease in the PCBM absorption peak at 336 nm. After an hour of annealing, the PCBM absorption peak at 336 nm stopped decreasing, and a large number of 12 μm crystallites occupied 15% of the visible film area. The growth process slowed at longer annealing times. This is likely a result of the depletion of all of the free PCBM within the film. Because optical microscopy is only sensitive to crystals larger than ~1 μm, this analysis does not account for nano-scale PCBM aggregates that are known to form during the early periods of annealing and could still be present even after long periods of annealing.[22] Therefore, these techniques can only quantify a limited region of the kinetics of growth of PCBM crystallites. However, this analysis does establish a strong basis for demonstrating the fundamental morphological instability of annealed P3HT/PCBM films. After initial nucleation, PCBM crystallites continued to grow through

migration of PCBM within the disordered regions of the polymer matrix until the chemical potential of PCBM dissolved in the amorphous P3HT is balanced with the chemical potential of PCBM in a crystallite. Therefore, the ultimate extent of overgrowth observed in these films is a complex function of the solubility and mobility of PCBM in the polymer matrix, the number of nucleation sites, the crystallinity of the polymer within the film, and the film composition. For the addition of C_{60} to the fullerene phase of polymer/fullerene blends to be effective, it must modify the growth kinetics of the fullerene crystallites such that the extent of fullerene overgrowth is reduced.

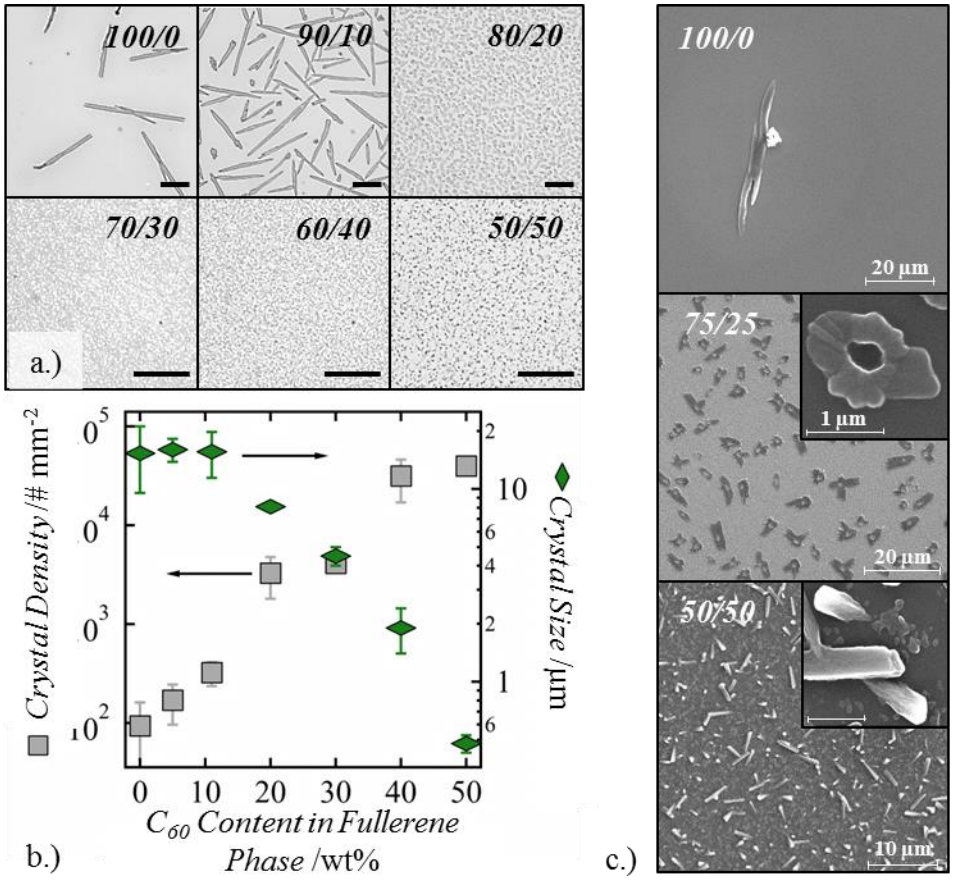

Figure 4.3. a.) Optical micrographs of films with varying PCBM/C_{60} content in the fullerene phase of a P3HT:fullerene film annealed for 2 hours at 150ºC. *(Scale Bar is 50 μm)*, b.) Summary of the average crystal size and number of visible "overgrown" crystals at 2 hrs. annealing, c.) Scanning electron micrographs of PCBM/C60 films after 1 hour annealing at 150ºC on silicon wafers.

In order to quantify the extent of overgrowth when C_{60} is incorporated into the fullerene phase of P3HT/PCBM blends, we fabricated P3HT/PCBM/C_{60} blends with a constant P3HT:fullerene weight ratio and varied PCBM/C_{60} content in the fullerene phase. Figure 4.3a shows the optical micrographs of P3HT:fullerene films with increasing C_{60} content in the fullerene phase. These films were annealed at 150 ºC for 2 hours. After applying the same analysis to these images as in Figure 4.2, Figure 4.3b shows the number density and the average size of visible "overgrown" crystals as a function of PCBM/C_{60} content in the fullerene phase. Scanning electron micrographs of PCBM/Fullerene films annealed at 150 °C for 1 hour are also shown in Figure 3C to access smaller length scales. The extent of overgrowth is strongly dependent on the C_{60} composition in these films. From the optical micrographs, it is clear that the presence of C_{60} causes a significant increase in the number density of crystallites while also simultaneously decreasing the average size of the visible overgrown crystals. The SEM images in Figure 3C also show that the morphology of the individual crystallites was significantly affected by the incorporation of C_{60} in the fullerene phase. As the C_{60} content is increased to 25 wt% in the fullerene phase, the crystallites are clearly much less needle-like and instead form disc-like or flower-like structures. As the C_{60} content in the fullerene phase increases to 50 wt%, apparent crystal size decreases and the morphology becomes increasingly faceted. The degree to which crystals overgrow also appears to decrease but they tend to form faster during annealing. Where the 100% PCBM films took more than 1 hour at 150 °C to reach a fully stabilized morphology, very small quantities of C_{60} in the fullerene phase resulted in extensive crystallization within 5-10 minutes of annealing at 150 °C. However, once this initial growth ceased, the crystals maintained their smaller size even after very long annealing periods at 150 °C.

In order to test the stability of polymer/fullerene blends that incorporate C_{60} against accelerated aging conditions, P3HT:fullerene films with varying PCBM/C_{60} content were annealed at 150 °C and then aged at 90 °C. This temperature is somewhat higher than what is expected for typical solar-cell operating conditions but it is also lower than typical annealing temperatures. This experiment was also designed to test whether high-temperature annealing alone provided enhanced thermal stability for devices during operation since it had been previously observed that annealing at higher temperatures stabilizes P3HT/PCBM blends.[11] These films were again monitored using optical microscopy as shown in Figure 4.4. In order to better resolve small crystallites, SEM images were also taken for samples corresponding to the optical micrographs of films annealed for 5 minutes at 150 °C and then aged at 90 °C.

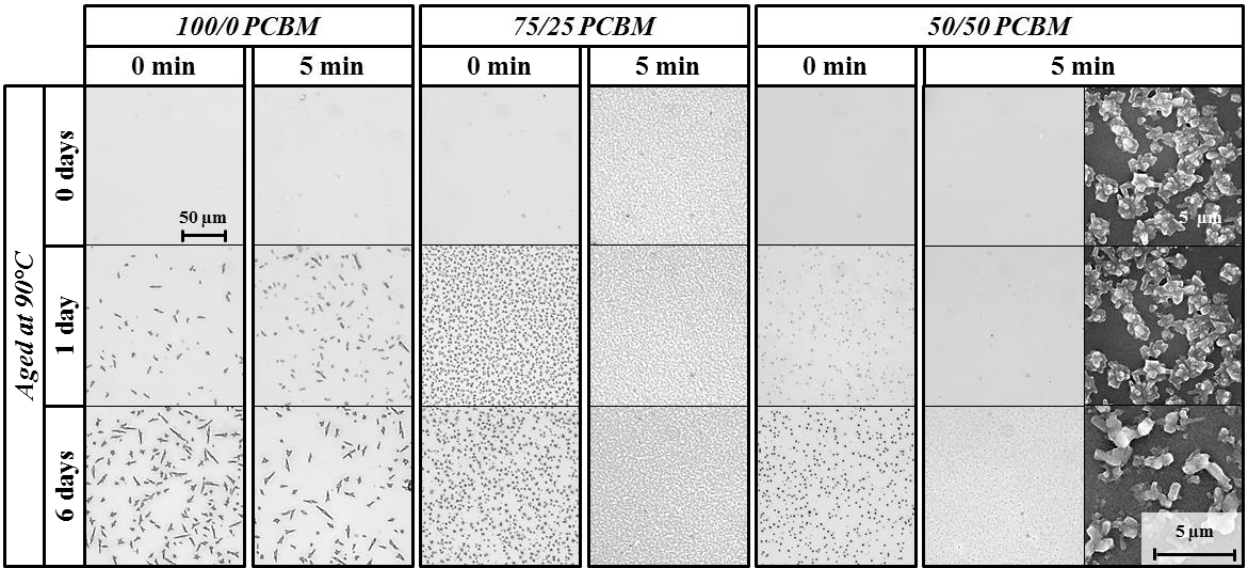

Figure 4.4. Optical micrographs of films with varying PCBM/C_{60} that have been annealed at 150°C and aged at 90°C. Right column are scanning electron micrographs of the 50/50 films annealed for 5 minutes and aged for varying times.

absorption spectra were also obtained for these films and are presented in Figure 4.5 along with analysis of crystal size for each film. After 6 days of aging at 90 °C, the P3HT:fullerene films with 100/0 PCBM/C_{60} composition in the fullerene phase resulted in the same final aggregate size of ~10 µm regardless of the annealing condition. This observation is contrary to some reports claiming that high temperature annealing stabilizes P3HT/PCBM blends to crystal overgrowth.[11] Interestingly, annealing the 50/50 PCBM/C_{60} blend did make the films significantly more stable to overgrowth when compared to films that were not annealed before aging. Aging the P3HT:fullerene blends with 50/50 PCBM/C_{60} ratio for 6 days resulted in crystals with an average size of 3 µm if they were not annealed first. However, identical films subjected to 5 minutes of annealing at 150 °C resulted in ~300 nm crystals after 6 days of aging. This represents an order of magnitude difference in crystal size with and without annealing.

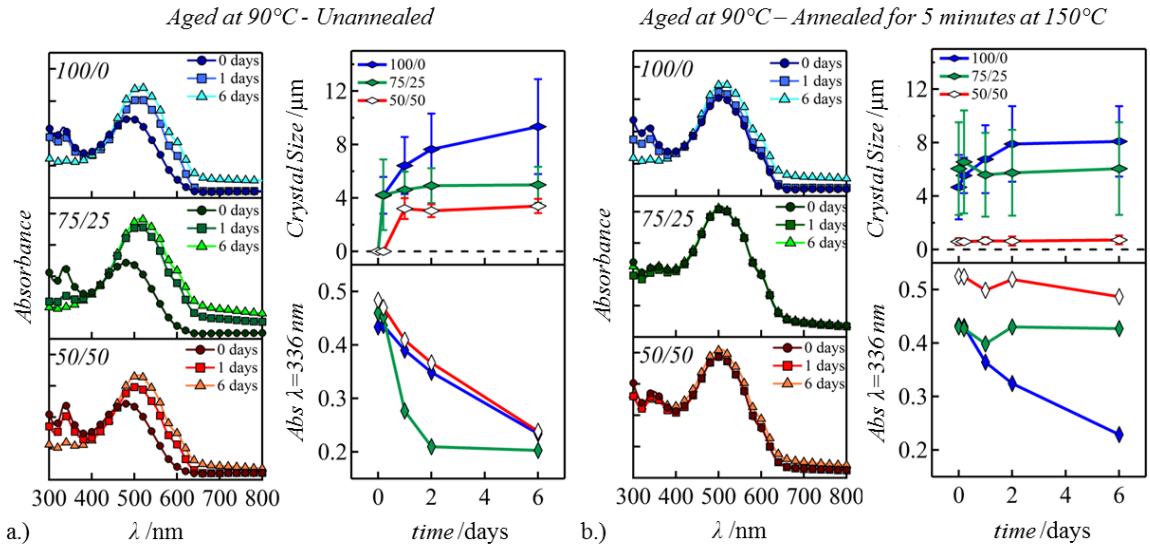

Figure 4.5. a.) P3HT:fullerene films with varying PCBM/C_{60} content aged at 90°C without annealing, b.) P3HT:fullerene films with varying PCBM/C_{60} content annealed for 5 minutes at 150°C and then subsequently aged at 90°C.

The absorption spectra in Figure 4.5 provide further insight into the crystal overgrowth shown in Figure 4.4. Regardless of the composition of the fullerene phase, the absorption peak at 336 nm decreased and the average crystal size increased as a function of aging time when the films were not annealed. Therefore, aggregates large enough to be fully opaque to the spectrometer were forming throughout the films. For the annealed 100/0 PCBM/C_{60} film, the absorbance behavior was very similar to when it was not annealed. This is not surprising considering the long-time scale of PCBM overgrowth leaves plenty of free PCBM to continue to diffuse to growing crystallites when no C_{60} is present. For the annealed 75/25 PCBM/C_{60} film, after 5 minutes of annealing, large aggregates have already formed on the surface and the absorbance at 336 nm has already decreased. Therefore, aging the film at 90 °C had very little effect on the crystal size and absorbance at 336 nm. This was also the case for the 50/50 PCBM/C_{60} films. Interestingly, the absorbance at 336 nm stayed relatively constant even when compared when the film was not annealed. This verifies that the crystallites formed in this film are sufficiently small that they are still transparent to the spectrometer and that they are more stable to further growth than films that do not incorporate C_{60}.

4.2 PCBM/C_{60} Organic Field-Effect Transistors (OFETs)

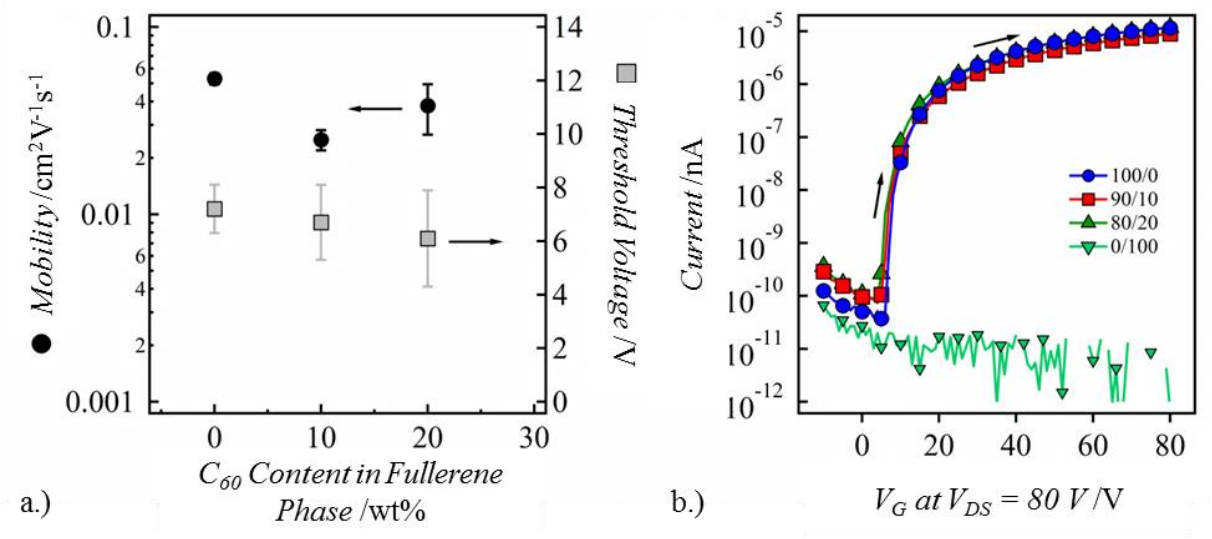

Figure 4.6. a.) Electron mobility and threshold voltage as a function of PCBM composition, b.) Forward sweep of transfer curve for OFETS made from PCBM/C_{60} blends of different composition.

To this point, this work has focused on the characterization of the extent of overgrowth of PCBM crystallites from P3HT:fullerene films after different thermal treatments with varying PCBM/C_{60} composition in the fullerene phase. This characterization showed that, at relatively high C_{60} loadings, PCBM crystal overgrowth is reduced and the morphology is modified. Results also suggest that this approach could lead to more thermally stable OPVs. However, for this approach to be viable, the modification of the morphology of the fullerene phase must occur without a significant reduction of the electron transport properties in the fullerene phase. To test the effect of addition of C_{60} on the electron mobility of PCBM, we fabricated organic field-effect transistors (OFETs) from PCBM/C_{60} solutions with varying C_{60} content (no P3HT). Figure 4.6a shows the measured field-effect mobility and threshold voltage from these devices and Figure 4.6b, the current–voltage (I–V) characteristic of representative devices. Overall, the electron mobility decreases slightly with the addition of C_{60} to PCBM with values of 0.05 $cm^2/V{\cdot}s$ in pure PCBM and 0.03–0.04 cm^2/Vs in the PCBM/C_{60} mixtures. This observation is not surprising

given that prior theoretical work has also shown little effect of polycrystalline structures on the electron mobility of pure C_{60} transistors.[35] The poor performance of 0/100 C_{60} devices is a result of poor film adhesion to the substrate. In fact, films with PCBM content below ~75 wt% did not form films with quality that is high enough to be tested using this approach.

4.3 P3HT/PCBM/C_{60} Organic Solar Cells (OSCs)

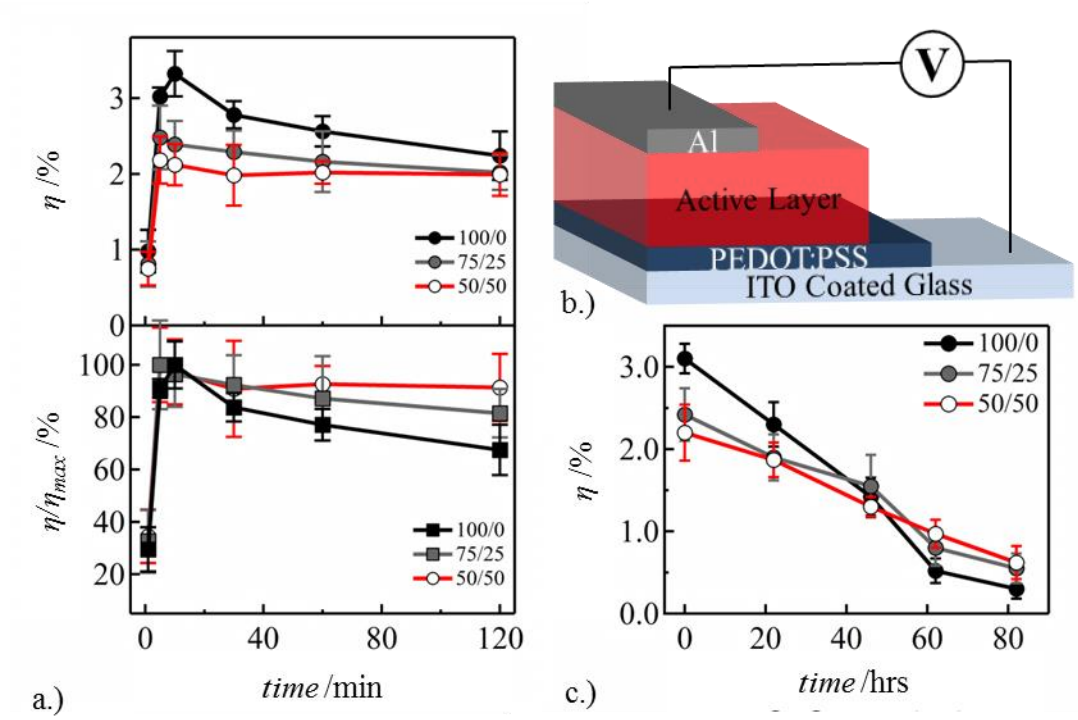

Figure 4.7. a.) Efficiency and normalized efficiency of P3HT:fullerene devices with varying C_{60} content as a function of annealing time, b.) Schematic of layers of OSCs fabricated for this study, c.) Efficiency of P3HT:fullerene devices with varying C_{60} content as a function of aging time after being annealed for 5 minutes at 150°C.

The morphological studies of the effects of addition of C_{60} into the fullerene phase of P3HT/PCBM solar cells have, to this point, been based on experiments conducted on 'free' films coated on glass. There are a number of studies that show that the presence of a top electrode on P3HT/PCBM active layers can significantly affect the kinetics of PCBM diffusion and also

modify the extent of vertical phase segregation. [36, 37] It is therefore, difficult to directly infer device performance from only the observations of morphology in P3HT/PCBM active layers annealed without a confining top electrode. In order to test whether the incorporation of C_{60} into the fullerene phase of P3HT:fullerene films leads to more thermally stable OSCs, we have fabricated devices with an aluminum electrode evaporated onto the active layer before applying the thermal treatment (post-annealing). The performance of the OSCs was then tested after different thermal treatments. The first thermal treatment consisted of an annealing time study at 150 °C. As shown in Figure 4.7a, the 100/0 PCBM/C_{60} devices show the best peak power conversion efficiency, 3.3%±0.3%, after 10 minutes of annealing. The 75/25 PCBM/C_{60} and 50/50 PCBM/C_{60} devices' peak efficiencies occurred after only 5 minutes of annealing and had values of 2.5%±0.4% and 2.2%±0.3% respectively. However, the performance achieved for the 50/50 PCBM/C_{60} devices after annealing for 120 minutes was still 91% of its original value whereas the performance of the 100/0 PCBM/C_{60} devices were already at 68% of their peak performance. We also performed an aging study where devices annealed for 5 minutes at 150 °C were subsequently placed at an elevated temperature (90 °C) for a longer time and tested periodically to evaluate performance. The results of this test are shown in Figure 7D. After 80 hours of aging, significant degradation of performance of all devices in the study was observed. The 100/0 PCBM/C_{60} devices' performance degraded 90% from 3.2%±0.2% to 0.3%±0.2%. Comparing these results to the devices incorporating C_{60}, the 72/25 PCBM/C_{60} devices degraded 78% from 2.4%±0.4% to 0.6%±0.2%, and the 50/50 PCBM/C_{60} devices degraded 71% from 2.2%±0.3% to 0.7%±0.2%. Therefore, under accelerated aging conditions, the 50/50 PCBM/C_{60} devices showed significant improvement over the 100/0 PCBM/C_{60} devices both in terms of relative performance to its peak efficiency and also in final efficiency.

4.4 GISAXS Characterization of P3HT/PCBM/C_{60} Composite Thin-Films

GISAXS measurements were acquired using Anton Paar SAXSess small angle X-ray scattering instrument. The sample to detector distance was calibrated (260.2 mm) and samples were run in point collimation. Figure 4.8 shows the GISAXS data collected from P3HT/fullerene films with 100/0 PCBM/C_{60} ratio. The samples were measured with an incident angle (α_i) of 0.2°. This is between the critical angles of the film ($\alpha_{c,film}$=0.16°-0.18°) and the underlying glass substrate ($\alpha_{c,glass}$=0.22°) and therefore is in the dynamic regime where DWBA is necessary for theoretical treatment of the data.[23] There are two main visible features in the 2D patterns that can be used to analyze the nanostructures within P3HT/fullerene blends: *1.)* the small angle scattering intensity in the off-specular plane, which can be characterized by a horizontal line cut along the Q_y direction at constant Q_z at the Yoneda peak, and *2.)* the (100) crystal plane of P3HT crystallites that can be analyzed using a radial average at a constant magnitude of the scattering vector Q = 0.38 $Å^{-1}$.[24]

The results of these averages are summarized in Figure 4.8b as a function of annealing time for all P3HT/fullerene blend compositions and annealing times. For cuts at constant Q_z = 0.016 $Å^{-1}$, we obtain primarily information about the lateral order of structures in the films. Figure 4.8d shows that, as annealing time increases, the scattering profiles systematically shift towards lower angles and the intensity at low Q increases. This is consistent with the increases in size of the fullerene domains, located within the bulk heterojunctions that are observed in SEM and optical microscopy (Figure 4.3). The averages in Figure 4.8b show that the overall P3HT crystal fraction increases with increasing annealing time and that the P3HT crystal fibers have strong preferential ordering parallel to the substrate surface.

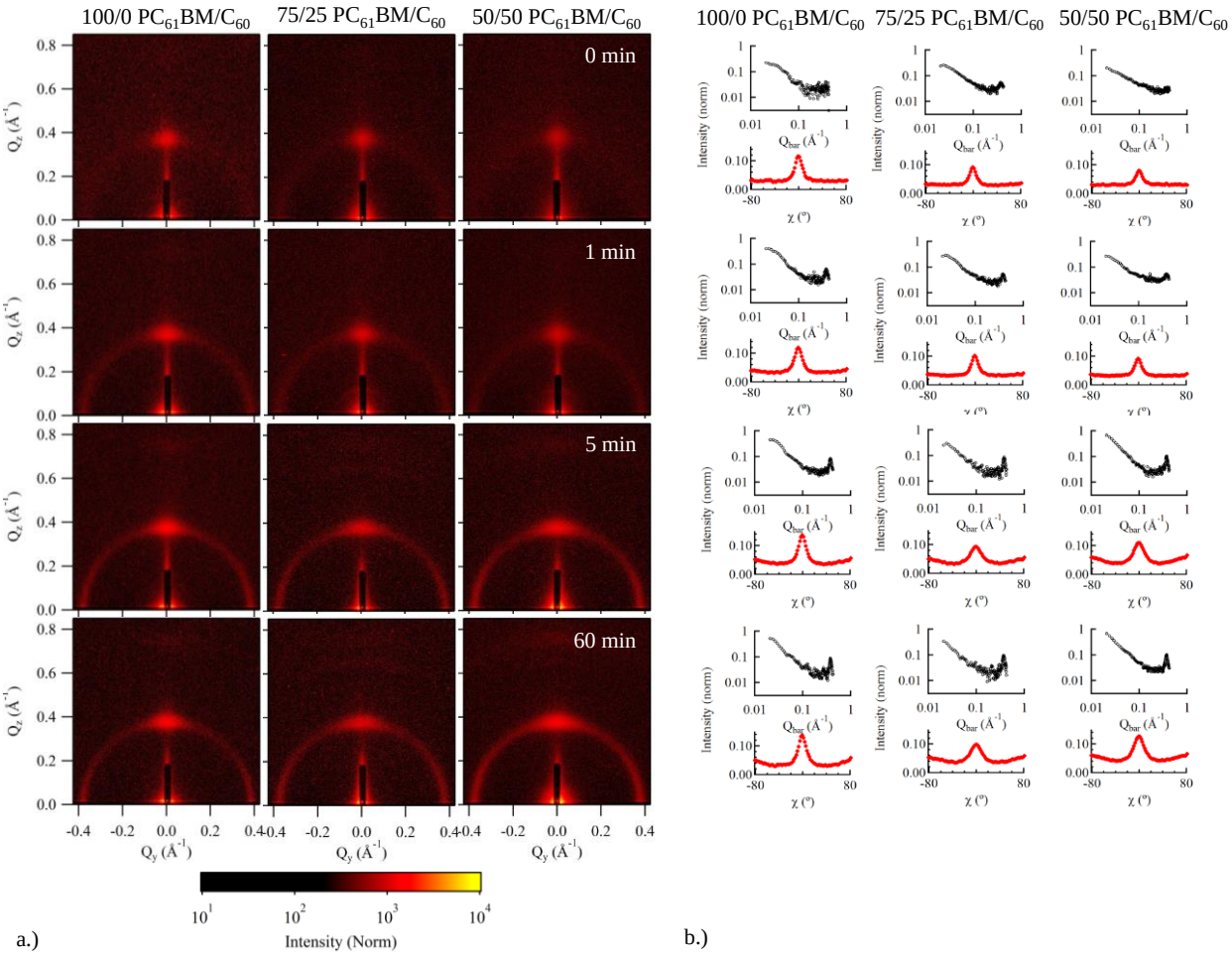

Figure 4.8 a.) GISAXS measurements on blended films (α_i=0.2°), b.) Top is Q_y line cut at Q_z=0.016 Å^{-1} and top is the azimuthal average.

GISAXS also provides a possible explanation for why the 50/50 PCBM/C_{60} blend outperforms a 100/0 PCBM/C_{60} blended film in terms of thermal stability at long times. Based on the horizontal line cuts shown in Figure 4.9b, it is clear that for long annealing times and extensive aging, the 50/50 blends still maintain smaller fullerene aggregates than that of the 100/0 blend. This suggests that more P3HT/fullerene interface is also maintained as a result of the formation of smaller fullerene crystallites that are induced from the presence of C_{60}. These observations are also consistent with the SEM and microscopy observations. From the 2D profiles it is also clear

that the off specular scattering intensity at small angles is larger for samples containing C_{60} impurities after annealing and aging. This implies that smaller aggregates are present in these films.[25] Unfortunately, the lowest Q values that can be accessed with our GISAXS are quite limited. Therefore, this technique is unable to characterize any aggregate growth once it exceeds more than ~45 nm.

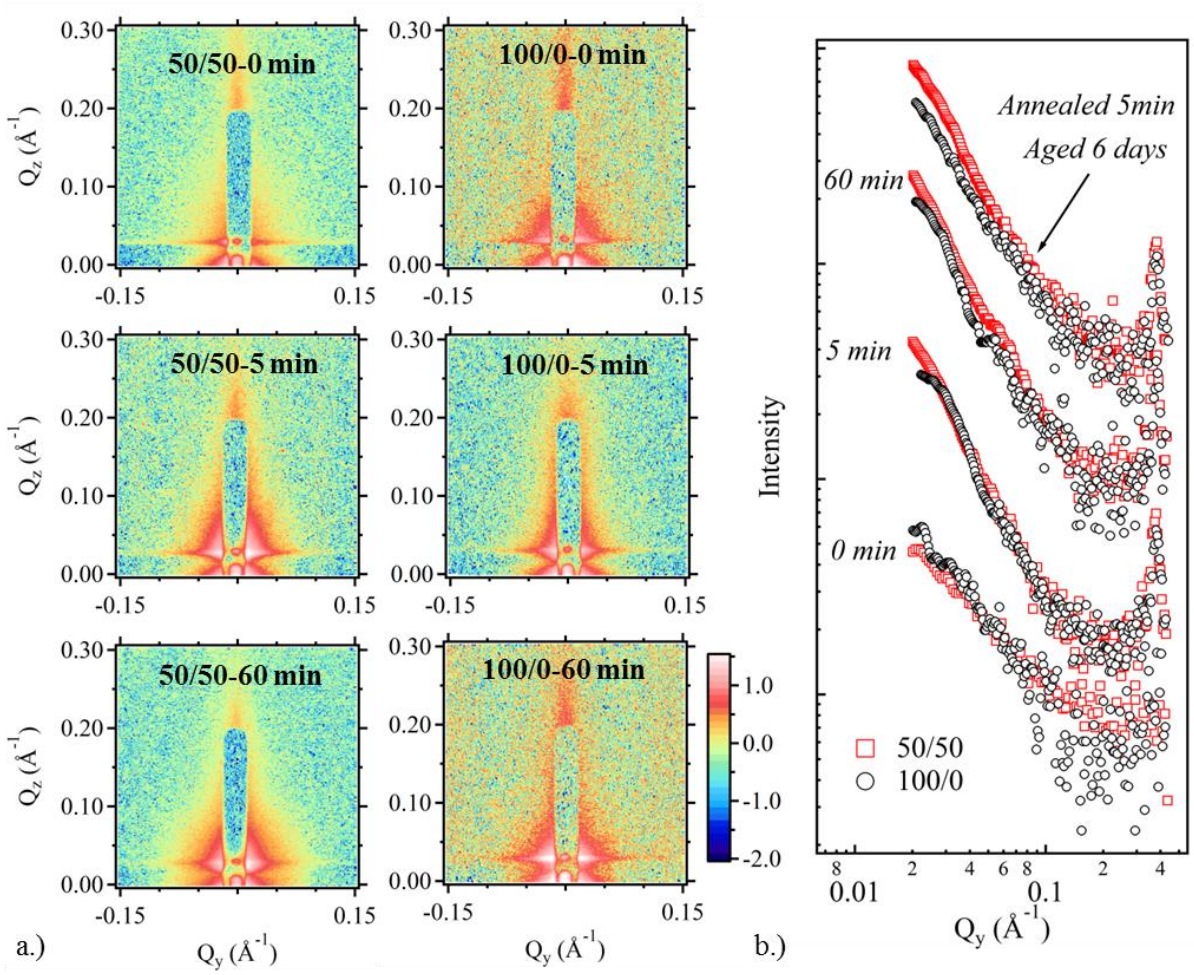

Figure 4.9: a.) 2D scattering patterns from P3HT/fullerene blends annealed at 150°C with 100/0 and 50/50 PCBM:C_{60} in the fullerene phase as a function of annealing time, b.) horizontal line cuts at Q_z = 0.026 $Å^{-1}$ obtained from the 2D profiles showing the development of aggregates in the polymer matrix for both annealed and aged films with 100/0 and 50/50 PCBM:C_{60} in the fullerene phase.

The performance data shown in Figure 4.7 show C_{60} incorporation into the fullerene phase of P3HT/PCBM solar cells can be used to improve the thermal stability of devices under accelerated aging conditions. The primary mechanism of this improvement is the formation of smaller overgrown domains in P3HT/PCBM that incorporate increasing amounts of C_{60}. The performance characteristics of P3HT/PCBM/C_{60} devices are consistent with the observations of films that were annealed and aged under similar thermal conditions. Particularly relevant is the absorbance of the PCBM peak at 336 nm. The 50/50 PCBM/C_{60} blend maintained a relatively constant absorbance that was greater than 100/0 PCBM/C_{60} films after extended periods of annealing and aging. In both cases, the maintenance of this peak is correlated to improved relative performance and in the case of aging, an overall better absolute efficiency. This suggests that the smaller crystal size formed in the 50/50 PCBM/C_{60} films observed with microscopy is also maintained in devices made with the same composition. The improvement relative to the 100/0 PCBM/C_{60} films therefore likely results from an increased interface between P3HT/PCBM and possible a prevention of mechanical damage to the devices as a result of very large aggregate growth. It is important to note that the devices fabricated here were prepared using the same optimized conditions for P3HT/PCBM solar cells without C_{60} incorporation. Therefore, the efficiency of devices incorporating PCBM/C_{60} devices could be optimized to further improve the peak efficiencies achieved in these studies. Furthermore, it may be possible to also utilize other fullerene mixtures (C_{60}, C_{70}, $PC_{61}BM$, $PC_{71}BM$ and others) to further reduce the driving force to form crystals without affecting the electron mobility of the fullerene phase. This is the subject of ongoing research. In this work we highlight the modification of the P3HT/PCBM active layer by addition of C_{60} using the processing conditions that have been optimized for traditional devices.

4.5 Methods and Materials

Poly(3-hexylthiophene) (Sepiloid P100) used in this study was purchased from Rieke Metals (Lincoln, NE). [6,6]-Phenyl C_{61} butyric acid methyl ester was purchased from SES Research (Houston, TX) for the open films studies and American Dye Source for OSCs (Quebec, Canada). PEDOT:PSS (PVP AL 4083) was supplied by Clevios (Germany). The ITO used for solar cells was supplied by Colorado Concept Coatings ($15\Omega/m^2$) and was cut into 1.5 × 1.5 cm squares. Chlorobenzene, anhydrous, 99.8% was supplied by Sigma Aldrich (St. Louis, MO).

Two active layer solutions were prepared in chlorobenzene with identical P3HT:fullerene weight ratios. The first consisted of 18 mg/mL P3HT and 12 mg/mL PCBM. The second consisted of 18 mg/mL P3HT, 6 mg/mL PCBM, 6 mg/mL C_{60}. Intermediate compositions were prepared by mixing different ratios of these two stock solutions. Therefore all films possess the same P3HT content, but varying PCBM/C_{60} content. These differences are reflected by labeling the relative weight fraction of the fullerene phase comprised of PCBM (e.g. 75/25 PCBM/C_{60} refers to 75 wt% PCBM and 25 wt% C_{60} in the fullerene phase). Films were spun-cast onto clean and dried glass slides at 1100 rpm for 60 seconds. Thermal treatments were applied *in vacuo* (< 1 torr). Absorption spectroscopy measurements were made over a wavelength range of 300 nm to 1000 nm using a Thermo Scientific Evolution 300 UV-Vis spectrophotometer. Scanning Electron Microscopy (SEM) was performed using an FEI Sirion SEM. Optical Micrographs were obtained with using a Zeiss Axiovert 40 CFL Inverted Microscope.

Coating solutions were prepared with a concentration of 10 mg/mL in chlorobenzene except for a 0/100 C_{60} solution which has a concentration of 5 mg/mL. Heavily n-doped silicon wafer was used as a substrate as well as a gate electrode. Thermally grown SiO_2 (200 nm) on the wafer acted as a gate dielectric layer. Surface of the oxide was cleaned by plasma for 4 min, coated with dilute benzocyclobutene (BCB; 1:20 vol/vol in mesitylene) by spin-coating (3 krpm for 60

sec) in air, and thermally cured at 250 °C on a hotplate for 2 h under argon environment. PCBM/C_{60} solution was then spun onto the substrate (2 krpm for 60 sec). OFETs were finished by depositing 35 nm thick gold electrodes through a shadow mask defining a transistor channel with a width of 1000 μm and a length of 100 μm. Electrical characteristics of OFETs were measured by using an HP4145B semiconductor parameter analyzer under nitrogen conditions.

ITO coated glass substrates were cleaned via a series of ultrasonic baths in a mild detergent, deionized water, acetone, and isopropyl alcohol. The substrates were removed from the last bath and dried using N_2. They were then treated with air plasma for 10 min under vacuum (200 mTorr). Once clean, substrates were coated with filtered PEDOT:PSS. The PEDOT:PSS was spin-coated, in air, on top of the ITO surface from solution to obtain a layer roughly 40 nm thick. All solar cells maintained the same P3HT:fullerene weight ratio, with 18 mg of P3HT and 12 mg per mL of solvent (chlorobenzene). C_{60} content was varied on a wt% basis and the ratios refer to the PCBM/C_{60} ratio in the fullerene phase. Active layer solutions were stirred at 60 °C overnight in an inert atmosphere and filtered before use through a 250 nm PTFE syringe filter. These solutions were spin-coated at 1000 rpm for 60 sec onto the PEDOT:PSS layer. 100 nm of aluminum was deposited via thermal evaporation under high vacuum (~2×10^{-6} torr). The devices were then annealed at 150 °C for varying times under nitrogen. Aging at 90 °C was also carried out under nitrogen. The completed devices were immediately tested in air upon their completion using 100 W/m^2 calibrated AM 1.5 light source.

References:

1. Vandewal, K.; Himmelberger, S.; Salleo, A. Structural Factors That Affect the Performance of Organic Bulk Heterojunction Solar Cells. *Macrom* **2013**, *46*, 6379–6387.

2. Bull, T. a; Pingree, L. S. C.; Jenekhe, S. a; Ginger, D. S.; Luscombe, C. K. The Role of Mesoscopic PCBM Crystallites in Solvent Vapor Annealed Copolymer Solar Cells. *ACS Nano* **2009**, *3*, 627–36.

3. Dang, M. T.; Hirsch, L.; Wantz, G. P3HT:PCBM, Best Seller in Polymer Photovoltaic Research. *Adv. Mater.* **2011**, *23*, 3597–3602.

4. Siegfried, M. J.; Choi, K.-S. Elucidating the Effect of Additives on the Growth and Stability of Cu2O Surfaces via Shape Transformation of Pre-Grown Crystals. *J. Am. Chem. Soc.* **2006**, *128*, 10356–7.

5. Voroshazi, E.; Verreet, B.; Aernouts, T.; Heremans, P. Long-Term Operational Lifetime and Degradation Analysis of P3HT:PCBM Photovoltaic Cells. *Sol. Energy Mater. Sol. Cells* **2011**, *95*, 1303–1307.

6. Jørgensen, M.; Norrman, K.; Krebs, F. C. Stability/degradation of Polymer Solar Cells. *Sol. Energy Mater. Sol. Cells* **2008**, *92*, 686–714.

7. Richards, J. J.; Rice, A. H.; Nelson, R. D.; Kim, F. S.; Jenekhe, S. a.; Luscombe, C. K.; Pozzo, D. C. Modification of PCBM Crystallization via Incorporation of C 60 in Polymer/Fullerene Solar Cells. *Adv. Funct. Mater.* **2013**, *23*, 514–522.

8. Noriega, R.; Rivnay, J.; Vandewal, K.; Koch, F. P. V; Stingelin, N.; Smith, P.; Toney, M. F.; Salleo, A. A General Relationship Between Disorder, Aggregation and Charge Transport in Conjugated Polymers. *Nat. Mater.* **2013**, *12*, 1038–44.

9. Müller, C.; Ferenczi, T. a. M.; Campoy-Quiles, M.; Frost, J. M.; Bradley, D. D. C.; Smith, P.; Stingelin-Stutzmann, N.; Nelson, J. Binary Organic Photovoltaic Blends: A Simple Rationale for Optimum Compositions. *Adv. Mater.* **2008**, *20*, 3510–3515.

10. Zhao, J.; Swinnen, A.; Assche, G. Van; Manca, J.; Vanderzande, D.; Mele, B. Van Phase Diagram of P3HT/PCBM Blends and Its Implication for the Stability of Morphology. *J. Phys. Chem. B* **2009**, *113*, 1587–91.

11. Chen, D.; Liu, F.; Wang, C.; Nakahara, A.; Russell, T. P. Bulk Heterojunction Photovoltaic Active Layers via Bilayer. *Nano Lett.* **2011**, *11*, 2071–2078.

12. Treat, N. D.; Brady, M. a.; Smith, G.; Toney, M. F.; Kramer, E. J.; Hawker, C. J.; Chabinyc, M. L. Interdiffusion of PCBM and P3HT Reveals Miscibility in a Photovoltaically Active Blend. *Adv. Energy Mater.* **2011**, *1*, 82–89.

13. Bertho, S.; Oosterbaan, W. D.; Vrindts, V.; D'Haen, J.; Cleij, T. J.; Lutsen, L.; Manca, J.; Vanderzande, D. Controlling the Morphology of Nanofiber-P3HT:PCBM Blends for Organic Bulk Heterojunction Solar Cells. *Org. Electron.* **2009**, *10*, 1248–1251.

14. Sivula, K.; Ball, Z. T.; Watanabe, N.; Fréchet, J. M. J. Amphiphilic Diblock Copolymer Compatibilizers and Their Effect on the Morphology and Performance of Polythiophene:Fullerene Solar Cells. *Adv. Mater.* **2006**, *18*, 206–210.

15. Yang, J.; Zhu, R.; Hong, Z.; He, Y.; Kumar, A.; Li, Y.; Yang, Y. A Robust Inter-Connecting Layer for Achieving High Performance Tandem Polymer Solar Cells. *Adv. Mater.* **2011**, *23*, 3465–70.

16. Tsai, J.-H.; Lai, Y.-C.; Higashihara, T.; Lin, C.-J.; Ueda, M.; Chen, W.-C. Enhancement of P3HT/PCBM Photovoltaic Efficiency Using the Surfactant of Triblock Copolymer Containing Poly(3-Hexylthiophene) and Poly(4-Vinyltriphenylamine) Segments. *Macromolecules* **2010**, *43*, 6085–6091.

17. Li, C.-Z.; Chien, S.-C.; Yip, H.-L.; Chueh, C.-C.; Chen, F.-C.; Matsuo, Y.; Nakamura, E.; Jen, A. K.-Y. Facile Synthesis of a 56π-Electron 1,2-Dihydromethano-[60]PCBM and Its Application for Thermally Stable Polymer Solar Cells. *Chem. Commun. (Camb).* **2011**, *47*, 10082–4.

18. Zhang, Q.; Wang, M.; Wooley, K. Nanoscopic Confinement of Semi-Crystalline Polymers. *Curr. Org. Chem.* **2005**, *9*, 1053–1066.

19. Jamieson, F. C.; Domingo, E. B.; McCarthy-Ward, T.; Heeney, M.; Stingelin, N.; Durrant, J. R. Fullerene Crystallisation as a Key Driver of Charge Separation in Polymer/fullerene Bulk Heterojunction Solar Cells. *Chem. Sci.* **2012**, *3*, 485.

20. Li, L.; Tang, H.; Wu, H.; Lu, G.; Yang, X. Effects of Fullerene Solubility on the Crystallization of Poly(3-Hexylthiophene) and Performance of Photovoltaic Devices. *Org. Electron.* **2009**, *10*, 1334–1344.

21. Clark, J.; Chang, J.-F.; Spano, F. C.; Friend, R. H.; Silva, C. Determining Exciton Bandwidth and Film Microstructure in Polythiophene Films Using Linear Absorption Spectroscopy. *Appl. Phys. Lett.* **2009**, *94*, 163306.

22. Wu, W.-R.; Jeng, U.-S.; Su, C.-J.; Wei, K.-H.; Su, M.-S.; Chiu, M.-Y.; Chen, C.-Y.; Su, W.-B.; Su, C.-H.; Su, A.-C. Competition Between Fullerene Crystallization Upon Annealing of Bulk. *ACS Nano* **2011**, *5*, 6233–6243.

23. Müller-Buschbaum, P. Grazing Incidence Small-Angle X-Ray Scattering: An Advanced Scattering Technique for the Investigation of Nanostructured Polymer Films. *Anal. Bioanal. Chem.* **2003**, *376*, 3–10.

24. Rauscher, M.; Salditt, T.; Spohn, H. Small-Angle X-Ray Scattering Under Grazing Incidence: The Cross Section in the Distorted-Wave Born Approximation. *Phys. Rev. B* **1995**, *52*, 1–11.

25. Salleo, A.; Kline, R. J.; DeLongchamp, D. M.; Chabinyc, M. L. Microstructural Characterization and Charge Transport in Thin Films of Conjugated Polymers. *Adv. Mater.* **2010**, *22*, 3812–38.

Chapter 5. Conjugated Polymer Organogel Emulsions

As has been identified in Chapter 4, the optimization of the intrinsic charge transport properties of polymer/fullerene composite thin-film starts with the morphological characteristics of the polymer phase. Conjugated polymer films typically are comprised of two distinct archetypical structures, a disordered polymer region and an ordered one. In the disordered regions, charge transport is dominated by intra-chain charge migration. Therefore, efficient charge transport over long distances (length scale of several polymer chains), requires efficient hopping between isolated chains. In the ordered polymer regions, however, charge migration has more flexibility. Due to π-π bonds that extend out from the backbone, favorable inter-chain interactions can occur that permit efficient charge transfer from chain to chain. This is depicted in Figure 5.1. Favorable π-π interactions, in some cases, also result in increased chain stiffness within the polymer aggregate leading to enhanced intra-chain charge transport as well.

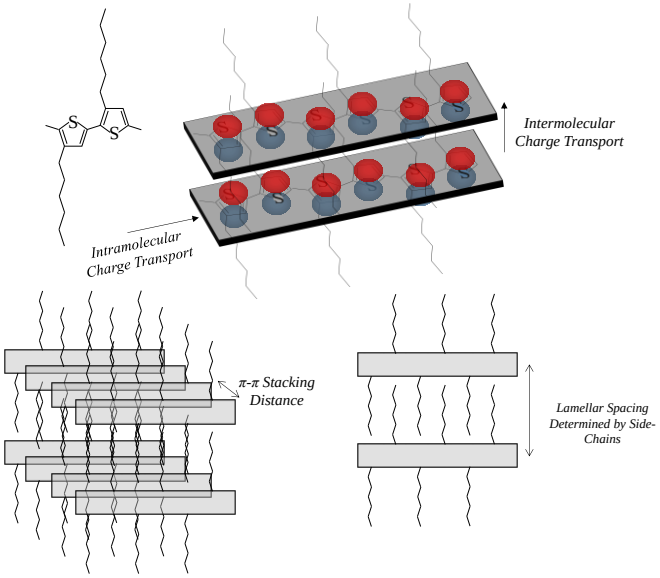

Figure 5.1. Schematic diagram of charge transport pathways for conjugated polymers (intra-chain and inter-chain) and of lamellar stacking of conjugated polymers due to their side chains.

Due to the steric interactions of side chains, conjugated polymers often aggregate to form crystalline lamellae, where the side chains act as an insulating spacer between backbone segments as shown in Figure 5.1. The formation of polymer aggregates typically occurs in the late stages of drying, where inter-chain interactions are facilitated across the solvent. Upon solidification, these states become kinetically trapped and are distributed through the disordered regions of the polymer. Due to the shear intrinsic to most thin-film coating techniques, these lamellae align parallel to the substrate's surface. Therefore, anisotropic hole-transport is a common feature of "as-cast" conjugated polymer thin-films, and for these films charge transport will be strongly preferences along the plane of the substrate. From the concept of the ordered heterojunction, optimized thin-films should possess prefer charge transport perpendicular to the substrate surface. This chapter outlines a formulation strategy that can circumvent the preferential alignment of conjugated polymer crystallites parallel to the substrate surface and instead produce a random orientation.

5.1 Conjugated Polymer Organogels: Isotropic Transport over Large Distance

A general property of many conjugated polymers is their tendency to form thermoreversible organogels provided the appropriate solvent conditions.[1,2] The organogel phase forms often as a result of supersaturation of the polymer in solution, which leads to self-assembly of polymer chains into ordered aggregates. Provided a sufficiently high polymer concentration, mechanical percolation of these aggregates can occur. This results in the formation of an organogel. The term gel refers viscoelastic fluid that crosses over to possess a high storage modulus than loss modulus in rheology. The gelation of poly(3-alkylthiophenes) has been extensively studied and it has been found that the degree of super-saturation dictates the kinetics of self-assembly, which has a significant influence over the network morphology and intrinsic interconnectivity of the

gel.[3] Regio-regular P3HT is known to form such organogels where the fibrillar aggregated phase has very high hole-mobility as compared the disordered phase. A TEM image of a 3 wt% P3HT organogel is shown in Figure 5.2a. The TEM micrograph demonstrates that these fibrillar organogels have a highly interconnected morphology.

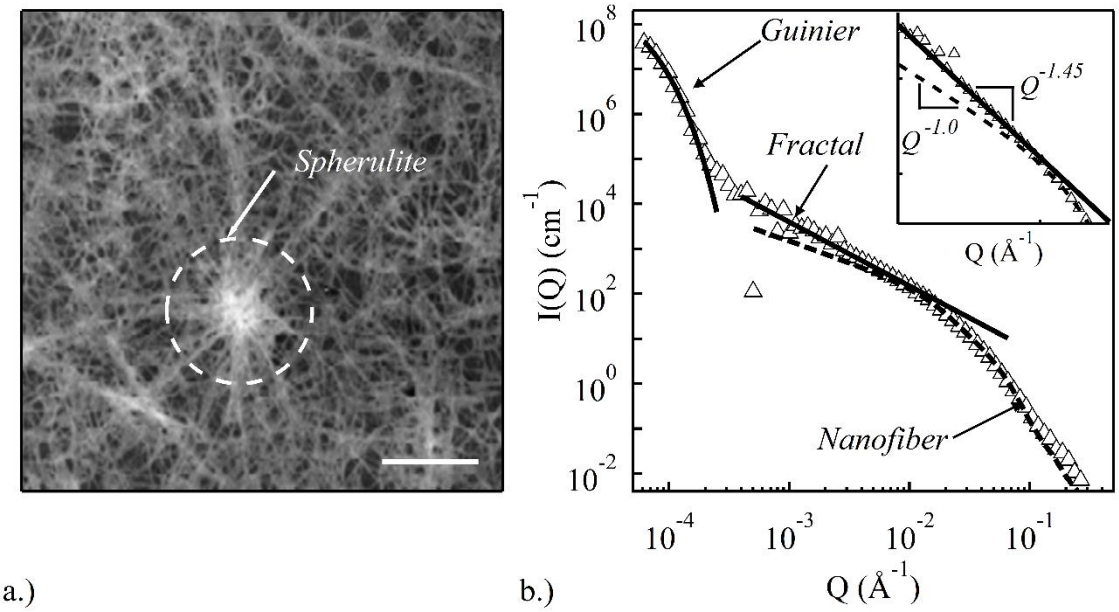

Figure 5.2. a.) STEM images of a dried 3 wt% organogel. (scale bar is 1 μm) b.) Combined USANS/SANS profile of a 3 wt% organogel. The solid lines are Guinier and Power-Law fits to the scattering curve and the dotted line is the parallelepiped fit. The inset shows the deviation of the scattering from the gel from the nanofiber model at $Q \sim 9\times10^{-3}$ Å^{-1}.

SANS measurements were also performed on a 3 wt% P3HT organogel formed in p-xylene to characterize its morphology over a wide range of length scales. Figure 5.2b shows the combined USANS/SANS profile of a 3 wt% organogel in (d10) p-xylene. The power-law behavior of the scattering profile between 9×10^{-3} Å^{-1} < Q < 2.5×10^{-4} Å^{-1} is characteristic of a fractal network structure and is also consistent with the TEM images (Figure 5.1a).[4] Fractal structures are observed in many natural and synthetic networked systems.[5] These structures are defined by self-

similarity that extends over several size scales.[6] The fractal dimension (D_f) quantifies the dependence between mass and volume for a fractal object ($M \sim r^{D_f}$). In the case of P3HT organogels, this is proportional to the density of the fiber network. The fractal dimension of the 3 wt% organogel is $D_f = 1.45 \pm 0.1$ and the range of self-similarity spans between ~70 nm and 2.5 μm. The scattering signal at larger angles, $Q > 1\times10^{-2}$ Å^{-1}, is dominated by the form factor of the individual fibers and for P3HT this can be approximated as a parallelepiped (Equation 5.1), where a, b, and c are the height, width and length of the parallelepiped.[7]

$$5.1 \quad P(Q) = \frac{2}{\pi}\int_0^{\pi/2}\int_0^{\pi/2}\left[\frac{\sin(Qa\sin\alpha\cos\beta)}{Qa\sin\alpha\cos\beta}\frac{\sin(Qb\sin\alpha\sin\beta)}{Qb\sin\alpha\sin\beta}\frac{\sin(Qc\cos\alpha)}{Qc\cos\alpha}\right]^2 \sin\alpha d\alpha d\beta$$

The form factor shown in Equation 5.1 is fit to the high-Q region of the 3 wt% organogel in Figure 5.2b yielding cross-sectional dimensions $a = 46 \pm 18$ Å and $b = 208 \pm 28$ Å for the height and width respectively. For this fit, the parameter c was set to be much greater than $2\pi/Q^*$ of the lower bound of the fitting range to ensure it had no influence over the cross-section shape of the fiber. The agreement between the model and data in Figure 5.2b demonstrates that this model is a good approximation for the cross-sectional shape of the individual nanofibers. The rectangular shape and dimensions also agree well with previous observations based on AFM, electron microscopy experiments and known crystal structures. In the opposite extreme, at very low angles ($Q < 2.5\times10^{-4}$ Å^{-1}), the scattering is mostly dominated by the spherulitic centers that are visible in Figure 5.2a. The onset of the upturn, occurring at Q^*, is related to the upper size limit of the fractal region. A characteristic dimension for this can be estimated by evaluating $2\pi/Q^* \approx$ 2.5 μm.

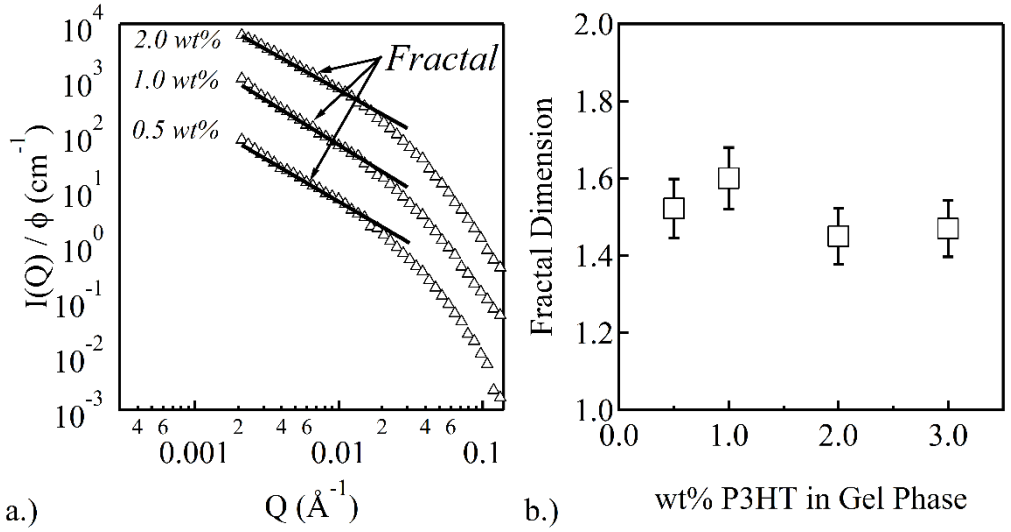

Figure 5.3. a.) SANS data for 2.0 wt%, 1.0 wt%, and 0.5 wt% organogels. Data fits are overlaid corresponding to power-law dependence for a fractal. Data is normalized by concentration and shifted by a factor of ten vertically with respect to the 2.0 wt% data set for clarity. b.) Fractal dimension as a function of wt% P3HT in the gel phase of the 'parent' organogels.

SANS data from a concentration series of P3HT organogels are shown in Figure 5.3a with overlaid power-law fits in the fractal region. The bulk organogels show a relatively constant fractal dimension, $D_f \sim 1.45$, across all gel concentrations as shown in Figure 5.3b. This suggests that, within this concentration range, the network structure is similar for all of the organogels even though the total fiber content is changing. The 0.5 wt% P3HT organogel is a weak gel and cannot support its own weight upon inversion of the container. However, with increasing concentration of P3HT, the gel strengthens and becomes highly elastic. The increase in elasticity comes from an increase in the interconnectivity of the network and in the nanofiber concentration as a greater amount of P3HT crystallizes. Dielectric spectroscopy measurements have shown that P3HT organogels can transport charge efficiently over large distances owing to their intrinsic interconnectivity.[3] P3HT organogels form over the course of several hours into three-dimensional fibrillar networks when gelled in moderate organic solvents like p-xylene,

toluene or benzene. The fibrillar aggregates in the organogels possess a high degree of crystallinity and represent a thermodynamically stable state. Therefore, if it were possible to produce a thin-film P3HT organogel, it would be an excellent candidate for improving hole transport in conjugated polymer/fullerene solar cells.

Unfortunately, long gelation times, network heterogeneity, and elasticity make organogels difficult to process into thin-films without destruction of the intrinsic isotropic charge transport properties.[8] To overcome the challenges associated with deposition of P3HT organogels, we chose to emulsify preformed poly(3-hexylthiophene) organogels in water. In this way, dispersions of P3HT micro-organogels can be produced. These micro-organogels were shown to maintain the intrinsic connectivity of their parent organogels in the dispersion phase using contrast matching in Small Angle Neutron Scattering (SANS). The random, three dimensional structure of these organogels is also maintained upon deposition in the solid-state as demonstrated using Grazing Incidence Wide Angle X-ray Scattering (GIWAXS), a result that has not been shown with any other approach.[9]

5.2 Organogel Emulsion Generation and Characterization

The formation of stable nano-porous gel particles is achieved by emulsifying P3HT organogels in water. P3HT/p-xylene (or (d10) p-xylene for SANS) organogels are made using the procedure outlined by Malik.[78] First, a known amount of P3HT is fully dissolved into p-xylene at a temperature above 80˚C (Figure 5.4a). This sample is cooled to 20˚C and allowed to gel for 24 hours in a tightly closed container (Figure 5.4b). An aqueous solution containing 5 mM SDS (or (d25) SDS for SANS) is then added to the organogel yielding 2 mL of 10 vol% organogel in water (Figure 5.3c). This two-phase mixture is sonicated with a Branson Sonifier (model S-450-D) using a total of ten 1 s pulses and a power of 120 W. This protocol is sufficient to produce a

visibly homogenous dispersion and to maintain identical processing conditions for sample comparison (Figure 5.4d). After emulsification, the gel particles are allowed to sit overnight, and after one day of rest, a cream layer that is rich in p-xylene, forms for all samples. This fraction is separated from the rest of the sample and discarded. The remaining dispersion does not cream or aggregate with time showing that long-term colloidal stability is achieved. Zeta-potential measurements of the stable P3HT dispersions show values of -70 mV ± 5 mV. This indicates that SDS is present at the oil/water interface and is responsible for the long term stability of the dispersion. Subsequent dialysis of the emulsions shows that stability is retained even when the SDS concentration is decreased to levels below 40 nm. The value of zeta-potential remains relatively unchanged over several orders of magnitude of SDS concentration. Interestingly however, stable dispersions cannot be produced using such low surfactant concentrations before sonication. In fact, SDS concentration exceeding 500 μM is necessary to stabilize sub-micron gel particles during the sonication process.

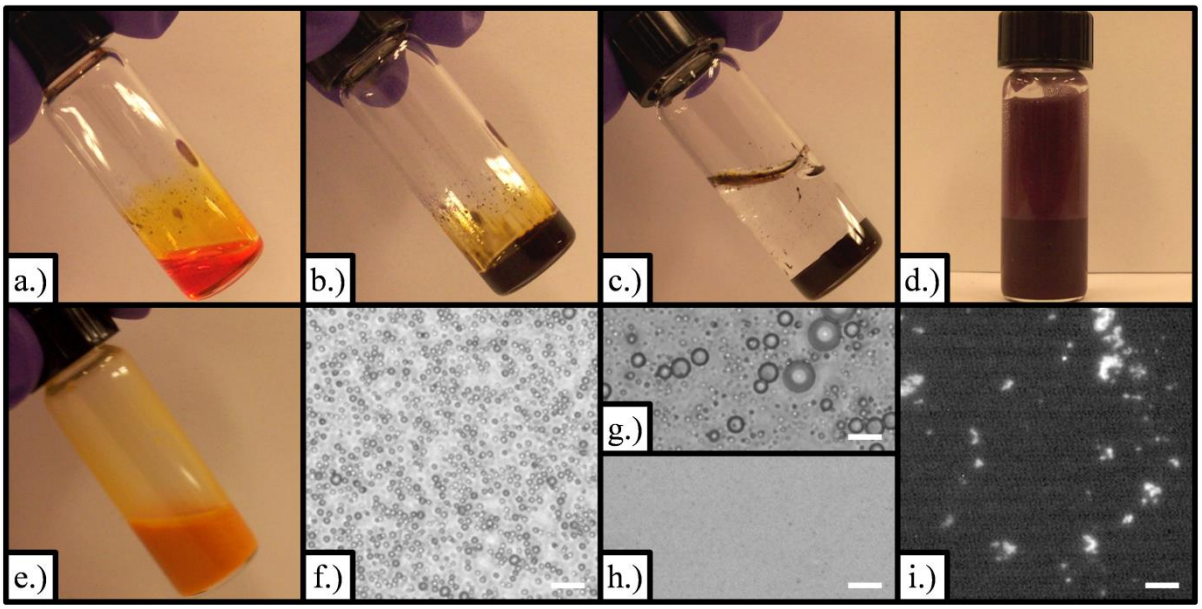

Figure 5.4. Emulsification process of P3HT organogels to generate the gel particles - a.) 3 wt% P3HT/p-xylene solution at 80˚C. b.) 3 wt% P3HT/p-xylene at 20˚C, c.) 5 mM SDS solution on top of gel before sonication. d.) Dispersion immediately after sonication. e.) Dispersion heated to

80˚C after sonication. f.) Bright field micrograph of dispersion immediately after sonication, g.) Bright field micrograph of creamed layer. h.) Bright field micrograph of the dispersion after the creamed layer is discarded. Gel particles are small and not observable with regular light microscopy. i.) Fluorescence micrograph of aggregated gel particles excited by λ = 450 nm. *(Scale bars are 10 μm)*

Subsequent heating of the dispersion after sonication causes the P3HT in the gel particles to melt, and like its 'parent' organogel it recovers its characteristic orange color (Figure 5.4e). Pure P3HT is insoluble in water and does not melt until ~170˚C, so there must be sufficient solvent remaining within the gel particles to dissolve the polymer. Figure 1f shows an optical micrograph of the dispersion immediately after sonication. A large number of small p-xylene droplets (~2-5 μm) are clearly visible. Over time these droplets coalesce and form a cream layer at the top of the container (Figures 5.5g). When this layer is removed, the product is a stable and homogeneous purple dispersion without any visible aggregates or solvent droplets (Figure 5.4h). This stable dispersion contains crystalline P3HT particles that can be observed after coating using fluorescence microscopy (Figure 5.4i).

The viscosity of cooled P3HT solutions in p-xylene increases steadily with increasing polymer concentration until, at concentrations above ~1 wt%, the samples gel and no longer flow upon jar inversion (Figure 5.4b). To better understand the rheological behavior of the gel particle dispersions over a wide range of concentrations, a 40 vol% dispersion was prepared from a 3 wt% organogel and the viscosity was measured at various dilutions as a function of shear rate (Figure 5.5).

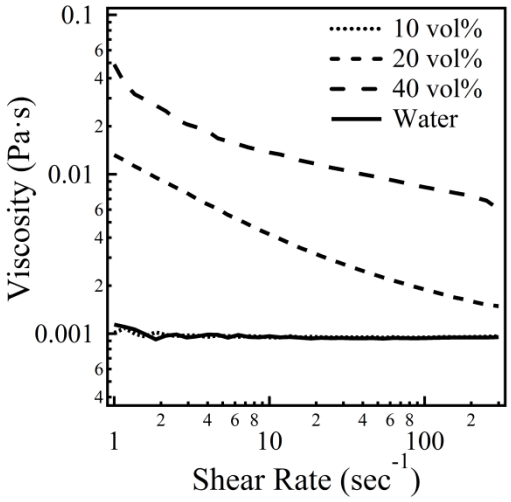

Figure 5.5. Viscosity (Pa·s) for a 40 vol%, 20 vol%, and 10 vol% of a 3 wt% organogel dispersed in water.

The concentrated dispersion was diluted to 20 vol% and 10 vol% to quantify the effect of gel particle loading on the viscosity. Both the 40 vol% and 20 vol% samples show non-Newtonian shear-thinning behavior that is identified by a decrease in the viscosity as a function of increasing shear rate. This behavior is characteristic of interparticle interactions that develop in concentrated colloidal dispersions.[10] When diluted to 10 vol%, the interparticle interactions become negligible and the solution shows a constant viscosity as a function of shear rate that is effectively equal to that of water. Figure 5.5 shows that the rheology is strongly dependent on the vol% of the dispersion with larger loadings possessing a higher zero-shear viscosity. These rheological measurements are consistent with the observed fluid properties of the dispersions and verify that the organogels are effectively fractured and fully dispersed in the bulk water phase.

The likelihood of electronic doping could be enhanced by the choice of water as the continuous phase or by the use of a surfactant for stabilization against particle aggregation. In order to monitor for these possible affects, the optical properties of P3HT within the dispersed gel particles were characterized using UV-Visible absorption and with fluorescence spectroscopy.

The absorption spectra from gel particle samples made from 3 wt%, 2 wt%, 1 wt%, and 0.5 wt% 'parent' organogels are shown in Figure 5.6a. The observed peaks are typical for crystalline P3HT and they are the result of interchain vibronic coupling. The lowest-energy absorption peak, $A_{0\text{-}0}$, occurs at ~2.05 eV and the second, $A_{0\text{-}1}$, at ~2.25 eV. Work by Spano et al. relates the ratio of the intensities of the $A_{0\text{-}0}/A_{0\text{-}1}$ peaks in the absorption spectra to the degree of intrachain order.[11] Interestingly, the $A_{0\text{-}0}/A_{0\text{-}1}$ peak ratio increases with increasing P3HT concentration as shown in Figure 5.6b, which according to Spano's theory should reflect an increase in intramolecular order. The increase in the $A_{0\text{-}0}/A_{0\text{-}1}$ peak ratio is accompanied also by a slight red-shift in the $A_{0\text{-}0}$ peak position from 2.05 eV to 2.00 eV. This increase is enough to notice a visible color change in the transmittance from purple to blue as shown in Figure 5.6c.

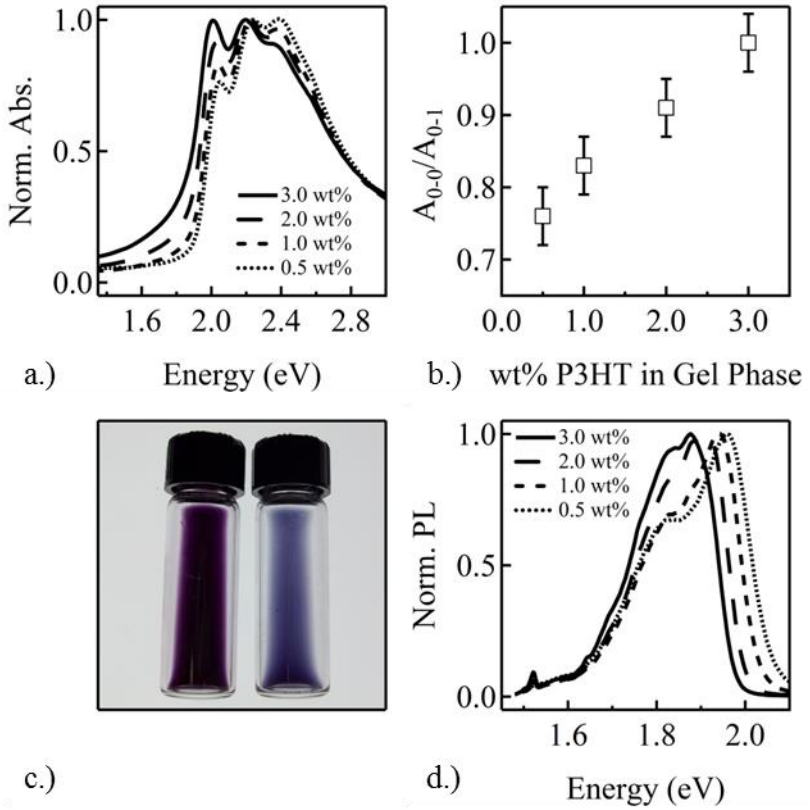

Figure 5.6. a.) UV-Visible absorption spectroscopy of P3HT organogel dispersions b.) $A_{0\text{-}0}/A_{0\text{-}1}$ peak ratio and c.) Images of dispersions made from 0.5 wt% (purple) and 3 wt% (blue) P3HT

organogels and d.) Photoluminescence measurements of the dispersions. Excitation was at 550 nm.

Photoluminescence (PL) spectra of the dispersions are shown in Figure 5.6d. The position of the maximum PL Peak shifts from 1.9 eV to 1.8 eV over the concentration series. There is also a lower energy feature that increases in relative intensity with increasing P3HT content. This increase is in accordance with the increasing relative absorption of the $A_{0\text{-}0}$ peak. The absorption spectra and presence of photoluminescence show that the polymer is not significantly doped by the presence of water or SDS in the dispersion. These observations are consistent the spectroscopy of freeze-dried gels measured at different aggregation times, which had $A_{0\text{-}0}/A_{0\text{-}1}$ ratios exceeding 1.00. This also suggests that it is possible to tailor the choice of surfactant in the continuous phase to suit a specific coating process without necessarily influencing the optical or electronic properties of the polymer. Indeed, we have also prepared stable gel particle dispersions using the same protocol but replacing SDS with Brij 35, cetyl trimethylammonium bromide (CTAB), and Pluoronic 85. While these dispersions have not been fully characterized, they closely resemble those prepared with SDS in terms of stability, fluid behavior and optical absorbance.

The local fiber density in the P3HT organogels and the corresponding elasticity control the fracture process from sonication during gel particle formation. The protocol that is used for sonication supplies a uniform power throughout the sample. Gel particle formation is very sensitive to the sonication power and to the organogel strength. Therefore, the use of a standard protocol is critical to produce gel particles with reproducible structures. Under the external stress that is imposed by sonication, the organogel selectively fractures in regions of low fiber density because these will be the weaker parts of the networks. In the high-density, spherulitic regions, there are a larger numbers of nanofibers that more effectively distribute the stresses. These

stronger regions can retain the network integrity if the yield stress is greater than the local applied stress. Because fiber density and gel elasticity increase with increasing P3HT weight fraction, it is expected that the gel particles will be more structurally similar to the 'parent gels' in dispersions made from the higher concentration organogels as compared to lower concentration organogels. Correspondingly, it is anticipated that dispersions made from the lower concentration organogels will produce more particles with collapsed network structures.

Volume-weighted size distributions obtained from Dynamic Light Scattering (DLS) measurements are shown in Figure 5.7 for dispersions prepared from 3.0, 2.0, 1.0, and 0.5 wt% P3HT organogels. Two distinct particle populations are evident in each sample and the distributions can be modeled well by a sum of two log-normal functions. From these fits, the hydrodynamic radii of the two populations within the dispersions are obtained and shown in Figure 5.7b. This analysis was repeated for four separate dispersions prepared under identical conditions at each concentration. The results represent the average hydrodynamic radii for each population and the error bars represent one standard deviation. For larger P3HT concentrations, the larger particles make up the majority component (~75 vol%) of the total dispersion and it is expected that they will also retain most of the 'parent' organogel structure. In contrast, we expect that smaller particle populations will also include network fragments from the low-density regions of the 'parent' organogels. The increase in size for both the larger and smaller particle populations as a function of P3HT concentration verifies that this is an important variable in determining particle size distribution. This is also an important result because it shows that the particle sizes can be systematically modified. As shown in Figure 5.7c, the small and large fragments can also be fractionated using centrifugation. After centrifugation of a 2 wt% gel dispersion at 1000 rpm for 20 minutes, the supernatant contains the majority of the smaller

fragments. Larger particles are located at the bottom of the centrifuge tubes and can be easily re-dispersed after separation. This shows that while the initial distributions after emulsification are broad, the distribution can be refined further before coating if necessary. Scanning electron micrographs of the large fragments (Figure 5.7d) show that gel particles are not aggregated and have an average size consistent with that measured using DLS.

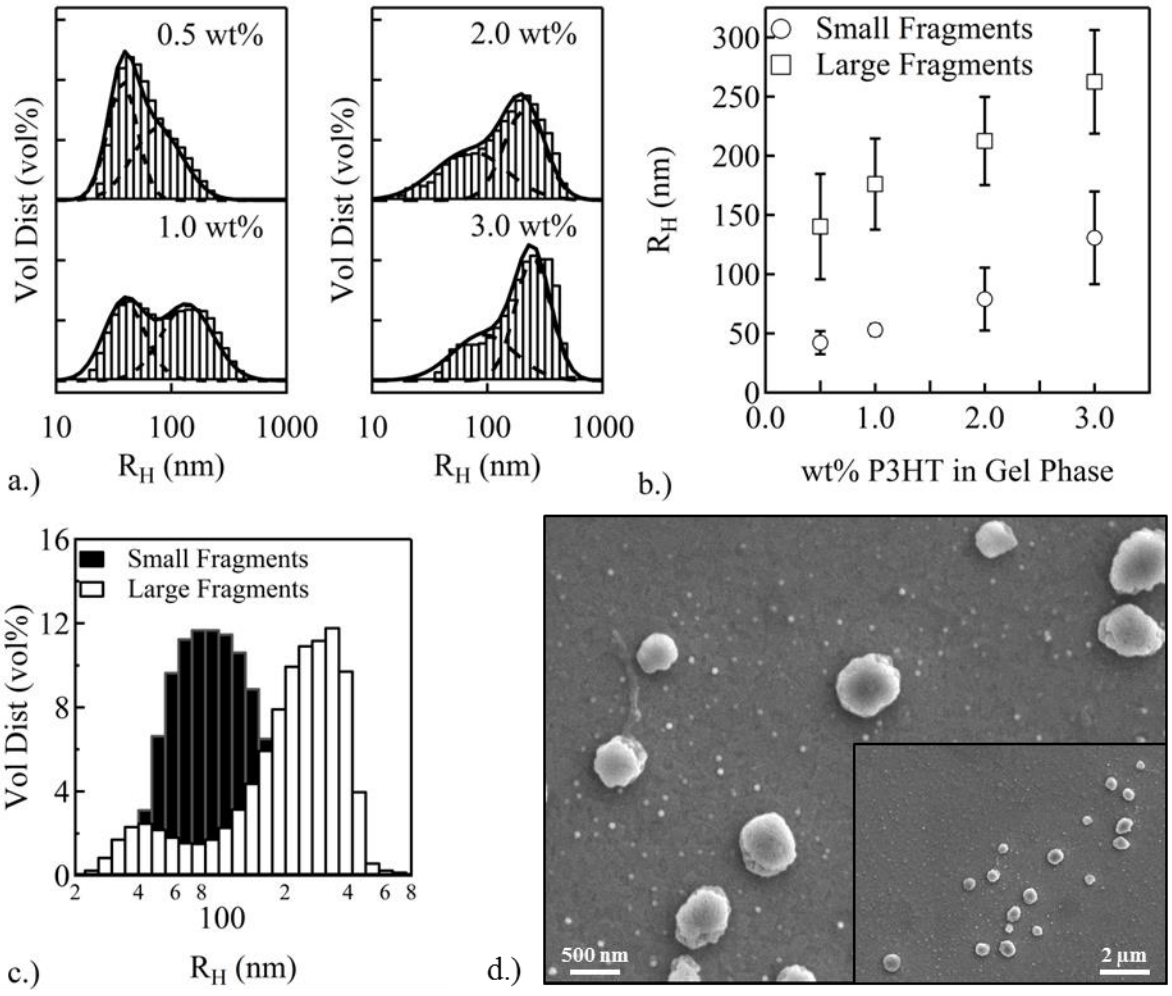

Figure 5.7. a.) DLS of dispersions with of 0.5 wt%, 1.0 wt%, 2.0 wt%, 3.0 wt% P3HT in the gel phase. The solid line is a linear sum of two log-normal distributions (dashed line) used to fit the raw DLS data. b.) Average hydrodynamic radius for the small and large fragments obtained from the log-normal fits. Error bars represent the standard deviation in size for four separate dispersions prepared independently at each concentration. c.) DLS data of separated small and large fragments obtained after a 2 wt% gel dispersion was centrifuged, d.) SEM images of diluted large fragments.

5.3 SAXS and Contrast Matching in SANS for the Structural Characterization of P3HT Organogel Emulsions

While the DLS data provides powerful insight into the size and concentration of gel particles within the dispersion, it does not reveal much about their internal structure. Therefore, it still remains to be proven that the particles retain the porosity and network structure of the original bulk organogels. To this end, SAXS and SANS experiments were performed on several gel particle dispersions as a function of P3HT content in the organogel phase. In order to characterize the nature of the P3HT fibers contained within these emulsion droplets, we first performed SAXS measurements on a 3wt% micro-organogel. The *I(Q)* vs *Q* data is shown in Figure 5.8.

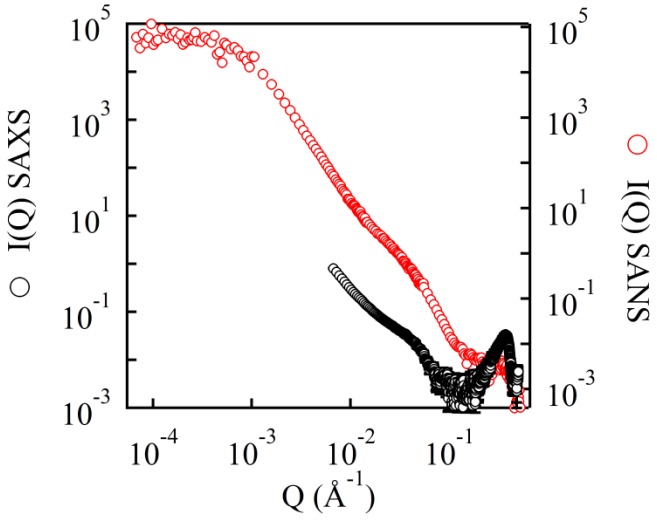

Figure 5.8. SAXS (black circles) and combined SANS/USANS (red circles) profiles from 10vol% of a 5 wt% organogel dispersed in 5 mM sodium dodecyl sulfate solution.

The average size of the emulsion droplets exceeds 500 nm in diameter, which is outside the resolution of the SAXSess instrument. Therefore, the characteristic Guinier region is absent in the SAXS data. We are interested in the internal structure of these micro-organogel particles, but

unfortunately the SAXS data is a complex convolution all of the many interfaces present within the sample. Based on the known composition and densities, the *SLD* of all the components of the micro-organogel can be calculated and their corresponding contrast terms with water for X-rays can be calculated for each component (Table 5.1).

Table 5.1. Contrast terms for both SAXS and SANS for four components in the organogel emulsions.

	X-Rays			**Neutrons**	
	$SLD \times 10^6$ [Å^{-2}]	$\Delta SLD^2 \times 10^{12}$ [Å^{-4}]		$SLD \times 10^6$ [Å^{-2}]	$\Delta SLD^2 \times 10^{12}$ [Å^{-4}]
p-xylene	8.00	2.25	*(D10)-p-xylene*	5.86	0.03
H_2O	9.50	0.00	*(D25)-SDS*	5.83	0.02
SDS	9.30	0.04	*P3HT*	0.69	24.88
P3HT	10.30	0.64	*90.5% (D2)-H_2O*	5.68	0.00

Based on this table, the greatest contribution to the SAXS intensity is coming from p-xylene/water interface, where the interface of interest is the P3HT/p-xylene interface. Therefore, we turned to SANS measurements. In neutron scattering, the *SLD* of a material is dependent on their isotopic content instead of their electron density.[12] Therefore by selective isotopic labeling, it is possible to highlight certain regions of the material of interest. For our samples, we exploit the fact deuterated water (*SLD* = 6.33×10^{-6}) and water (*SLD* = -0.56×10^{-7}) have very large *SLD* differences. Therefore, we can vary the contrast terms over a large range without effecting the stability or structural characteristics of the emulsion. In order to minimize the scattering from (d10) p-xylene/water interface and (d25) SDS within the sample, we performed a contrast matching experiment with the bulk aqueous phase by varying H_2O and D_2O content. *A priori*, the *SLD* of deuterated p-xylene is known. However, because the scattering contribution from the deuterated surfactant layer that decorates the outer edge of the oil droplet is not known, we employed contrast variation on a p-xylene emulsion in order to determine the contrast match point. The SANS scattering profiles taken at a single detector position of the emulsion are shown

in Figure 5.9a as a function of bulk phase D_2O content. To determine the match point, $I^{1/2}(Q \rightarrow 0)$ vs $\%D_2O$ is plotted in Figure 5.9b.[13] The linear trend shows that the majority of the scattering of the sample comes from an object with a fixed average *SLD* otherwise this dependency would be quadratic.

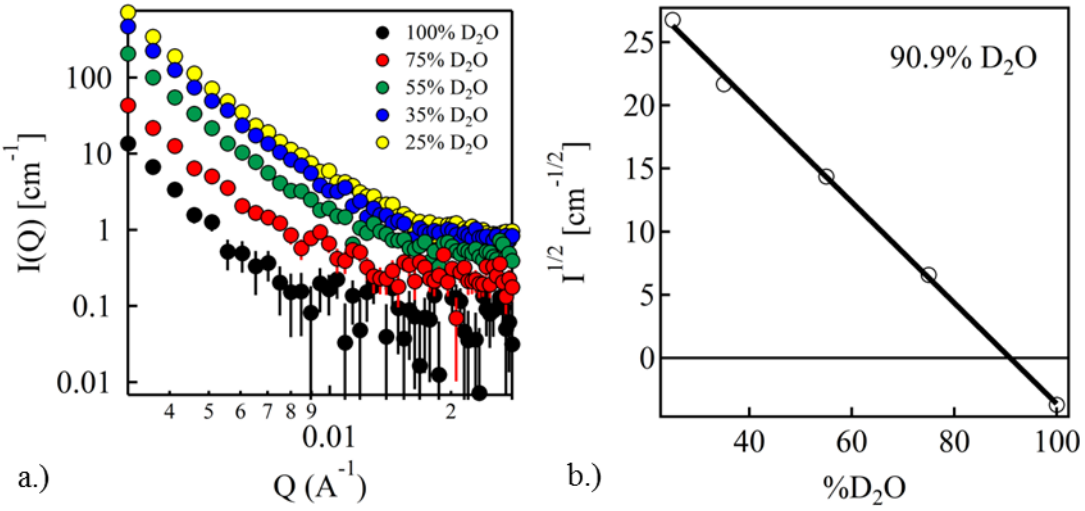

Figure 5.9 a.) SANS profiles for p-xylene emulsion in d-SDS solutions with varying D_2O/H_2O content, b.) Plot of $I^{1/2}(Q=0.003\ Å^{-1})$ vs $\%D_2O$ which defines the contrast match point a homogenous dispersion.

According to equation 5.2, at low-Q a plot of $I^{1/2}(Q=0.003\ Å^{-1})$ vs $\%D_2O$ in the aqueous phase should be linear. As shown in Figure 5.9b, this is the case, and the contrast match point can be determined as the x-intercept.

$$5.2 \quad \lim_{Q \rightarrow 0} \left(P(Q)S(Q) \right) = 1 \quad \therefore \quad I(0) = \phi V_{part} \Delta SLD^2$$

Using this approach, the contrast match point was determined to be 90.9 vol% D_2O in the aqueous phase. The SLD value is very close to the value for (d10) p-xylene verifying that the (d25)-SDS does not contribute significantly to the scattering intensity. As can be seen in Table 5.1, SANS measurements done at the contrast match point significantly enhance the sensitivity to

the P3HT/p-xylene interface while nearly eliminating the contrast term for the oil/water interface as compared to measurements made in SAXS. The same sample measured using the contrast matched aqueous phase is shown in Figure 5.9. Even with SANS, the micro-organogel particles are outside of the resolution limit of the instrument. Therefore, USANS was also performed on these samples and the desmeared USANS data is combined with the SANS data to capture the I(Q) vs Q behavior over the whole Q-range. From the SANS profile, it is clear that the samples have three characteristic regions:

1.) Low-*Q* scattering dominated by the p-xylene/water interface.
2.) Intermediate-*Q* scattering dominated by the P3HT fibers contained within the emulsion droplet.
3.) High-*Q* scattering dominated by the (100) Bragg peak from P3HT crystallites present within the emulsion droplet.

To compare the effect of changing the network properties of the parent organogel structure on the micro-organogel dispersions, we prepared four emulsions all with different wt% parent organogels. The SANS data for these micro-organogels is shown in Figure 5.10a along with a representation of the proposed structure for the gel particles. Figure 5.10a shows the scattering profiles for the dispersions at each concentration scaled by volume fraction and shifted by a factor of ten relative to the 3 wt% sample for clarity. Figure 5.10b shows the high-*Q* region of the gel particle data plotted together with the SANS data from the corresponding bulk organogels. At high concentrations, the high-*Q* regions of the gel particles and the corresponding organogels align very well after scaling by the difference in concentration. This suggests that, as expected, the nanofiber structure is maintained after the emulsification process that is used to form the gel particles. In contrast, the 0.5 wt% and 1.0 wt% gel particle dispersions show some significant deviation from the scattering of the ‘parent’ organogels. This observation could result from the lower signal to noise ratio of the scattering in these samples but it may also indicate a

modification of the structure due to the weaker nature of these networks. Figure 5.10.c shows the proposed structure for gel particle when the network structure is retained (i.e. at high P3HT concentrations).

The SAXS measurements shown in Figure 5.10.d also confirm that the crystalline structure of the P3HT is retained in the gel particles. Specifically, the presence of the (100) Bragg diffraction peak is evident for each sample. The other crystal peaks cannot be resolved because of the strong background scattering signal from water at larger angles. Nonetheless, the peak position at Q = 0.375 $Å^{-1}$ corresponds to a plane spacing of 16.5 Å that is consistent with the spacing between alkyl chains in crystalline P3HT. Using the Scherrer equation (Equation 5.3) an estimate for the average crystal domain size, τ, is possible, where λ = 1.54 Å and β is the FWHM obtained from the Gaussian fit.[14]

$$\tau = \frac{0.9\lambda}{\beta \cos\left(\theta/2\right)} \qquad 5.3$$

This size is estimated to be τ = 36 Å for each sample except when the dispersion is formed from the 0.5 wt% P3HT organogels. The low value for this micro-organogel particle is likely a result of the high solvent background with respect to the scattering signal and not necessarily an indicator of a significant change in the crystal size. The resulting values are consistent with the known height of P3HT nanofibers.[15]

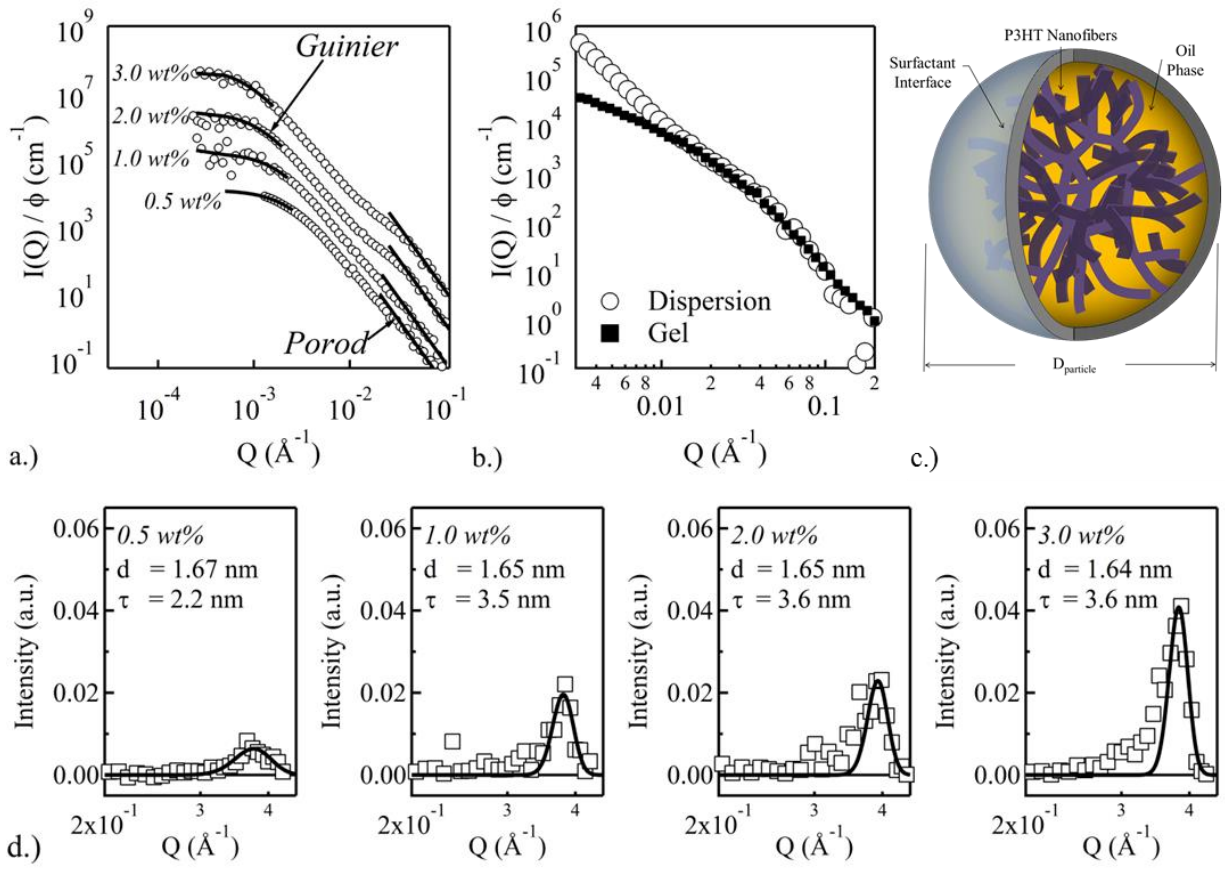

Figure 5.10. a.) SANS of gel particle dispersions prepared from bulk gels in 90.5 vol% D_2O/H_2O with 0.5 wt%, 1.0 wt%, 2.0 wt%, 3.0 wt% P3HT in the gel phase. Lines are power-law and Guinier fits to the high-Q Porod region (Q^{-4}) and the low-Q Guinier region respectively. b.) High-Q region of overlaid SANS data for 3 wt% gel particles (open circles) and a 3 wt% organogel (closed squares). Data are normalized by concentration. c.) Representation of hypothesized structures of a gel particle. d.) WAXS data from gel particles with increasing P3HT concentration in the gel phase from left to right. The Gaussian fits of the data are overlaid and d-spacing and average crystal size from the Scherrer analysis is shown for each sample.

The most definitive evidence to support the hypothesis that the gel particles retain the network structure of their 'parent' organogels comes from a direct comparison of the amount of solvent-polymer interface in each sample. From the SANS data it is possible to directly quantify and compare the porosity of the micro-organogel particles and their parent organogels without having to assume any specific structural models. This is accomplished by calculating the total amount of P3HT-solvent interface in the samples directly from the scattering profiles. The specific surface

area, $\overline{S_V}$, total area per gram of P3HT, is a quantitative measure of porosity related to the total amount of solvent/solid interface in a sample. The specific surface area is calculated from the Porod approximation and the volume fraction of P3HT determined using the invariant. Note that, due to the initial creaming of large solvent drops right after emulsification, the volume fraction of the remaining P3HT is not necessarily the same as that used for sample preparation. However, because we have accurately determined the scattering length density of all the components, the calculation of the invariant allows us to accurately determine the final P3HT volume fraction in the micro-organogel dispersions.

The Porod approximation, shown in Equation 5.3 describes the scattering dependence at high-Q when there is a sharp interface between two phases with different scattering length densities. This expression is general and only requires the presence of a sharp boundary between two phases with a constant scattering length density.[16]

$$5.4 \quad \Sigma = \frac{\lim_{Q\to\infty} I(Q)Q^4}{2\pi\left(\Delta SLD\right)^2}$$

In equation 5.4, ΔSLD is the scattering length density difference between the P3HT and (d10)-p-xylene ($SLD_{\text{(d10)-p-xylene}} = 5.7\times10^{-6}$ Å^{-2} and $SLD_{\text{P3HT}} = 1.1\times10^{-6}$ Å^{-2}) and Σ is the total amount of solid/solvent interface per volume of sample. It is possible to extract Σ for all of the samples after fitting SANS data of the organogels and the micro-organogel particles between 1.2×10^{-1} Å^{-1} > Q > 4.8×10^{-2} Å^{-1}. The data Q > 1.0×10^{-1} Å^{-1} is not included in the fit because the assumption of uniform scattering length density breaks down. In this high-Q range, the crystalline lattice of P3HT results in Bragg diffraction peaks.

The invariant, shown in Equation 5.4, is used to determine the total volume fraction of P3HT, ϕ, within each sample after sonication and particle formation.[7] This expression is also general and

independent of the nature of the scattering object. It is also calculated directly from the SANS profile. The integral in the calculation of the invariant must be evaluated from $Q = 0$ to $Q = \infty$, requiring extrapolation from the real data to low-Q and high-Q. The high-Q extrapolation is achieved by extending the fit of the Porod region. This contributes ~20% to the total value of the invariant for the organogels and ~13% for the micro-organogel dispersions. The extrapolation to $Q = 0$ is achieved using the Guinier approximation and it is found that its contribution to the final value of the invariant is negligible.

$$5.5 \quad Inv = \int_0^\infty \left(I(Q)Q^2 \right) dQ = 2\pi \left(\Delta SLD \right)^2 \phi \left(1 - \phi \right)$$

The final volume fraction of P3HT in the dispersions was determined for all samples by using the value obtained from the integral and the known scattering contrast between P3HT and (d10)-p-xylene. The volume fraction calculated for the bulk organogels were within ~ 5% of the expected volume fraction from preparation. In contrast, the micro-organogel dispersions showed a 10% increase in volume fraction that is attributed to the loss of solvent during the creaming process. Finally, the specific surface area is calculated using Equation 4.5.

$$5.6 \quad \overline{S_V} = \Sigma / \rho_{P3HT} \phi$$

The results of this analysis, applied to the micro-organogel particles and their corresponding 'parent' organogels, are shown in Figure 5.11. The specific surface area of the 3 wt% bulk organogel is 620 m^2/g P3HT and this value is relatively constant for all other bulk organogels. For comparison, the average specific surface area obtained from the fit of the parallelepiped model is 580 m^2/g P3HT. This demonstrates that despite the relatively dense organogel network observed in TEM, the surface area is still dominated by the fiber cross-section.

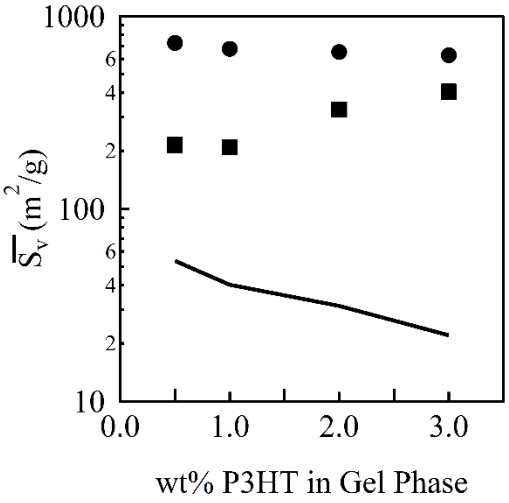

Figure 5.11. Specific Surface Area (m^2/g) versus wt% P3HT in the gel phase for the organogels (solid circles) and gel particle dispersions (solid squares). The solid line corresponds to the calculated specific surface area that is expected for solid spheres with radii equal to the R_H determined by DLS.

In contrast, the values for micro-organogel particle dispersions show stronger concentration dependence. With increasing P3HT weight fraction in the 'parent' organogel, the specific surface area of the micro-organogel particles increases and become increasingly similar to the organogels. This suggests that dispersions formed from stronger gels retain more of the network structure from the 'parent' gels. The difference in specific surface area from the organogels to the micro-organogel particles could be explained by a partial collapse of the network structure for the weakest parts of the gels. To better understand the extent of network collapse, it is useful to compare the calculated values to the specific surface area for solid spherical P3HT particles of the same size. In this case, the specific surface area is dominated by the outer surface of the particles. Equation 5.7 is used to estimate the specific surface area of the corresponding solid dispersions, $\overline{S_{V,sphere}}$ from DLS results.

$$\overline{S_{V,sphere}} = \sum_{0}^{\infty}\left[\phi_i\left(3/\left(\rho_{P3HT}R_{i,H}\right)\right)\right] \quad 5.7$$

The value is calculated by weighting specific surface area of each particle size by its volume fraction. The results of this analysis show that the gel particles have a much larger interfacial area than could be accounted for if they were comprised solely of solid particles. The large values for the specific surface area and the fact that the P3HT contained within the dispersions can be resolubilized upon increasing temperature (Figure 5.4.e) show that the dispersions contain true micro-organogel particles with an internal network structure comparable to their 'parent' organogels.

4.4 Characterization of Films produced from P3HT Organogel Emulsions

Using simple spray coating, we have produced uniform, densely packed thin films of gel particles as shown in Figure 5.12. The SEM image shows that the dispersions form a porous film upon coating. These films were produced without dialyzing excess surfactant from the solution. Excess surfactant is clearly visible at the edges of the image in Figure 5.12.

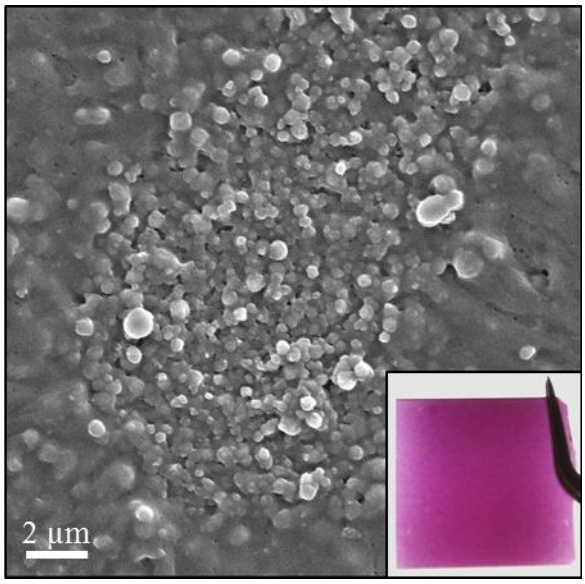

Figure 5.12. SEM of 1 wt% gel particle dispersion spray-coated to form a thin-film on ITO coated glass. Inset shows image of spray-coated gel particle film produced from a 1 wt% gel particle dispersion.

In order to assess the isotropy of crystalline domains within these films, GISAXS was performed on spray-coated films and compared to an annealed P3HT/PCBM film spin coated from chlorobenzene. Both profiles were measured at an incident angle of α_i = 0.2° and are shown in Figure 5.13.

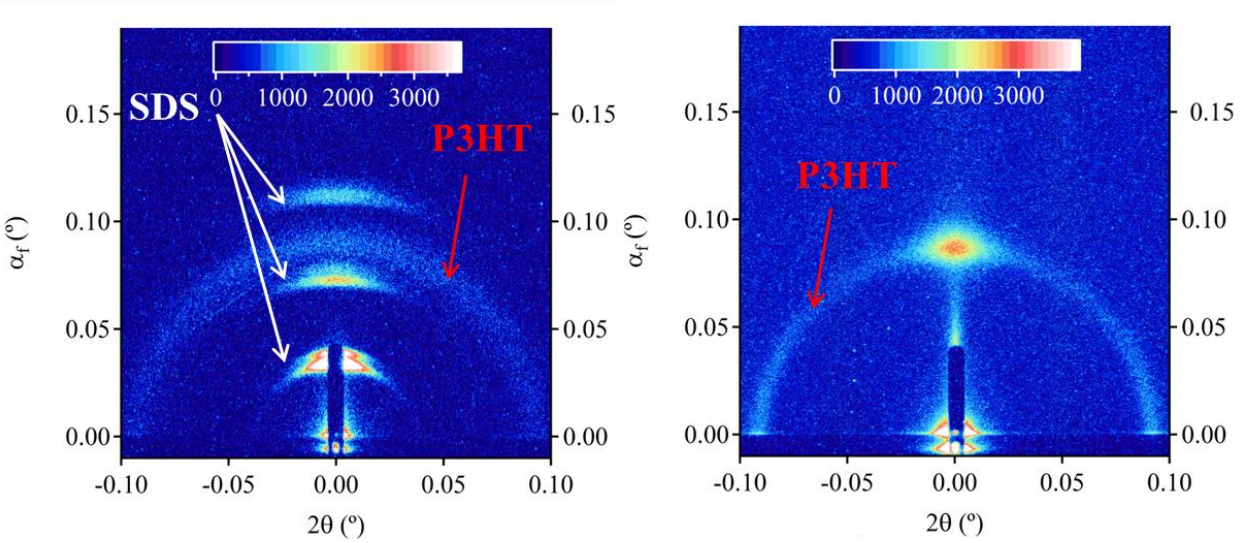

Figure 5.13. GISAXS images of 3 wt% gel dispersion coated onto glass substrate (left) and that of a P3HT/PCBM blend coated on glass (right).

There are a number of wide angle features present in the GISAXS measurements of the films made from spray-coated micro-organogel dispersions. SDS is still present during the coating process and clearly aggregates. Its crystalline features are denoted by white arrows in Figure 5.13. It appears to aggregate into lamellae along the film's surface and in the interstitial spaces between the organogel dispersion particles. The P3HT (100) crystalline peak at Q=0.375 $Å^{-1}$ is also present in the GISAXS pattern. The radial distribution of scattering intensity for a given Bragg feature contained within a film relates to the distribution of crystalline domains within the film's volume. Comparing the (100) P3HT Bragg peak's crystalline distribution of the P3HT/PCBM annealed film to that of the organogel dispersion, it is clear that the organogel possesses more uniform distribution of domains. Based on the GISAXS pattern, it is expected

that hole-transport through the P3HT/PCBM would be highly anisotropic, with higher mobility in the plane of the substrate compared to out of plane. The film made from P3HT organogel emulsions would have superior transport out of the substrate plane, meaning that holes could travel faster through the film thickness, potentially improving performance of solar cells where charge transport limits performance.

4.5 Materials and Methods

Absorption and photoluminescence spectroscopy experiments were performed on the gel particle dispersions after diluting the original samples to 0.5 vol%. Absorption spectroscopy measurements were made from 300 nm to 1000 nm using a Thermo Scientific Evolution 300 UV-Vis spectrophotometer. Photoluminescence measurements were made in the range from 580 nm to 900 nm with a 550nm excitation using Photon Technology International (PTI) Inc. model QM2001-4 Spectrofluorimeter. The samples were measured in a 10 mm quartz cuvette using water as background. Dynamic Light Scattering (DLS) measurements were also performed on these diluted samples using a Malvern Zetasizer NANO ZS instrument with a 178˚ backscattering geometry. In order to obtain the volume distributions from the DLS data, intensity weighted distributions obtained using a non-negatively constrained least squares (NNLS) fitting algorithm were transformed to volume distribution using Mie Theory and the known index of refraction of the samples. Viscosity measurements were performed using an Anton Paar Rheometer (MCR 301) with double-gap concentric cylinder geometry (26.7 mm OD and 24.7 mm ID bob / 0.92 mm gap size/40 mm length). A step shear rate ramp was applied over a range of 0.001 s^{-1} to 1000 s^{-1}. Transmission Electron Microscopy (TEM) was performed on the 3 wt% bulk organogel using an FEI Tecnai TEM. The images were collected using high angle annular dark field (HAADF) scanning TEM mode with a single tilt holder with 0.18 nm resolution.

Scanning Electron Microscopy (SEM) was performed using an FEI Sirion SEM on a thin-film prepared by spray-coating a gel particle dispersion onto glass coated with indium-doped tin oxide. The film was sputtered with a thin-layer of gold to prevent charging.

Small angle neutron scattering (SANS) and ultra-small angle neutron scattering (USANS) measurements were performed at the National Institute of Standards and Technology Center for Neutron Research in Gaithersburg, MD. SANS measurements were performed on the NG3 30 meter instrument using detector distances of 1.3 m and 7 m with a neutron wavelength of 5 Å and at 13 m with a neutron wavelength of 8 Å to cover a broad Q-range ($0.001\ Å^{-1} < Q < 0.5\ Å^{-1}$). USANS measurements were performed on the BT5 perfect crystal diffractometer further extending the measured q range to beyond $0.0001\ Å^{-1}$. USANS data was reduced and desmeared using the NIST IGOR Pro Macros.[26] Contrast matching of the organic solvent and the continuous phase was used to highlight scattering from P3HT contained within the gel particle particles (i.e. the scattering contribution from the oil and water interface was eliminated). This was accomplished by varying the H_2O/D_2O ratio in the continuous phase of the dispersions until the scattering length density matched the value of deuterated p-xylene. In this way it was possible to examine the P3HT structure within the gel particle particles. The contrast match point for (d10)-p-xylene was determined experimentally to be 90.5 vol% D_2O in the bulk phase. This corresponds to a scattering length density of $5.68\times10^{-6}\ Å^{-2}$. The scattering length density of P3HT was also determined experimentally by varying the hydrogenated and deuterated content of p-xylene in a series of otherwise identical 0.85 ± 0.03 vol% organogels after one day of gelation time. The scattering length density of P3HT within the gel phase was determined to be $8.78\times10^{-7}\ Å^{-2}$ corresponding to a mass density of crystalline P3HT of 1.43 g/cm^3. This value also agrees well with measured densities obtained from dilute nanofiber dispersions. Small angle

neutron scattering (SANS) measurements were performed on 'parent' organogels of 3.0, 2.0, 1.0, and 0.5 wt% and on the corresponding gel particle dispersions. The SANS data was normalized to an absolute scale by measuring the incident neutron flux and was also corrected for transmission and empty cell scattering. The data is presented as the absolute intensity versus *Q*.

References.

1. Malik, S.; Nandi, A. K. Influence of Alkyl Chain Length on the Gelation Mechanism of Thermoreversible Gels of Regioregular Poly (3-Alkyl Thiophenes) in Xylene. *J. Appl. Polym. Sci.* **2006**, *103*, 2528–2537.

2. Newbloom, G. M.; Weigandt, K. M.; Pozzo, D. C. Structure and Property Development of Poly(3-Hexylthiophene) Organogels Probed with Combined Rheology, Conductivity and Small Angle Neutron Scattering. *Soft Matter* **2012**, *8*, 8854–8864.

3. Newbloom, G. M.; Weigandt, K. M.; Pozzo, D. C. Electrical, Mechanical, and Structural Characterization of Self-Assembly in Poly(3-Hexylthiophene) Organogel Networks. *Macromolecules* **2012**, *45*.

4. Teixeira, J. Small-Angle Scattering by Fractal Systems. *J. Appl. Crystallogr.* **1988**, *21*, 781–785.

5. Lebedev, D. V.; Filatov, M. V.; Kuklin, a. I.; Islamov, a. K.; Stellbrink, J.; Pantina, R. a.; Denisov, Y. Y.; Toperverg, B. P.; Isaev-Ivanov, V. V. Structural Hierarchy of Chromatin in Chicken Erythrocyte Nuclei Based on Small-Angle Neutron Scattering: Fractal Nature of the Large-Scale Chromatin Organization. *Crystallogr. Reports* **2008**, *53*, 110–115.

6. Beaucage, G. Determination of Branch Fraction and Minimum Dimension of Mass-Fractal Aggregates. *Phys. Rev. E* **2004**, *70*, 031401.

7. Lindner, P, Zemb, T. *Neutrons, X-Rays and Light: Scattering Methods Applied to Soft Condensed Matter*; North-Holland, 2002.

8. Koppe, M.; Brabec, C. J.; Heiml, S.; Schausberger, A.; Duffy, W.; Heeney, M.; McCulloch, I. Influence of Molecular Weight Distribution on the Gelation of P3HT and Its Impact on the Photovoltaic Performance. *Macromolecules* **2009**, *42*, 4661–4666.

9. Richards, J. J.; Weigandt, K. M.; Pozzo, D. C. Aqueous Dispersions of Colloidal Poly(3-Hexylthiophene) Gel Particles with High Internal Porosity. *J. Colloid Interface Sci.* **2011**, *364*, 341–50.

10. Pal, R. *Rheology of Particulate Dispersions and Composites*; 2007; pp. 1–300.

11. Spano, F. C.; Introduction, I. The Spectral Signatures of Frenkel Polarons In. **2010**, *43*, 429–439.

12. Feigin, L.A., Svergun, D. I. *Structure Analysis by Small-Angle X-Ray Scattering and Neutron Scattering*.

13. Glatter, O.; Kratky, O. *Small Angle X-Ray Scattering*; Academic Press Inc., 1982.

14. Salleo, A.; Kline, R. J.; DeLongchamp, D. M.; Chabinyc, M. L. Microstructural Characterization and Charge Transport in Thin Films of Conjugated Polymers. *Adv. Mater.* **2010**, *22*, 3812–38.

15. Newbloom, G. M.; Kim, F. S.; Jenekhe, S. A.; Pozzo, D. C. Mesoscale Morphology and Charge Transport in Colloidal Networks of Poly(3-Hexylthiophene). *Macromolecules* **2011**, *44*, 3801–3809.

16. Schmidt, B. Y. P. W. Small-Angle Scattering Studies of Disordered , Porous and Fraetal Systems. **1991**, 414–435.

Chapter 6. Structural Characterization of Composite Nanoparticles

Aqueous dispersions of semiconducting nanoparticles have shown promise as a robust and scalable platform for the production of efficient polymer/fullerene active layers in organic photovoltaic applications. Semiconducting nanoparticles are a composite of both an n-type and p-type semiconductor contained within a single nanoparticle. In order to realize efficient organic solar cells from these materials, there is a need to understand how the size and internal distribution of materials within each nanoparticle contributes to photocurrent generation in a nanoparticle derived device. Therefore, characterizing the internal distribution of conjugated polymer and fullerene within the dispersion is the first step to improving performance. To date, study of polymer/fullerene structure within these nanoparticles has been limited to microscopy techniques of deposited nanoparticles. In this chapter, we use contrast variation with small angle neutron scattering to determine the internal distribution of poly(3-hexylthiophene) and [6,6] phenyl-C_{61}-butyric acid methyl ester inside the composite nanoparticles as a function of formulation while in dispersion. Based on these measurements, we connect the formulation of these nanoparticles with their internal structure.

6.1. Stuhrmann Analysis: Contrast Variation Neutron Scattering for Inhomogeneous Dispersions

The structural interrogation of inhomogeneous nanoparticles, composed of more than one component with unique scattering length densities, using small angle scattering have typically been limited to particles with an axisymmetric distribution of scattering length density.[1] There are a great number of examples of particles that fall into this category including surfactant micelles, nanoparticles decorated with polymer brushes, and vesicles.[2,3] The scattering profiles for these particles are frequently treated using infinitely thin shells with unique contrast terms constructed such that they reproduce the radial variation of scattering length density.[4,5] The

overall structure can then be described by the form factor of each shell multiplied by the phase factor that accounts for their relative separation.[6] This simple analytical approach cannot be used to describe the scattering of particles with eccentric inhomogeneities (e.g. egg-yolk particles) or those with domains whose center of mass does not correspond to the particle's center of mass (e.g. Janus particles).[7] For such particles, limited analytical treatments exist to adaquately describe their scattering profiles, and thus model independent approaches have been primarily used.[8]

This is also the case for the scattering of complex protein assemblies. Often protein domains are distributed non-uniformly throughout the particle's volume. In order to obtain an adequate description of the particle's shape, Stuhrmann developed a general model-independent approach to characterize internal inhogeneities using contrast variation.[9,10] Contrast variation is commonly applied in small angle neutron scattering (SANS) because partial or full deuteration can be used to selectively highlight regions of a material without significantly changing its chemical characteristics. By measuring the same protein in solutions with varying amounts of H_2O and D_2O, Stuhrmann demonstrated that the dependence of scattering intensity for any inhomogeneous particle can be decomposed into separate terms as shown in Equation 1.

$$6.1 \quad I(Q, SLD) = I_{\text{inh}}(Q) + \Delta SLD \times I_{\text{cross}}(Q) + \Delta SLD^2 \times I_{\text{homo}}(Q)$$
$$where\ \Delta SLD = \left(SLD_m - SLD_{solv}\right)$$

For homogenous particles without internal inhomogeneities, *I(Q)* is the product of the form factor *P(Q)* and the structure factor *S(Q)*. In most cases, measurements are made in dilute solution so as to minimize interactions between particles so that $S(Q) \rightarrow 1$ and the scattering profile is dominated by *P(Q)*.[11,12] A large number of analytical form factor models for homogenous particles exist to predict the scattering profile.[13–15] For inhomogenous particles, the scattering profile is a function of the overall particle's shape, $I_H(Q)$, the shape function of its

inhomogeneities, $I_{IH}(Q)$ and a structural correlation term, $Ics(Q)$. Taken together, these functions reconstruct the scattering from the entire particle.

In this description, the scattering from an object with average scattering length density, ρ_m, has a quadratic dependence on contrast between the object and its solvent, $\Delta\rho$. By measuring the sample in at least three different solvent contrasts, the terms in Equation 6.1 can be fit at every Q value to the known contrast term and the constituent basis functions ($I_H(Q)$, $I_{IH}(Q)$, $I_{cs}(Q)$) of the shape can be recovered. In principle, the form factor of the object is thus separated from the form factor of the inhomogeneities and the basis functions can now be fit independently using analytical models for homogenous particles.

Despite the power of this description, it often proves difficult to identify adequate analytical models for the basis functions. This was found for proteins where the complex shape is determined by the secondary and tertiary structure and not known *a priori*. It is also true in the case of polydisperse composite nanoparticles. In order to obtain information about samples whose basis functions cannot be fit with analytical form factor models, Stuhrmann derived Equation 6.2 to describe the dependence of the radius of gyration (R_g) on contrast. Stuhrmann derived the quadratic dependence of R_g of a particle on the inverse of the ΔSLD.

$$6.2 \quad R_g^2 = R_c^2 + \alpha/\Delta SLD - \beta/\Delta SLD^2$$

In Equation 6.2, R_c is the radius of gyration of the particle at infinite contrast (i.e. if it were homogeneous), α describes the relative distribution of scattering length density radially from the particle's center of mass, and β is measure of the distance of the center of mass of the particle to the center of mass of its heterogeneous components. In effect, the overall shape of the particle is described by R_c and the distribution of inhomogeneities by α and β. The result of this analysis

showed that a plot of R_g^2 as a function of $1/\Delta SLD$ is a unique fingerprint that can be used to identify materials by their average distribution of internal inhomegeneities.[10]

To date, the approach developed by Stuhrmann has been primarily applied to proteins. Here we extend it to describe composite nanoparticles comprised of conjugated polymers and fullerenes. These nanoparticles are being developed as the active component in organic photovoltaics[16–18]. In this application the distribution of polymer and fullerene domains internal to the particle is expected to have a significant influence over the photovoltaic performance of devices derived from them. Because of the production process of these particles, they are generally spherical but somewhat polydisperse in size, and a large variety of potential structures can be anticipated (e.g. core-shell, heteroaggregates, and Janus particles).[19,20] Because appropriate analytical models for eccentric particles are relatively limited, we propose that the method developed by Stuhrmann is a simple and more versatile approach to characterize the complex structure of these dispersions. In order to gain physical insight into the Stuhrmann behavior of these complex structures, we first calculate the scattering profiles of model particles to develop suitable 'fingerprints'. To do this, we developed a simulation tool that directly calculates the scattering pattern from a real space representation of the object. Using this approach, the scattering profiles from several anticipated structures are modelled directly as a function of solvent contrast. From these profiles, Stuhrmann plots, R_g^2 versus $1/\Delta SLD$, are constructed. Comparing the Stuhrmann plots of modeled particles to those that we have measured demonstrates the simplicity and utility of the Stuhrmann approach particularly when coupled with the real space modeling tool. While the techniques developed here are applied only to composite conjugated polymer/fullerene nanoparticles, they are described generally and are therefore applicable to any particle comprised of more than one component.

6.2. Implementation of Stuhrmann Analysis to real particles

To obtain Stuhrmann plots for inhomogeneous particles, the traditional Guinier approximation is modified to include the explicit dependence of R_g and $I(0)$ *on* $\Delta\rho$ (Equation 6.3).[11]

$$6.3 \quad I(Q) = I(0)\exp\left(\left(QR_g\left(SLD\right)\right)^2 \Big/ 3\right)$$

By fitting Equation 6.3 with the implicit inclusion of Equation 6.2 simultaneously for each solvent contrast, the weighted error at each contrast is combined to obtain the best fit. From this fit, α, β, and R_c are determined directly.

SANS experiments were performed to validate that this approach can characterize real polymer/fullerene composite nanoparticles. The particles are produced through an emulsification process that can lead to both polydisperse distributions in both particle size and shape. Therefore, these particles have proved difficult to fit using analytical core/shell models. Figure 6a shows the scattering profiles of a D_{avg}=120 nm P3HT/PCBM (PDI=0.2 as determined by DLS) latex dispersion produced by emulsifying a P3HT and PCBM with a 1:1 wt ratio in chloroform. SANS measurements were then carried out on identical samples for each of the contrast values and the data is fit at low Q using Equation 6.5.

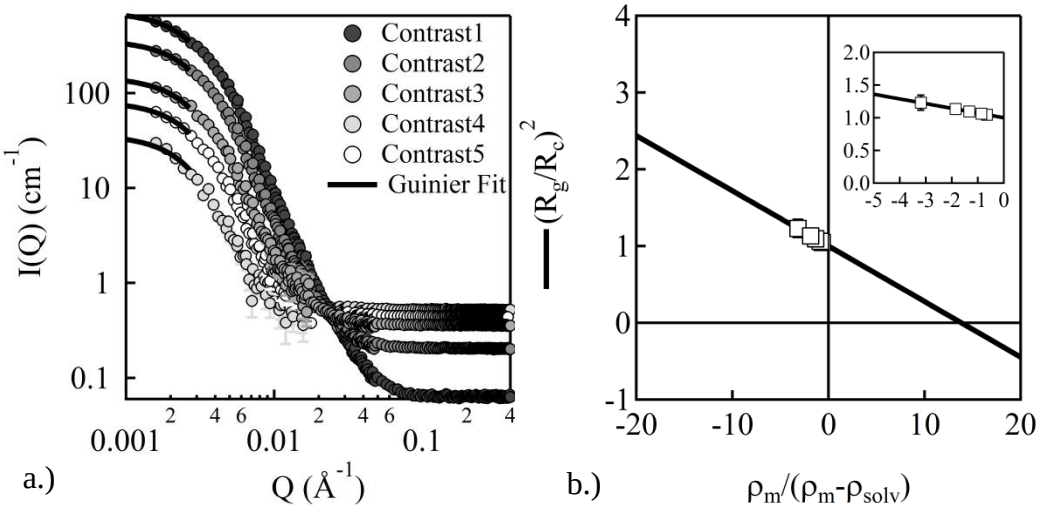

Figure 6.1. a.) Scattering profiles from P3HT/PCBM composite nanoparticle along with the fit to Equation 5, b.) Stuhrmann plot derived for the nanoparticle dispersion shown in a.) The inset highlights the region of contrast where the measurement was made.

From the Stuhrmann plot, it is evident that this dispersion is inhomogeneous as indicated by the fact that there is a dependence of the R_g on SLD_{solv}. For simplicity and so that particles of different size and SLD_m can be appropriately compared, the Stuhrmann plot is normalized by the fitted value of R_c and the SLD_{solv} made dimensionless to mimic the form given in Equation 6.1. From the fit, α =-0.05, which implies that the lower scattering length density component is farther from the center of mass of the particle. The R_c value fit for this sample was 54.3 nm and the fitted of $\beta = 1.32\times10^{-12}$ is effectively zero. The relatively small value of α suggests that there is likely some PCBM dispersed within the P3HT rich shell, consistent with the finite solubility of PCBM in P3HT, and these particles are on average core-shell.[21]

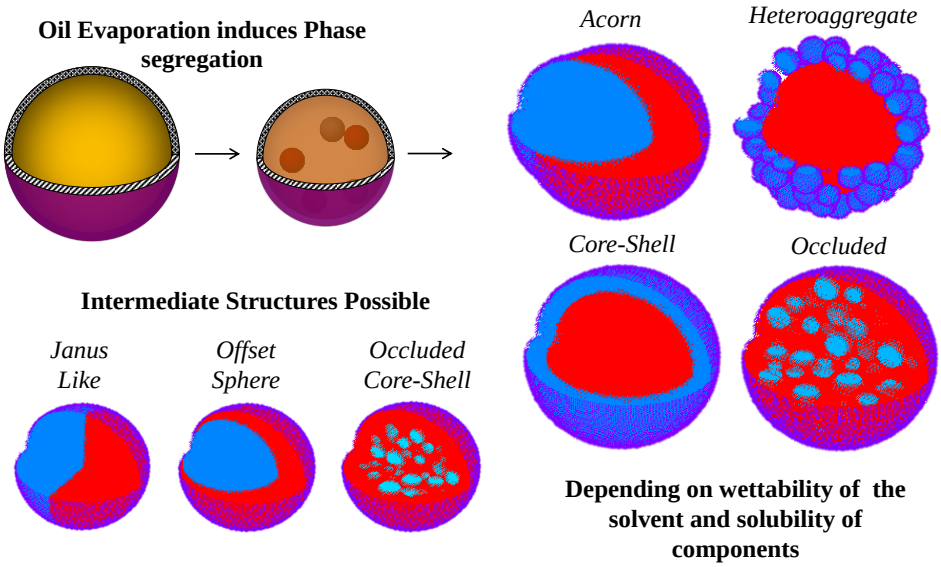

Figure 6.2. Model for structure formation predicted by Loxley based on the relative wettability of oil/water interface on solidifying phases within an oil droplet.

Composite nanoparticles formed through the removal of solvent from an emulsion are expected to exhibit a wide range of internal morphologies depending on the method of production as depicted in Figure 6.2.[22,23] As elucidated by Loxley et al, the phase segregation of non-volatile components in an emulsion as a volatile oil is removed is a function primarily of the relative wettability of the solvent to the oil-water interface.[19] As oil is removed from the emulsion, solid phases of the polymer/fullerene components begin to form within emulsion droplets and can be sufficiently mobile that they can migrate inside the drop. The propensity of the solvent to wet the oil-water interface and the maximum solubility of each component in that particular solvent will ultimately determine the internal distribution of components in the particle. For such systems, a number of possible structures could form: core-shell particles, occluded, Janus, and uniform. In order to predict the scattering patterns from the great degree of structural diversity that we anticipate, we must turn to Monte Carlo modeling, a method that allows the calculation of the contrast dependent scattering profile for any object that can be represented in a voxelgram.

6.3. Monte Carlo Representation and Calculation of Scattering Profiles

The real space voxelgram of a particle is constructed in a custom written set of macros using the programming software IGOR Pro from Wavemetrics. It was developed to accurately calculate the scattering intensity in absolute scale from a user defined particle of arbitrary internal complexity and shape. In order to construct a representation of the the particle, a series of 'if…then' statements are used to specify the position of internal components of a particle in a voxelgram, a uniformly spaced lattice of dimension ($N \times N \times N$). Based on the desired structure, each point on the lattice is assigned a scattering length density value, *SLD*, in $Å^{-2}$.

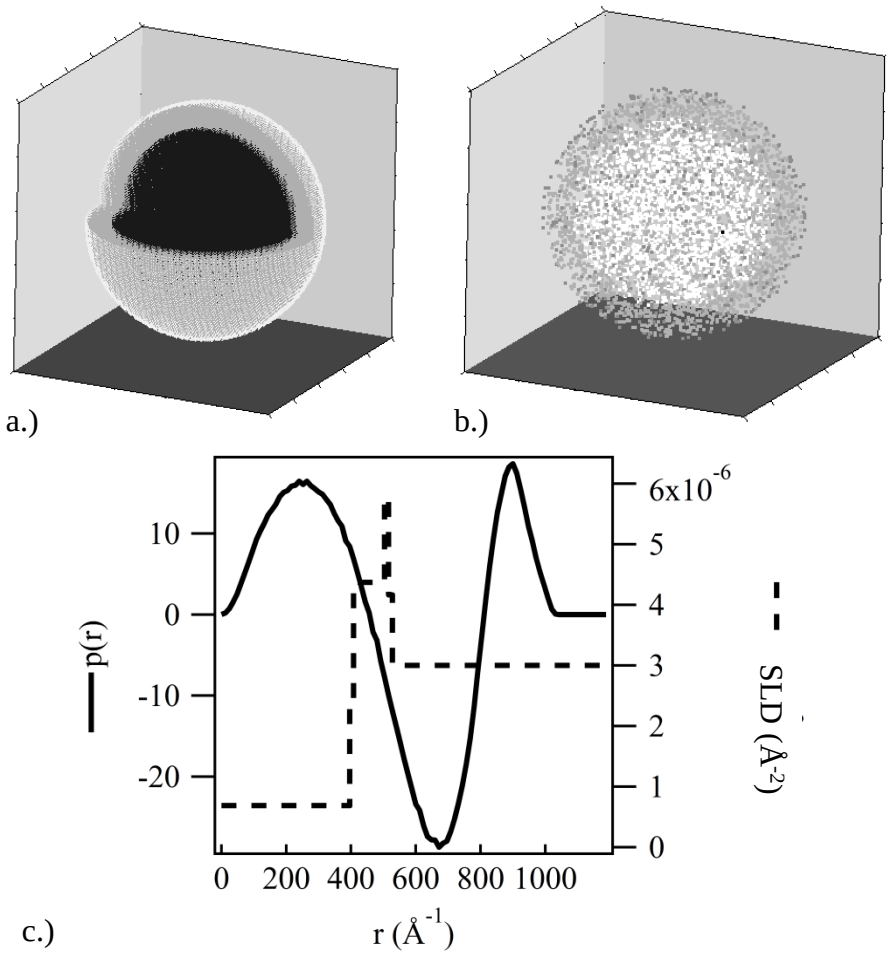

Figure 6.3. 50 vol% conjugated polymer core/50 vol% fullerene shell nanoparticle (R = 50nm with 1.5 nm surfactant layer), a.) Lattice representation, b.) Monte Carlo Sampling of Lattice, and c.) binned $p(r)$ calculated for core-shell nanoparticle where $SLD_{solv} = 3.0\times10^{-6}$ Å^{-2} along with the radial distribution of scattering length density. Monte Carlo representation is colorized by ΔSLD.

Figure 6.1a shows a lattice representation of a core-shell particle. Once the real space model is constructed, it is in principle possible to directly calculate its scattering profile. The computation time scales with k^2, and therefore Monte Carlo sampling is utilized to calculate this with fewer points than required to represent the entire particle structure. Efficient Monte Carlo sampling techniques have been developed previously to directly calculate the scattered intenstiy from a real space representation of a particle.[24] Monte Carlo sampling is carried out using the random

number generator available in Igor Pro. Random numbers are generated for x, y, and z coordinates within the box volume. These coordinates are rounded to the nearest lattice point. The whole box volume is sampled, but the code rejects elements where SLD_i=SLD_{solv}. Sampling continues until the total number of points generated reaches a specified value. Each domain with a unique scattering length density is sampled a number of times that is directly proportional to the relative volume fraction of that domain within the particle volume as shown in Figure 6.3b. If *k* is the total number of Monte Carlo points, then in one iteration *1/2*k(k-1)* point-pair distances are calculated. Averaging multiple iterations provides a means to estimate the precision of the calculation. For the calculations performed here, at least 10^8 point pairs were binned into the histrogram to obtain sufficient precision. The accuracy of the calculation is dependent on the total number of points selected and therefore, a minimum number of Monte Carlo points is required to accurately represent the smallest volume fraction domains contained within the particle.

In order to calculate the scattering profile, the point-pair distances are used to bin the product of ΔSLD_i and ΔSLD_j into a histogram whose size spans the box size. Ultimately, the binned histogram is normalized such that Equation 6.4 is satisfied and *p(r)*, the pair distance distribution function, is recovered.

$$6.4 \quad I(0) = \int_0^\infty p(r)dr = \phi_{part} \frac{1}{V_{part}} \left[\sum_i^N \left(SLD_i - SLD_s \right) V_i \right]^2$$

Here ϕ_{part} is the volume fraction of particles in solution, V_{part} is the volume of the particle, and V_i is the volume of element *i*. The normalized *p(r)* histogram for a core-shell particle is shown in Figure 6.3c. After the normalization of *p(r)*, the scattering intensity in absolute scale can be numerically determined by integration over a specified *Q*-range using Equation 6.5.[11]

$$6.5 \quad I(Q) = \int_0^\infty p(r) \frac{\sin(Qr)}{Qr} dr$$

Using this approach, structures of arbitrary complexity can be generated and because of explicit inclusion of SLD_{solv}, the effects of varying solvent contrast can be assessed. Validation that this approach accurately reproduces the scattering intensity of a core-shell particle in absolute scale is shown in Figure 6.4.[14] In both the model and the direct calculation, a realistic incoherent background is added.

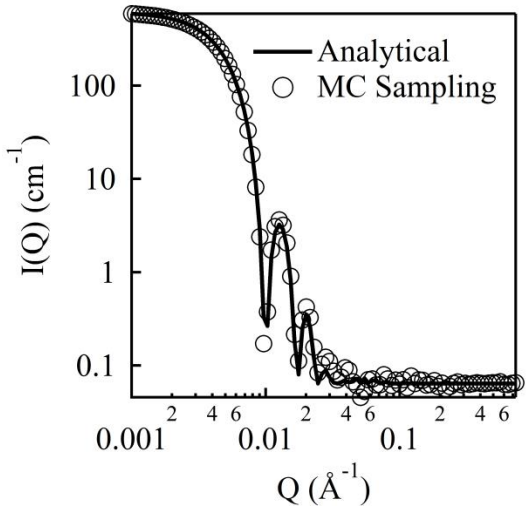

Figure 6.4. Comparison of core-shell model of a P3HT/PCBM latex calculated using the analytical expression implemented in SASView and the scattering pattern derived from the Monte Carlo calculation implemented in IGOR Pro.

At low-Q, the direct calculation method exactly reproduces the scattering from the analytical model. At high-Q, the calculation deviates slightly from the model. This is a result of the use of a lattice of finite size to represent the particle. Higher accuracy is possible at the expense of computation time through the use of a finer lattice. The accuracy of this method is adequate to apply the Guinier approximation without introducing error. For homogenous particles, when scattering profiles are obtained at sufficiently low-Q ($QR_g < 1$) the plot of $ln(I(Q))$ *vs.* Q^2 is

linear. Fitting to the Guinier approximation allows extraction of values for *I(0)* and R_g, where R_g is independent on solvent contrast (homogeneous particle).

6.4. Stuhrmann Plots as Fingerprints for Structure

Based on what is known from Loxley's theory predicting phase segregation of solidified components within a liquid droplet, a large number of theoretical structures were generated and their Stuhrmann plots derived. Five representative structures are depicted in Figure 6.5 with the simulated scattering profiles at different contrasts and corresponding incoherent backgrounds added. The corresponding Stuhrmann plots are also shown for each model constructed from the fitting results of Equation 6.3. For simple comparison, the fitted R_g^2 values are normalized by dividing by R_c^2 and the x-axis is also normalized by multiplying by ρ_m. This is convenient way to represent the Stuhrmann plot as it eliminates size and average contrast effects from Stuhrmann representation, allowing for direct comparison of particles that have different sizes, structures and contrast.

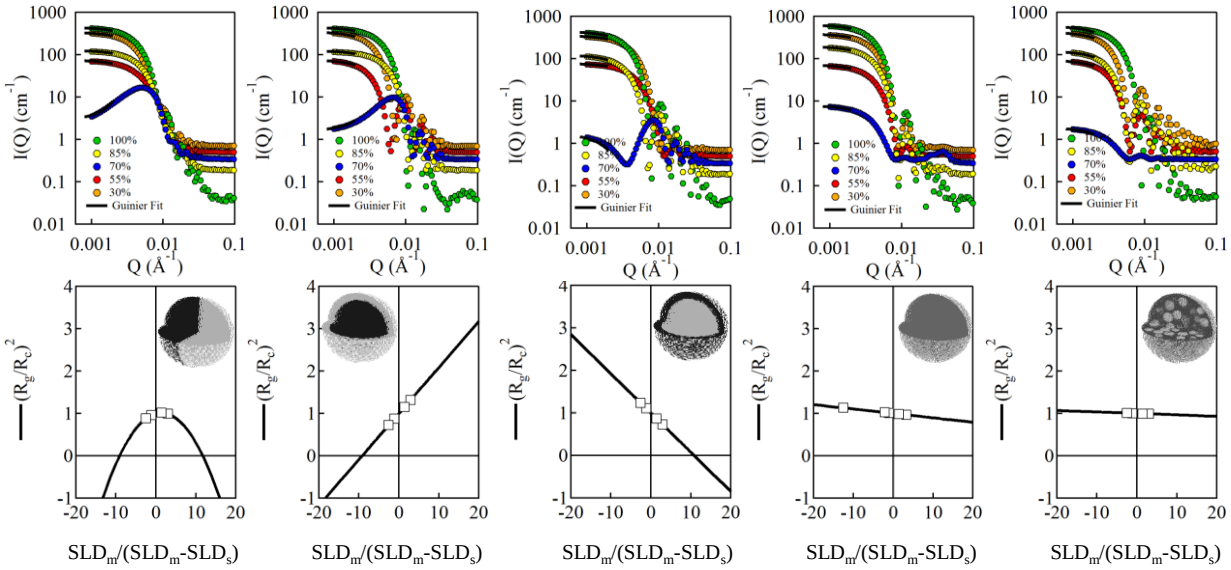

Figure 6.5. Calculated scattering profiles at 5 different contrasts for five different shapes - left to right ("Janus", core-shell (P3HT core), core-shell (PCBM core), uniform, and occluded) with corresponding Stuhrmann plots and lattice representations. Coloration of pixels correspond to the scattering length density assigned to that pixel with black corresponding to *SLD*=0.0×10^{-6} Å^{-2}

and white *SLD*=6.3×10^{-6} Å^{-2}. The simultaneous Guinier Fit to Equation 6.3 is plotted as a solid line for each contrast.

As is evident from Figure 6.5, the Stuhrmann plots of axisymmetric particles (core-shell, uniform, occluded) are linear due to the center of mass corresponding directly to the center of scattering length density. The only particle simulated here with a non-zero β is the Janus nanoparticle. This results in a parabolic Stuhrmann plot. For the two core-shell particles, β is zero and the value of α is determined by the radial distribution of higher and lower scattering length density domains. If P3HT is at the core of the nanoparticle, then α is positive. If P3HT is in the shell of the nanoparticle, then α is negative. It is expected that if a particle has a uniform distribution of material throughout the nanoparticle, then both α and β are zero. This should be the case for both the uniform nanoparticle which is simulated to possess no explicit heterogeneity and the occluded nanoparticle where small nuclei have formed in the interior. However, both show a small, but finite slope. This is a result of the explicit inclusion of surfactant shell in the model, which means that all of the particles simulated will show a small amount of heterogeneity. The value for α is small because the contribution of the surfactant to the overall nanoparticle size is very small.

These simulations demonstrate the utility of the Stuhrmann plot in identifying key structural features of nanoparticle dispersions without any *a priori* knowledge about the sample. This information is not only valuable in being able to identify an appropriate model to fit a sample measured at multiple contrasts, but also underlines the fact that for inhomogeneous nanoparticles, measuring the sample at multiple contrasts is critical to being able to uniquely identify its structure. As shown in Figure 6.6a, when contrast between the continuous phase and the particles is large, the scattering from particles that are the same size and average *SLD* but different internal structures are almost indistinguishable. However, near the contrast match point,

Figure 6.6b, there are clear differences in the scattering patterns that arise from the distinct differences in form factor of the internal inhomogeneities.

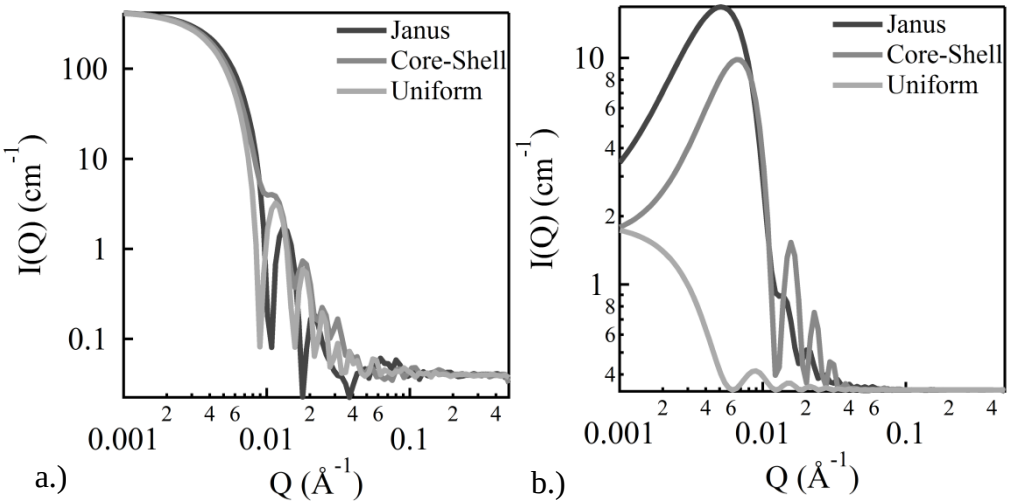

Figure 6.6. Simulation of different nanoparticles (R=50 nm with 1.5 nm surfactant layer, SLD_m=2.8×10^{-6} Å^{-2}) - Janus, Core-Shell, and Uniform at a.) SLD_{solv} = 6×10^{-6} Å^{-2}, and b.) SLD_{solv} = 3×10^{-6} Å^{-2}.

Another valuable aspect of the use of the Stuhrmann plot is that it is not restricted to monodisperse nanoparticles. Stuhrmann plots of polydisperse core-shell particles with a Gaussian distribution of particle radii but with identical internal compositions are plotted in Figure 6.7a as well as for particle compositions having a fixed particle radius but variable internal compositions, Figure 6.7b. In Figure 6.7a, as the particle size distribution changes with a fixed internal composition, the normalized Stuhrmann representation does not change. This is a direct result of the normalization of the Stuhrmann plot with respect to R_c. Effectively, when normalized by length scale, the distribution of scattering length density is the same regardless of particle radius. Figure 6.7b shows the simulated Stuhrmann plots for particles with a fixed size and distribution of internal composition. In this model, it is assumed that the P3HT and PCBM domains are pure phases and therefore, when the composition changes, the core/shell ratio changes accordingly. The model is constructed such that the average composition of all three

dispersions is the same, but the distribution of composition varies and can even include samples with pure P3HT or pure PCBM. As the PDI increases, the value of α systematically decreases. Nonetheless, even for relatively large PDI values, the Stuhrmann plot correctly predicts the distribution of material within the particle with P3HT on average being located in the core as shown by the positive value of α.

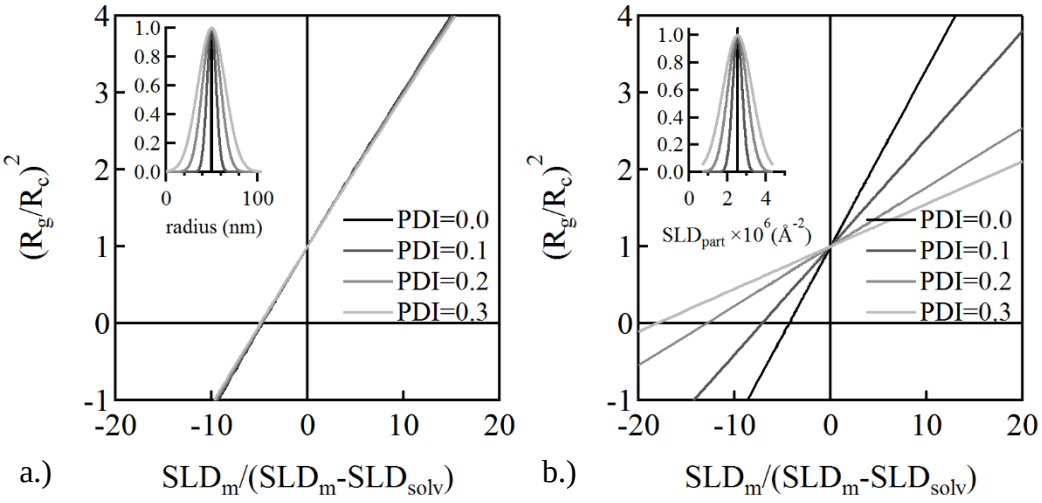

Figure 6.7. Stuhrmann plot of P3HT/PCBM core/shell particles with P3HT in the core that have a Gaussian distribution of a.) P3HT/PCBM radius, and b.) internal composition, SLD_{part}.

6.5: P3HT/PCBM CNPs: A model for structure

Four different dispersions were prepared with different methods and measured at five different contrasts in order to obtain similar Stuhrmann plots from a diverse set of nanoparticle formulations, Figure 6.8. The particles all have a constant 1:1 P3HT to fullerene weight ratio and a similar average particle size. Different particles show varying degrees of dependence of the radius gyration on the changing contrast of the aqueous phase. The sample in Figure 6.8a was prepared by dissolving P3HT and PCBM in chloroform. Based on the Stuhrmann plot, this formulation results in a core-shell particle where P3HT is enriched in the shell due to the negative α value and β=0. This also agrees with the recently published findings using X-ray

composition imaging for particles by Ulum *et al*.[25] The sample in Figure 6.8b is a 1:1 P3HT/fullerene latex where the fullerene phase has 5 wt% C_{60} and 95 wt% PCBM. In chapter 4, we discuss the effect of the addition of C_{60} to the fullerene phase of P3HT/PCBM composites. This has shown that C_{60} nucleates the growth of PCBM.[26] We hypothesized that this would also alter the extent of phase segregation within the particle. This particle formulation shows a structure characteristic of eccentric or anisotropic phase segregation based on the quadratic dependence of the Stuhrmann plot. From the results shown in Table 6.1, β is large and α is also large and positive. This indicates that PCBM is preferentially segregated to the shell of the particle, and that the center of mass of the fullerene phase does not coincide with the center of mass of the particle. The presence of a relatively small amount of C_{60} is shown to have a significant influence over the distribution of PCBM within the particle volume. The samples in Figure 6.8c and Figure 6.8d correspond to the "postgel" and "pregel" respectively. The "postgel" sample displays a similar quadratic profile to the P3HT/PCBM/C_{60} latex, suggesting the particle is eccentric. However, for these particles there is a smaller β value and a large, negative α value. On average, these particles have an enriched P3HT shell with an eccentric distribution of internal components. As shown in Figure 6.8d, the "pregel" sample shows almost complete uniformity because α is zero and β is also very small.

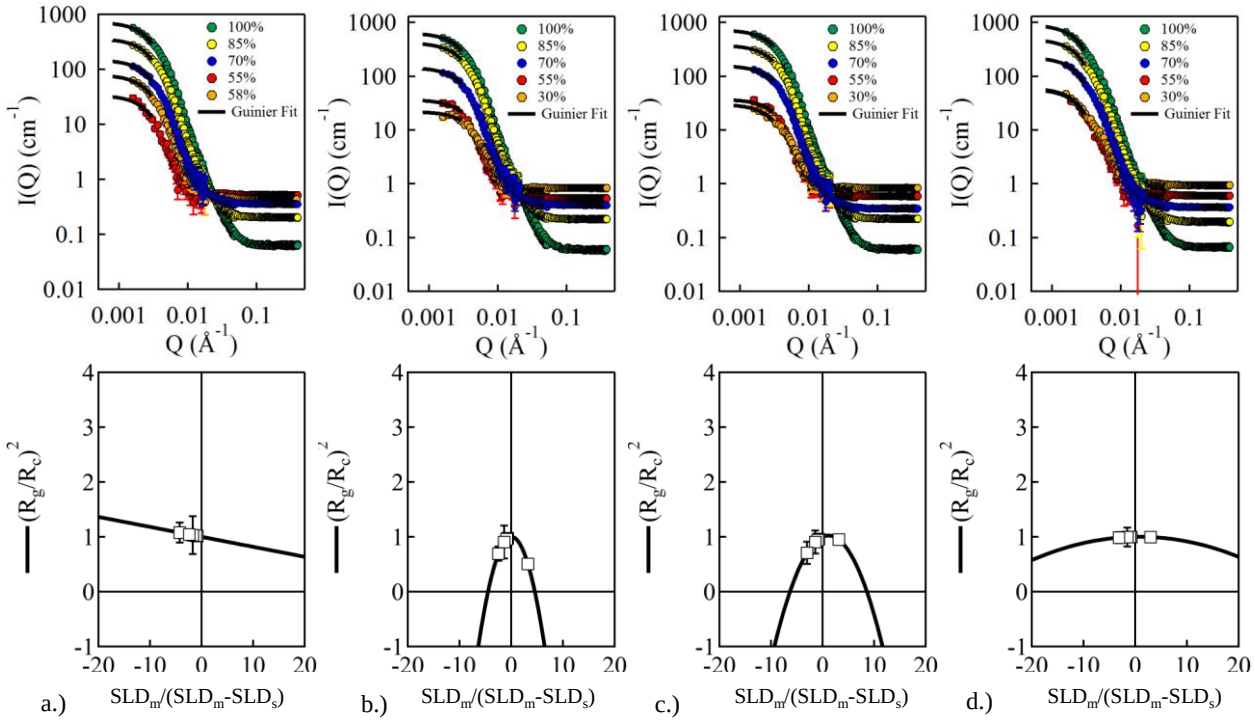

Figure 6.8. Upper: SANS profiles for each sample measured at 5 unique contrasts and corresponding the Guinier fits (solid line). Lower: Stuhrmann plots of R_g^2 v $SLD_{part}/\Delta SLD$ for a.) 50/50 P3HT/PCBM latex dispersions, b.) P3HT/$PC_{60}BM$/C_{60} dispersions, c.) 50/50 P3HT/PCBM postgel and d.) 50/50 P3HT/PCBM pregel.

Based on our previous work, this indicates that the porous and uniform organogel structure is preserved even when formed in the presence of PCBM.

Table 6.1. Stuhrmann analysis results for P3HT/fullerene SNPs with variations in method of preparation.

	50/50 $CHCl_3$	**PCBM/C_{60} $CHCl_3$**	**Toluene Postgel**	**Toluene Pregel**
η_{P3HT}	58%	57%	58%	55%
SLD_{part} ($Å^{-2}$)	2.52×10^{-6}	2.57×10^{-6}	2.67×10^{-6}	2.74×10^{-6}
α	-0.016	0.066	-0.066	-0.002
β	1.32×10^{-12}	8.54×10^{-8}	3.20×10^{-8}	2.70×10^{-9}
R_c (nm)	54.2	51.4	49.4	61.5

These results verify that it is possible to form a variety of structures based on the method of nanoparticle preparation. This is not surprising considering the complex behavior shown in P3HT/PCBM thin-film composites.[27–29] Changing the method or the relative composition of

materials affects not only photovoltaic performance, but also fullerene aggregation from the disordered regions of the P3HT matrix. The specific internal structure directly influences the amount of interface that is available for exciton dissociation and also the percolation of these phases for effective charge transport. Efficient bulk heterojunction structures balance the total available interface for exciton dissociation with the formation of efficient charge transport pathways to the external electrodes. Considering the extension of this insight to a polymer/fullerene SNPs, it is likely desirable for domains within the nanoparticle to be uniformly distributed and interconnected. The "pregel" sample is the only dispersion that appears to have a uniform distribution of P3HT and PCBM throughout the nanoparticle's volume. Understanding how particle formulation determines the internal structure is therefore critically important to make SNPs that are likely to yield efficient active layers and devices. To investigate this point further, dispersions of P3HT/PCBM were prepared from chloroform with a fixed size but with varying P3HT/PCBM ratio. The scattering profiles and the Stuhrmann plot for each particle are shown in Figure 6.9.

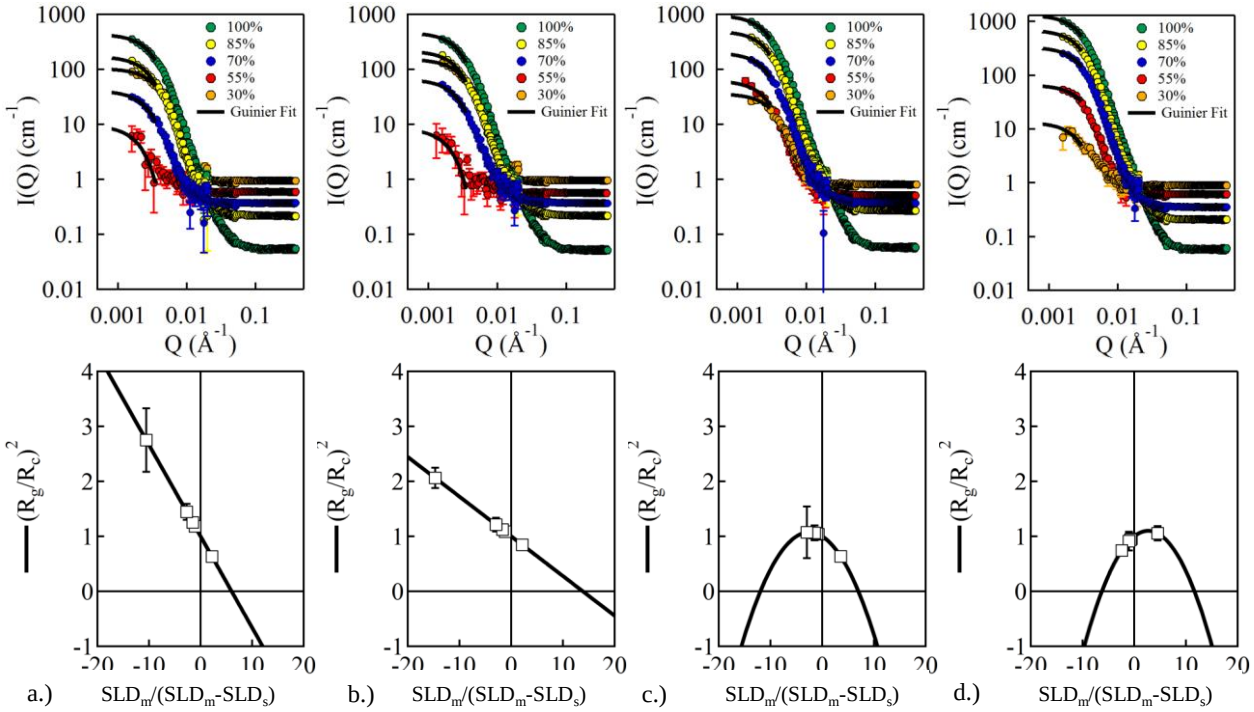

Figure 6.9. Upper: Scattering profiles with corresponding Guinier fits (solid lines) for composite P3HT/PCBM particles created from chloroform as a function of composition a.) 30/70 P3HT/PCBM, b.) 40/60 P3HT/PCBM, c.) 60/40 P3HT/PCBM, and d.) 70/30 P3HT/PCBM. Lower: Stuhrmann plot corresponding to each particle.

As the P3HT content of the particle increases, the value of α increases eventually switching from negative to positive. This implies that the particles tend toward increasing uniformity as P3HT content is increased. It is also surprising that even in P3HT deficient particles, P3HT is enriched in the shell. During the removal of solvent from the emulsion droplet, the largest concentration gradients occur near the shell. P3HT and PCBM have comparable solubility in chloroform so it is expected that for PCBM rich particles, PCBM would be the first species to supersaturate. Therefore, either P3HT has faster nucleation and growth kinetics than PCBM or PCBM is preferentially segregated to the core of the particle. For P3HT rich particles, α is small and β is large, suggesting that these particles are eccentric. Based on this degree of eccentricity, the center of mass of the particle is displaced from its center of scattering length density by ~10% of its radius. The presence of varying amounts of surfactant at the SNP/water interface can account

for the slight variations in SLD_{part} from the expected values as a function of composition. Generally, however, the particles show a decrease in SLD_{part} with increasing P3HT content, an expected effect of changing the composition of the SNP.

Table 6.2. Simultaneous fitting results from Stuhrmann analysis for P3HT/PCBM SNPs as a function of composition.

	30/70	**40/60**	**50/50**	**60/40**	**70/30**
η_{P3HT}	36%	46%	58%	66%	76%
SLD_{part} ($Å^{-2}$)	3.30×10^{-6}	3.39×10^{-6}	2.52×10^{-6}	2.68×10^{-6}	2.27×10^{-6}
α	-0.15	-0.08	-0.02	-0.05	0.05
β	0.00	0.00	1.32×10^{-12}	2.80×10^{-8}	2.30×10^{-8}
R_c (nm)	52.8	57.0	54.2	57.1	57.0

Based on the results presented, it is possible to hypothesize a mechanism for how the specific morphology of SNPs results from any given preparation method. As organic solvent is removed during the evaporation phase of the particle preparation process, soluble components are enriched in the emulsion droplet. Once supersaturated, nucleation and growth of P3HT and/or PCBM rich phases can occur. In an emulsion droplet, nucleation could either be dominated by heterogeneous nucleation at the oil/water interface or by homogenous nucleation in the bulk phase of the emulsion droplet as depicted in Figure 6.10. If nucleation occurs primarily through a heterogeneous mechanism at the oil/water interface, a shell forms that would, upon full removal of solvent, result in a core-shell particle.[19]

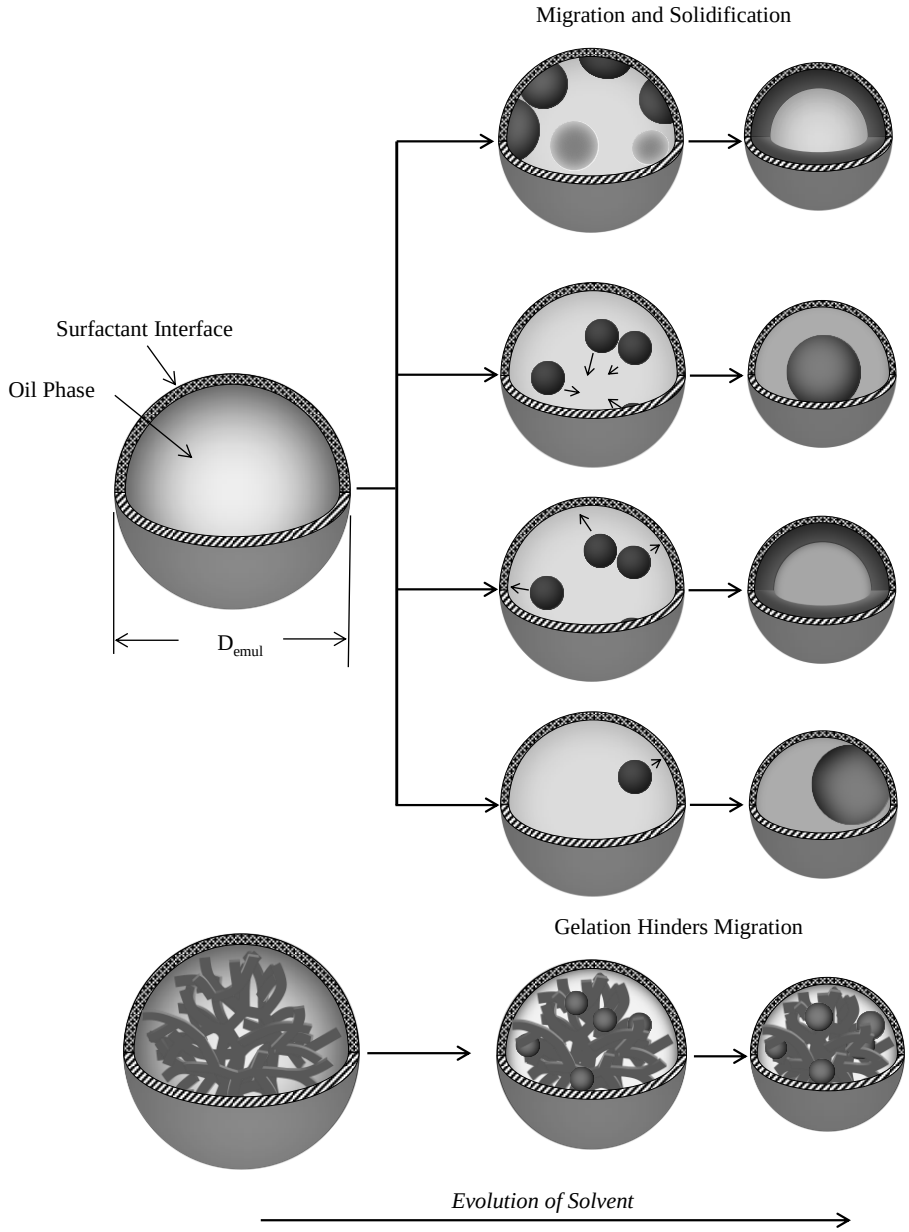

Figure 6.10. Schematic diagram of the segregation of components internal to an emulsion droplet during the removal of oil. The dark colorized regions are the PCBM-rich phases and the lighter colors are P3HT rich phases.

If homogeneous nucleation is dominant, then the relative migration of polymer and fullerene phases within the droplet will determine the ultimate distribution of internal components. The migration of these phases will be determined by the preference of the solvent for the oil/water interface. The removal of solvent from the emulsion phase occurs at the oil/water interface where it can dissolve into bulk water, be incorporated into the hydrophobic core of micelles in solution,

and be brought to the surface of the emulsion and evaporate. The structure of the SNP is therefore determined in part by the rate of diffusion of P3HT and PCBM domains to the core or the shell (depending on affinity) of the emulsion. Since fast solvent removal from emulsion droplets can effectively arrest these processes, it is unlikely that truly equilibrated structures are forming at all times. This is particularly true for dispersions prepared from chloroform solutions where the typical time for complete removal of solvent is just a few minutes. Arrested particle migration caused by rapid solvent removal can account for the formation of eccentric particles. The value of using the P3HT organogel is that gelation of the solution prior to emulsification hinders migration of the internal components during the removal of solvent. Because the P3HT organogel spans the entire volume of the emulsion droplet, the resulting internal components remain uniformly distributed in the resulting SNP.

Without the use of Stuhrmann analysis to describe the SANS data from these particles, it would have been difficult to gain information about their internal structure. This can be understood when we examine the DLS and SEM data for each of the particles in this study shown in Figure 6.11. From the DLS data, it is clear that while it is possible to control the average diameter of the particles, there is in some cases a large distribution of particle size. Also, in some cases, the particles deviate from spherical structures and take on ellipsoidal shapes. Therefore, any analytical form factor model would need to have multiple dimensions of polydispersity just to describe the homogenous component of the scattering profile. Then the internal structure of the particle would have to be parameterized as a function of the homogenous shape function. Clearly the number of parameters that this would require would make extracting quantitative information from such a model very uncertain. Stuhrmann analysis ignores these details and provided a direct

probe of the inhomogeneous component, which is the component of the scattering profile that is most desirable from the perspective of design of these particles.

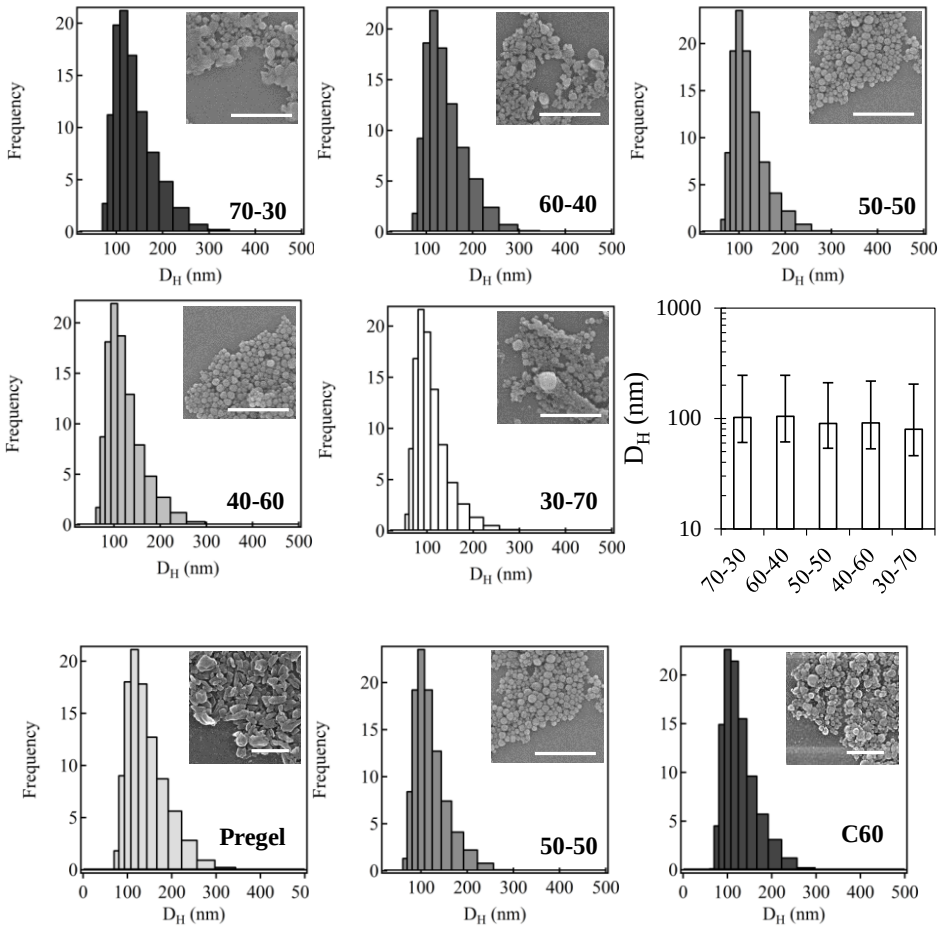

Figure 6.11. DLS and SEM data for all the P3HT/PCBM SNPs used in this study. From these results it is clear that the particles are polydisperse in both size and shape, making Stuhrmann analysis necessary.

6.6: Extension of this analysis to other SNP systems

The information that can be extracted from the approach outline in chapter 6.6 is not limited to only to parameters α, β and R_c. In fact, as long as the SLD_{solv} is known at every contrast measured, then it is possible to extract more quantitative measurements including the radial distribution of material within the particles, the total interfacial area of heterogeneities within the particles, and the average contrast of the materials (and therefore their densities). To test this

theory, we prepared identical particle dispersions using the latex approach with chlorobenzene as a solvent. This time instead of sonication, the emulsions were passed through an extruder with 100 nm pore size. Emulsions prepared in this way will have average diameters of ~150 nm. This means that for typical particle loadings (10 mg/mL polymer and 18 mg/mL fullerene) the resulting CNP particle diameter should be ~36 nm. Therefore, we prepared identical emulsions containing a variety of polymers and fullerene species as well as solids content to expand our understanding of phase segregation and its relationship to the polymer and fullerene characteristics. The results of the Stuhrmann analysis for this data are shown in Table 6.3.

Table 6.3. Stuhrmann Analysis for CNPs produced by emulsifying using 100 nm Extruder.

Poly	Fullerene	SLD_{part} ($Å^{-2}$)	ϕ_{solid}	R_{pred} (Å)	R_{part} (Å)	α	β
RR-P3HT	$PC_{61}BM$	2.93E-06	3.02%	22.6	22.1	0.050	3.0E-09
RR-P3HT	$PC_{71}BM$	2.85E-06	1.42%	17.6	15.2	-0.001	3.63E-09
PCDTBT	$PC_{71}BM$	3.15E-06	1.48%	17.8	18.5	-0.004	8.80E-10
Rrand-P3HT	$PC_{71}BM$	2.99E-06	1.33%	17.2	17.4	0.001	0.0
PBTTT	$PC_{71}BM$	2.85-06	1.42%	17.6	17.8	-0.002	8.80E-10
PIDT-PhanQ	$PC_{71}BM$	3.41E-06	1.36%	17.3	17.0	-0.002	0.0

Based on these results, it is possible to determine the scattering length density of all of the pure components within the particles and these are summarized in Section 6.7 in Table 6.4. Further we can see that the particles made with chlorobenzene generally have very small magnitude of α suggesting a uniform radial distribution of material. However, the relatively large β values for RR-P3HT, PCDTBT, and PBTTT suggest that these particles segregate to form eccentric particles. An additional interesting observation is the change in sign of α for identical particles containing $PC_{71}BM$ and $PC_{61}BM$. This is a clear indicator that the general tendency for P3HT/$PC_{61}BM$ particles to form P3HT shell particles is not universal for all polymer/fullerene nanoparticles. It is also possible to determine the average thickness of the d-SDS shell that

contributes to the scattering profile, which is $L_{d\text{-}SDS}$ = 3 Å. This value is derived from the known adsorption properties of SDS onto the polymer/water interface and confirmed by the contribution of this adsorbed layer to the average scattering length density of the particles, and is consistent with a low-density surface coverage of surfactant.[30] With this information, further analysis is possible using the basic functions defined in Equation 6.1 in order to obtain length scale of fullerene aggregates within the nanoparticle and the relative amount of polymer/fullerene interface.

6.7 Materials and Methods

The poly(3-hexylthiophene) (P3HT) was Sepiolid P100 grade purchased from Rieke Metals (Lincoln, NE). The [6,6] phenyl-C60-butyric acid methyl ester (PCBM) was purchased from SES Research (Houston, TX). The deuterated sodium dodecyl sulfate (d-SDS) was used as received from CDN isotopes (Quebec, Canada). P3HT/PCBM particle dispersions were produced by dissolving known amounts of P3HT and PCBM into chloroform. The organic solution was then emulsified in a 40 mM d-SDS aqueous solution using a Branson Sonifier 450 at 70% intensity for 15, one second pulses with 1 second delay between each pulse. The resulting emulsion was then placed in a 10 mL round bottom flask and stirred under vacuum at room temperature to remove the chloroform from the emulsion. This process resulted in stable composite nanoparticles containing the desired ratio of P3HT/PCBM. The dispersions described here had a 1:1 P3HT/PCBM mass ratio corresponding to 57 vol % P3HT. The average particle size of the composite nanoparticles can be changed by modifying the total solids content of the solution. Here, we created dispersions using 40 mg/mL total solids resulting in composite nanoparticles with an average hydrodynamic radius of 65 nm measured using dynamic light scattering (Malvern ZetaSizer). The final concentration of solids in the solution was corroborated

using thermo gravimetric analysis (TGA). The P3HT/PCBM ratio was also verified by re-dissolving a dried dispersion into a good solvent, obtaining the absorption spectra from these solutions, and using the known extinction coefficients to determine the total content of each component. All solutions have the same total P3HT/PCBM solids content (ϕ = 0.25%) and a uniform d-SDS concentration. After dialysis of the excess d-SDS (needed for efficient emulsification) to a solution of 5 mM d-SDS, the five different contrasts were prepared by diluting the stock dispersion into solutions of varying H_2O/D_2O content to make identical samples dispersed in solvent with varying contrast. The neutron scattering experiments were carried out on the NG3 beam line at NCNR in Gaithersburg, Maryland. The samples were measured at a sample-to-detector distance of 13 m using lenses and λ = 8.5 Å, and λ = 6 Å at 6 meters and 1 meter.[31] The counting times at each position were dependent on the contrast of the solvent to the particles, and were varied to achieve adequate statistics. Sample transmission was measured at the largest sample-to-detector distance for each wavelength and beam flux measurements were used to convert the scattering profiles to absolute scale [cm^{-1}]. The simulated composite nanoparticles in this paper have *R*=50 nm and explicitly include a 1.5 nm layer of d-SDS with pure domains of P3HT and PCBM. Several different structures, which are all possibilities in the experimental system, are modeled to have 1:1 P3HT/PCBM mass ratio.

Table 6.4. Scattering Length Densities and Densities of Pure Components determined using Contrast Variation Small Angle Neutron Measurements

Abbreviation	**Composition**	**ρ (g/cm^3)**	**SLD ($Å^{-2}$)**
RR-P3HT	$C_{10}H_{25}S$	1.12	6.9E-07
PCDTBT	$C_{44}H_{48}N_8S_3$	0.94	1.4E-06
Rrand-P3HT	$C_{10}H_{25}S$	1.23	7.6E-07
PBTTT	$C_{42}H_{62}S_4$	1.22	6.2E-07
PIDT-PhanQ	$C_{84}H_{82}S_2N_2$	1.11	1.6E-06

$PC_{71}BM$	$C_{82}H_{14}O_2$	1.78	5.3E-06
$PC_{61}BM$	$C_{72}H_{14}O_2$	1.51	4.4E-06
d-SDS	$C_{12}D_{25}O_4S$	1.09	6.1E-06

References:

1. Feigin, L. A.; Svergun, D. I. Structure Analysis by Small-Angle X-Ray and Neutron Scattering. *Acta Polym.* **1989**, *40*, 224.

2. Marshall, J. C.; Cosgrove, T.; Leermakers, F.; Obey, T. M.; Dreiss, C. a Detailed Modeling of the Volume Fraction Profile of Adsorbed Polymer Layers Using Small-Angle Neutron Scattering. *Langmuir* **2004**, *20*, 4480–8.

3. Pedersen, J. S. Analysis of Small-Angle Scattering Data from Colloids and Polymer Solutions: Modeling and Least-Squares Fitting. *Adv. Colloid Interface Sci.* **1997**, *70*, 171–210.

4. Larson-Smith, K.; Jackson, A.; Pozzo, D. C. Small Angle Scattering Model for Pickering Emulsions and Raspberry Particles. *J. Colloid Interface Sci.* **2010**, *343*, 36–41.

5. Pedersen, J. S. Structure Factors Effects in Small-Angle Scattering from Block Copolymer Micelles and Star Polymers. *J. Chem. Phys.* **2001**, *114*, 2839.

6. Guinier, A.; Fournet, G. *Small Angle Scattering of X-Rays*; Wiley, New York, 1955; p. 7.50.

7. Kaya, H. Scattering Behaviour of Janus Particles. *Appl. Phys. A.* **2002**, *74*, 507–509.

8. Futterer, T.; Vliegenthart, G. A.; Lang, P. R. Particle Scattering Factor of Janus Micelles. *Macromolecules* **2004**, *37*, 8407–8413.

9. Stuhrmann, H. B.; Koch, M. H.; Parfait, R.; Haas, J.; Ibel, K.; Crichton, R. R. Shape of the 50S Subunit of Escherichia Coli Ribosomes. *Proc. Natl. Acad. Sci. U. S. A.* **1977**, *74*, 2316–20.

10. Stuhrmann, H. B.; Miller, a. Small-Angle Scattering of Biological Structures. *J. Appl. Crystallogr.* **1978**, *11*, 325–345.

11. Lindner, P, Zemb, T. *Neutrons, X-Rays and Light: Scattering Methods Applied to Soft Condensed Matter*; North-Holland, 2002.

12. Glatter, O.; Kratky, O. *Small Angle X-Ray Scattering*; Academic Press Inc., 1982.

13. Kline, S. R. Reduction and Analysis of SANS and USANS Data Using IGOR Pro. *J. Appl. Crystallogr.* **2006**, *39*, 895–900.

14. SasView SasView, http://www.sasview.org/.

15. Tjioe, E.; Heller, W. T. ORNL_SAS : Software for Calculation of Small-Angle Scattering Intensities of Proteins and Protein Complexes. *J. Appl. Crystallogr.* **2007**, *40*, 782–785.

16. Piok, T.; Gadermaier, C.; Wenzl, F. P.; Patil, S.; Montenegro, R.; Landfester, K.; Lanzani, G.; Cerullo, G.; Scherf, U.; List, E. J. W. The Photophysics of Organic Semiconducting Nanospheres: a Comprehensive Study. *Chem. Phys. Lett.* **2004**, *389*, 7–13.

17. Landfester, B. K.; Montenegro, R.; Scherf, U.; Güntner, R.; Asawapirom, U.; Patil, S.; Neher, D.; Kietzke, T. Semiconducting Polymer Nanospheres in Aqueous Dispersion Prepared by a Miniemulsion Process. *Adv. Mater.* **2002**, *14*, 651–655.

18. Andersen, T. R.; Larsen-Olsen, T. T.; Andreasen, B.; Böttiger, A. P. L.; Carlé, J. E.; Helgesen, M.; Bundgaard, E.; Norrman, K.; Andreasen, J. W.; Jørgensen, M.; *et al.* Aqueous Processing of Low-Band-Gap Polymer Solar Cells Using Roll-to-Roll Methods. *ACS Nano* **2011**, *5*, 4188–96.

19. Loxley, A.; Vincent, B. Preparation of Poly(methylemethacrylate) Microcapsules with Liquid Cores. *J. Colloid Interface Sci.* **1998**, *208*, 49–62.

20. Kietzke, T.; Neher, D.; Kumke, M.; Ghazy, O.; Ziener, U.; Landfester, K. Phase Separation of Binary Blends in Polymer Nanoparticles. *Small* **2007**, *3*, 1041–8.

21. Troshin, P. a.; Hoppe, H.; Renz, J.; Egginger, M.; Mayorova, J. Y.; Goryachev, A. E.; Peregudov, A. S.; Lyubovskaya, R. N.; Gobsch, G.; Sariciftci, N. S.; *et al.* Material Solubility-Photovoltaic Performance Relationship in the Design of Novel Fullerene Derivatives for Bulk Heterojunction Solar Cells. *Adv. Funct. Mater.* **2009**, *19*, 779–788.

22. Richards, J. J.; Weigandt, K. M.; Pozzo, D. C. Aqueous Dispersions of Colloidal Poly(3-Hexylthiophene) Gel Particles with High Internal Porosity. *J. Colloid Interface Sci.* **2011**, *364*, 341–50.

23. Ulum, S.; Holmes, N.; Darwis, D.; Burke, K.; David Kilcoyne, A. L.; Zhou, X.; Belcher, W.; Dastoor, P. Determining the Structural Motif of P3HT:PCBM Nanoparticulate Organic Photovoltaic Devices. *Sol. ENERGY Mater. Sol. CELLS* **2013**, *110*, 43–48.

24. Henderson, S. J. Monte Carlo Modeling of Small-Angle Scattering Data from Non-Interacting Homogeneous and Heterogeneous Particles in Solution. *Biophys. J.* **1996**, *70*, 1618–27.

25. Ulum, S.; Holmes, N.; Darwis, D.; Burke, K.; David Kilcoyne, a. L.; Zhou, X.; Belcher, W.; Dastoor, P. Determining the Structural Motif of P3HT:PCBM Nanoparticulate Organic Photovoltaic Devices. *Sol. Energy Mater. Sol. Cells* **2013**, *110*, 43–48.

26. Richards, J. J.; Rice, A. H.; Nelson, R. D.; Kim, F. S.; Jenekhe, S. a.; Luscombe, C. K.; Pozzo, D. C. Modification of PCBM Crystallization via Incorporation of C 60 in Polymer/Fullerene Solar Cells. *Adv. Funct. Mater.* **2013**, *23*, 514–522.

27. Dang, M. T.; Hirsch, L.; Wantz, G. P3HT:PCBM, Best Seller in Polymer Photovoltaic Research. *Adv. Mater.* **2011**, *23*, 3597–3602.

28. Zhao, J.; Swinnen, A.; Assche, G. Van; Manca, J.; Vanderzande, D.; Mele, B. Van Phase Diagram of P3HT/PCBM Blends and Its Implication for the Stability of Morphology. *J. Phys. Chem. B* **2009**, *113*, 1587–91.

29. Müller, C.; Ferenczi, T. a. M.; Campoy-Quiles, M.; Frost, J. M.; Bradley, D. D. C.; Smith, P.; Stingelin-Stutzmann, N.; Nelson, J. Binary Organic Photovoltaic Blends: A Simple Rationale for Optimum Compositions. *Adv. Mater.* **2008**, *20*, 3510–3515.

30. Stuhrmann, H. B. Neutron Small-Angle Scattering of Biological Macromolecules in Solution. *J. App* **1974**, *7*, 173–178.

31. Glinka, C. J.; Barker, J. G.; Hammouda, B.; Krueger, S. The 30 m Small-Angle Neutron Scattering Instruments at the National Institute of Standards and Technology. *J. Appl. Crystallogr.* **1998**, *31*, 430–445.

Chapter 7. Photoconductive AFM Measurements of CNPs

Based on the characterization of CNPs using contrast variation neutron scattering in Chapter 6, there are three characteristic structures that can be present, the core-shell particle, eccentric particles, and particles with relatively uniform distribution. It is expected that there will significant differences in their photovoltaic performance based on their structural features.[1–6] This is due to the fact that the internal structure will determine the efficiency of exciton dissociation as well as charge transport.[3] As shown in Figure 7.1, we expect that the best performing CNPs will be those that have uniform distributions of P3HT and PCBM domains within their internal volume. This ensures that both holes and electrons have equal transport efficiencies out of the particle's interior as well as sufficient interface for exciton dissociation.[7] In core-shell particles, there is sufficient interface so that many excitons may be readily dissociated. However, due to the enrichment of one component over the other in the shell, charge transport out of the particle will be hindered.[8,9] In the case of an eccentric particle, there is likely a lower amount of interface available for exciton dissociation, and the ability of charges to reach electrodes will depend on the specific orientation of the particles relative to the electron and hole transport layers that are present in typical device geometries. Therefore, misalignment of the electron or hole conducting domains with electron and hole buffer layers will lead to inefficient carrier extraction. A uniform distribution of material in the particle volume ensures that there is both sufficient interface for excitons dissociate and a clear pathway for transport of charges out of the interior domains of a CNP.[10]

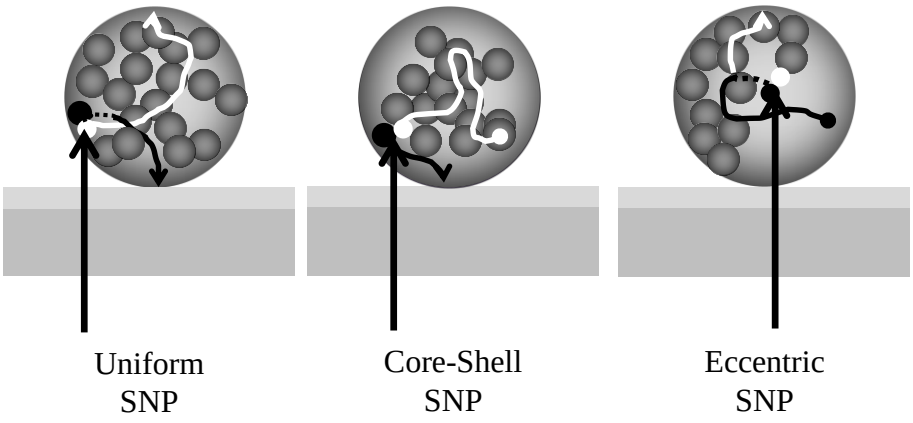

Figure 7.1. Schematic of exciton diffusion, dissociation, and transport through the domains of a CNP as a function of internal morphology.

In order to validate this hypothesis, it is necessary to evaluate the intrinsic charge generation properties of different particle formulations while eliminating the possible convolution of these results from processes that are extrinsic to the particles (e.g. particle-particle charge transport in multilayers).

7.1 Monolayer Generation of CNPs using Electrostatic Assembly.

To do this, it is first necessary to generate a uniform monolayer of particles so that factors like interparticle transport and non-uniform illumination of individual particles do not influence the measurement. In order to create monolayers, we developed a novel electrostatic deposition technique. Using electrostatic deposition, it is possible induce spontaneous assembly of CNPs onto a negatively charged PEDOT:PSS film as shown in Figure 7.2a.[11] The methodology is relatively simple. The surface charge of the surface that is to be coated is determined as a function of pH via streaming potential measurements (Figure 7.2b). Based on these measurements, PEDOT:PSS always has a strong negative charge regardless of the pH. For negative surfaces (e.g. PEDOT:PSS) and positive particles (DTAB stabilized dispersions), the pH and the bulk concentration of DTAB are tuned such that both particles and surface have large

opposite surface charges and also such that there is as little ‘free’ surfactant as possible while maintaining colloidal stability. In this case, a pH=7 was chosen. The reduction of ‘free’ DTAB minimizes the competitive adsorption of surfactant on the PEDOT:PSS film and ensures the formation of particle monolayers over the PEDOT:PSS surface. The optimum concentration of surfactant was found by measuring the Zeta Potential of the particles as a function of DTAB concentration (Figure 7.6c). At a concentration of around 2 mM DTAB the Zeta potential of the CNPs began to decrease suggesting desorption of surfactant from the CNP/water interface. This is the point where the chemical potential of adsorption of DTAB to the CNP surface matches that of the bulk solubility of DTAB. Reducing the bulk DTAB concentration too much reduces the particle charge and, eventually, will also lead to particle aggregation and flocculation. Nevertheless, we find that the best coating conditions are found when the surfactant concentration is less than 2 mM and the Zeta Potential is still greater than 30 mV. At this point, the dispersion is still colloidally stable and positively charged, but there is very little ‘free’ DTAB to compete for the surface. ITO films coated with PEDOT:PSS are shown to readily form dense monolayers of CNPs after just 30 minutes of exposure to dispersions containing 0.1 vol% CNPs and 0.5 mM DTAB.

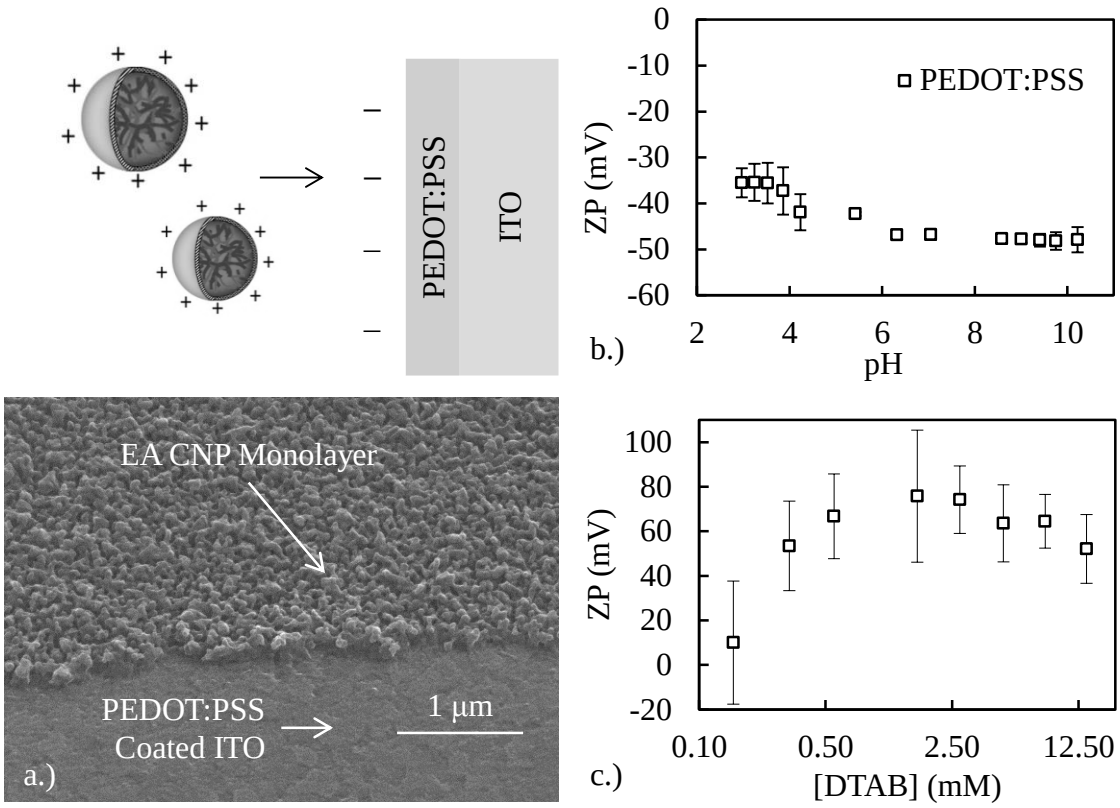

Figure 7.2 a.) Schematic showing the electrostatic deposition procedure and SEM of dense CNP monolayer film deposited in PEDOT:PSS coated ITO, b.) Streaming potential measurement of ITO substrate and PEDOT:PSS coated ITO substrate as a function of pH, and c.) Zeta Potential of 60 nm CNP dispersion as a function of DTAB concentration.

This methodology has been extended to many other surfaces and surfactant types. The details of these experiments are outlined in great detail and theory underlying the assembly of CNPs onto charged surfaces elucidated in Chapter 8.

7.2. Photoconductive AFM Measurements of CNPs

Characterization of photoconductivity of bulk heterojunction active layers with a conductive probe atomic force microscopy (AFM) has recently been realized as a powerful technique to relate surface topology to solar cell performance metrics.[12,13] In the current manifestation of the technique, a bulk-heterojunction active layer is deposited onto a transparent conductor and

mounted into an AFM. The film is electrically connected to a gold coated AFM tip with a very sharp point (R_{tip}~10nm*)*. Simultaneously, the film is illuminated from below with a light source that is focused to a very tight point (D_{light} ~ 100 μm). In either contact or tapping mode, the tip is then scanned over the surface of the film that is illuminated by the light source and the current and voltage are controlled and measured independently with an external source meter as a function of the tip position. In this way, simultaneously with traditional force measurements like topography and phase behavior, electrical parameters such as short circuit current density, dark current, and photocurrent under variable voltage bias can be measured. In addition, new implementations of this technique extract dynamical information using a pulsed light source and studying the kinetics of relaxation of the photovoltage response. This measurement is called time-resolved AFM (trAFM).

In order to characterize the intrinsic charge generation properties of individual nanoparticles with different formulations and morphologies, we employed photoconductive AFM (pcAFM). These measurements were performed on electrostatically deposited monolayers of pregel, eccentric, and core-shell CNPs with identical P3HT/fullerene ratio. Using pcAFM, we showed that it is possible to individually measure the photocurrent nanoparticles in isolation from each other. In this way, it is possible to isolate the intrinsic carrier generation and transport properties within each nanoparticle without any influence from extrinsic device properties and other nanoparticles. While these measurements cannot necessarily be used at this time to quantitative predict the performance of workign photovoltaic devices processed from our model CNPs, they provide a direct probe of the performance of each nanoparticle which we can then relate to their known internal structure. In the pcAFM measurement, gold tip is used along with monochromatic light (λ=532 nm).

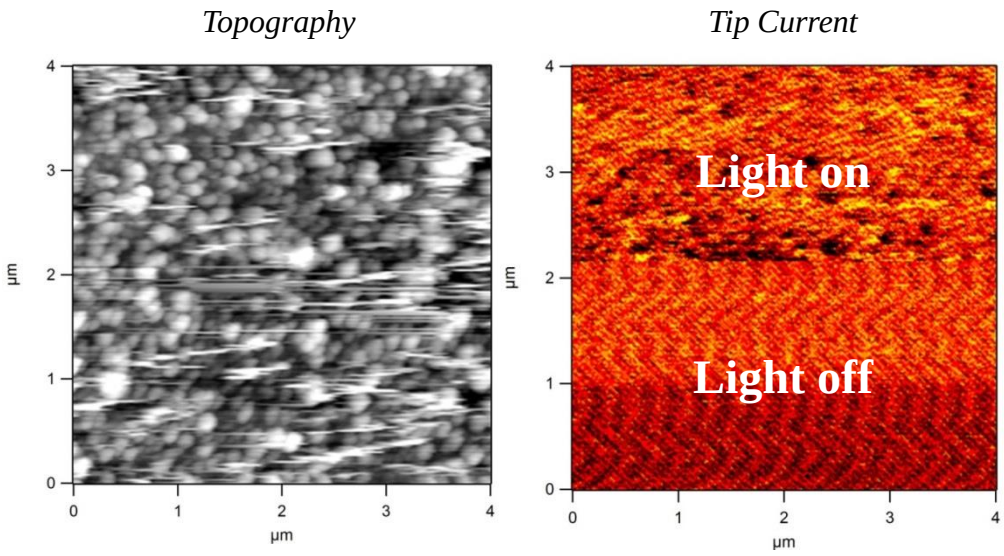

Figure 7.3. (left) Topography scan of electrostatically absorbed particle monolayers, and (right) photocurrent measured with the light off and then switched on.

The AFM is then rastered over the surface of illuminated particles under zero tip bias. The tip voltage is maintained at zero as it raster scans over the sample surface in Figure 7.3. In the image scan in Figure 7.3, the film is comprised of a relatively dense assembly of pregel particles deposited uniformly over the entire film surface. For the first half of the scan (from 0-2 µm) in the y-direction, the sample remains in the dark. It is clear that with the light off, nothing but noise is measured. This implies both that the particles do not generate measureable photocurrent under zero bias, and there are no anomalous instrument responses which generate current during scanning. At 2.2 µm, the diode is turned on and the sample illuminated. Immediately, bright and dark spots appear in the photocurrent scan that are distinct from the noise measurement before the light is turned on. This confirms that the current measured is intrinsic to the particles deposited on the surface. To further verify the fact that this current measurement was not substrate related, a measurement under bias is shown for a region of film that has a much lower surface coverage (Figure 7.4)

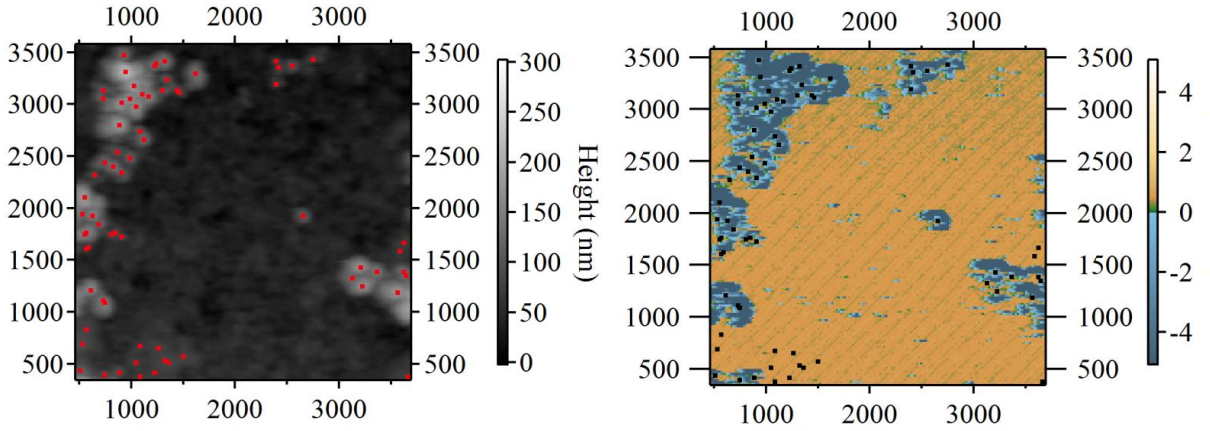

Figure 7.4. (left) Topography scan, (right) Current from tip-Surface Bias = 1V under illumination of sparsely coating CNPs.

From the current scan in Figure 7.4, it is clear that the current is strongly correlated with the positions of the particles and the PEDOT:PSS coated ITO film can be distinguished from particles. Figures 7.3 and 7.4 demonstrate the efficacy of this technique as a probe for individual nanoparticle performance.

Therefore, pcAFM experiments measure the performance of many isolated nanoparticles that act as individual nano-sized solar cells as shown in Figure 7.5. At the same time that photocurrent information is obtained, pcAFM also acquires a topological image that provides a means to correlate the particle position and size to the photocurrent. For the images acquired, the resolution is 15 nm/pixel so that differences in nanoscale photocurrent generation can be differentiated.

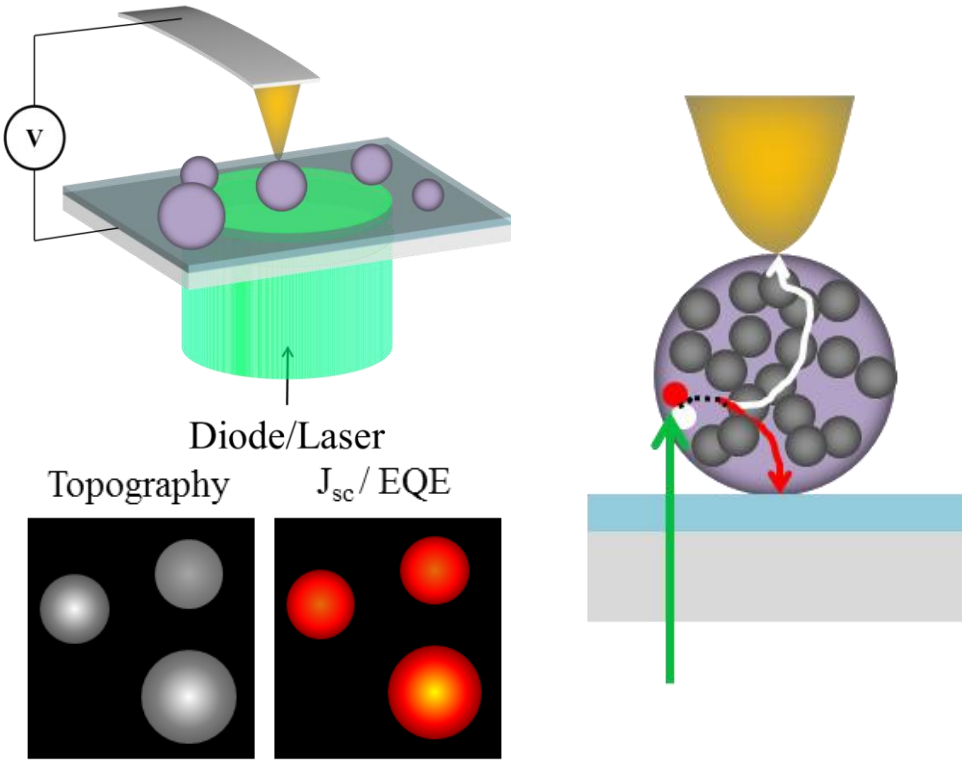

Figure 7.5. Schematic of pcAFM measurements on CNPs electrostatically deposited onto PEDOT:PSS/ITO substrates.

Photocurrent images were taken for each nanoparticle formulation and representative histograms are shown in Figure 7.6. Based on these results, it is clear that the pregel particle has the best single-particle performance when compared to the core-shell or eccentric particles. This is indicated by the significantly larger hole (up to 4 pA) and electron currents (~1 pA) that are consistently observed for films produced from these particles. The core-shell particle showed moderate hole-current with maximum values ~ 1 pA, but almost no electron current, whereas the eccentric particle showed larger hole currents (up to 2 pA) than the core-shell particle, but also higher electron currents (< 1 pA). These results support the proposed structural models for these particles. The core-shell particle has a P3HT rich shell, and therefore, it is more difficult for photogenerated electrons to be transported out of the particle leading to higher rates internal

recombination and subsequently lower measured photocurrents. The eccentric particle showed moderate hole and electron currents, which is consistent with orientation dependence of electron and hole current generation. Finally, the pregel particles that were prepared using the organogel porous framework showed the best performance because of the uniform distribution of both semiconductor materials within the CNP. This ensures that there is a large amount of p/n junction interface for exciton dissociation and that the rate of hole and electron transport out of the CNP is also effective because there is no preferential enrichment of one material over the other at the particle's surface.

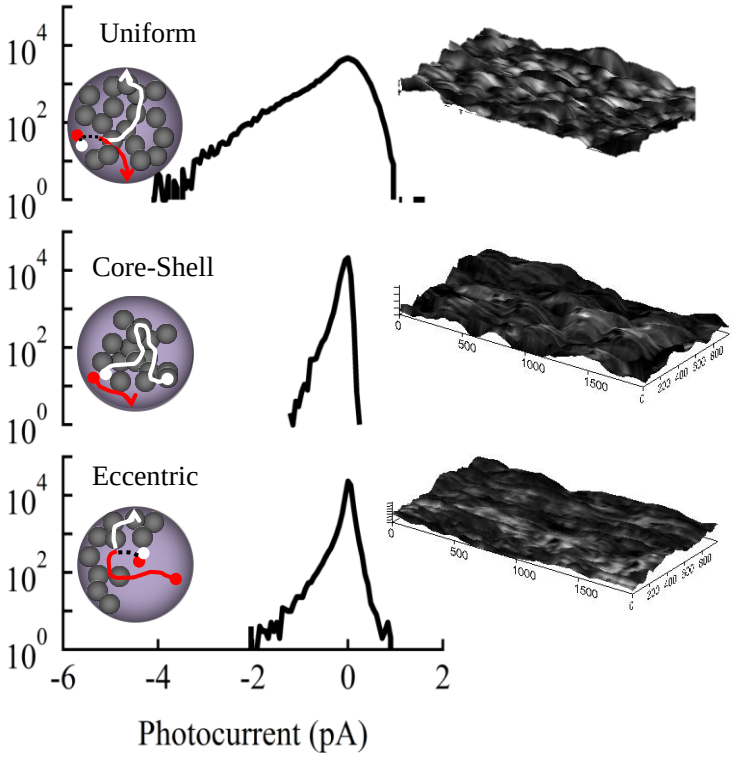

Figure 7.6. Histograms of photocurrent produced from monolayer films of uniform, core-shell, and eccentric particles. The particles all have the same overall composition and correspond to the toluene pregel, P3HT/PCBM from chloroform, and P3HT/PCBM/C_{60} from chloroform respectively. Representative Topological Scans are shown in the inset colorized by the photocurrent maps.

7.3 Analysis of pcAFM Measurements

Further analysis of the photocurrent topology maps is possible. From the topography scans in it is possible to identify the position and diameter of each sphere using a simple algorithm that calculates the local slope at each pixel. If the slope is negative leading away from the pixel in all directions, then it is considered to be a local maximum. The height and pixel position are then stored and the data set filtered for overlapping pixels and topography defects. An example of this process is shown in Figure 7.7a and Figure 7.7b.

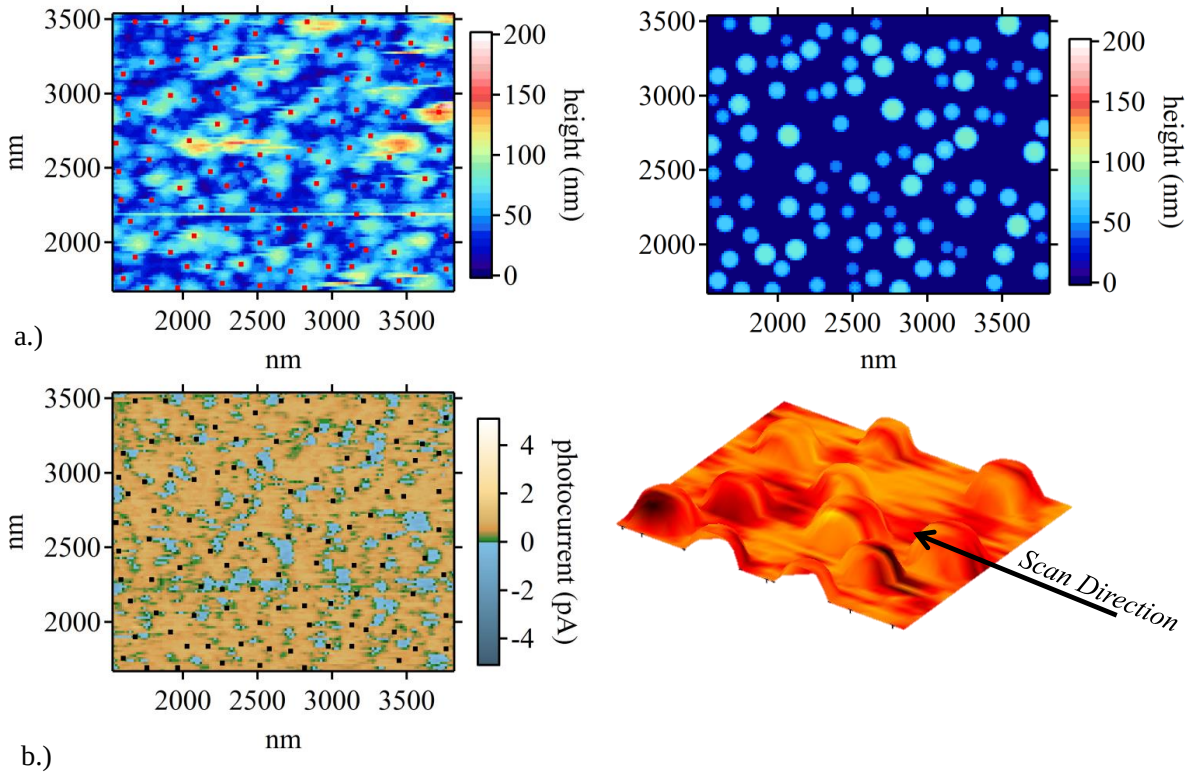

Figure 7.7. a.) Cropped topology (left) and analyzed topology (right) of electrostatically assembled pregel film, and b.) The measured photocurrent scan from the topography in a.) (left) and 3-D topology colorized by the photocurrent (right).

The dots plotted on both the topography and the photocurrent scans are the position of spheres accepted by the algorithm. As is visible from the photocurrent scans, the positions of the particles correspond well with peaks in measured photocurrent. However, almost in all cases the

center of the spheres identified in the topography scan do not correspond to the center of measured photocurrent. This more clearly illustrated in Figure 7.7b where the 3-D simulated topography is plotted and colorized by the measured photocurrent for a small section of the image. This effect can be understood when the scan direction is taken into account. At the point that the tip encounters a particle as it scans over the surface of the film, it comes into contact and immediately the photocurrent generated within the particle is measured. This fast change in topography causes deflection of the AFM tip for which the controller immediately compensates. As the scan head reaches the maximum of the particle, it is likely that the tip cannot maintain electrical contact with the particle due to the rapidly changing topography. Therefore, there is a clear maximum in photocurrent measured on the leading edge of the particles.

With this algorithm, it is possible to do a more detailed analysis of the photocurrent and topology data measured for the particles. As is visible in the topography scans, these particles have a rather large polydispersity, so there are a large number of particles with different sizes on the surface. This allows us to analyze the photocurrent generated from identically made particles as a function of their size. The results of this analysis are shown in Figure 7.8.

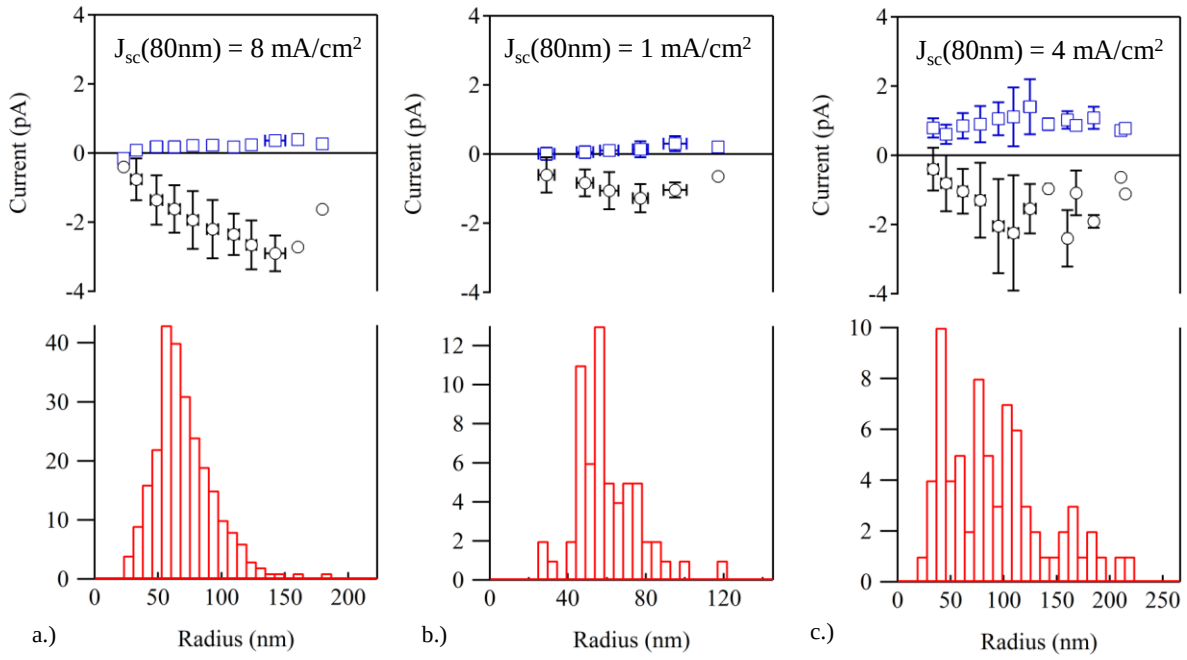

Figure 7.8. Further analysis of photocurrent and topography maps taken with pcAFM for a.) Uniform Particles, b.) Core-Shell Particles, c.) Janus Particles.

Also in Figure 7.8 are estimates for the short circuit current density estimated by taking the photocurrent values measured here and normalizing to the cross-sectional area of the particles. For the best performing particles, the total photocurrent generated is ~8 mA/cm^2, on the same order of magnitude as efficient bulk heterojunction thin film active layers composed of P3HT and PCBM.[14]

7.4 Materials and Methods

General Preparation of Nanoparticle Dispersions: The poly(3-hexylthiophene) (P3HT) was Sepiolid P100 grade purchased from Rieke Metals (Lincoln, NE). The [6,6] phenyl-C60-butyric acid methyl ester (PCBM) was purchased from SES Research (Houston, TX). The deuterated sodium dodecyl sulfate (d-SDS) was used as received from CDN isotopes (Quebec, Canada). P3HT/PCBM particle dispersions were produced by dissolving known amounts of P3HT and PCBM into organic solvent. For P3HT/PCBM nanoparticles produced from chloroform and

toluene, the volume fraction of total solids was held constant at 3.1%. This organic phase was added to 40 mM d-SDS dissolved in D_2O in a 1:10 o/w ratio, and using a Branson Sonifier 450, emulsified at 70% intensity for 15 seconds, using 1 second pulses with a 1 second delay between pulses. The resulting stable emulsion was placed in a 10 mL round bottom flask and stirred under vacuum at room temperature to remove the organic solvent from the emulsion.[11,21] This process resulted in stable composite nanoparticles containing the desired ratio of P3HT/PCBM. For this work, we created dispersions with a concentration of 2.5 vol% total solids and the method usually resulted in composite nanoparticles with an average hydrodynamic radius of 65 nm as measured using dynamic light scattering (Malvern Zetasizer). The exact concentration of solids in the solution was also corroborated using thermo gravimetric analysis (TGA) with a TA Q50 after the final dispersions were prepared. The P3HT volume percent, η_{P3HT}, of the dispersed nanoparticles was also verified again after preparation by re-dissolving a dry dispersion in a good solvent (i.e. chloroform). The absorption spectra of re-dissolved samples were measured again and, using known extinction coefficients (ε_{P3HT}=53.2 mL/(mg·cm) λ=462 nm, ε_{PCBM}=60.8 mL/(mg·cm) λ=330 nm, ε_{C60}=90.0 λ=333 nm) we determined the total content of each component in the particles. There was generally very good agreement between formulation and the resulting compositions.

Electrostatic Assembly of CNP Monolayers: For CNP prepared using SDS, the stabilizing agent was subsequently exchanged with dodecyl trimethylammonium bromide (DTAB) (Aldrich, St. Louis, 99.9% reagent grade) to produce cationic particles. This exchange was performed by extensive dialysis that was also monitored with zeta potential measurements using a Zetasizer Nano with a reusable Dip Cell. To exchange surfactant, the dispersion's surfactant concentration was first reduced from 40 mM to 1 mM SDS, and then ultrafiltration was used to fully exchange

the remaining SDS with a 40 mM DTAB solution using 100 kDa Millipore filter. A number of washes were performed to ensure complete removal of SDS. The resulting DTAB stabilized dispersion was then dialyzed to a concentration of 5 mM DTAB to remove free surfactant. This stock nanoparticle solution was further diluted to a final concentration of 0.5 mM DTAB and 0.1 vol% CNPs. Spin-coated PEDOT:PSS (Clevios Al 4083) films (3500 rpm for 1 minute) on 15 mm × 15 mm ITO substrates were prepared and baked at 140°C for 30 minutes. These films were then extensively washed with DI water to remove excess PSS. The films were then dipped into the CNP coating solution for 30 minutes, where electrostatic attraction between the cationic nanoparticles and the anionic PEDOT:PSS film resulted in monolayer adsorption. The films were rinsed with copious DI water to remove excess particles and dried under nitrogen and vacuum for one day.

Photoconductive AFM: Photoconductive Atomic Force Microscopy was carried out on an Asylum Research MFP-3D BIO system. Gold-coated contact mode AFM tips with a force constant of 0.2 N/m (Budget Sensors, Cone-GB) were used for all experiments. A 532 nm wavelength illumination with intensity of 218 W/cm^2 was used prior to entering the microscope optics and aligned directly under the AFM tip. The tip-sample contact force was kept to a minimum, typically ~10 nN to avoid damaging the film. No external voltage bias was applied to the AFM tip.[13,15]

References:

1. Kietzke, T.; Neher, D.; Kumke, M.; Ghazy, O.; Ziener, U.; Landfester, K. Phase Separation of Binary Blends in Polymer Nanoparticles. *Small* **2007**, *3*, 1041–8.

2. Montenegro, R.; Landfester, K. Metastable and Stable Morphologies During Crystallization of Alkanes in Miniemulsion Droplets. *Langmuir* **2003**, *19*, 5996–6003.

3. Ulum, S.; Holmes, N.; Darwis, D.; Burke, K.; David Kilcoyne, A. L.; Zhou, X.; Belcher, W.; Dastoor, P. Determining the Structural Motif of P3HT:PCBM Nanoparticulate Organic Photovoltaic Devices. *Sol. ENERGY Mater. Sol. CELLS* **2013**, *110*, 43–48.

4. Kietzke, T. Nanostructured Solar Cells Based on Semiconducting Polymer Nanospheres (SPNs) of M3EH-PPV and CN-Ether-PPV. *Proc. SPIE* **2004**, *5215*, 206–210.

5. Richards, J. J.; Whittle, C. L.; Shao, G.; Pozzo, L. D. Correlating Structure and Photocurrent for Composite Semiconducting Nanoparticles with Contrast Variation Small-Angle Neutron Scattering and Photoconductive Atomic Force Microscopy. *ACS Nano* **2014**, *8*, 4313–24.

6. Richards, J. J.; Weigandt, K. M.; Pozzo, D. C. Aqueous Dispersions of Colloidal Poly(3-Hexylthiophene) Gel Particles with High Internal Porosity. *J. Colloid Interface Sci.* **2011**, *364*, 341–50.

7. Kietzke, T.; Neher, D.; Kumke, M.; Montenegro, R.; Landfester, K.; Scherf, U. A Nanoparticle Approach To Control the Phase Separation in Polyfluorene Photovoltaic Devices. *Macromolecules* **2004**, *37*, 4882–4890.

8. Moulé, a. J.; Meerholz, K. Controlling Morphology in Polymer–Fullerene Mixtures. *Adv. Mater.* **2008**, *20*, 240–245.

9. Moulé, A. J.; Meerholz, K. Morphology Control in Solution-Processed Bulk-Heterojunction Solar Cell Mixtures. *Adv. Funct. Mater.* **2009**, *19*, 3028–3036.

10. Dennler, G.; Scharber, M. C.; Brabec, C. J. Polymer-Fullerene Bulk-Heterojunction Solar Cells. *Adv. Mater.* **2009**, *21*, 1323–1338.

11. Winkler, K.; Paszewski, M.; Kalwarczyk, T.; Kalwarczyk, E.; Wojciechowski, T.; Gorecka, E.; Pociecha, D.; Holyst, R.; Fialkowski, M. Ionic Strength-Controlled Deposition of Charged Nanoparticles on a Solid Substrate. *J. Phys. Chem. C* **2011**, *115*, 19096–19103.

12. Ginger, D. S.; Giridharagopal, R.; Rayermann, G.; Reid, O.; Moore, D.; Shao, G. Z. Time-Resolved Electrostatic Force Microscopy on Conjugated Polymer Blends. *Abstr. Pap. Am. Chem. Soc.* **2011**, *242*.

13. Coffey, D. C.; Reid, O. G.; Rodovsky, D. B.; Bartholomew, G. P.; Ginger, D. S. Mapping Local Photocurrents in Polymer/fullerene Solar Cells with Photoconductive Atomic Force Microscopy. *Nano Lett.* **2007**, *7*, 738–44.

14. Dang, M. T.; Hirsch, L.; Wantz, G. P3HT:PCBM, Best Seller in Polymer Photovoltaic Research. *Adv. Mater.* **2011**, *23*, 3597–3602.

15. Rice, A. H.; Giridharagopal, R.; Zheng, S. X.; Ohuchi, F. S.; Ginger, D. S.; Luscombe, C. K. Controlling Vertical Morphology Within the Active Layer of Organic Photovoltaics Using Poly(3-Hexlythiophene) Nanowires and Phenyl-C61-Butyric Acid Methyl Ester. *ACS Nano* **2011**, *5*, 3132–3140.

Chapter 8. Ionic Surfactant Mediated Assembly of Aqueous Conjugated Polymer Nanoparticles

A significant challenge in the development of colloidal dispersions for thin-film deposition is the strong coupling between the interaction between colloidal particles and the characteristics of the resulting film.[1,2] This is particularly true for optoelectronic applications where functional colloidal particles must be deposited in such a way as to form a high quality film, but not sacrifice the performance of the active materials.[3] An example of this is in the development of composite nanoparticle dispersions for organic photovoltaic applications.[4–6] These nanoparticle formulations possess two key characteristics that must be optimized in order to create high performance thin-film active layers in photovoltaic applications. First, the intrinsic characteristics such as diameter, composition, and internal distribution of conjugated polymer and fullerene must be optimized during formulation in order to achieve the highest possible internal quantum efficiency within each particle. Second, the extrinsic properties of the nanoparticle formulation must be optimized such that the production of high quality films that fully exploit the intrinsic nanoparticle properties. In Chapters 6 and 7, we have detailed the development of characterization tools for the study of the intrinsic characteristics of composite nanoparticles, and in this chapter, we will describe one method to produce high density monolayers of these particles on device relevant geometries.

A general property of a large number of materials is their ability to assume a surface charge when placed in high dielectric constant media, such as water.[7–9] The magnitude and sign of this charge will depend specifically on the charging mechanism. Whether it be dissociation of ionizable surface groups, adsorption of ionic species or acid-base interactions that induces this charging effect, a diffuse double-layer comprised of counter-ions will form at the surface-water interface that balances the net surface charge to maintain neutrality. The magnitude and sign of

this double-layer is related to the surface charge density. In the case of conjugated polymer/fullerene nanoparticles, they are stabilized against coalescence typically by adsorbed surfactant.[10–13] Ionic surfactants such as sodium dodecyl sulfate (C12S), adsorb tail-down on the hydrophobic surface of the particle and the head group dissociates providing both steric and electrostatic stability. Because of the sulfate head group, the zeta potential, ζ, of an aqueous composite nanoparticle (R=50 nm) will be -70 mV.[14] In the case of C12S, the diffuse double-layer will therefore be comprised characterized by an enrichment of sodium ions and depletion of free C12S unimers near the particle water interface.

While by a different mechanism, many substrates used for thin-film active layers of organic photovoltaics such as inorganic oxides (ITO, ZnO, MoO_3, V_2O_5) will assume a surface charge in water related to the acid base properties of the oxide surface. The sign of these charges will be pH dependent with the point of zero charge (pzc) marking the pH at which this charge is neutralized. For the case of acid/base charging, when there is a positive surface charge, the diffuse double-layer will be enriched with hydroxide counter-ions and deficient in hydronium and visa-versa in the case of negatively charged surfaces. Other organic electrode materials like PEDOT:PSS will also charge when placed in water.[15] The magnitude of charge on a surface can be quantified using a streaming potential measurement as shown in Figure 8.1 for PEDOT:PSS coated ITO and ZnO coated ITO.[16,17] These substrates are one example of the transparent conductor used in both normal and inverted OPV geometries.[18,19] From Figure 8.1, it is clear that at neutral pH ZnO coated surfaces will possess a positive surface charge and PEDOT:PSS coated surfaces a negative one.

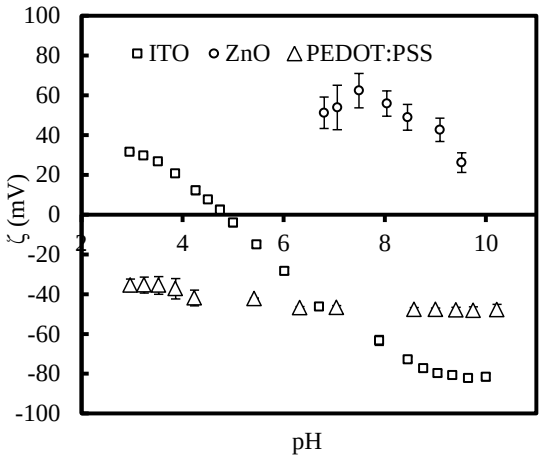

Figure 8.1. Streaming potential measurements for ITO, ZnO, and PEDOT:PSS coated ITO surfaces.

Because of the strong charge assumed by both the device relevant surfaces and aqueous SNPs, it should be possible to identify the appropriate conditions that spontaneous electrostatic assembly (EA) of SNP can occur onto these surfaces. Thin-films, composed of isolated colloidal particles, produced from this process have several key advantages over films produced using solution casting techniques. First, EA avoids drying during the thin-film deposition process which can result in surfactant co-deposition alongside the SNP, leading to insulating surfactant layers in the interstitial spaces between particles. Second, EA facilitates the formation of self-terminating monolayers of particles which will help eliminate unavoidable packing defects caused by the evaporation of water in the late stages of drying. Third, colloidal particles tend to adsorb at the air-water interface so that when dry, a surfactant will form an insulating layer between the substrate and the particles hindering charge transport. Fourth, multilayers of particles will hinder charge transport to the external electrodes due to bottlenecks caused by interparticle transport. Finally, EA can be performed on any surface with a charge regardless of its geometry. Therefore, developing EA techniques for these colloidal particles enables the production of photovoltaic devices onto surfaces of arbitrary complexity.

8.1. Zeta Potential to Monitor Surface Charge Density

Aqueous dispersions of SNPs can be stabilized by a variety of small molecule surfactants including nonionic, cationic, and anionic. For the purposes of this work, we have focused our attention on linear chain cationic surfactants terminated with tetramethylammonium bromide (TAB) head group (C12TAB, C14TAB, C16TAB) and two anionic surfactants with a sulfate (S) head group (C12S, and C16S). The surfactant concentration of stable SNPs dispersions is very different from that necessary to stabilize the oil/water interface during nanoparticle formulation.[20] Figure 8.2a shows interfacial tension measurements of C12S and C12TAB surfactants at the oil/water interface. From this plot, and often reported in the literature, the point at which the interfacial tension of the oil-water interface is the point at which the interface is saturated with surfactant unimers and this usually occurs around the CMC of the surfactant.[21] Therefore for an emulsion, where the amount of interfacial area is much higher due to the nano-size of the emulsion droplets (R=100nm), the surfactant concentration must be above the CMC (15 mM) in order to fully stabilize the oil-water interface against coalescence as shown in Figure 8.2b.

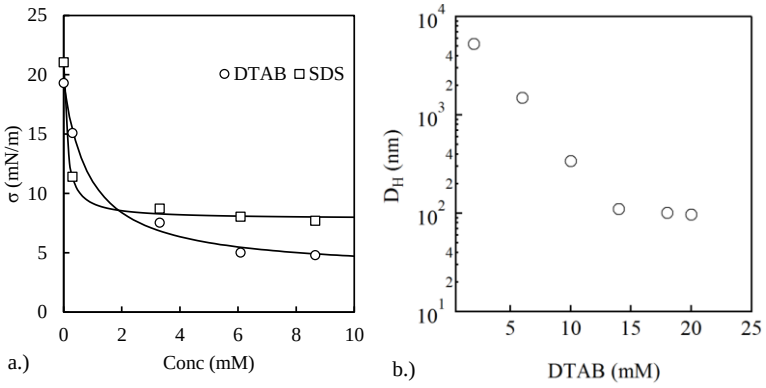

Figure 8.2. a.) Interfacial tension as a function of surfactant content (C12S and C12TAB) at the chloroform/water interface, b.) Z-avg size as determined by Dynamic Light Scattering (DLS) as a function of the bulk surfactant concentration for C12TAB.

Because of the need for a large amount of surfactant in the particle formulation process, the surfactant concentration in SNP formulations is large, typically anywhere from 1-5X the CMC. This concentration is far larger than that necessary to stabilize the solid polymer/water interface. Therefore, alongside SNPs is likely a large quantity of free surfactant unimers and micelles. The amount of free surfactant present in a SNP dispersion can be expressed as shown in Equation 8.1 where the excess surfactant concentration, C_{exc}, the bulk surfactant concentration, C_{bulk}, the volume fraction of particles in the dispersion, ϕ_{part}, the particle radius, R_{part}, the adsorbed surfactant density, Γ_{AS}.[22]

$$8.1 \quad C_{exc} = C_{bulk} - \frac{3\Gamma_{AS}\phi_{part}}{N_{av}R_{part}}$$

Therefore, the excess surfactant concentration will be a function of particle size, volume fraction, surfactant type and concentration. If the excess surfactant content is much greater than the fraction of adsorbed surfactant on the particle surface, spontaneous EA of SNP onto charge surfaces is hindered. This is shown in Figure 8.3a. As the bulk surfactant concentration, in this case C12TAB, is varied for a fixed particle size and volume fraction, there is a maximum in the amount of apparent deposition that occurs as the concentration is decreased. At both high and low surfactant concentrations, no deposition is apparent. At some critical surfactant content, spontaneous electrostatic assembly of positively charged SNPs onto negatively charged PEDOT:PSS coated glass is possible. This can be understood within the context of a simple competitive adsorption model.[23] The SNPs will assume the same charge as the free surfactant heads groups. When a negatively charged surface is introduced to the dispersion, surfactant will quickly adsorb head-down to the surface in order to balance the charge. At sufficiently high concentration of surfactant, surface adsorbates of free surfactant can form that at high

concentration hinder the spontaneous assembly of particles via two mechanisms. First, if surface micelles are present, they can provide a steric barrier preventing close approach of the positively charged SNP to the surface. Second, adsorbed unimers screen the surface charge so that the SNPs do have a strong driving force to migrate toward the surface. This is shown schematically in Figure 8.3b.

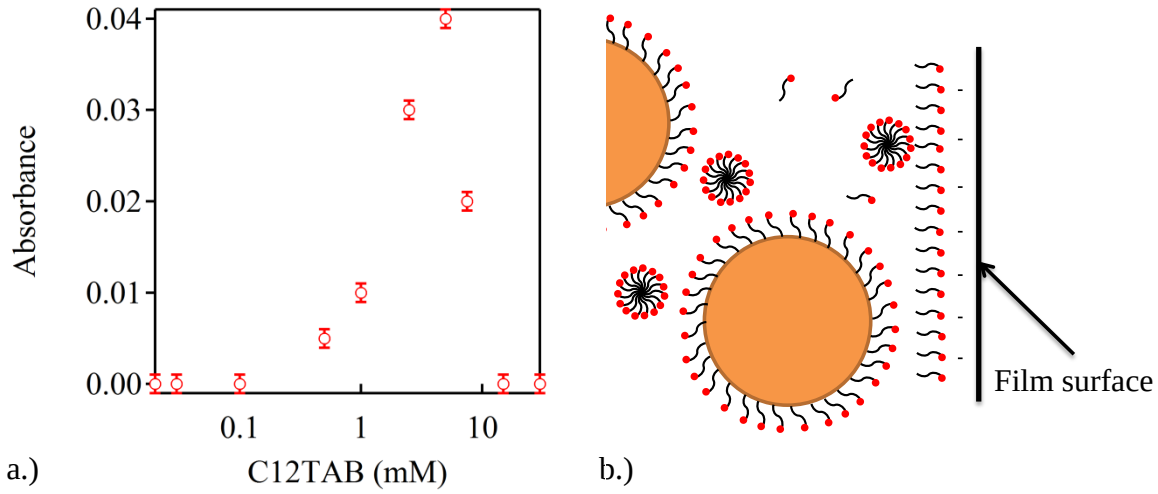

Figure 8.3. a.) UV-Vis absorbance data for C12TAB coated SNP adsorption as a function of bulk surfactant concentration and b.) Schematic representation of competitive adsorption of surfactant preventing the electrostatic assembly of SNPs to oppositely charged surfaces.

Based on this model, in order to maximize the surface coverage of SNPs on a desired electrode surface using EA, it is necessary to reduce to the free surfactant concentration as much as possible so as to minimize competitive adsorption.[24] As seen in Figure 8.2b, this has an unintended consequence of destabilizing the SNPs in dispersion. Therefore, at very low surfactant concentrations, the particles do no adsorb to the surface and instead simply aggregated and fell out of dispersion. Therefore, the ability to adsorb particles is a balance between minimizing competitive adsorption and compromising the stability of the dispersion.

This effect is a direct manifestation of the adsorption term in Equation 8.1, Γ_{ads},. In dilute surfactant concentration dispersions, $\Gamma_{AS,}$ can be described using a Langmuir adsorption isotherm model, Equation 8.3.[25] The Langmuir adsorption model assumes single site and monolayer adsorption.

$$8.2 \quad \Gamma_{AS} = \Gamma_S \frac{K_{ads} C_{bulk}}{1 + K_{ads} C_{bulk}} \quad \text{where} \quad A + S \underset{}{\overset{K_{ads}}{\rightleftharpoons}} AS$$

Equation 8.2 states that there exists a dynamic equilibrium between an adsorbate species, [A], and the available surface sites, [S]. The surface density, Γ_{AS}, at any bulk surfactant concentration can be predicted from the density of surface sites, Γ_S, and the equilibrium constant, K_{ads}.

There are two ways that the adsorption characteristics of ionic surfactants can be monitored at the particle interface. The first is conductivity. By far the most mobile species in the dispersion is the free surfactant. Therefore, the conductivity of the coating solution will be dominated by the free surfactant concentration. Below the CMC, the limiting molar conductance of the desired surfactant can be determined. From measurements of bulk conductivity data, the free surfactant concentration can be calculated and based on the known particle concentration and size, Γ_{ads}, calculated. The drawback to this approach is that for many surfactants, the molar concentration of adsorbed surfactant is a small fraction of the bulk surfactant concentration. Therefore, in many cases, except at very high particle volume fractions or small particle sizes, conductivity measurements are not a sensitive probe for the adsorbed surfactant concentration. Instead, we chose an alternative method and measured the electrophoretic mobility of a particle at a fixed $\phi_{part.}$ The electrophoretic mobility is related to the surface potential of the mobile particles.[26] Because the SNPs have a significantly large scattering cross-section than either free surfactant or surfactant micelles, electrophoretic mobility is a very sensitive probe of charge density on the

particle's surface, and because the only source of charge dissociation for the SNPs is the presence of adsorbed ionic surfactant, a sensitive probe of adsorbed surfactant concentration.

For spheres, the relationship between electrophoretic mobility, zeta potential, and surface charge density is a complicated function of the Debye parameter (Equation 8.3), κ.[9] The relationship between these parameters is a function of the motion of a sphere under an applied electric field. The motion, known as electrophoretic mobility, is a balance between the electrophoretic forces imposed on the particles and ions to migrate and the requirement that the distribution of ions around the particle maintain charge neutrality. In Equation 8.3, e is the electronic charge, ε is the dielectric constant of water, ε_0 is the permittivity of free space and kT is the Boltzmann's constant multiplied by the temperature.

$$8.3 \quad \kappa = \sqrt{\frac{2e^2 z^2 N_{AV}^2 C}{\varepsilon \varepsilon_0 kT}}$$

While in the Hückel ($\kappa R_{part} < 0.1$) and Smoluchowski ($\kappa R_{part} > 200$) regimes, these expressions are trivial to derive, the only source of ionic strength in our system is the ionic surfactant.[8] Therefore, as the surfactant concentration is reduced, κR_{part}, is also reduced. For these experiments κR_{part} is typically in the range of 1-50. In this range, only numerical solutions developed by O'Brien and White are adequate to describe the relationship between the measurements of electrophoretic mobility, zeta potential and surface charge density.[27] Using the O'Brien and White model, the measured dimensionless electrophoretic mobility, dimensionless zeta potential, and surface charge density for R_{part}=27nm model particles are shown in Figure 8.4a as a function of C12TAB concentration. In Figure 8.4b, the adsorption data is linearized by plotting C_{bulk}/Γ_{AS} vs. Γ_{AS}. This plot shows excellent linearity and the slope is $-K_{ads}$ and the intercept is $1/(K_{ads}\Gamma_S)$. The fitted values are Γ_S =0.19±0.05 nm^{-2} and K_{ads}=0.29±0.09 mM^{-1}. These

values are smaller than those found for adsorbed monolayers of C12S at the air/water interface (Γ_S =6 nm^{-2} and K_{ads}=1.1 mM^{-1}).[28] This could suggest that either, not all surfactant head groups that adsorb to the CNP/water interface are charged, or that each surfactant molecule occupies a larger volume on the SNP surface than the air/water interface.

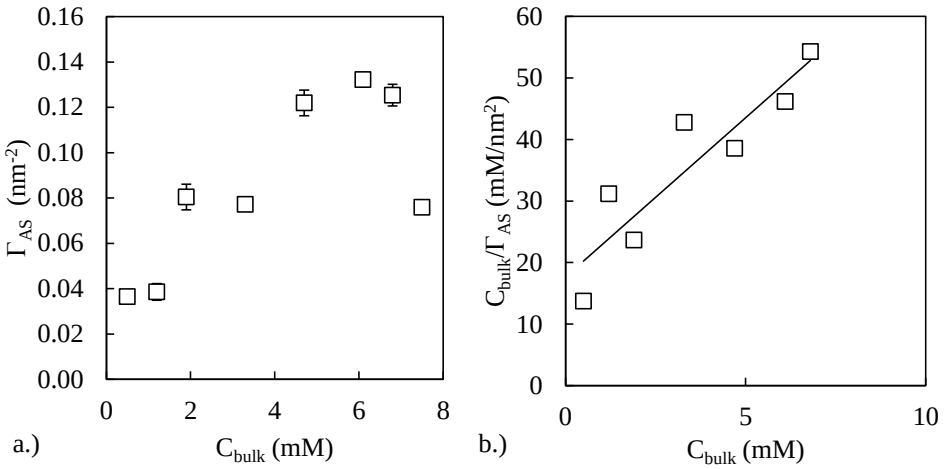

Figure 8.4 a.) Summary of electrophoresis data for C12TAB stabilized R_{part}=27 nm SNP dispersions reduced from dimensionless mobility to surface charge density, b.) Linearization of Langmuir adsorption isotherm. Line is the best fit through the data.

8.2. Choosing the appropriate surfactant for Electrostatic Deposition.

Given the fact that the ionic surfactant is in dynamic equilibrium with the particles' surface, it is possible, given the right conditions, to exchange surfactants. Using membrane ultrafiltration with the appropriate filter size, many dilution/wash cycles can be repeated and the C12TAB surfactant used to stabilize a model colloid particle can be easily replaced by other cationic surfactants, nonionic surfactants, or even anionic surfactants without compromising the stability of the dispersion. The conditions necessary to exchange anionic surfactant for cationic surfactants are outline in the supplemental information section, but briefly, first the DTAB concentration is reduced then excess anionic surfactant is added such that $C_{anionic}>>>C_{cationic}$. In this way, any crystallization or coascervate phases that form due to the presence of a mixture of oppositely

charged surfactants does not impact the stability of the particles, and these phases can be easily filtered out of the dispersion later.[29,30] Figure 8.5 demonstrates the successful exchange of Rrand-P3HT SNPs initially stabilized with C12TAB and then exchanged with C14TAB, C16TAB, and C12S, and C16S. The sign and magnitude of the charge on the particle surface switches depending on whether the particles are stabilized with anionic, cationic, or nonionic surfactants and the surfactant tail length.

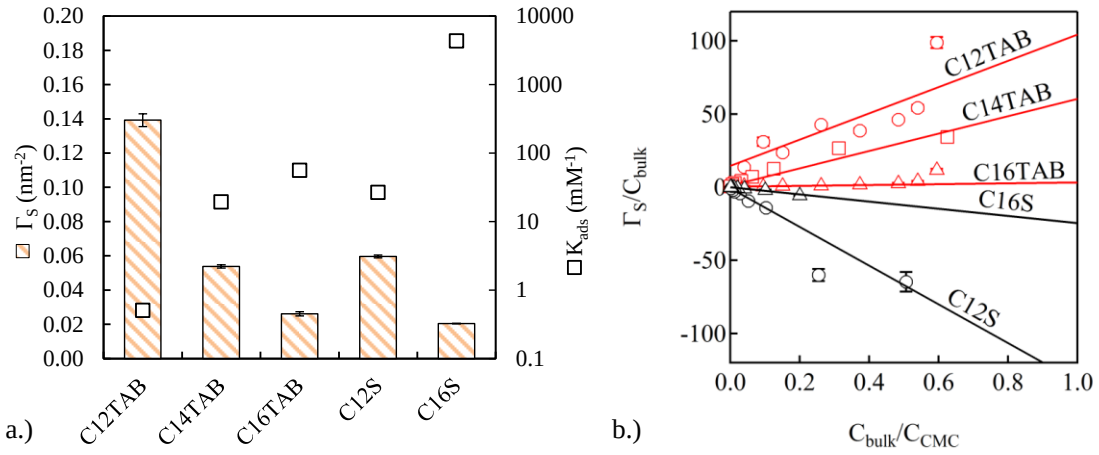

Figure 8.5 a.) TAB series (C12TAB, C14TAB, C16TAB) and S series (C12S, C16S), b.) Linearization of Langmuir adsorption isotherm. Line is the best fit through the data.

This demonstrates the flexibility afforded by the reversible adsorption of surfactant to the particle/water interface that allows for easy removal and replacement. Therefore, it is possible to consider the characteristics of the surfactant that are ideal for EA, but maybe not for particle production as these can be easily swapped out later.

Based on the model for competitive adsorption of surfactant to the substrate surface, the surfactant characteristics that are necessary to allow the formation of high density EA monolayers can be defined within the context of the Langmuir adsorption isotherm coefficients. The ideal surfactant would have the highest Γ_S and K_{ads}. This ensures that the charge density on

the particle's surface is large and the excess surfactant content for a given bulk surfactant concentration high. The surfactant should also have a sufficiently high diffusivity such that once adsorbed at the substrate/water interface, it can readily desorb to allow for the deposition of the SNP. Measurements for Γ_S and K_{ads} as a function of surfactant type are shown in Figure 8.5b as calculated from electrophoretic mobility measurements and fit with Equation 8.2. Based on these results, C16S and C16TAB should make the best surfactants that we have considered as while their Γ_S are smaller than the shorter chain length analogues, the values for K_{ads} are many orders of magnitude larger, suggesting a significant reduction in the excess surfactant concentration.

Adsorption of C12-16TAB coated particles are monitored using UV-Vis and this data summarized in Figure 8.6a. These data show that as concentration of surfactant decreases, some improvement in particle absorption is possible. However, significant coating densities are still not observed. This demonstrates that the degree of competitive adsorption is significantly reduced as surfactant concentration is decreased for a fixed particle content and size. Another interesting observation is highlighted in Figure 8.6b. For a given ratio of surfactant concentration to its CMC value, there is a consistent decrease in the UV-Vis absorption of particles as the alkyl chain length increases.

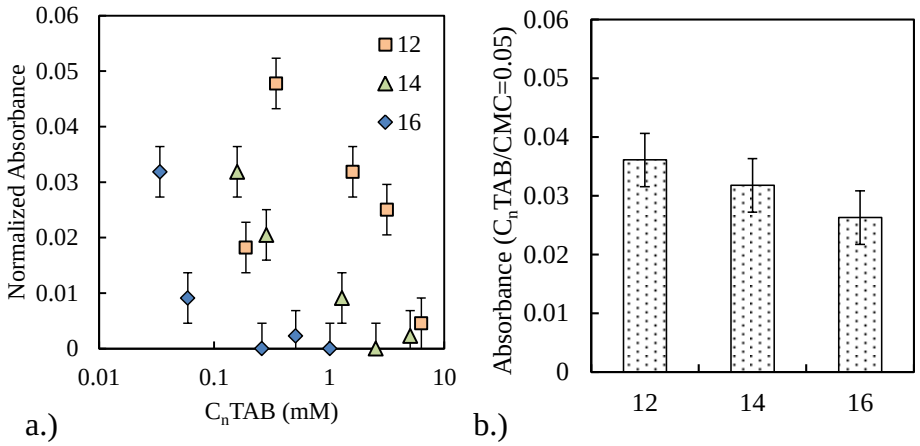

Figure 8.6 a.) UV-Vis Absorbance data for adsorption of Rrand model SNP to glass slides as a function surfactant concentration, b.) Absorbance for a fixed ratio of concentration of C_nTAB to its CMC value.

This result has been observed for the deposition of charged colloidal particles onto charged surfaces and can be rationalized when the Debye screening length is taken into account.[31] The surfactant is the only source of salt in these experiments. Therefore, the ionic strength of the solution containing C16TAB at conditions where competitive adsorption is minimized is orders of magnitude lower than that of C12TAB. Because of the concentration of surfactant used in Figure 8.6, the Debye length is larger for C16TAB than for C12TAB. This implies that the mutual repulsion of SNP already deposited on the surface is stronger for C16TAB resulting in lower density surface coverage. Based on the Debye screening length argument alone, a model for hexagonal close packing of spherical colloidal particles on a flat surface can be proposed as shown in Figure 8.7. In this model, the distance separating the nearest neighbor is the particle radius and the Debye screening length. Therefore, as κR_{part}, decreases, so does the fractional area coverage, θ, as shown in Equation 8.4.

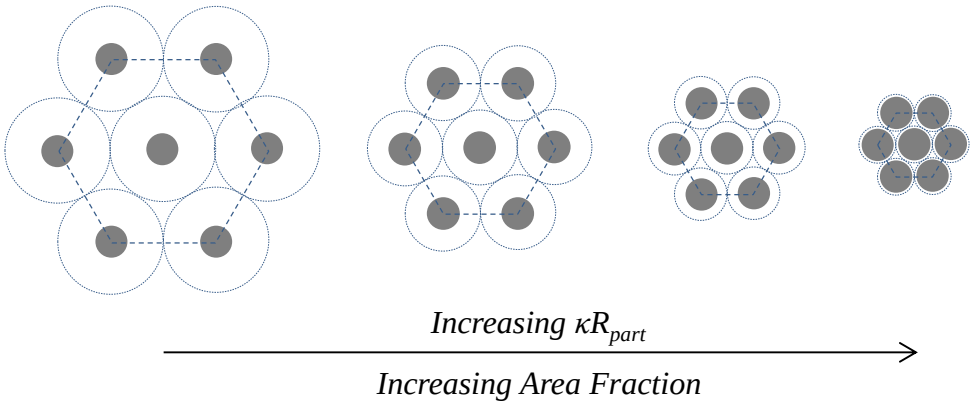

Figure 8.7. Schematic highlighting the effect of κ on the density of particles EA on a flat surface for a fixed particle diameter and changing Debye length.

While this is only a simple model, it is instructive in that it predicts the scaling relationship between fractional area coverage of particles and κR_{part}. Based on this simple relationship, $\kappa R_{part,}$ must be large to achieve a high density surface coverage.

$$8.4 \quad \theta \sim \frac{\pi\left(\kappa R_{part}\right)^2}{2\sqrt{3}\left(\kappa R_{part}+1\right)^2}$$

The easiest way to make κR_{part} larger is to add salt in order to increase κ. Based on DLVO calculations, 500 mM NaCl should be sufficient to completely screen the particle-particle repulsion on the surface. To test this theory, process diagrams for both C16TAB and C16S were produced as a function of both salt and surfactant content (Figure 8.7).

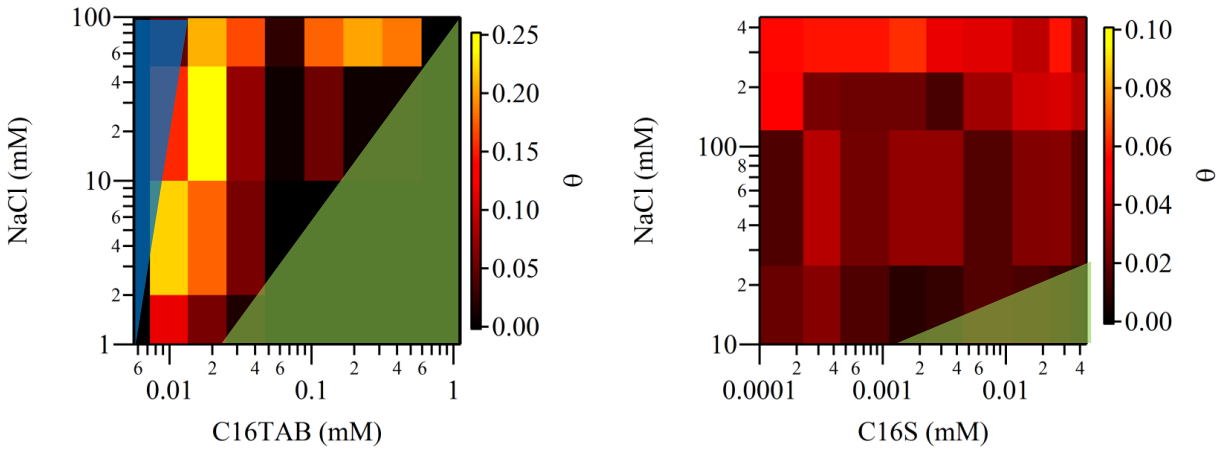

Figure 8.8. Adsorption phase diagrams for C16TAB and C16S as a function of salt content as a function of salt and surfactant content. The blue region shows areas where the dispersions were unstable, and the green regions shows where no deposition was observed.

Figure 8.8 confirms that the highest surface coverage for EA is at low surfactant contents and high salt. However, what is also apparent is that for both C16TAB and C16S there are regions where no electrostatic adsorption is possible (highlighted in green) and regions where too little surfactant leads to particle destabilization (highlighted in blue). Another important factor to note is that the clear trends in the deposition data, the maximum fractional area coverage (θ_{max}=25%)

is far from the theoretical maximum for close-packed systems (θ_{max}=91%) and for disordered systems (θ_{max}=82%).

Another important observation comes from measured zeta potential data for these particles as a function at increased ionic strength. Figure 8.9 shows the surface density coverage of C16TAB determined from the measured electrophoretic mobility of the particles along with the Langmuir adsorption isotherm fits to the surface density data.

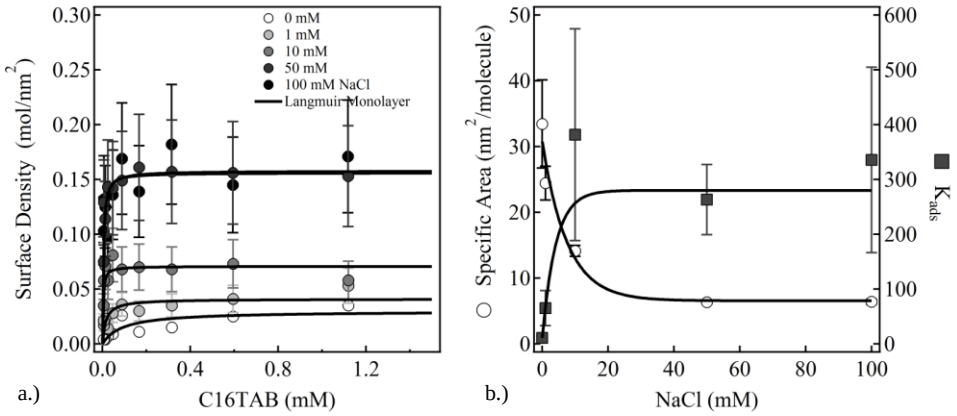

Figure 8.9. a.) Summary of adsorption isotherms calculated from the measured electrophoretic mobility data for C16TAB as a function of NaCl concentration, and b.) Langmuir adsorption model fit parameters as a function of NaCl concentration.

The results of these fits show that the adsorption of C16TAB to the particle/water interface is also salt dependent. In low-ionic strength water, the mutual repulsion of surfactant head groups on the particle surface is sufficient to prevent close packing of TAB head groups onto the particle's surface. The fits to the adsorption data are shown in Figure 8.8b and from this result it is clear that as the salt content increases, the area occupied by the surfactant on the surface decreases, consistent with an increase in surfactant density. It is also apparent from the K_{ads} data that as the NaCl content increases, the equilibrium shifts toward a higher ratio of adsorbed surfactant at the particle surface to bulk surfactant.

8.3. Device design criteria using Electrostatic Adsorption

Having completed the characterization of the process windows for the deposition of both C16TAB and C16S particles, it is important to reconsider the mechanism for particle deposition. We have established the complex interplay between surfactant charging/adsorption behavior on salt content and surfactant type. We have also studied the effect that surfactant characteristics have on the SNP stability. Missing from this picture though, is the adsorption of surfactant to the substrate. The adsorption process windows Figure 8.8 suggest that high surface density coverage may not be achievable given this set of materials. However, EA for the deposition of colloidal particles still has some distinct advantages to solution casting techniques. Some of these are summarized in Figure 8.10.

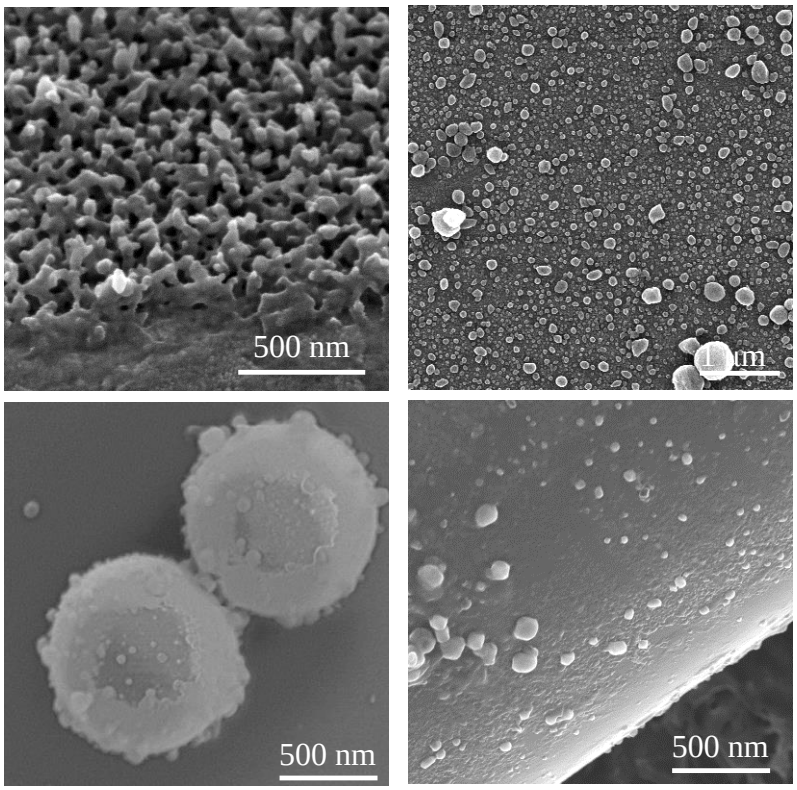

Figure 8.10. (top left) Densely electrostatically assembled monolayer film of R_{part}=30 nm, (top right) polydisperse particle set EA as a monolayer, (bottom left) SNPs electrostatically

assembled onto charged silica spheres, (bottom right) SNPs electrostatically assembled onto charged silica fibers.

The micrograph in Figure 8.10 (top left) show the electrostatic deposition of SNPs onto PEDOT:PSS coated ITO can form, under certain conditions, monolayers with up to 50% area coverage. Under the conditions that this film was deposited, however, the coating solution became heavily aggregated so it is likely that these particles deposited as clusters leading the highly porous structure seen in the micrograph. In the top right (SEM), a low density monolayer is shown that demonstrates that the technique is flexible even for very polydisperse samples. Because the curvature of the particle is unlikely to affect Γ_S of the surfactant, the size distribution on the surface should be related to the relative diffusivity of the particles in the suspension. The bottom two micrographs demonstrate another interesting feature of the development of EA techniques. Under the right deposition conditions, it is possible to create composite materials by assembling SNP onto metal oxide spheres (bottom left) or metal oxide fibers (bottom right).

8.4 Materials and Methods

The model dispersion used throughout this work was made using Rrand-P3HT obtained from Rieke Metals, Inc (Lincoln, NE). Rrand P3HT (153 mg) was dissolved into 10 mL of chloroform and stirred at room temperature for 2 hours. 50 mL 50 mM DTAB, purchased from Sigma Aldrich, was then added with the chloroform solution to a round bottom flask. A pre-emulsion was produced by vigorous stirring over the course of 1 hour. The resulting pre-emulsion was then sonicated at 50% intensity for 5 minutes. The sample was immediately evacuated to a pressure of 100 mtorr and the chloroform slowly removed while stirring at 20 °C. The resulting dispersion particles had a R_H = 27 nm. Absorption spectroscopy measurements were made from

300 nm to 1000 nm using a Thermo Scientific Evolution 300 UV-Vis spectrophotometer. In order to obtain the volume distributions from the DLS data, intensity weighted distributions obtained using a non-negatively constrained least squares (NNLS) fitting algorithm were transformed to volume distribution using Mie Theory and the known index of refraction of the samples. Scanning Electron Microscopy (SEM) was performed using an FEI Sirion SEM on samples mounted on silicon wafers and sputtered with gold at 18 mA for 30 seconds. Electrophoretic mobility and DLS data were measured using Malvern ZetaSizer Nano and electrophoretic mobilities corrected using Electrokinetic modeling Utilities provided as part of Malverns ZetaSizer Software. All other reagents were purchased from Aldrich.

References:

1. Pal, R. *Rheology of Particulate Dispersions and Composites*; 2007; pp. 1–300.

2. Singh, K.; Tirumkudulu, M. Cracking in Drying Colloidal Films. *Phys. Rev. Lett.* **2007**, *98*, 218302.

3. Richards, J. J.; Whittle, C. L.; Shao, G.; Pozzo, L. D. Correlating Structure and Photocurrent for Composite Semiconducting Nanoparticles with Contrast Variation Small-Angle Neutron Scattering and Photoconductive Atomic Force Microscopy. *ACS Nano* **2014**, *8*, 4313–24.

4. Ulum, S.; Holmes, N.; Darwis, D.; Burke, K.; David Kilcoyne, A. L.; Zhou, X.; Belcher, W.; Dastoor, P. Determining the Structural Motif of P3HT:PCBM Nanoparticulate Organic Photovoltaic Devices. *Sol. ENERGY Mater. Sol. CELLS* **2013**, *110*, 43–48.

5. Holmes, N. P.; Burke, K. B.; Sista, P.; Barr, M.; Magurudeniya, H. D.; Stefan, M. C.; Kilcoyne, A. L. D.; Zhou, X.; Dastoor, P. C.; Belcher, W. J. Nano-Domain Behaviour in P3HT:PCBM Nanoparticles, Relating Material Properties to Morphological Changes. *Sol. Energy Mater. Sol. Cells* **2013**, *117*, 437–445.

6. Andersen, T. R.; Larsen-Olsen, T. T.; Andreasen, B.; Böttiger, A. P. L.; Carlé, J. E.; Helgesen, M.; Bundgaard, E.; Norrman, K.; Andreasen, J. W.; Jørgensen, M.; *et al.* Aqueous Processing of Low-Band-Gap Polymer Solar Cells Using Roll-to-Roll Methods. *ACS Nano* **2011**, *5*, 4188–96.

7. Marinova, K. G.; Alargova, R. G.; Denkov, N. D.; Velev, O. D.; Petsev, D. N.; Ivanov, I. B.; Borwankar, R. P. Charging of Oil - Water Interfaces Due to Spontaneous Adsorption of Hydroxyl Ions. *Langmuir* **1996**, *12*, 2045–2051.

8. Berg, J. C. *An Introduction to Interfaces and Colloids - Bridge to Nanoscience*; 2009; pp. 1–300.

9. Israelachvili, J. N. *Intermolecular and Surface Forces*; Third.; Elsevier, 2011; pp. 1–674.

10. Landfester, B. K.; Montenegro, R.; Scherf, U.; Güntner, R.; Asawapirom, U.; Patil, S.; Neher, D.; Kietzke, T. Semiconducting Polymer Nanospheres in Aqueous Dispersion Prepared by a Miniemulsion Process. *Adv. Mater.* **2002**, *14*, 651–655.

11. Landfester, K. Synthesis of Colloidal Particles in Miniemulsions. *Annu. Rev. Mater. Res.* **2006**, *36*, 231–279.

12. Landfester, K. The Generation of Nanoparticles in Miniemulsions. *Adv. Mater.* **2001**, *13*, 765–768.

13. Landfester, B. K.; Montenegro, R.; Scherf, U.; Güntner, R.; Asawapirom, U.; Patil, S.; Neher, D.; Kietzke, T. Semiconducting Polymer Nanospheres in Aqueous Dispersion Prepared By. *Adv. Mater.* **2002**, *14*, 651–655.

14. Richards, J. J.; Weigandt, K. M.; Pozzo, D. C. Aqueous Dispersions of Colloidal Poly(3-Hexylthiophene) Gel Particles with High Internal Porosity. *J. Colloid Interface Sci.* **2011**, *364*, 341–50.

15. Kosmulski, M. The pH-Dependent Surface Charging and the Points of Zero Charge. *J. Colloid Interface Sci.* **2002**, *253*, 77–87.

16. Erickson, D.; Li, D. Streaming Potential and Streaming Current Methods for Characterizing Heterogeneous Solid Surfaces. *J. Colloid Interface Sci.* **2001**, *237*, 283–289.

17. Walker, S. L.; Bhattacharjee, S.; Hoek, E. M. V.; Elimelech, M. A Novel Asymmetric Clamping Cell for Measuring Streaming Potential of Flat Surfaces. *Langmuir* **2002**, *18*, 2193–2198.

18. Sun, Y.; Seo, J. H.; Takacs, C. J.; Seifter, J.; Heeger, A. J. Inverted Polymer Solar Cells Integrated with a Low-Temperature-Annealed Sol-Gel-Derived ZnO Film as an Electron Transport Layer. *Adv. Mater.* **2011**, *23*, 1679–83.

19. Lloyd, M. T.; Peters, C. H.; Garcia, A.; Kauvar, I. V.; Berry, J. J.; Reese, M. O.; McGehee, M. D.; Ginley, D. S.; Olson, D. C. Influence of the Hole-Transport Layer on the Initial Behavior and Lifetime of Inverted Organic Photovoltaics. *Sol. Energy Mater. Sol. Cells* **2011**, *95*, 1382–1388.

20. Bibette, J.; Morse, D. C.; Witten, T. A.; D.A., W. Stability Criterion for Emulsions. *Phys. Rev. Lett.* **1992**, *69*, 2439–2444.

21. Engl, W.; Backov, R.; Panizza, P. Controlled Production of Emulsions and Particles by Milli- and Microfluidic Techniques. *Curr. Opin. Colloid Interface Sci.* **2008**, *13*, 206–216.

22. Bibette, J.; Calderon, F. L.; Poulin, P. Emulsions : Basic Principles. *Reports Prog. physics. Phys. Soc.* **1999**, *969*, 969–1033.

23. Lee, E. M.; Koopal, L. K. Adsorption of Cationic and Anionic Surfactants on Metal Oxide Surfaces : Surface Charge Adjustment and Competition Effects. *J. Colloid Interface Sci.* **1996**, *177*, 478–489.

24. Zhang, R.; Somasundaran, P. Advances in Adsorption of Surfactants and Their Mixtures at Solid/solution Interfaces. *Adv. Colloid Interface Sci.* **2006**, *123-126*, 213–29.

25. Bunauer, S.; Deming, L. S.; Deming, W. E.; Teller, E. On a Theory of the van Der Waals Adsorption of Gases **1940**, *1139*, 1723–1732.

26. Laurence Boulange-Petermann, A. Doren, B. Baroux, M.-N. B.-F. Zeta Potential Measurements on Passive Materials. *J. Colloid Interface Sci.* **1995**, *171*, 179–186.

27. Mangelsdorf, C. S.; White, L. R. Effects of Stern-Layer Conductance on Electrokinetic Transport Properties of Colloidal Particles. *J. Chem. Soc. Faraday Trans.* **1990**, *86*, 2859.

28. Chang, C.; Franses, E. I. Adsorption Dynamics of Surfactants at the Air/Water Interface: A Critical Review of Mathematical Models, Data, and Mechanisms. *Coll and Surf A* **1995**, *100*, 1–45.

29. Tah, B.; Pal, P.; Mahato, M.; Talapatra, G. B. Aggregation Behavior of SDS/CTAB Catanionic Surfactant Mixture in Aqueous Solution and at the Air/water Interface. *J. Phys. Chem. B* **2011**, *115*, 8493–9.

30. Bakshi, M. S. Micelle Formation by Anionic and Cationic Surfactants in Binary Aqueous Solvents. *J. Chem. Soc. Faraday Transcr.* **1993**, *89*, 4323–4326.

31. Winkler, K.; Paszewski, M.; Kalwarczyk, T.; Kalwarczyk, E.; Wojciechowski, T.; Gorecka, E.; Pociecha, D.; Holyst, R.; Fialkowski, M. Ionic Strength-Controlled Deposition of Charged Nanoparticles on a Solid Substrate. *J. Phys. Chem. C* **2011**, *115*, 19096–19103.

Chapter 9. Future Work and Conclusions

Throughout this thesis, there has been a consistent emphasis on the importance of the study of the morphology of thin-film active layers produced by solution casting or from dispersions of composite nanoparticles. We have shown that modifying the distribution of conjugated polymer and fullerene within the active layer of conjugated polymer/fullerene composites significantly changes their performance. Of course, this is only a small snapshot of the work that is ongoing within the community to understand the important role that morphology has to play in the design and optimization of photovoltaic devices.[1–5] It remains to be seen whether new device engineering strategies, better synthesis techniques, and further improvement in the deposition of these materials can translate into commercially relevant thin-film polymer based solar cell technology.

Indeed significant challenges remain, which were not a specific focus of this thesis, but are ongoing engineering challenges. First is stability. Current polymer solar cells have poor long-term stability.[6–8] Even with encapsulation, typical lifetimes for polymer based solar cells are less than 1 year. It is an open question as to which features specifically contribute to this degradation, but most often it is degradation of electrode material, polymer photolysis, and intercalation of water and oxygen into the active layer that induces localized trap sites. The second major challenge is the elimination of glass in the manufacturing process.[9,10] The great promise of polymer solar cells cannot be realized without the application of scalable roll-to-roll processing, which is very difficult to realize without flexible substrates. Another challenge is solar spectrum harvesting efficiency. Current record holders such as PBT-based conjugated polymers possess a bandgap of 1.6 eV, which based on single-junction device physics is still suboptimal.[11,12] However, while these materials possess extremely high internal quantum efficiencies (reaching

100%), the external quantum efficiency is still only ~60% for the best performers. Therefore, active-layer thickness needs to be effectively doubled. As has been widely found empirically, as active layer thickness is increased above ~100 nm, it is typically found that the internal quantum efficiency decreases.

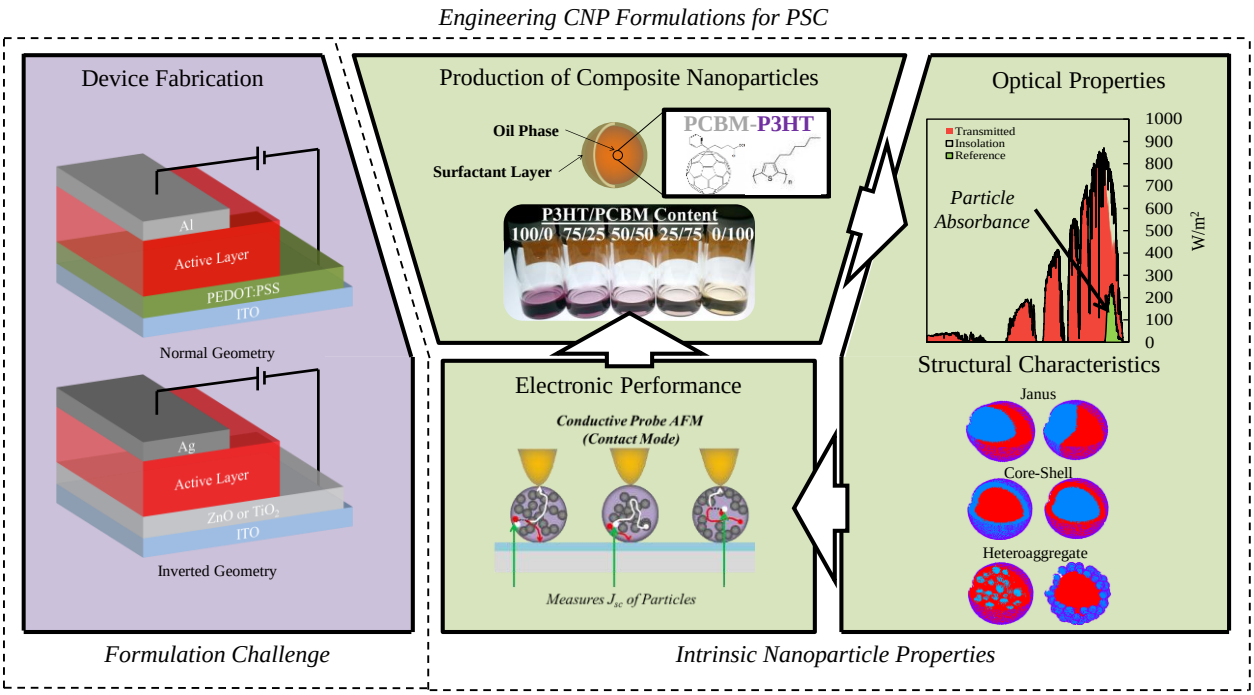

Figure 9.1. Schematic showing a general strategy for the design and engineering of CNP based polymer solar cells.

Chapters 2, 5-8 of this thesis outline the basis for the rational design scheme of CNPs for polymer solar cell applications. The power of this scheme as emphasized in Figure 9.1 is that the properties of the CNPs can be studied in isolation from the properties of their formulation, and further that the resulting device properties will always be a strong function of the properties of individual CNP acting in aggregate. We propose that by understanding the performance of individual CNPs, it is possible to not only predict the resulting properties of devices produced from those formulations, but also to improve performance independently from the specific

device architecture. This capability is a direct result of the work outline in this thesis and supported by the papers published on the subject. We have also outlined a vision for the steps necessary to formulations of CNPs for device applications. [13,14] Looking to the future, there are many potential areas of work that could potentially be impactful in this field. These include:

- Increasing the diameter of the nanoparticle formulations so that a greater fraction of light is absorbed per particle.
- Tuning the oil removal process such that core-shell particle formation is universally suppressed so gelation is not needed as a mechanism to create uniformly distributed particles.
- Employ lower band-gap conjugated polymers or make all conjugated polymer CNPs that have the potential to further improve the performance.
- Study interparticle charge transport affects, specifically related to how easily charge is transported through surfactant in present in the interstitial space of the particles and how contact area between particles influences the rate of charge transfer.

These are just a handful of necessary and interesting questions as they pertain to the overall design strategies outlined in Figure 9.1.

References:

1. Ulum, S.; Holmes, N.; Darwis, D.; Burke, K.; David Kilcoyne, a. L.; Zhou, X.; Belcher, W.; Dastoor, P. Determining the Structural Motif of P3HT:PCBM Nanoparticulate Organic Photovoltaic Devices. *Sol. Energy Mater. Sol. Cells* **2013**, *110*, 43–48.

2. Holmes, N. P.; Burke, K. B.; Sista, P.; Barr, M.; Magurudeniya, H. D.; Stefan, M. C.; Kilcoyne, A. L. D.; Zhou, X.; Dastoor, P. C.; Belcher, W. J. Nano-Domain Behaviour in P3HT:PCBM Nanoparticles, Relating Material Properties to Morphological Changes. *Sol. Energy Mater. Sol. Cells* **2013**, *117*, 437–445.

3. Stapleton, A.; Vaughan, B.; Xue, B.; Sesa, E.; Burke, K.; Zhou, X.; Bryant, G.; Werzer, O.; Nelson, A.; David Kilcoyne, a. L.; *et al.* A Multilayered Approach to Polyfluorene Water-Based Organic Photovoltaics. *Sol. Energy Mater. Sol. Cells* **2012**, *102*, 114–124.

4. Wu, W.-R.; Jeng, U.-S.; Su, C.-J.; Wei, K.-H.; Su, M.-S.; Chiu, M.-Y.; Chen, C.-Y.; Su, W.-B.; Su, C.-H.; Su, A.-C. Competition Between Fullerene Crystallization Upon Annealing of Bulk. *ACS Nano* **2011**, *5*, 6233–6243.

5. Tate, M. P.; Hillhouse, H. W. General Method for Simulation of 2D GISAXS Intensities for Any Nanostructured Film Using Discrete Fourier Transforms. *J. Phys. Chem. C* **2007**, *111*, 7645–7654.

6. Jorgensen, M.; Norrman, K.; Krebs, F. C. Stability/degradation of Polymer Solar Cells. *Sol. Energy Mater. Sol. Cells* **2008**, *92*, 686–714.

7. Bertho, S.; Janssen, G.; Cleij, T. J.; Conings, B.; Moons, W.; Gadisa, A.; D'Haen, J.; Goovaerts, E.; Lutsen, L.; Manca, J.; *et al.* Effect of Temperature on the Morphological and Photovoltaic Stability of Bulk Heterojunction Polymer:fullerene Solar Cells. *Sol. Energy Mater. Sol. Cells* **2008**, *92*, 753–760.

8. Bibette, J.; Morse, D. C.; Witten, T. A.; D.A., W. Stability Criterion for Emulsions. *Phys. Rev. Lett.* **1992**, *69*, 2439–2444.

9. Krebs, F. C.; Tromholt, T.; Jørgensen, M. Upscaling of Polymer Solar Cell Fabrication Using Full Roll-to-Roll Processing. *Nanoscale* **2010**, *2*, 873–86.

10. Krebs, F. C. Fabrication and Processing of Polymer Solar Cells: A Review of Printing and Coating Techniques. *Sol. Energy Mater. Sol. Cells* **2009**, *93*, 394–412.

11. Venkatesan, S.; Ngo, E. C.; Chen, Q.; Dubey, A.; Mohammad, L.; Adhikari, N.; Mitul, A. F.; Qiao, Q. Benzothiadiazole-Based Polymer for Single and Double Junction Solar Cells with High Open Circuit Voltage. *Nanoscale* **2014**, 0–7.

12. Meillaud, F.; Shah, a.; Droz, C.; Vallat-Sauvain, E.; Miazza, C. Efficiency Limits for Single-Junction and Tandem Solar Cells. *Sol. Energy Mater. Sol. Cells* **2006**, *90*, 2952–2959.

13. Richards, J. J.; Weigandt, K. M.; Pozzo, D. C. Aqueous Dispersions of Colloidal Poly(3-Hexylthiophene) Gel Particles with High Internal Porosity. *J. Colloid Interface Sci.* **2011**, *364*, 341–50.

14. Richards, J. J.; Whittle, C. L.; Shao, G.; Pozzo, L. D. Correlating Structure and Photocurrent for Composite Semiconducting Nanoparticles with Contrast Variation Small-Angle Neutron Scattering and Photoconductive Atomic Force Microscopy. *ACS Nano* **2014**, *8*, 4313–24.

Bibliography

Administration, E. I. (2013). *Annual Energy Outlook 2013*. Retrieved from http://www.eia.gov/renewable/

Agüero, J. R., Member, S., & Steffel, S. J. (2011). Integration Challenges of Photovoltaic Distributed Generation on Power Distribution Systems. In *IEEE Power and Energy Society General Meeting* (pp. 1–6). doi:10.1109/PES.2011.6039097

Al-Ibrahim, M., Ambacher, O., Sensfuss, S., & Gobsch, G. (2005). Effects of solvent and annealing on the improved performance of solar cells based on poly(3-hexylthiophene): Fullerene. *Applied Physics Letters*, *86*(20), 1–3. doi:10.1063/1.1929875

Andersen, T. R., Larsen-Olsen, T. T., Andreasen, B., Böttiger, A. P. L., Carlé, J. E., Helgesen, M., … Krebs, F. C. (2011). Aqueous processing of low-band-gap polymer solar cells using roll-to-roll methods. *ACS nano*, *5*(5), 4188–96. doi:10.1021/nn200933r

Babonneau, D. (2010). FitGISAXS : software package for modelling and analysis of GISAXS data using IGOR Pro. *Journal of Applied Crystallography*, *43*(4), 929–936. doi:10.1107/S0021889810020352

Bakshi, M. S. (1993). Micelle Formation by Anionic and Cationic Surfactants in Binary Aqueous Solvents. *Journal of Chemistry Society of Faraday Transcripts*, *89*(24), 4323–4326.

Barker, J. G., Glinka, C. J., Moyer, J. J., Kim, M. H., Drews, a. R., & Agamalian, M. (2005). Design and performance of a thermal-neutron double-crystal diffractometer for USANS at NIST. *Journal of Applied Crystallography*, *38*(6), 1004–1011. doi:10.1107/S0021889805032103

Baroud, C. N., Gallaire, F., & Dangla, R. (2010). Dynamics of microfluidic droplets. *Lab on a chip*, *10*(16), 2032–45. doi:10.1039/c001191f

Beaucage, G. (2004). Determination of branch fraction and minimum dimension of mass-fractal aggregates. *Physical Review E*, *70*(3), 031401. doi:10.1103/PhysRevE.70.031401

Begovic, M. M., Kim, I., Novosel, D., Aguero, J. R., & Rohatgi, A. (2012). Integration of Photovoltaic Distributed Generation in the Power Distribution Grid. *2012 45th Hawaii International Conference on System Sciences*, 1977–1986. doi:10.1109/HICSS.2012.335

Berg, J. C. (2009). *An Introduction to Interfaces and colloids - Bridge to Nanoscience* (pp. 1–300).

Bertho, S., Janssen, G., Cleij, T. J., Conings, B., Moons, W., Gadisa, A., … Vanderzande, D. (2008). Effect of temperature on the morphological and photovoltaic stability of bulk heterojunction polymer:fullerene solar cells. *Solar Energy Materials and Solar Cells*, *92*(7), 753–760. doi:10.1016/j.solmat.2008.01.006

Bertho, S., Oosterbaan, W. D., Vrindts, V., D'Haen, J., Cleij, T. J., Lutsen, L., … Vanderzande, D. (2009). Controlling the morphology of nanofiber-P3HT:PCBM blends for organic bulk heterojunction solar cells. *Organic Electronics*, *10*(7), 1248–1251. doi:10.1016/j.orgel.2009.06.018

Bibette, J., Calderon, F. L., & Poulin, P. (1999). Emulsions : basic principles. *Reports on progress in physics. Physical Society*, *969*, 969–1033.

Bibette, J., Morse, D. C., Witten, T. A., & D.A., W. (1992). Stability Criterion for Emulsions. *Physical Review Letters*, *69*(16), 2439–2444.

Brabec, C. J., Sariciftci, N. S., & Hummelen, J. C. (2001). Plastic Solar Cells. *Advanced Functional Materials*, *11*(1), 15–26. doi:10.1002/1616-3028(200102)11:1<15::AID-ADFM15>3.0.CO;2-A

Brabec, Christoph J. (2004). Organic photovoltaics: technology and market. *Solar Energy Materials and Solar Cells*, *83*(2-3), 273–292. doi:10.1016/j.solmat.2004.02.030

Bull, T. a, Pingree, L. S. C., Jenekhe, S. a, Ginger, D. S., & Luscombe, C. K. (2009). The role of mesoscopic PCBM crystallites in solvent vapor annealed copolymer solar cells. *ACS nano*, *3*(3), 627–36. doi:10.1021/nn800878c

Bunauer, S., Deming, L. S., Deming, W. E., & Teller, E. (1940). On a Theory of the van der Waals Adsorption of Gases.

Chang, C.; Franses, E. I. Adsorption Dynamics of Surfactants at the Air/Water Interface: A Critical Review of Mathematical Models, Data, and Mechanisms. *Colloid and Surfaces A* **1995**, *100*, 1–45.

Chen, D., Liu, F., Wang, C., Nakahara, A., & Russell, T. P. (2011). Bulk Heterojunction Photovoltaic Active Layers via Bilayer. *Nano Letters*, *11*, 2071–2078.

Clark, J., Chang, J.-F., Spano, F. C., Friend, R. H., & Silva, C. (2009). Determining exciton bandwidth and film microstructure in polythiophene films using linear absorption spectroscopy. *Applied Physics Letters*, *94*(16), 163306. doi:10.1063/1.3110904

Coffey, D. C., Reid, O. G., Rodovsky, D. B., Bartholomew, G. P., & Ginger, D. S. (2007). Mapping local photocurrents in polymer/fullerene solar cells with photoconductive atomic force microscopy. *Nano letters*, *7*(3), 738–44. doi:10.1021/nl062989e

Conibeer, G. (2007). Third-Generation Photovoltaics. *Materials Today*, *10*(11), 42–50.

Cunningham, P. D., & Hayden, L. M. (2008). Carrier Dynamics Resulting from Above and Below Gap Excitation of P3HT and P3HT/PCBM Investigated by Optical-Pump Terahertz-Probe Spectroscopy. *Journal of Physical Chemistry C*, *112*(21), 7928–7935. doi:10.1021/jp711827g

Dang, M T, Hirsch, L., & Wantz, G. (2011). P3HT:PCBM, Best Seller in Polymer Photovoltaic Research. *Advanced Materials*, *23*(31), 3597–3602. doi:10.1002/adma.201100792

Dang, Minh Trung, Hirsch, L., & Wantz, G. (2011). P3HT:PCBM, Best Seller in Polymer Photovoltaic Research. *Advanced Materials*, *23*(31), 3597–3602. doi:10.1002/adma.201100792

Demers, H.; Ramachandra, R.; Drouin, D.; Jonge, N. de (2012) The Probe Profile and Lateral Resolution of Scanning Transmission Electron Microscopy of Thick Specimens. *Microscopy and Microanalytics.*, (18), 582–590.

Dennler, G., Scharber, M. C., & Brabec, C. J. (2009). Polymer-Fullerene Bulk-Heterojunction Solar Cells. *Advanced Materials*, *21*(13), 1323–1338. doi:10.1002/adma.200801283

Ehlers, J., Hepp, K., Board, E., Beig, R., Domcke, W., Frisch, U., … Jaffe, R. L. (2009). *Applications of Synchrotron Light to Scattering and Diffraction in Materials and Life Sciences* (pp. 1–330).

EIA. (2007). *Overview Energy Perspectives Consumption by Source*.

El Chaar, L., Lamont, L. a., & El Zein, N. (2011). Review of photovoltaic technologies. *Renewable and Sustainable Energy Reviews*, *15*(5), 2165–2175. doi:10.1016/j.rser.2011.01.004

Engl, W., Backov, R., & Panizza, P. (2008). Controlled production of emulsions and particles by milli- and microfluidic techniques. *Current Opinion in Colloid & Interface Science*, *13*(4), 206–216. doi:10.1016/j.cocis.2007.09.003

Erickson, D., & Li, D. (2001). Streaming Potential and Streaming Current Methods for Characterizing Heterogeneous Solid Surfaces. *Journal of colloid and interface science*, *237*(2), 283–289. doi:10.1006/jcis.2001.7476

Feigin, L. A., & Svergun, D. I. (1989). Structure analysis by small-angle X-ray and neutron scattering. *Acta Polymerica*, *40*(3), 224. doi:10.1002/actp.1989.010400317

Feigin, L.A., Svergun, D. I. (n.d.). *Structure Analysis by Small-Angle X-Ray Scattering and Neutron Scattering*.

Fthenakis, V. (2009). Sustainability of photovoltaics: The case for thin-film solar cells. *Renewable and Sustainable Energy Reviews*, *13*(9), 2746–2750. doi:10.1016/j.rser.2009.05.001

Futterer, T., Vliegenthart, G. A., & Lang, P. R. (2004). Particle Scattering Factor of Janus Micelles. *Macromolecules*, *37*, 8407–8413.

Ginger, D. S., Giridharagopal, R., Rayermann, G., Reid, O., Moore, D., & Shao, G. Z. (2011). Time-resolved electrostatic force microscopy on conjugated polymer blends. *Abstracts of Papers of the American Chemical Society*, *242*. Retrieved from <Go to ISI>://WOS:000299378306346

Glatter, O., & Kratky, O. (1982). *Small Angle X-Ray Scattering*. Academic Press Inc.

Glinka, C. J., Barker, J. G., Hammouda, B., & Krueger, S. (1998). The 30 m Small-Angle Neutron Scattering Instruments at the National Institute of Standards and Technology. *Journal of Applied Crystallography*, *31*(May 1991), 430–445.

Green, M. A., Emery, K., Hishikawa, Y., & Warta, W. (2009). Solar Cell Efficiency Tables, *2008*, 85–94. doi:10.1002/pip

Gregg, B. A., Ferrere, S., & Pichot, F. (2002). Interfacial Processes in Organic-Based Solar Cells. *Organic Photovoltaics II*, *4465*(303), 31–42.

Guinier, A., & Fournet, G. (1955). *Small angle scattering of X-rays* (p. 7.50). Wiley, New York.

Günes, S., Neugebauer, H., & Sariciftci, N. S. (2007). Conjugated polymer-based organic solar cells. *Chemical reviews*, *107*(4), 1324–38. doi:10.1021/cr050149z

Hegedus, S., & Luque, A. (2011). Achievements and Challenges of Solar electricity from Photovoltaics. *Handbook of Photovoltaic Science and Engineering, Second Edition*, 1–38.

Henderson, S. J. (1996). Monte Carlo modeling of small-angle scattering data from non-interacting homogeneous and heterogeneous particles in solution. *Biophysical journal*, *70*(4), 1618–27. doi:10.1016/S0006-3495(96)79725-4

Holmes, N. P., Burke, K. B., Sista, P., Barr, M., Magurudeniya, H. D., Stefan, M. C., … Belcher, W. J. (2013). Nano-domain behaviour in P3HT:PCBM nanoparticles, relating material properties to morphological changes. *Solar Energy Materials and Solar Cells*, *117*, 437–445. doi:10.1016/j.solmat.2013.06.003

Hoppe, H., & Sariciftci, N. S. (2006). Morphology of polymer/fullerene bulk heterojunction solar cells. *Journal of Materials Chemistry*, *16*(1), 45. doi:10.1039/b510618b

Hoppe, H., & Sariciftci, N. S. (2011). Organic solar cells: An overview. *Journal of Materials Research*, *19*(07), 1924–1945. doi:10.1557/JMR.2004.0252

Israelachvili, J. N. (2011). *Intermolecular and Surface Forces* (Third., pp. 1–674). Elsevier.

Jamieson, F. C., Domingo, E. B., McCarthy-Ward, T., Heeney, M., Stingelin, N., & Durrant, J. R. (2012). Fullerene crystallisation as a key driver of charge separation in polymer/fullerene bulk heterojunction solar cells. *Chemical Science*, *3*(2), 485. doi:10.1039/c1sc00674f

Jorgensen, M., Norrman, K., & Krebs, F. C. (2008). Stability/degradation of polymer solar cells. *Solar Energy Materials and Solar Cells*, *92*(7), 686–714. doi:DOI 10.1016/j.solmat.2008.01.005

Jørgensen, M., Norrman, K., & Krebs, F. C. (2008). Stability/degradation of polymer solar cells. *Solar Energy Materials and Solar Cells*, *92*(7), 686–714. doi:10.1016/j.solmat.2008.01.005

Kawai, T., Nazakazono, M., Sugimoto, R., & Yoshino, K. (19992). Crystal Structure of Poly(3-alkythiophene) and Its Doping Affect. *Journal of The Physical Society of Japan*, *61*(9), 3400–3406.

Kaya, H. (2002). Scattering behaviour of Janus particles. *Applied Physics A.*, *74*, 507–509.

Kietzke, T. (2004). Nanostructured solar cells based on semiconducting polymer nanospheres (SPNs) of M3EH-PPV and CN-Ether-PPV. *Proceedings of SPIE, 5215*, 206–210. doi:10.1117/12.505458

Kietzke, T. (2007). Recent Advances in Organic Solar Cells. *Advances in OptoElectronics*, *2007*, 1–15. doi:10.1155/2007/40285

Kietzke, T., Neher, D., Kumke, M., Ghazy, O., Ziener, U., & Landfester, K. (2007a). Phase separation of binary blends in polymer nanoparticles. *Small*, *3*(6), 1041–8. doi:10.1002/smll.200600606

Kietzke, T., Neher, D., Kumke, M., Ghazy, O., Ziener, U., & Landfester, K. (2007b). Phase separation of binary blends in polymer nanoparticles. *Small (Weinheim an der Bergstrasse, Germany)*, *3*(6), 1041–8. doi:10.1002/smll.200600606

Kippelen, B., & Brédas, J.-L. (2009). Organic photovoltaics. *Energy & Environmental Science*, *2*(3), 251. doi:10.1039/b812502n

Kline, S. R. (2006). Reduction and analysis of SANS and USANS data using IGOR Pro. *Journal of Applied Crystallography*, *39*(6), 895–900. doi:10.1107/S0021889806035059

Koppe, M., Brabec, C. J., Heiml, S., Schausberger, A., Duffy, W., Heeney, M., & McCulloch, I. (2009). Influence of Molecular Weight Distribution on the Gelation of P3HT and Its Impact on the Photovoltaic Performance. *Macromolecules*, *42*(13), 4661–4666. doi:10.1021/ma9005445

Kosmulski, M. (2002). The pH-dependent surface charging and the points of zero charge. *Journal of colloid and interface science*, *253*(1), 77–87. doi:10.1006/jcis.2002.8490

Krebs, Frederik C, Tromholt, T., & Jørgensen, M. (2010). Upscaling of polymer solar cell fabrication using full roll-to-roll processing. *Nanoscale*, *2*(6), 873–86. doi:10.1039/b9nr00430k

Krebs, Frederik C. (2009). Fabrication and processing of polymer solar cells: A review of printing and coating techniques. *Solar Energy Materials and Solar Cells*, *93*(4), 394–412. doi:10.1016/j.solmat.2008.10.004

Krebs, Frederik C., Biancardo, M., Winther-Jensen, B., Spanggard, H., & Alstrup, J. (2006). Strategies for incorporation of polymer photovoltaics into garments and textiles. *Solar Energy Materials and Solar Cells*, *90*(7-8), 1058–1067. doi:10.1016/j.solmat.2005.06.003

Krebs, Frederik C., Gevorgyan, S. a., & Alstrup, J. (2009). A roll-to-roll process to flexible polymer solar cells: model studies, manufacture and operational stability studies. *Journal of Materials Chemistry*, *19*(30), 5442. doi:10.1039/b823001c

Lake, J. a. (1967). An iterative method of slit-correcting small angle X-ray data. *Acta Crystallographica*, *23*(2), 191–194. doi:10.1107/S0365110X67002440

Landfester, B. K., Montenegro, R., Scherf, U., Güntner, R., Asawapirom, U., Patil, S., … Kietzke, T. (2002b). Semiconducting Polymer Nanospheres in Aqueous Dispersion Prepared by. *Advanced Materials*, *14*(9), 651–655.

Landfester, K. (2001). The Generation of Nanoparticles in Miniemulsions. *Advanced Materials*, *13*(10), 765–768. doi:10.1002/1521-4095(200105)13:10<765::AID-ADMA765>3.0.CO;2-F

Landfester, K. (2006). Synthesis of Colloidal Particles in Miniemulsions. *Annual Review of Materials Research*, *36*(1), 231–279. doi:10.1146/annurev.matsci.36.032905.091025

Landfester, Katharina. (2009). Miniemulsion polymerization and the structure of polymer and hybrid nanoparticles. *Angewandte Chemie (International ed. in English)*, *48*(25), 4488–507. doi:10.1002/anie.200900723

Larson-Smith, K., Jackson, A., & Pozzo, D. C. (2010). Small angle scattering model for Pickering emulsions and raspberry particles. *Journal of colloid and interface science*, *343*(1), 36–41. doi:10.1016/j.jcis.2009.11.033

Laurence Boulange-Petermann, A. Doren, B. Baroux, M.-N. B.-F. (1995). Zeta Potential Measurements on Passive Materials. *Journal of colloid and interface science*, *171*(1), 179–186.

Lazzari, Remi. (2010). IsGISAXS Manual. Retrieved from http://ln-www.insp.upmc.fr/axe4/Oxydes/IsGISAXS/isgisaxs.htm

Lazzari, Rémi, Leroy, F., & Renaud, G. (2007). Grazing-incidence small-angle x-ray scattering from dense packing of islands on surfaces: Development of distorted wave Born approximation and correlation between particle sizes and spacing. *Physical Review B*, *76*(12), 125411. doi:10.1103/PhysRevB.76.125411

Lebedev, D. V., Filatov, M. V., Kuklin, a. I., Islamov, a. K., Stellbrink, J., Pantina, R. a., … Isaev-Ivanov, V. V. (2008). Structural hierarchy of chromatin in chicken erythrocyte nuclei based on small-angle neutron scattering: Fractal nature of the large-scale chromatin organization. *Crystallography Reports*, *53*(1), 110–115. doi:10.1134/S1063774508010136

Lee, E. M., & Koopal, L. K. (1996). Adsorption of Cationic and Anionic Surfactants on Metal Oxide Surfaces : Surface Charge Adjustment and Competition Effects. *Journal of colloid and interface science*, *177*, 478–489.

Lee, S. H., Lee, Y. B., Park, D. H., Kim, M. S., Cho, E. H., & Joo, J. (2011). Tuning optical properties of poly(3-hexylthiophene) nanoparticles through hydrothermal processing. *Science and Technology of Advanced Materials*, *12*(2). doi:10.1088/1468-6996/12/2/025002

Li, C.-Z., Chien, S.-C., Yip, H.-L., Chueh, C.-C., Chen, F.-C., Matsuo, Y., … Jen, A. K.-Y. (2011). Facile synthesis of a 56π-electron 1,2-dihydromethano-[60]PCBM and its application for thermally stable polymer solar cells. *Chemical communications (Cambridge, England)*, *47*(36), 10082–4. doi:10.1039/c1cc14446d

Li, G., Shrotriya, V., Huang, J., Yao, Y., Moriarty, T., Emery, K., & Yang, Y. (2005). High-efficiency solution processable polymer photovoltaic cells by self-organization of polymer blends. *Nature Materials*, *4*(11), 864–868. doi:10.1038/nmat1500

Li, LiGui, Lu, G., Yang, X., & Zhou, E. (2007). Progress in polymer solar cell. *Chinese Science Bulletin*, *52*(2), 145–158. doi:10.1007/s11434-007-0001-y

Li, Ligui, Tang, H., Wu, H., Lu, G., & Yang, X. (2009). Effects of fullerene solubility on the crystallization of poly(3-hexylthiophene) and performance of photovoltaic devices. *Organic Electronics*, *10*(7), 1334–1344. doi:10.1016/j.orgel.2009.07.016

Lindner, P, Zemb, T. (2002). *Neutrons, X-rays and Light: Scattering Methods Applied to Soft Condensed Matter*. North-Holland.

Lloyd, M. T., Peters, C. H., Garcia, A., Kauvar, I. V., Berry, J. J., Reese, M. O., … Olson, D. C. (2011). Influence of the hole-transport layer on the initial behavior and lifetime of inverted organic photovoltaics. *Solar Energy Materials and Solar Cells*, *95*(5), 1382–1388. doi:10.1016/j.solmat.2010.12.036

Loxley, A., & Vincent, B. (1998). Preparation of Poly(methylemethacrylate) Microcapsules with Liquid Cores. *Journal of colloid and interface science*, *208*, 49–62.

Malik, S., & Nandi, A. K. (2006). Influence of Alkyl Chain Length on the Gelation Mechanism of Thermoreversible Gels of Regioregular Poly (3-alkyl thiophenes) in Xylene. *Journal of Applied Polymer Science*, *103*, 2528–2537. doi:10.1002/app

Manceau, M., Rivaton, A., Gardette, J.-L., Guillerez, S., & Lemaître, N. (2009). The mechanism of photo- and thermooxidation of poly(3-hexylthiophene) (P3HT) reconsidered. *Polymer Degradation and Stability*, *94*(6), 898–907. doi:10.1016/j.polymdegradstab.2009.03.005

Mangelsdorf, C. S., & White, L. R. (1990). Effects of stern-layer conductance on electrokinetic transport properties of colloidal particles. *Journal of the Chemical Society, Faraday Transactions*, *86*(16), 2859. doi:10.1039/ft9908602859

Marinova, K. G., Alargova, R. G., Denkov, N. D., Velev, O. D., Petsev, D. N., Ivanov, I. B., & Borwankar, R. P. (1996). Charging of Oil - Water Interfaces Due to Spontaneous Adsorption of Hydroxyl Ions. *Langmuir*, *12*, 2045–2051.

Marshall, J. C., Cosgrove, T., Leermakers, F., Obey, T. M., & Dreiss, C. a. (2004). Detailed modeling of the volume fraction profile of adsorbed polymer layers using small-angle neutron scattering. *Langmuir*, *20*(11), 4480–8. Retrieved from http://www.ncbi.nlm.nih.gov/pubmed/15969155

Medford, A. J., Lilliedal, M. R., Jørgensen, M., Aarø, D., Pakalski, H., Fyenbo, J., & Krebs, F. C. (2010). Grid-connected polymer solar panels: initial considerations of cost, lifetime, and practicality. *Optics express*, *18 Suppl 3*(May), A272–85.

Meillaud, F., Shah, a., Droz, C., Vallat-Sauvain, E., & Miazza, C. (2006). Efficiency limits for single-junction and tandem solar cells. *Solar Energy Materials and Solar Cells*, *90*(18-19), 2952–2959. doi:10.1016/j.solmat.2006.06.002

Montenegro, R., & Landfester, K. (2003). Metastable and Stable Morphologies during Crystallization of Alkanes in Miniemulsion Droplets. *Langmuir*, *19*(15), 5996–6003.

Moslehi, K., Kumar, R., & Member, S. (2010). A Reliability Perspective of the Smart Grid. *IEEE*, *1*(1), 57–64.

Moulé, a. J., & Meerholz, K. (2008). Controlling Morphology in Polymer–Fullerene Mixtures. *Advanced Materials*, *20*(2), 240–245. doi:10.1002/adma.200701519

Moulé, A. J., & Meerholz, K. (2009). Morphology Control in Solution-Processed Bulk-Heterojunction Solar Cell Mixtures. *Advanced Functional Materials*, *19*(19), 3028–3036. doi:10.1002/adfm.200900775

Müller, C., Ferenczi, T. a. M., Campoy-Quiles, M., Frost, J. M., Bradley, D. D. C., Smith, P., … Nelson, J. (2008). Binary Organic Photovoltaic Blends: A Simple Rationale for Optimum Compositions. *Advanced Materials*, *20*(18), 3510–3515. doi:10.1002/adma.200800963

Müller-Buschbaum, P. (2003). Grazing incidence small-angle X-ray scattering: an advanced scattering technique for the investigation of nanostructured polymer films. *Analytical and bioanalytical chemistry*, *376*(1), 3–10. doi:10.1007/s00216-003-1869-2

Newbloom, G M, Kim, F. S., Jenekhe, S. A., & Pozzo, D. C. (2011). Mesoscale Morphology and Charge Transport in Colloidal Networks of Poly(3-hexylthiophene). *Macromolecules*, *44*(10), 3801–3809. doi:10.1021/ma2000515

Newbloom, G M, Weigandt, K. M., & Pozzo, D. C. (2012). Structure and property development of poly(3-hexylthiophene) organogels probed with combined rheology, conductivity and small angle neutron scattering. *Soft Matter*, *8*(34), 8854–8864. doi:10.1039/c2sm26114f

Newbloom, Gregory M, Weigandt, K. M., & Pozzo, D. C. (2012). Electrical, Mechanical, and Structural Characterization of Self-Assembly in Poly(3-hexylthiophene) Organogel Networks. *Macromolecules*, *45*(8). doi:10.1021/ma202564k

Noriega, R., Rivnay, J., Vandewal, K., Koch, F. P. V, Stingelin, N., Smith, P., … Salleo, A. (2013). A general relationship between disorder, aggregation and charge transport in conjugated polymers. *Nature materials*, *12*(11), 1038–44. doi:10.1038/nmat3722

Pal, R. (2007). *Rheology of Particulate Dispersions and Composites* (pp. 1–300).

Pedersen, J. S., Posselt, D., & Mortensen, K. (1990). Analytical treatment of the resolution function for small-angle scattering. *Journal of Applied Crystallography*, *23*(4), 321–333. doi:10.1107/S0021889890003946

Pedersen, Jan Skov. (1997). Analysis of small-angle scattering data from colloids and polymer solutions: modeling and least-squares fitting. *Advances in Colloid and Interface Science*, *70*, 171–210. doi:10.1016/S0001-8686(97)00312-6

Pedersen, Jan Skov. (2001). Structure factors effects in small-angle scattering from block copolymer micelles and star polymers. *Journal of Chemical Physics*, *114*(6), 2839. doi:10.1063/1.1339221

Percus, J. K., & Yevick, G. J. (1958). Analysis of Classical Statistical Mechanics by Means of Collective Coordinates. *The Physical Review*, *110*(1), 1–13.

Pingree, L. S. C., Reid, O. G., & Ginger, D. S. (2009). Electrical Scanning Probe Microscopy on Active Organic Electronic Devices. *Advanced Materials*, *21*(1), 19–28. doi:10.1002/adma.200801466

Piok, T., Gadermaier, C., Wenzl, F. P., Patil, S., Montenegro, R., Landfester, K., … List, E. J. W. (2004). The photophysics of organic semiconducting nanospheres: a comprehensive study. *Chemical Physics Letters*, *389*(1-3), 7–13. doi:10.1016/j.cplett.2004.03.018

Rauscher, M., Salditt, T., & Spohn, H. (1995). Small-angle X-Ray Scattering Under Grazing Incidence: The Cross Section in the Distorted-Wave Born Approximation. *Physical Review B*, *52*(23), 1–11.

Rice, A. H., Giridharagopal, R., Zheng, S. X., Ohuchi, F. S., Ginger, D. S., & Luscombe, C. K. (2011). Controlling Vertical Morphology within the Active Layer of Organic Photovoltaics Using Poly(3-hexlythiophene) Nanowires and Phenyl-C61-Butyric Acid Methyl Ester. *ACS Nano*, *5*(4), 3132–3140.

Richards, J. J., Rice, A. H., Nelson, R. D., Kim, F. S., Jenekhe, S. a., Luscombe, C. K., & Pozzo, D. C. (2013). Modification of PCBM Crystallization via Incorporation of C 60 in Polymer/Fullerene Solar Cells. *Advanced Functional Materials*, *23*(4), 514–522. doi:10.1002/adfm.201201100

Richards, J. J., Weigandt, K. M., & Pozzo, D. C. (2011). Aqueous dispersions of colloidal poly(3-hexylthiophene) gel particles with high internal porosity. *Journal of colloid and interface science*, *364*(2), 341–50. doi:10.1016/j.jcis.2011.08.037

Richards, J. J., Whittle, C. L., Shao, G., & Pozzo, L. D. (2014). Correlating structure and photocurrent for composite semiconducting nanoparticles with contrast variation small-angle neutron scattering and photoconductive atomic force microscopy. *ACS nano*, *8*(5), 4313–24. doi:10.1021/nn405914g

Salleo, A., Kline, R. J., DeLongchamp, D. M., & Chabinyc, M. L. (2010). Microstructural characterization and charge transport in thin films of conjugated polymers. *Advanced materials (Deerfield Beach, Fla.)*, *22*(34), 3812–38. doi:10.1002/adma.200903712

SasView. (n.d.). Retrieved from SasView, http://www.sasview.org/

Schmidt, B. Y. P. W. (1991). Small-Angle Scattering Studies of Disordered , Porous and Fraetal Systems, 414–435.

Schubert, M. B., & Werner, J. H. (2006). Flexible solar cells for clothing. *Materials Today*, *9*(6), 42–50. doi:10.1016/s1369-7021(06)71542-5

Shrotriya, V. (2009). Polymer power. *Nature Photonics*, *3*(8), 447–449. Retrieved from <Go to ISI>://WOS:000268935200015

Siegfried, M. J., & Choi, K.-S. (2006). Elucidating the effect of additives on the growth and stability of Cu2O surfaces via shape transformation of pre-grown crystals. *Journal of the American Chemical Society*, *128*(32), 10356–7. doi:10.1021/ja063574y

Singh, K., & Tirumkudulu, M. (2007). Cracking in Drying Colloidal Films. *Physical Review Letters*, *98*(21), 218302. doi:10.1103/PhysRevLett.98.218302

Sivula, K., Ball, Z. T., Watanabe, N., & Fréchet, J. M. J. (2006). Amphiphilic Diblock Copolymer Compatibilizers and Their Effect on the Morphology and Performance of Polythiophene:Fullerene Solar Cells. *Advanced Materials*, *18*(2), 206–210. doi:10.1002/adma.200501787

Spano, F. C., Clark, J., Silva, C., & Friend, R. H. (2009). Determining exciton coherence from the photoluminescence spectral line shape in poly(3-hexylthiophene) thin films. *The Journal of chemical physics*, *130*(7), 074904. doi:10.1063/1.3076079

Spano, F. C., & Introduction, I. (2010). The Spectral Signatures of Frenkel Polarons in, *43*(3), 429–439.

Stapleton, A., Vaughan, B., Xue, B., Sesa, E., Burke, K., Zhou, X., … Dastoor, P. (2012). A multilayered approach to polyfluorene water-based organic photovoltaics. *Solar Energy Materials and Solar Cells*, *102*, 114–124. doi:10.1016/j.solmat.2012.03.016

Stribeck, N. (2009). *Applications of Synchrotron Light to Scattering and Diffraction in Materials and Life Sciences*. (M. Gomez, A. Nogales, M. C. Garcia-Gutierrez, & T. A. Ezquerra, Eds.) (Vol. 776, pp. 23–60). Berlin, Heidelberg: Springer Berlin Heidelberg. doi:10.1007/978-3-540-95968-7

Stuhrmann, H B. (1974). Neutron Small-Angle Scattering of Biological Macromolecules in Solution. *Journal of App*, *7*(1), 173–178.

Stuhrmann, H B, Koch, M. H., Parfait, R., Haas, J., Ibel, K., & Crichton, R. R. (1977). Shape of the 50S subunit of Escherichia coli ribosomes. *Proceedings of the National Academy of Sciences of the United States of America*, *74*(6), 2316–20. Retrieved from http://www.pubmedcentral.nih.gov/articlerender.fcgi?artid=432161&tool=pmcentrez&rendertype=abstract

Stuhrmann, H. B., & Miller, a. (1978). Small-angle scattering of biological structures. *Journal of Applied Crystallography*, *11*(5), 325–345. doi:10.1107/S0021889878013473

Sun, Y., Seo, J. H., Takacs, C. J., Seifter, J., & Heeger, A. J. (2011). Inverted polymer solar cells integrated with a low-temperature-annealed sol-gel-derived ZnO Film as an electron transport layer. *Advanced materials (Deerfield Beach, Fla.)*, *23*(14), 1679–83. doi:10.1002/adma.201004301

Taden, A., Landfester, K., & Antonietti, M. (2004). Crystallization of dyes by directed aggregation of colloidal intermediates: a model case. *Langmuir : the ACS journal of surfaces and colloids*, *20*(3), 957–61. Retrieved from http://www.ncbi.nlm.nih.gov/pubmed/15773129

Tah, B., Pal, P., Mahato, M., & Talapatra, G. B. (2011). Aggregation behavior of SDS/CTAB catanionic surfactant mixture in aqueous solution and at the air/water interface. *The journal of physical chemistry. B*, *115*(26), 8493–9. doi:10.1021/jp202578s

Tang, W. (1985). Two layer organic photovoltaic cell. *Applied Physics Letters*, *48*(2), 183–185.

Tate, M.P., & Hillhouse, H. W. (2007). General Method for Simulation of 2D GISAXS Intensities for Any Nanostructured Film Using Discrete Fourier Transforms. *Journal of Physical Chemistry C*, *111*(21), 7645–7654. doi:10.1021/jp066111n

Tate, Michael P, Urade, V. N., Kowalski, J. D., Wei, T., Hamilton, B. D., Eggiman, B. W., & Hillhouse, H. W. (2006). Simulation and interpretation of 2D diffraction patterns from self-assembled nanostructured films at arbitrary angles of incidence: from grazing incidence (above the critical angle) to transmission perpendicular to the substrate. *The journal of physical chemistry. B*, *110*(20), 9882–92. doi:10.1021/jp0566008

Teixeira, J. (1988). Small-angle scattering by fractal systems. *Journal of Applied Crystallography*, *21*(6), 781–785. doi:10.1107/S0021889888000263

Tjioe, E., & Heller, W. T. (2007). ORNL_SAS : software for calculation of small-angle scattering intensities of proteins and protein complexes. *Journal of Applied Crystallography*, *40*(4), 782–785. doi:10.1107/S002188980702420X

Treat, N. D., Brady, M. a., Smith, G., Toney, M. F., Kramer, E. J., Hawker, C. J., & Chabinyc, M. L. (2011). Interdiffusion of PCBM and P3HT Reveals Miscibility in a Photovoltaically Active Blend. *Advanced Energy Materials*, *1*(1), 82–89. doi:10.1002/aenm.201000023

Troshin, P. a., Hoppe, H., Renz, J., Egginger, M., Mayorova, J. Y., Goryachev, A. E., … Razumov, V. F. (2009). Material Solubility-Photovoltaic Performance Relationship in the Design of Novel Fullerene Derivatives for Bulk Heterojunction Solar Cells. *Advanced Functional Materials*, *19*(5), 779–788. doi:10.1002/adfm.200801189

Tsai, J.-H., Lai, Y.-C., Higashihara, T., Lin, C.-J., Ueda, M., & Chen, W.-C. (2010). Enhancement of P3HT/PCBM Photovoltaic Efficiency Using the Surfactant of Triblock Copolymer Containing Poly(3-hexylthiophene) and Poly(4-vinyltriphenylamine) Segments. *Macromolecules*, *43*(14), 6085–6091. doi:10.1021/ma1011182

Ulum, S., Holmes, N., Darwis, D., Burke, K., David Kilcoyne, a. L., Zhou, X., … Dastoor, P. (2013a). Determining the structural motif of P3HT:PCBM nanoparticulate organic photovoltaic devices. *Solar Energy Materials and Solar Cells*, *110*, 43–48. doi:10.1016/j.solmat.2012.11.015

Umbanhowar, P. B., Prasad, V., & Weitz, D. a. (2000). Monodisperse Emulsion Generation via Drop Break Off in a Coflowing Stream. *Langmuir*, *16*(2), 347–351. doi:10.1021/la990101e

Urade, V. N., Bollmann, L., Kowalski, J. D., Tate, M. P., & Hillhouse, H. W. (2007). Controlling interfacial curvature in nanoporous silica films formed by evaporation-induced self-assembly from nonionic surfactants. II. Effect of processing parameters on film structure. *Langmuir : the ACS journal of surfaces and colloids*, *23*(8), 4268–78. doi:10.1021/la062641z

Vandewal, K., Himmelberger, S., & Salleo, A. (2013). Structural Factors That Affect the Performance of Organic Bulk Heterojunction Solar Cells. *Macrom*, *46*, 6379–6387.

Venkatesan, S., Ngo, E. C., Chen, Q., Dubey, A., Mohammad, L., Adhikari, N., … Qiao, Q. (2014). Benzothiadiazole-based polymer for single and double junction solar cells with high open circuit voltage. *Nanoscale*, 0–7. doi:10.1039/c4nr01040j

Vineyard, G. H. (1982). Grzing-Incidence Diffraction and the Distorted-Wave Approximation for the Study of Surfaces. *Physical Review B*, *26*(8), 1–14.

Voroshazi, E., Verreet, B., Aernouts, T., & Heremans, P. (2011). Long-term operational lifetime and degradation analysis of P3HT:PCBM photovoltaic cells. *Solar Energy Materials and Solar Cells*, *95*(5), 1303–1307. doi:10.1016/j.solmat.2010.09.007

Walker, S. L., Bhattacharjee, S., Hoek, E. M. V., & Elimelech, M. (2002). A Novel Asymmetric Clamping Cell for Measuring Streaming Potential of Flat Surfaces. *Langmuir*, *18*(6), 2193–2198. doi:10.1021/la011284j

Winkler, K., Paszewski, M., Kalwarczyk, T., Kalwarczyk, E., Wojciechowski, T., Gorecka, E., … Fialkowski, M. (2011). Ionic Strength-Controlled Deposition of Charged Nanoparticles on a Solid Substrate. *The Journal of Physical Chemistry C*, *115*(39), 19096–19103. doi:10.1021/jp206704s

Wolden, C. a., Kurtin, J., Baxter, J. B., Repins, I., Shaheen, S. E., Torvik, J. T., … Aydil, E. S. (2011). Photovoltaic manufacturing: Present status, future prospects, and research needs. *Journal of Vacuum Science & Technology A: Vacuum, Surfaces, and Films*, *29*(3), 030801. doi:10.1116/1.3569757

Wu, W.-R., Jeng, U.-S., Su, C.-J., Wei, K.-H., Su, M.-S., Chiu, M.-Y., … Su, A.-C. (2011). Competition between Fullerene Crystallization upon Annealing of Bulk. *ACS Nano*, *5*(8), 6233–6243.

Yang, J., Zhu, R., Hong, Z., He, Y., Kumar, A., Li, Y., & Yang, Y. (2011). A robust inter-connecting layer for achieving high performance tandem polymer solar cells. *Advanced materials (Deerfield Beach, Fla.)*, *23*(30), 3465–70. doi:10.1002/adma.201100221

Yobas, L., Martens, S., Ong, W.-L., & Ranganathan, N. (2006). High-performance flow-focusing geometry for spontaneous generation of monodispersed droplets. *Lab on a chip*, *6*(8), 1073–9. doi:10.1039/b602240e

Zhang, Q., Wang, M., & Wooley, K. (2005). Nanoscopic Confinement of Semi-Crystalline Polymers. *Current Organic Chemistry*, *9*(11), 1053–1066. doi:10.2174/1385272054368466

Zhang, R., & Somasundaran, P. (2006). Advances in adsorption of surfactants and their mixtures at solid/solution interfaces. *Advances in colloid and interface science*, *123-126*, 213–29. doi:10.1016/j.cis.2006.07.004

Zhao, J., Swinnen, A., Van Assche, G., Manca, J., Vanderzande, D., & Van Mele, B. (2009). Phase diagram of P3HT/PCBM blends and its implication for the stability of morphology. *The journal of physical chemistry. B*, *113*(6), 1587–91. doi:10.1021/jp804151a